# Precise Measurements of Few-Body Physics in Ultracold $^{39}$K Bose Gas

by

**Roman Chapurin**

B.S. Physics, University of Florida, 2012

M.S. Physics, University of Colorado, 2015

A thesis submitted to the

Faculty of the Graduate School of the

University of Colorado in partial fulfillment

of the requirements for the degree of

Doctor of Philosophy

Department of Physics

2019

This thesis entitled:
Precise Measurements of Few-Body Physics in Ultracold $^{39}$K Bose Gas
written by Roman Chapurin
has been approved for the Department of Physics

_____

Prof. Eric A. Cornell

_____

Prof. Jun Ye

Date _____

The final copy of this thesis has been examined by the signatories, and we find that both the content and the form meet acceptable presentation standards of scholarly work in the above mentioned discipline.

Roman Chapurin, (Ph.D., Physics)

Precise Measurements of Few-Body Physics in Ultracold $^{39}$K Bose Gas

Thesis directed by Prof. Eric A. Cornell

Ultracold atomic gases with tunable interactions offer an ideal platform for studying interacting quantum matter. While the few- and many-body physics are generally complex and intractable, the problem can be greatly simplified in an atomic gas by a controlled separation of relevant length and energy scales. Precise control of experimental parameters, via Feshbach resonances, optical potentials and radio-frequency radiation, enables deterministic measurements of few-body physics, including universal physics and the Efimov effect. This thesis presents our recent studies on precisely measuring two- and three-body physics in an ultracold Bose gas. I begin by describing our new apparatus used for generating and studying ultracold $^{39}$K gas samples. Then, I focus on our precision spectroscopy of Feshbach dimer binding energies, spanning three orders of magnitude and with sub-kilohertz resolution. These measurements enable us to locate a Feshbach resonance and determine scattering length values with unprecedented accuracy. Finally, I present our precise measurements locating an exotic three-body state, specifically the Efimov ground state. We find that the trimer state location significantly deviates from the value predicted by van der Waals universality. Due to small experimental and systematic uncertainties, our measurement is the strongest evidence of departure from the universal value and is the first observed deviation near a Feshbach resonance of intermediate strength.

## Dedication

To my family, for your unconditional support and encouragement.

## Acknowledgements

I was very fortunate to be surrounded by so many bright and exciting individuals during my PhD studies at JILA. I am forever thankful to Debbie Jin for giving me an opportunity and taking me under her wing. Debbie invested a significant amount of time in me and all her students, bettering us as scientists and helping us grow as individuals. I learned to question with humility, to always focus with great intensity on the important details in all aspects of life, to choose the less-traveled path, to find fun in the mundane, to be persistent and trust ones abilities, and to always ask "how difficult could that really be?". During the first four years of my PhD, Debbie was my academic advisor, a personal mentor and a role model; I hope to influence others in the same manner as she has. I want to express gratitude to Eric Cornell, Jun Ye, Cindy Regal, John Bohn and Krista Beck for support and encouragement after Debbie's passing, and all of JILA for coming together like family.

I want to thank my advisors Eric and Jun for forming the experimental team that accomplished the ambitious work presented in this thesis. Eric and Jun both have contagious personalities, inspiring and exciting everyone around them. I am always encouraged to explore new things and get things done after talking to them. I've always been impressed by Jun's ability to successfully lead multiple scientific endeavors, while maintaining extraordinary intensity, focus and devotion to his students. Jun's endless technical knowledge and intuition, along with a better memory retention than our lab's notebooks and computers, enabled fast progression in solving our toughest problems. I've always been impressed and inspired by Eric's unconventional approaches to solve simple and complex problems. Eric's energy is contagious, the lab's progress greatly benefited from the created

environment.

Building an atomic physics lab from scratch required great effort and could not have been accomplished without significant help. I am thankful to NIST and NSF for my graduate fellowships, which enabled me to "get to business" as soon as I stepped my foot on campus and to devote my focus fully on research. I am thankful to individuals of the $^{40}$K Fermi gas team I joined: Rabin Paudel, Tara Drake, and postdoc Yoav Sagi; they taught me a lot. I spent many days and nights with Rabin building up the apparatus; without his drive "to get things done today", it would have been very difficult to reach our goals in a timely manner. Additionally, we had multiple bright undergraduate students help with the construction. In particular, I want to thank Sean Braxton and Josh Giles for their hard work and persistence in getting things to work. I want to thank the KRb (now degenerate) polar molecules team for being good lab-neighbors and having empathy in building a complex apparatus, particularly Luigi DeMarco, Kyle Matsuda, Will Tobias, Giacomo Valtolina, Jacob Covey, Steven Moses, and Jamie Shaw. Additionally, others I've interacted with who underwent lab construction: Cornell/Ye eEDM team (Will Cairncross, Tanya Roussy, Kia Boon Ng, Yan Zhou, Yuval Shagam, Dan Gresh, Matt Grau), Ye Sr lab (Sara Campbell, Ed Marti, Aki Goban, Ross Hutson, Dhruv Kedar, Lindsay Sonderhouse), Thompson lab (Matt Norcia, Julia Cline), Nesbitt lab (Tim Large), Ye molecules lab (David Reens, Alejandra Collopy) and Regal lab (Brian Lester, Adam Kaufman) and Kaufman lab. I like to thank my office mates, Gil Porat, Tanya Roussy, Stephen Schoun, Yuval Shagam, and Marissa Weichman, for exchanging many ideas over the years.

It would have been difficult to construct such a complex apparatus without JILA's infrastructure and personnel. I spent a significant amount of time working with the instrument shop, particularly with Hans Green, Todd Asnicar, Tracy Keep, Kim Hagen, Blaine Horner, Kyle Thatche and Calvin Schwadron. Hans helped greatly during the initial construction, often working long days and nights with Rabin and I, and has been great to talk to for new ideas or encouragement. Todd always made sure that our shop requests were completed earlier than we anticipated. Custom, robust and low-noise electronics are the bread and butter of any atomic physics lab and I was

fortunate to learn from the JILA electronics group: Terry Brown, Carl Sauer, James Fung-A-Fat, Christopher Ho, and (unofficially) Jan Hall. Terry is a wizard of electronics and I've learned a lot from him. Carl was instrumental in solving many of our time-sensitive electronics problems by being quick and direct. Jan, who is always lurking around or soldering in the electronics shop, is full of technical wisdom and adventurous stories, often starring troublesome lasers. Our lab's stability and automation would not be possible without assistance from JILA's computing team, particularly J.R. Raith, Corey Keasling and Jim McKown, and building proctors, especially Dave Errickson and Jason Ketcherside. I am thankful to John Bohn and Jose D'Incao (our JILA theory colleagues), with who I can talk to beyond physics. The rest of the JILA staff and administration, especially Krista Beck, help us in so many ways that allow us truly focus on tackling scientific and technical challenges. I am thankful to all JILA fellows for keeping projects well-funded; the JILA grad students sleep well at night. Overall, the JILA culture and atmosphere are unlike any other. The fast-paced "whatever works" mentality (often entailing building own electronics, machining own parts or constructing homebuilt lasers), coupled with a great infrastructure and determined personnel, is always a good recipe for rapid scientific achievement and fast learning.

I spent the last two and a half years working with two talented individuals, Xin Xie and Michael Van de Graaff (Vandy). Prior to Debbie's passing, Xin, Vandy and I were Debbie's graduate students working on three different experiments. Afterward, Xin's and Vandy's laboratories were shut down and together we started our new venture, with Eric and Jun at the helm. We converted the new $^{40}$K Fermi lab to a $^{39}$K Bose machine in only 9 months. Such a rapid conversion would not have been possible without Xin and Vandy. Xin has an incredible work ethic and I am glad to have worked with a fellow stoic on challenging problems. She always encouraged everyone around her to push their limits. Vandy brought a lot of character and enthusiasm into our lab, and was willing to be the lab's perfectionist when needed. We also had help from hard working undergraduate students: Carlos Lopez-Abadia, Bjorn Sumner and Jared Popowski. Recently, we had a new graduate student Noah Schlossberger join our lab. With Xin (at the helm), Vandy, Noah and Jared, I know the lab is in good hands with many exciting results to come.

On a more personal note, I would like thank everyone who was there with me during my PhD years. I befriended many intelligent and fun individuals, including (forgive any exclusions) Rabin Paudel, Steven Moses, Luigi DeMarco, Sean Braxton, Dmitriy Zusin, Javier Orjuela-Koop, Maithreyi Gopalakrishnan, Joseph Samaniego, Peter Siegfried and Tim Livingston Large. I thank Gary Ihas for his mentorship and encouragement throughout the years. I am grateful to Aimee Graeber for all Colorado adventures and support. Last, I would like to thank my family for making sacrifices to help me get where I am today.

# Contents

**Chapter**

# Tables

**Table**

# Figures

**Figure**

# Chapter 1

# Introduction

## 1.1 Universal Physics with Ultracold Atoms

The world of quantum matter is fascinating. Systems exhibiting such phenomenon as superfluidity, superconductivity, quantum Hall physics, quantum magnetism and entanglement, enable quantum technologies for advanced sensing and computation. However, as the interaction strength and the system size increase, the complexity increases exponentially, making such systems harder to understand and engineer. For example, while systems that exhibit high-$T_c$ superconductivity, fractional quantum Hall effect, Hubbard model physics or topological order are deemed revolutionary, they are intricate and are of ongoing theoretical and experimental interest.

Since the onset of atom cooling and trapping [1, 2] and the first production of degenerate Bose [3], Fermi [4] and molecular gases [5], ultracold gases have been viewed as great quantum simulators of condensed matter systems [6, 7, 8, 9]. Precise control and imaging of atomic systems [10] enables simulation of quantum magnetism [9, 11], cold chemistry [11], high-$T_c$ superconductivity [12, 13, 14], a variety of many-body systems [15], disordered systems [16], synthetic gauge fields and quantum Hall physics [17, 18].

While quantum simulation with ultracold gases is a compelling topic, the physics of interacting ultracold gases is intriguing in its own right. The ability to control an ultracold system's dimensionality, thermal wavelength, quantum state, density, external potential and interactions (via Feshbach resonances [19]) enables one to achieve separation between the relevant length and energy scales, an important aspect for focusing on the fine details in a problem. For example, in

select studies, preparation of dilute, cold and interacting atomic samples enabled precise probing of few-particle energies [20] and correlations [21]. In the atomic sample of Ref. [21], the length scales pertaining to the interparticle spacing, the de Broglie wavelength $\lambda$, the effective range of interacting potential and confinement are irrelevant, if they are large compared to the s-wave scattering length $a$ characterizing interactions.

Furthermore, ultracold atomic systems with a clear separation between the relevant length and energy scales can also exhibit universal physics, where the macroscopic observables (e.g. energy, momentum, spectral response and dynamics) are invariant on the complex microscopic details of the system. For example, the thermodynamic properties of ultracold systems can be fully described by a set of universal relations (e.g. equation of state [22] and Tan's relations [23, 24]) and only a few quantities (e.g. temperature $T$, density $n$, s-wave scattering length $a$ and the short-ranged particle correlation quantity called the contact). The same universal relations apply to any chosen atomic species (that have the same quantum statistics) for any $T$, $n$, $a$ and in any phase, an intriguing result.

In systems exhibiting universal physics, all physical observables can be parametrized by a few dimensionless parameters, such as $na^3$ and $n\lambda^3$ that describe the strength of interactions and the level of quantum degeneracy, respectively. Then, since universal physics entails continuous scaling symmetry, transformations, such as $n \to \zeta^{-3}n$, $a \to \zeta a$ and $\lambda \to \zeta\lambda$, will leave all observables and their dynamics invariant when measured in rescaled units. For example, when scaled by the only relevant length scale in the problem (the interparticle spacing $n^{-1/3}$), the time evolution, the momentum distribution and the energy of an ultracold gas quenched to unitary ($|a| \to \infty$) are invariant on the atom density [25, 26]. The ability to significantly reduce the complexity of interacting many-body problems, regardless of the complex or unknown microscopic details, to a set of universal equations and a few quantities, is a powerful concept.

However, the principle of universality is limited. For example, while atomic physicists often approximate the interatomic interaction potential by a zero-range delta-function pseudopotential (giving rise to "contact" interactions and an isotropic scattering length $a$ at low energies) [27], the

real interatomic potentials are more complex. The short-ranged details of physical potentials are often nonuniversal, i.e. the details depend on the "real" quantum chemistry, the chosen atomic species, quantum numbers and collisional energy. Hence, unless all length scales in the problem are much larger than the physical extent (energy depth) of the interaction potential (and all energy scales are much smaller than the depth of the potential), nonuniversal corrections due to short-ranged physics must be incorporated. For van der Waals interactions, which are relevant for ultracold neutral atoms and Feshbach resonances, the van der Waals length $r_{\rm vdW}$ characterizes the range of interaction potential [28] and all length and energy scales in a problem (e.g. $|a|$, $\lambda$, $n^{-1/3}$, the mean field energy and the Feshbach dimer binding energy) must be $\gg r_{\rm vdW}$ and $\ll E_{\rm vdW} = \hbar^2/(mr_{\rm vdW}^2)$ for an ultracold atomic system to exhibit universal physics.

## 1.2 The Efimov Effect and Few-Body Physics

While the above inequalities can be met by using a cold, dilute and a near-resonantly interacting atomic sample, a quantum mechanism can break universality: the Efimov effect [29]. While initially introduced in the context of nuclear physics, the Efimov effect was first observed [30] in and has been extensively studied in ultracold atomic systems. This phenomenon is present in bosonic systems with near-resonant short-ranged (decay faster than $1/r^3$) interactions. In the Efimov effect, the short-ranged two-body interaction mediates three-body attraction at long distances and generates an effective three-body potential supporting an infinite number of Efimov bound states. While the introduction of discrete three-body states breaks the continuous aspect of universality, the Efimov effect possesses discrete symmetry and we recover some universal aspects. For example, each consecutive Efimov state meets the three-body threshold continuum ($E = 0, a < 0$) at particular $a$ value that is 22.7 times larger than the previous; $a_-$ is defined to be the ground state location [31]. Similarly, at unitarity, each consecutive three-body Efimov state has an energy that is a multiple of $22.7^j$ smaller than the energy of the previous state, where $j$ is an integer and the energy of the ground state is related to $a_-$. Owing to the long-range nature of the trimer states, the microscopic details of the interaction potential are irrelevant and gives rise to universal spacing

of the spectrum.

While the Efimov spectrum was predicted to be universal in Efimov's original work, the location of the states, determined by a single $a_-$ value, was presumed to depend on the microscopic details of interactions. However, observations across many atomic species and different Feshbach resonances [32, 33, 34, 35, 36, 37, 38, 39, 40, 41, 42, 43, 44, 45] noticed that the $a_-$ value can be directly deduced from the van der Waals length $r_{\mathrm{vdW}}$, with measured $a_-$ values being always within 20% of $-9\,r_{\mathrm{vdW}}$ [37, 46, 47, 48]. This is surprising, considering $r_{\mathrm{vdW}}$ value is solely determined by the atomic mass and a numerical constant $C_6$ [49, 50] characterizing the strength of the $1/r^6$ (long-ranged) van der Waals tail, and not determined by the short-ranged microscopic details. Theory indeed predicts a similar value of $a_- = -9.73\,r_{\mathrm{vdW}}$ [51, 52] and termed this phenomenon "van der Waals universality". Physically, a strong suppression of the three-body wavefunction at short distances prevents particles from accessing nonuniversal regions of interacting potentials.

The knowledge of the $C_6$ value for the chosen atomic species, together with the universal Efimov scaling, should allow prediction of the full Efimov spectrum to arbitrary-large $a$ and arbitrary-small $E$, a powerful concept. With $a_-$ value determining all the trimer state placements in the Efimov spectrum, the robustness and applicability of the unexpected van der Waals universality must be well understood and is a topic of ongoing debate [53, 54, 55, 56, 57]. In particular, understanding of Efimov features near narrow and intermediate Feshbach resonances, described by the dimensionless resonance strength parameter $s_{\mathrm{res}}$, is incomplete. Theoretical models predict that the three-body parameter should also, in addition to the van der Waals length, depend on the background scattering length and the $s_{\mathrm{res}}$ value. The few experimental measurements studying these dependencies suffer from large experimental uncertainties (e.g. see Fig. 5.2), finite-temperature systematic shifts and an insufficient characterization of the two-body potential, leading to inconclusive evidence of what affects the universal aspects in Efimov physics.

## 1.3 Thesis Contents

Our experimental goal is to precisely measure few-body physics using state-of-the-art techniques. To do so, we utilize Fano-Feshbach resonances, quantum state control and spectroscopic tools to precisely control experimental parameters such as atom number, temperature, density and the spin state of our sample.

In Chapter 2, I begin by describing our new apparatus used for generating ultracold $^{39}$K gas samples. Initially, this apparatus was assembled by Rabin Paudel and me for Debbie Jin, enabling production of degenerate $^{40}$K Fermi gas samples; see Rabin's thesis [58] for details on vacuum chamber assembly, testing of potassium sources and creating the new lab's first degenerate $^{40}$K samples. This thesis contains the details describing how we converted the lab to be used for generating and studying ultracold $^{39}$K (boson) gas samples. To my surprise, reaching degeneracy with $^{39}$K (making a Bose-Einstein condensate, BEC) was a more challenging engineering task than with $^{40}$K (making a degenerate Fermi gas). Based on previous experience and the new requirements, we made significant improvements, changes and additions to the apparatus during the conversion, including: improvements to the cooling laser systems, laser locks, magnetic field stability and imaging; change in cooling and state initialization techniques; addition of a sophisticated radiofrequency (RF) state control/spectroscopy system and a 50 W optical dipole trap system used for all-optical evaporation. We started the conversion in November 2016, achieved a $^{39}$K condensate in July 2017 and entered a productive data-taking stage in the beginning of 2018, after extensive calibrations and tuning of the machine. The stability, robustness and automation of the repurposed machine enabled precision studies of few-body quantum physics, the first "real" scientific studies in the new lab.

In Chapter 3, I detail some important tools we utilized to precisely probe two- and three-body physics. Specifically, I focus on our imaging system, RF control and spectroscopy, and magnetic field stabilization.

In Chapter 4, I focus on our precision spectroscopy of Feshbach dimer binding energies, span-

ning three orders of magnitude and with sub-kilohertz resolution. The accuracy and precision are enabled by the production and precise probing of pure molecular samples. These measurements allow us to locate a Feshbach resonance and determine scattering length values with unprecedented accuracy [20]. We use our data to fine-tune a state-of-the-art coupled-channel model, having real (nonuniversal) interaction potentials, and hence we further push the limits of few-body theory. Additionally, the results of our two-body measurements were crucial for our Efimov studies and for providing a two-body physics calibration to JPL/NASA Cold Atom Laboratory (CAL) collaboration, who are interested in performing Efimov studies in microgravity, with ultracold $^{39}$K gas on the international space station.

In Chapter 5, I present our precise measurement of the three-body Efimov ground state location $a_-$. We find that the trimer state location $a_-$ significantly deviates from the value predicted by van der Waals universality. Due to small experimental and systematic uncertainties, our measurement is the strongest evidence of departure from the universal value for both homonuclear and heteronuclear systems, and is the first observed deviation near a Feshbach resonance of intermediate strength, as depicted in Fig. 5.2. This deviation is intriguing, considering other measurements near similar Feshbach resonances, albeit with larger uncertainties, were consistent with universal predictions. Our hope is that future few-body theoretical studies can explain the origin of our observed $a_-$ deviation from the value predicted by van der Waals universality, and enable a better understanding of the limits on universal physics in ultracold systems.

In Chapter 6, I conclude the work presented in this thesis and provide some insight into our ongoing experiments and possible future directions.

# Chapter 2

# Apparatus and Techniques for Cooling $^{39}$K

## 2.1 Properties of $^{39}$K

The $^{39}$K isotope is an intriguing candidate for the exploration of quantum interactions in ultracold gases. Having multiple inter- and intra-spin state Feshbach resonances, $^{39}$K offers an opportunity to study resonances with differing properties (e.g. narrow and broad in terms of resonance width in magnetic field and/or resonance strength parameter $s_{\mathrm{res}}$) with the same apparatus [59]. Additionally, the existence of particular magnetic field values for which the gas is at unitarity for one spin state and $|a| \to 0\,a_0$ (non-interacting) for a different state, enables precision RF spectroscopy (Rabi and Ramsey) of strong interactions [21]. Lastly, the existence of short- and long-lived three-body Efimov states, whose lifetime is characterized by the inelasticity parameter $\eta$, near these Feshbach resonances allows a breadth of exotic few-body studies [38].

The relatively simple $^{39}$K hyperfine structure is shown in Fig. 2.1. Transitions between states can be made using radio-frequency (RF) radiation (e.g. magnetic-dipole transitions) and optical 770 nm (D1) and 767 nm (D2) light. The near-IR light can be readily generated using commercial laser sources. The Zeeman splittings of hyperfine states under external magnetic field $B$, best described by the F quantum number and its projection $\mathrm{m_F}$ along $B$, are conveniently presented in Figs. 2.2–2.4, where the $B$–field ranges are restricted to relevant values used throughout the thesis. Since RF transition frequencies between F and $\mathrm{m_F}$ states are $< 1$ GHz for moderate $B$–fields; microwave engineering is relatively simple. For precision spectroscopy of the $4\,^2\mathrm{S}_{1/2}$ hyperfine ground states, we use magnetically-insensitive RF transitions: transitions between differing F states

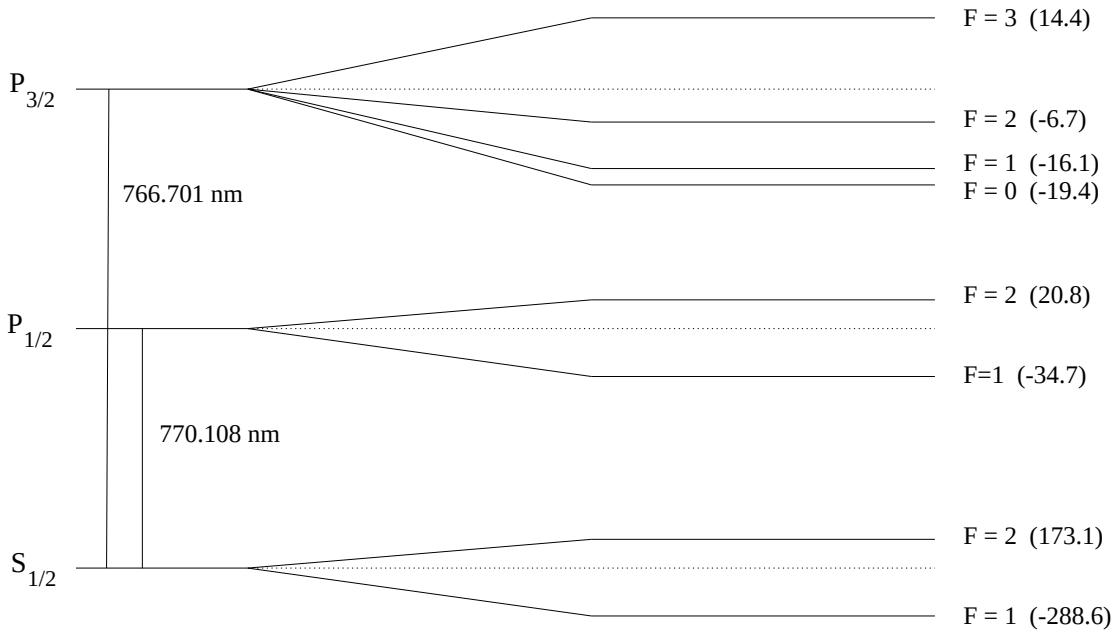


Figure 2.1: Hyperfine energy level diagram of $^{39}$K at zero magnetic field. Optical transition wavelengths 770.108 nm and 766.701 nm correspond to the D1 and D2 spectroscopic lines, respectively. Relative splittings (parenthesis) are in MHz.

at low $B$–field values and between differing $\mathrm{m_F}$ states (within same F manifold) at high $B$–field values.

Feshbach resonances occur in the $|4\,^2\mathrm{S}_{1/2}, \mathrm{F}=1\rangle$ ground states and our goal is to populate the largest and the coldest sample in those states. Since the only trappable $|\mathrm{F}=1\rangle$ state is $|\mathrm{F}=1, \mathrm{m_F}=-1\rangle$, having a positive magnetic moment at low $B$–field values (see Fig. 2.5), we strive to populate it specifically. Additionally, since we have a particular interest (stemming from our CAL collaboration) in the Feshbach and Efimov resonances of the $|\mathrm{F}=1, \mathrm{m_F}=-1\rangle$ state, focusing on the $|\mathrm{F}=1, \mathrm{m_F}=-1\rangle$ state from the beginning is beneficial.

The $|\mathrm{F}=1, \mathrm{m_F}=-1\rangle$ state can be magnetically levitated using only 14 G/cm $B$–field gradient near $B = 0\,\mathrm{G}$. However, at large $B$–field values $B > 82\,\mathrm{G}$, its magnetic moment becomes negative (see Fig. 2.5) and the state becomes untrappable. Therefore, any magnetic trap has a finite trap depth $U/k_\mathrm{B} = k_\mathrm{B}^{-1} \int_{0\,\mathrm{G}}^{82\,\mathrm{G}} \mu(B) dB = 1.5\,\mathrm{mK}$ for the $|1,-1\rangle$ state. Fig. 2.6 shows the trap

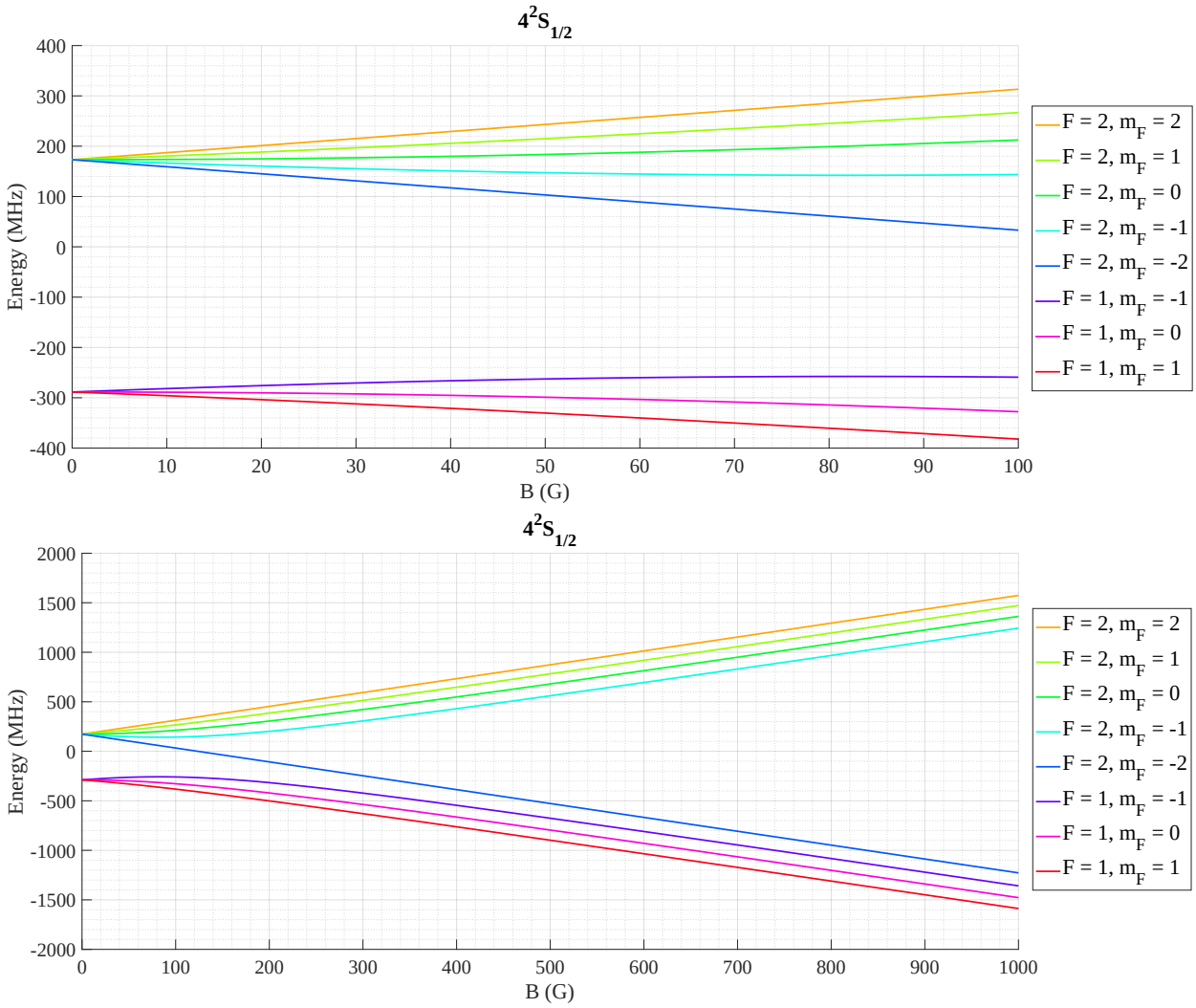


Figure 2.2: Hyperfine structure and the Zeeman splitting of the $4\,^2S_{1/2}$ ground state in $^{39}K$. Note that the curves in the top and bottom plots are same, albeit different $x$-axis scales.

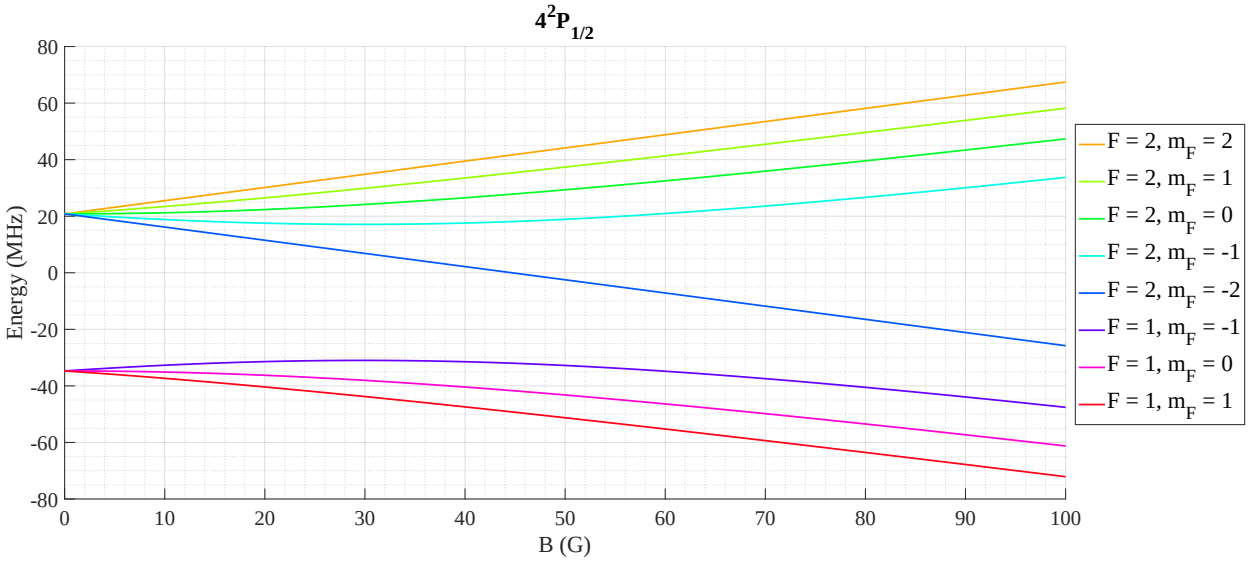


Figure 2.3: Hyperfine structure and the Zeeman splitting of the $4\,^2\mathrm{P}_{1/2}$ state in $^{39}$K.

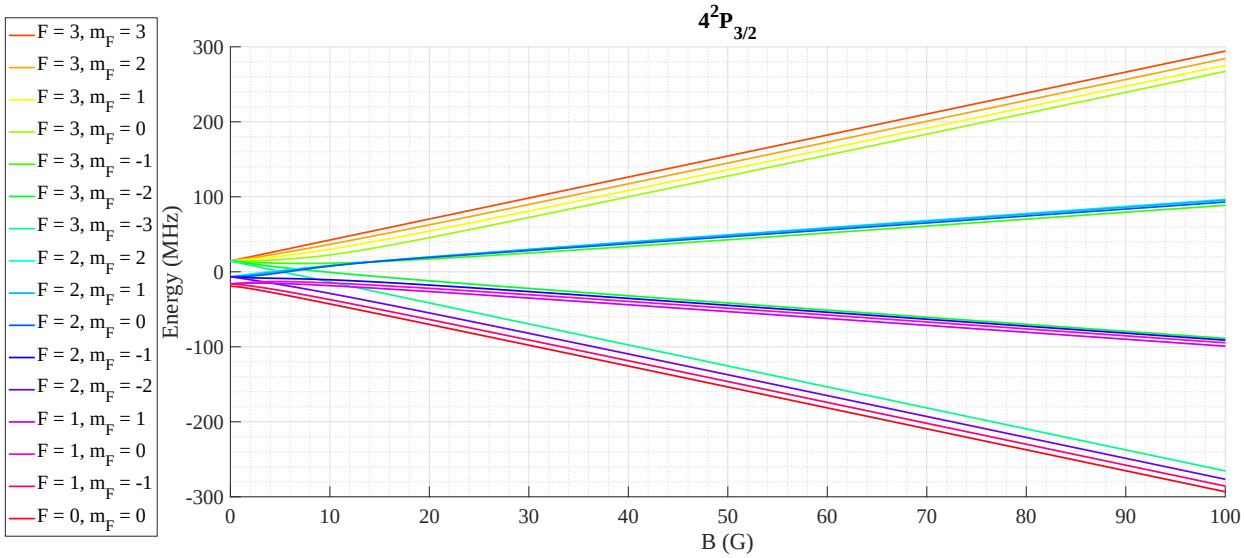


Figure 2.4: Hyperfine structure and the Zeeman splitting of the $4\,^2\mathrm{P}_{3/2}$ state in $^{39}$K.

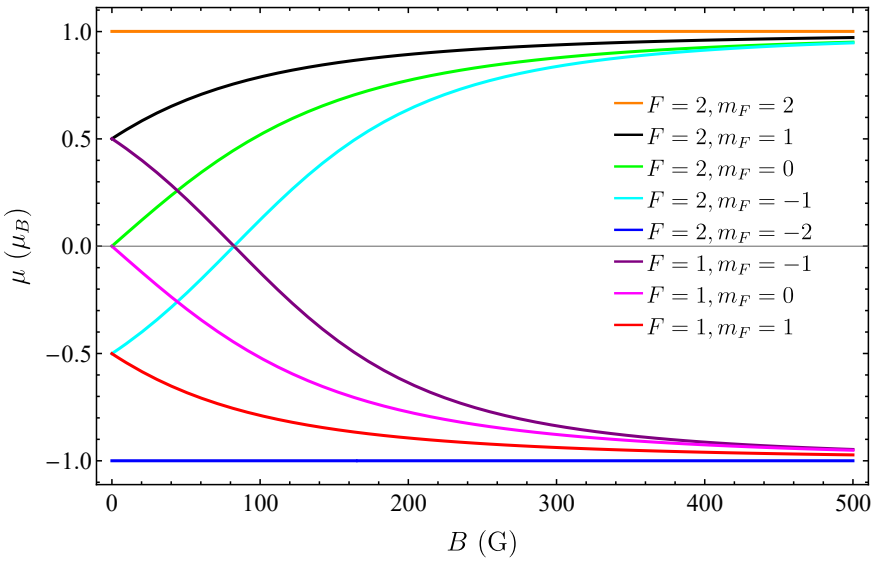


Figure 2.5: The magnetic moment $\mu$ of the $4\,^2\mathrm{S}_{1/2}$ hyperfine ground states in $^{39}$K, where $\mu$ is taken as the derivative of energies (shown in Fig. 2.2) with respect to $B$ and $\mu_B \approx 1.4\,\mathrm{MHz/G}$ is the Bohr magneton.

depth of a quadrupole trap (QT) with magnetic field profile

$$B(x, y, z) = \frac{b}{2}\sqrt{x^2 + y^2 + 4z^2}, \tag{2.1}$$

where $b$ is the gradient along the strong $z$ direction. Having such a small trap depth means that magnetic trapping of the $|1, -1\rangle$ state is only possible if the cloud temperature is $\mathcal{O}(100\,\mu\mathrm{K})$ or below, since the evaporation rate is approximately proportional to $\exp(-U/k_\mathrm{B}T)$ [60]. Therefore, we go to great lengths in reducing the temperature to $\mathcal{O}(10\,\mu\mathrm{K})$, utilizing Doppler and sub-Doppler laser cooling techniques and being particularly careful with the load of the magnetic quadrupole trap.

To study quantum few-body physics (such as the Efimov effect), we require temperatures $\mathcal{O}(10\text{–}100\,\mathrm{nK})$. Typically, reaching such low temperatures is achieved via evaporation in a magnetic potential (e.g. RF or microwave forced evaporation), followed by evaporation in an optical dipole trap. However, such an approach fails for $^{39}$K, which has a small and negative background scattering length, and therefore has a Ramsauer-Townsend minimum in the collision cross section vs. collisional energy [61, 62], as depicted in Fig. 2.7. This minimum suppresses rethermalizing

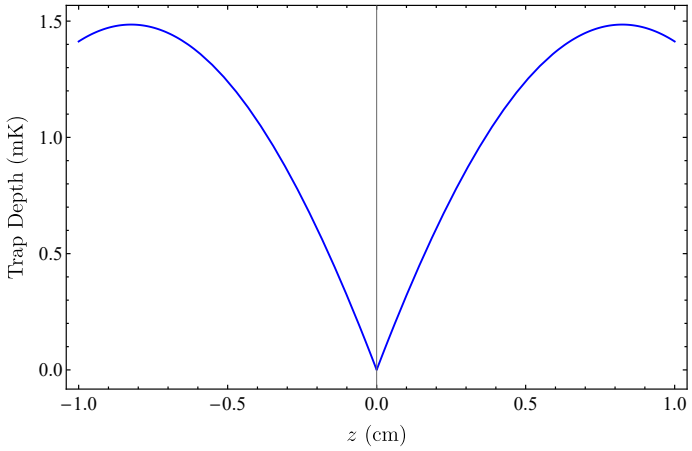


Figure 2.6: Quadrupole trap depth for the $|\mathrm{F}, \mathrm{m_F}\rangle = |1, -1\rangle$ state, where $z$ is the strong trap direction with 100 G/cm gradient and we ignore gravity. Due to the sign change in the $|1, -1\rangle$ state's magnetic moment near 82 G (see Fig. 2.5), the trap depth is limited to 1.5 mK.

collisions at energies near 400 $\mu$K, an unfortunate value as this is where elastic collisions are most needed for efficient evaporation. To circumvent this problem, we employ an all-optical evaporation technique. We perform evaporation in an optical dipole trap in the presence of an external magnetic field, whose value is tuned near a Feshbach resonance to enhance the elastic collision rate (see Fig. 2.8).

## 2.2 Overview of the Experimental Setup and the Cooling Procedure

Figs. 2.9 and 2.10 show an overview of our experimental setup. Details on vacuum chamber assembly and testing of potassium sources are found in Rabin Paudel's thesis [58]. Additional details on the science cell characterization are found in Jacob Covey's thesis [64], whose cell is identical to ours. Our apparatus consists of a three chamber setup: MOT1 (the first magneto-optical trap) glass cell with 9 windows and two "arms" with alkali sources, MOT2 stainless steel chamber with 7 viewports, and a fused silica science cell with 9 windows. The part of the vacuum chamber containing the science cell can be separated from the part containing the two MOT chambers via a gate valve closure. Two pump arms maintain the ultrahigh vacuum. Each arm contains a titanium sublimation pump (Ti filaments coat the steel components for pumping), an ion pump (with each

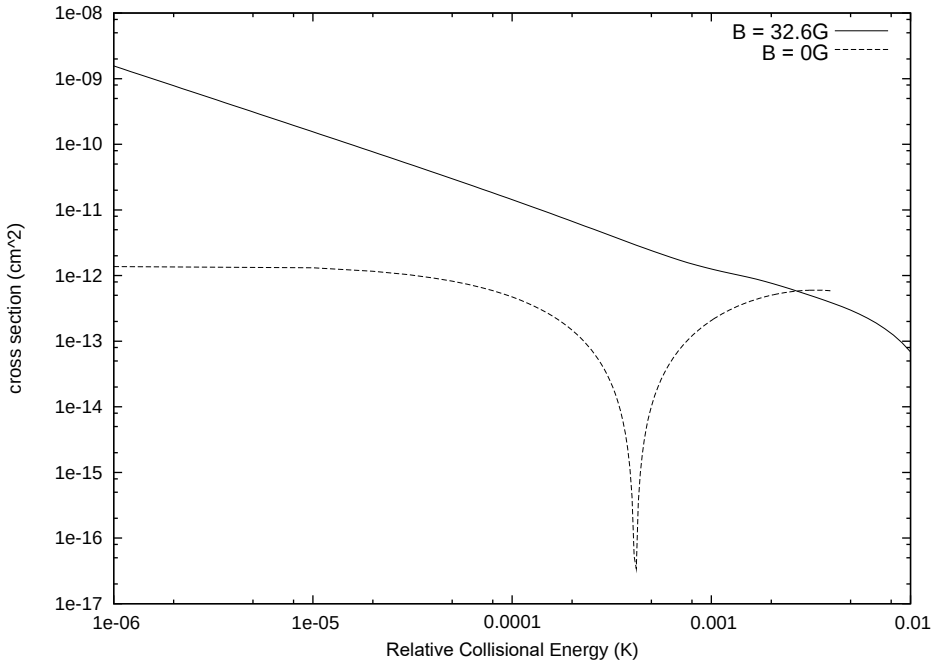


Figure 2.7: Elastic collision cross section of atoms in the $|\mathrm{F}=1,\mathrm{m_F}=-1\rangle$ hyperfine state vs. collision energy for two different magnetic fields. This figure is borrowed from John Bohn [63].

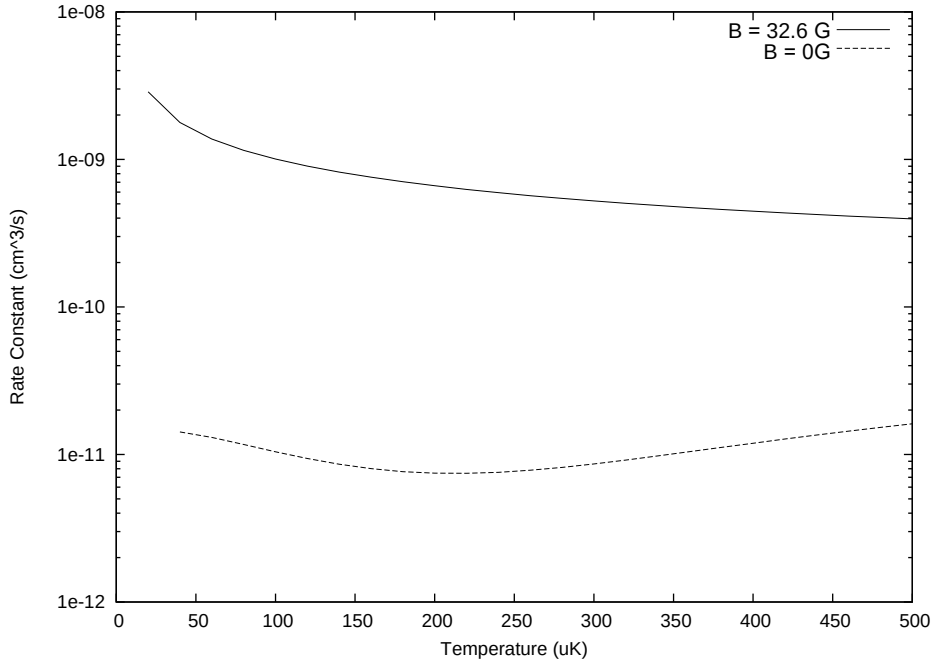


Figure 2.8: Thermally averaged collision rate of atoms in the $|\mathrm{F}=1,\mathrm{m_F}=-1\rangle$ hyperfine state vs. temperature for two different magnetic fields. This figure is borrowed from John Bohn [63].

measuring $< 10^{-11}$ Torr, the minimum reading), and a valve to allow connection to a turbo pump (if needed). So far, the titanium was deposited only once, where we fired for 40 s at 48 A with a 10 ramp up and ramp down times, since the vacuum chamber bakeout (we had no need as the pressure in our vacuum chamber remained low). We put a mu-metal shield on the ion pump closest to the science chamber to limit the effect of stray magnetic fields on our atoms. We have not broken vacuum since initial assembly and bake-out on September 2013 (for the MOT chambers side) and July 2014 (for the science chamber side), nor we have a desire to do so anytime soon.

Since we initially constructed the apparatus to create degenerate $^{40}$K Fermi gas samples, the system contains potassium enriched $^{40}$K sources: one dispenser with 7.1% enrichment level and two more with 14.1% level. Note, the system also it contains three Rb dispensers in a separate glass chamber "arm". We used the dispenser with 7.1% $^{40}$K enrichment in this thesis work, as this dispenser has a higher $^{39}$K content, the new isotope of interest for our ultracold Bose gas experiments. We run 3.5 A of current through the dispenser (1.8 V drop) to release potassium vapor via a chemical reaction $2\mathrm{KCl} + \mathrm{Ca} + \mathrm{heat} \rightarrow 2\mathrm{K} + \mathrm{CaCl_2}$, where we have measured (in a separate setup) the temperature threshold to be 350–400° C. To prevent the vapor from depositing on cell walls, we heat the entire MOT1 Pyrex chamber (along with the source arms) to 70° C via 14 current-servoed heaters (Omega Products KHLV-0502/5 and KHLV-105/5-P) attached directly to the glass. Additionally, we can increase the potassium vapor pressure, and hence the MOT loading rate, via light-induced atom desorption (LIAD), illuminating the glass chamber with three UV LEDs (365 nm, 1.2 W each, part LED Engin LZ1-00UV00). By UV illuminating the chamber only during the MOT load, this technique should enable a faster MOT load rate without the need to run the dispensers at a higher current. However, unlike others [65], we only saw a modest improvement of 20–30% in the MOT loading rate and a degraded atom number stability. Additionally, after several months of operation, the desorption UV light removed the majority of residual potassium deposits from the cell walls and we discontinued the LIAD use.

We continuously push atoms from the MOT1 chamber to the MOT2 chamber via a push beam, which has a linear polarization and whose frequency is red detuned from the D2 transition.

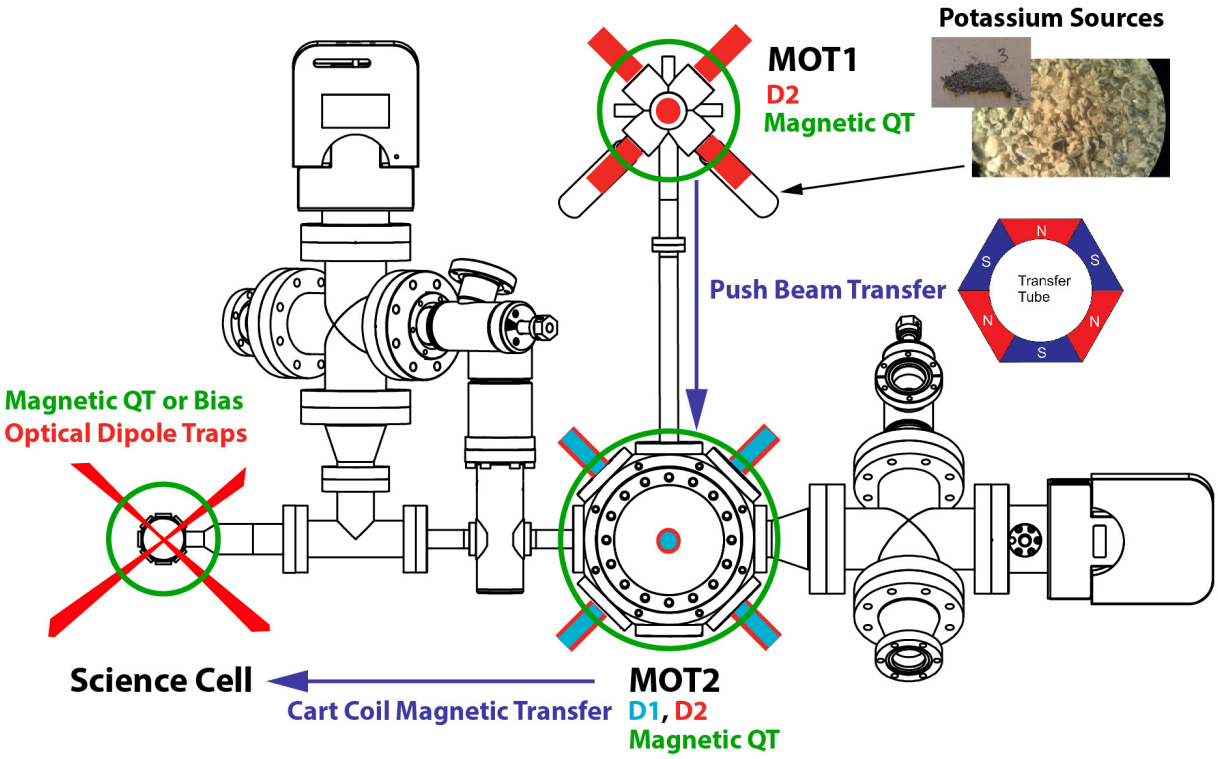


Figure 2.9: An overview sketch of the experimental cooling procedure.

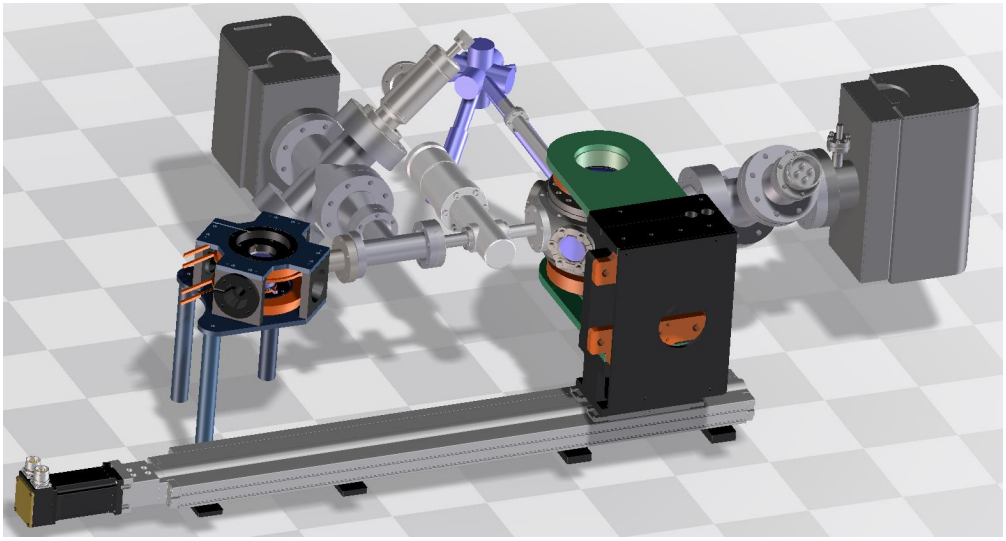

Figure 2.10: CAD drawing of our experimental apparatus.

A magnetic hexapole field, formed by machined "fridge magnet" pieces, guides atoms through the transfer tube and provides support against gravity. For similar push beam powers, the magnetic guide increases the push beam transfer efficiency by $\times 1.8$ (compared to without the guide) and reduces the MOT2 fill time by 35%. Our past experiments with the $^{40}$K isotope showed that this hexapole field enables atom velocities as slow as 20 m/s, corresponding to a 25 ms transfer time between the two MOT chambers separated by 47 cm. This is impressive, considering that atoms would fall 3 mm (compare this to 5.5 mm transfer tube inner radius) in 25 ms without the magnetic guide. We found that the rotation angle of the hexapole field (around the transfer tuber) is somewhat sensitive: the transferred atom number can vary by 50%.

After loading MOT2 with a sufficient number of atoms, we perform a series of MOT compression and sub-Doppler cooling stages. Then, we load atoms into a quadrupole trap and transfer them to the science cell via a cart transfer (MOT2 QT coils are attached to the cart). Then, we transfer atoms from the cart QT to (a similar) science QT and move the cart away from the science chamber. After which, we increase the science QT confinement and load a fraction of atoms into an optical dipole trap. Finally, we turn off the QT, turn on a magnetic field bias (tuned near a Feshbach resonance to increase elastic collisions) and perform all-optical evaporation, reaching $\mathcal{O}$(10–100 nK) final temperatures. While this procedure sounds relatively simple, in reality it was an extensive engineering task, requiring lengthy optimization procedures and a thorough understanding of each experimental knob. Lab photos in Figs. 2.11–2.12 show the complexity of the apparatus that enabled us to reach our goals. While some parts of the apparatus remained unchanged from the initial construction (for purposes of $^{40}$K cooling), major adjustments and improvements were made to transform this apparatus to a $^{39}$K cooling machine. The stability, robustness and automation of this machine enabled precision studies of few-body quantum physics.

## 2.3 Doppler Laser Cooling

Since we have a relatively narrow excited state hyperfine structure [66] (compare the hyperfine spacing to the $\Gamma/2\pi = 6.035$ MHz natural linewidth of the excited $4\,^2\mathrm{P}_{1/2}$ and $4\,^2\mathrm{P}_{3/2}$ states), laser

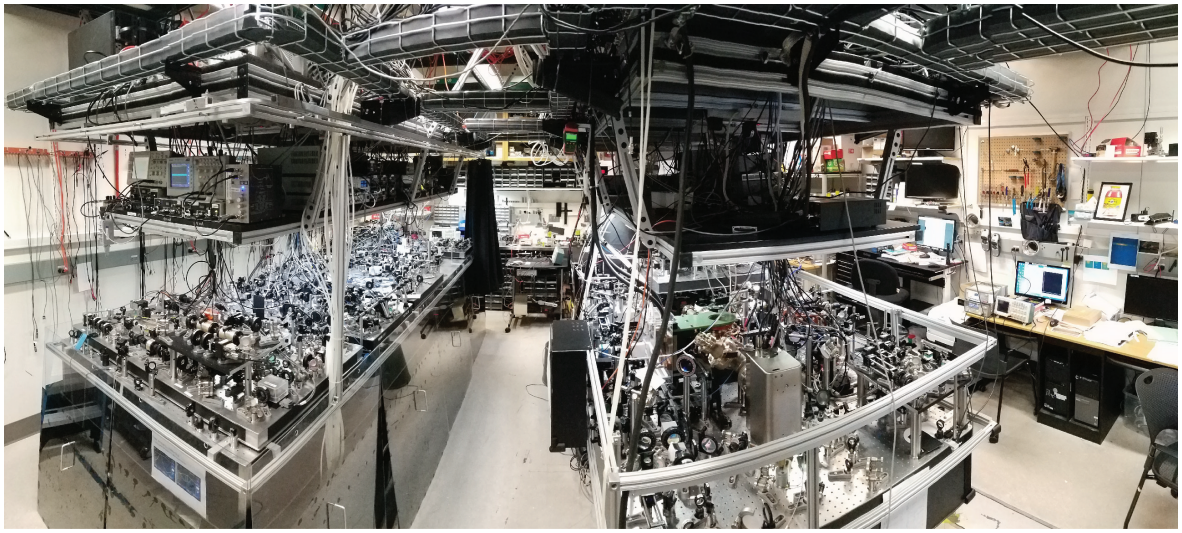

Figure 2.11: Overlooking the laboratory: laser sources (left) and science (right) optical tables.

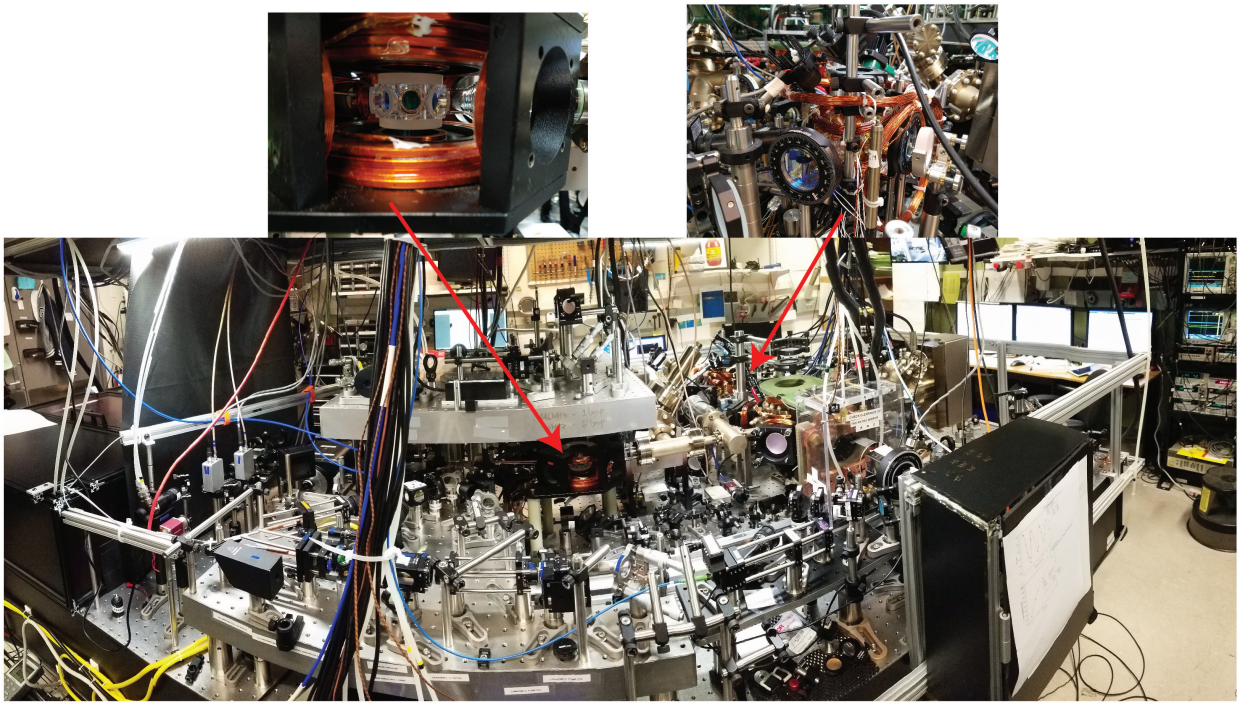

Figure 2.12: The vacuum chamber and the surrounding optics take up more than half of the science optical table; the rest of the space is taken by a 50 W 1064 nm laser system (black steel box) used for generating and controlling the optical dipole trap light. The two smaller images show the science cell (surrounded by magnetic field coils and RF antennas) and the MOT1 chamber (surrounded by large-aperture optics and magnetic coils).

cooling the $^{39}$K isotope is more difficult than its $^{40}$K counterpart. Due to the level crowding, off-

resonant scattering from the $|4\,^2\mathrm{S}_{1/2}, \mathrm{F}=2\rangle \rightarrow |4\,^2\mathrm{P}_{3/2}, \mathrm{F}'=3\rangle$ cooling transition (we refer to as "D2 trap", see Fig. 2.13) results in a quick accumulation of atoms in the $|4\,^2\mathrm{S}_{1/2}, \mathrm{F}=1\rangle$ ground state. Therefore, we require a strong repump beam on the $|4\,^2\mathrm{S}_{1/2}, \mathrm{F}=1\rangle \rightarrow |4\,^2\mathrm{P}_{3/2}, \mathrm{F}'=2\rangle$ transition (we refer to as "D2 repump") to have efficient laser cooling. In fact, our typical D2 repump beam power is almost 1:1 of D2 trap power for both MOT setups. This is a much stronger repump light than what we've previously used for $^{40}$K (1:3 repump-trap ratio for MOT1 and 1:12 for MOT2 [58]). Lastly, since the MOT atom number and temperature are determined by spontaneous emission [67] (and since our desire is to have the highest atom number with lowest temperatures), the trap and repump beams must be far (red-) detuned from their transitions and must be of high power.

### 2.3.1 D2 Laser System

The laser system used for generating, frequency-stabilizing and amplifying D2 laser light is shown in Fig. 2.14 and 2.15. Learning from previous experience, regarding the required laser power, stability and laser frequency modularity, we decided to have three separate 767 nm DBR laser sources (Photodigm PH767DBR080T8, TO-8 package, 80mW): one each for master, for trap and for repump light. We thoroughly enjoy working with DBR lasers; they are compact, have unmatched mechanical stability, small laser linewidth $< 500\,\mathrm{kHz}$ ($\ll 6.0\,\mathrm{MHz}$ natural linewidth of the excited states), efficient ($\sim 0.75\,\mathrm{mW/mA}$, we typically use 100–150 mA) and have a large mode-hop-free wavelength tuning range $\mathcal{O}(2\,\mathrm{nm})$ (coarse tuning using temperature and fine using current). Some of the negatives include astigmatic emission profile, linewidth broadening with age and sensitivity to back-reflections (requiring $\gtrsim 60\,\mathrm{dB}$ isolation). We stabilize each DBR laser temperature to within 1 mK using commercial TEC temperature controllers (Thorlabs TED8020). We use fast low-noise JILA laser diode current drivers to dynamically control DBR laser frequencies. We carefully choose the operating temperature and current to center lasing on the mode-hop-free range, in order to reduce spectral noise.

The master DBR laser frequency is stabilized to an atomic frequency reference (a heated

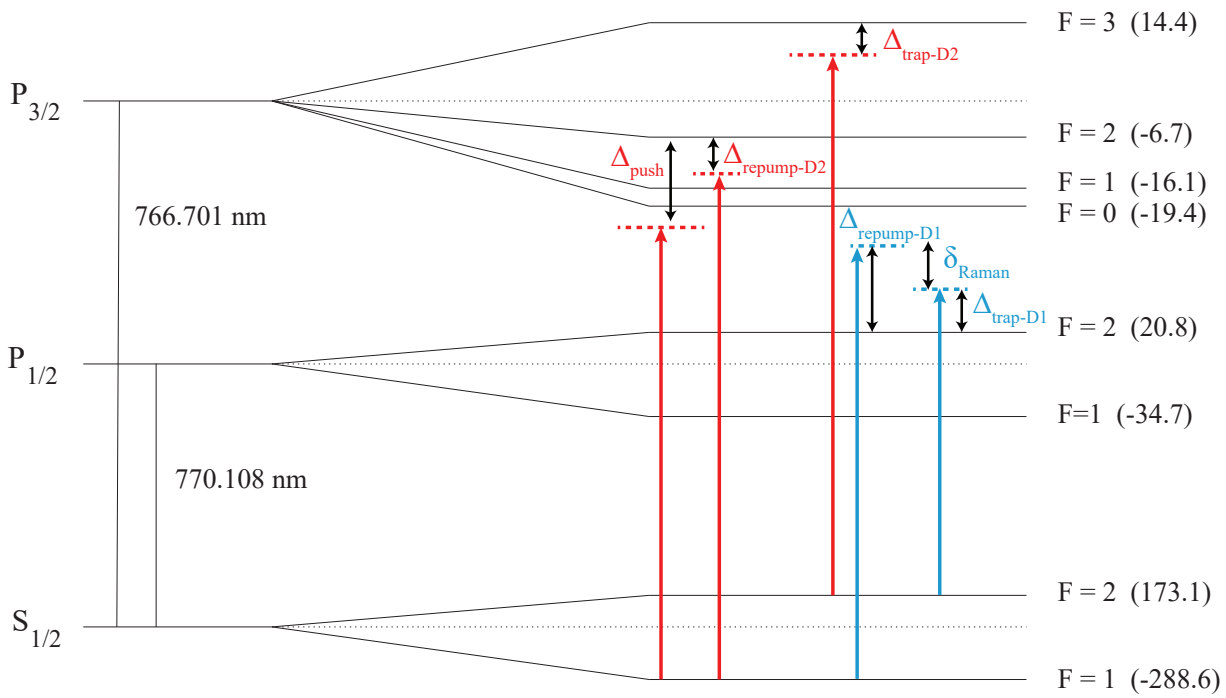


Figure 2.13: D1 and D2 laser cooling beam detunings.

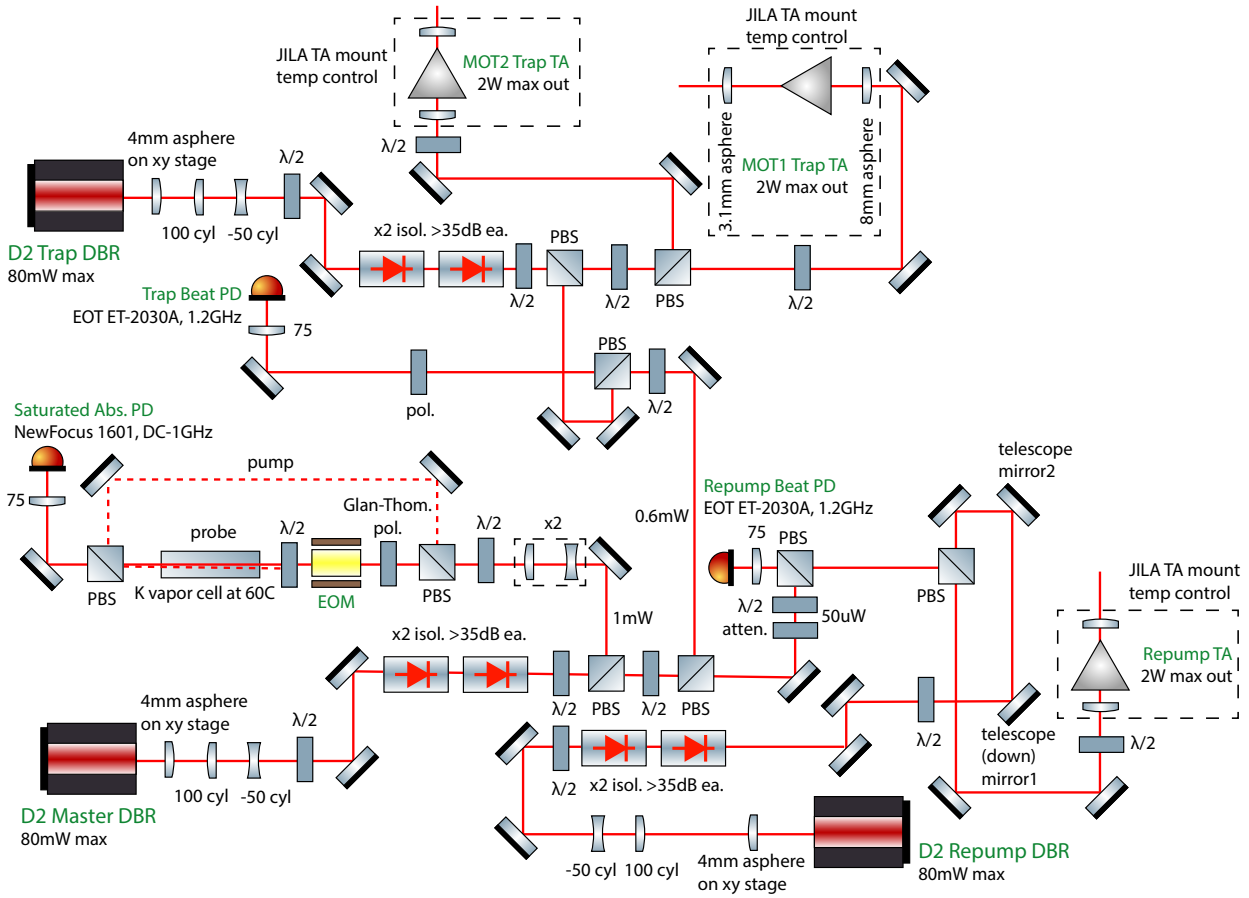


Figure 2.14: D2 laser system before the tapered amplifiers. The master laser is frequency stabilized to a saturated absorption spectroscopy setup and provides a frequency reference to the D2 trap and repump lasers via heterodyne beatnotes. Lenses are spherical unless specified and the numeric labels are in mm units.

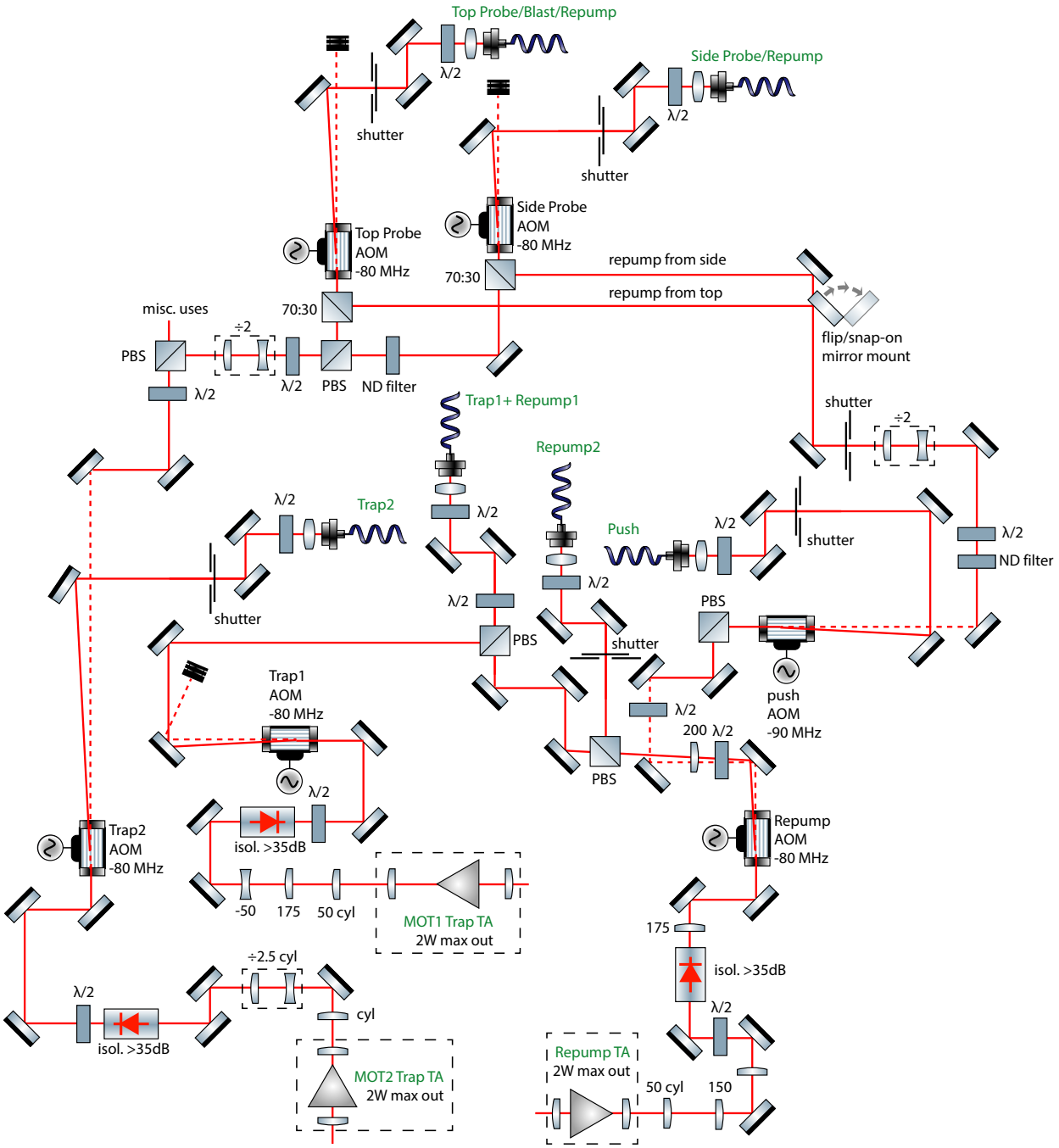


Figure 2.15: D2 laser system after the tapered amplifiers. While MOT1 trap and repump light share the same fiber, the light travels separately for MOT2. Push beam light is generated from the zeroth-order of the repump AOM. Top and side probe fibers deliver light to the science cell. The miscellaneous PBS port of the trap2 beam path is used for optical pumping, MOT2 absorption imaging, etc.

potassium vapor cell) via a Pound-Drever-Hall (PDH) locking technique (Doppler-free saturated absorption spectroscopy with a phase-modulated probe beam), as depicted in Fig. 2.16. The trap and repump laser frequencies are locked to the master laser frequency via a heterodyne offset lock, using a phased-locked loop with a JILA high-speed (10 MHz) PID loop filter, as shown in Fig.2.17. The modularity of this setup allows us to change the trap and repump laser frequencies at will: we can jump laser frequencies on a $\sim 50\,\mu$s timescale (set by the loop's P-I corner frequency, typically around 70 kHz) and have a large beatnote frequency locking dynamic range of 10–1200 MHz (the lower limit is set by the phase-frequency detector response and the higher limit is set by the transfer function of the Si photodetector). In fact, this modularity enabled us achieve $^{39}$K, $^{40}$K and $^{41}$K MOTs within 30 mins time, a useful sanity check prior to extensive system optimization on a particular isotope. Additionally, the high-speed and high-gain PID servo system enables one to establish phase-coherence between DBR laser sources, important for two-photon processes (e.g. the D1 Raman cooling transition in sub-Doppler gray molasses, to be discussed later). We can achieve phase coherence with negligible laser linewidth broadening: a narrow beatnote signal (phase-coherence) 10–15 dB on top of the broad beatnote signal (whose width is set by the laser linewidths) and small noise bumps (resulting from high servo gain).

Since we require a significant amount of D2 power, we amplify the DBR light with tapered amplifiers (TA) (Eagleyard part EYP-TPA-0765-02000-4006-CMT04-0000, 765 nm, maximum 2 W out, C-mount) mounted in JILA-made brass temperature-stabilized enclosures. We have three TAs for the D2 setup: one each for MOT1 trap, for MOT2 trap and for repump (MOT1 and MOT2 repump light are amplified by the same TA chip). While the TA chips typically output 1.5 W with only 10–20 mW seed power at 2.2 A drive current, the output spatial mode quality is not great, often allowing only $\lesssim 50\%$ single-mode (SM) fiber-coupling efficiency, even with multiple beam-shaping optics and an acousto-optic modulator (AOM). All laser light is routed to the science optical table by polarization-maintaining (PM) SM fibers. Due to bad fiber-coupling efficiency, we resort to air gap high-power fibers (ozOptics PMJ-A3AHPCA3AHPC-780-5/125) for high power ($> 100$ mW output) light delivery. Using standard fiber patch cables with epoxied fiber connectors

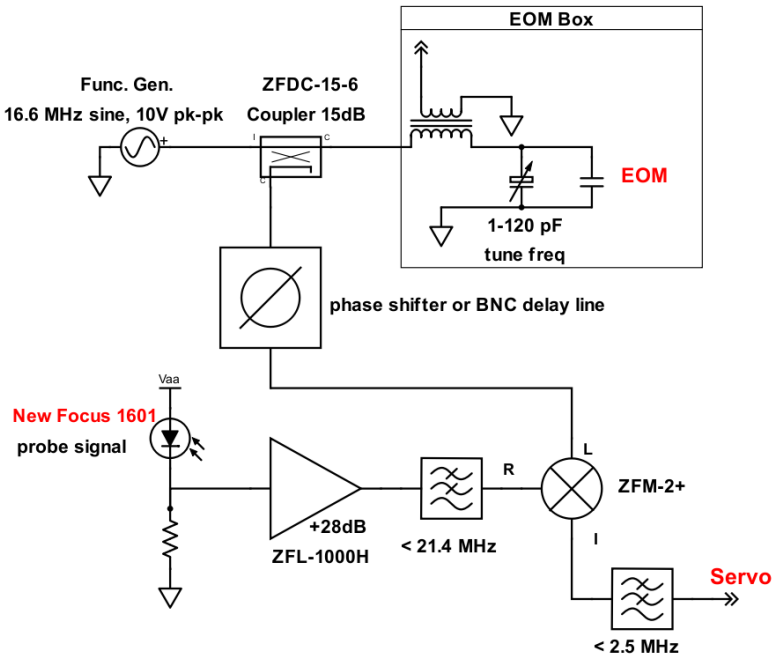


Figure 2.16: D2 laser PDH lock demodulation electronics. A 50 Ω function generator drives a homebuilt resonant EOM tank circuit that phase modulates the probe beam. After passing through a saturated absorption spectroscopy setup, the probe beam is detected on a PD. We demodulate the signal and send it to the PID servo (Vescent Photonics). We are careful to avoid residual amplitude modulation (RAM) in the probe beam and employ RAM-minimizing techniques suggested by Jan Hall [68].

(e.g. Thorlabs P3-630PM-FC) for MOT light delivery leads to power instability. Using the high-power fiber patches, we are able to deliver 200 mW repump and 250 mW trap light to MOT1 (D2 repump1 and trap1 share the same fiber), 150 mW repump and 150 mW trap light to MOT2 (D2 repump2 and trap2 have separate fibers). Due to stimulated Brillouin scattering, the output power is limited to $\lesssim 500$ mW for our 5 m fibers (a typical routing distance between the laser-source and science optical tables).

We use AOMs (e.g. Gooch & Housego 23080-1-LTD) for dynamic intensity control and to generate small laser frequency offsets. Fast (2 ms) mechanical shutters (Uniblitz LS6, 6 mm aperture) provide additional beam isolation. Since we generate a significant amount of resonant light, we are careful in terminating and attenuating the scattered light: we face all shutters away from the science table, surround the tables with laser curtains (cloth and polyester) and clear acrylic

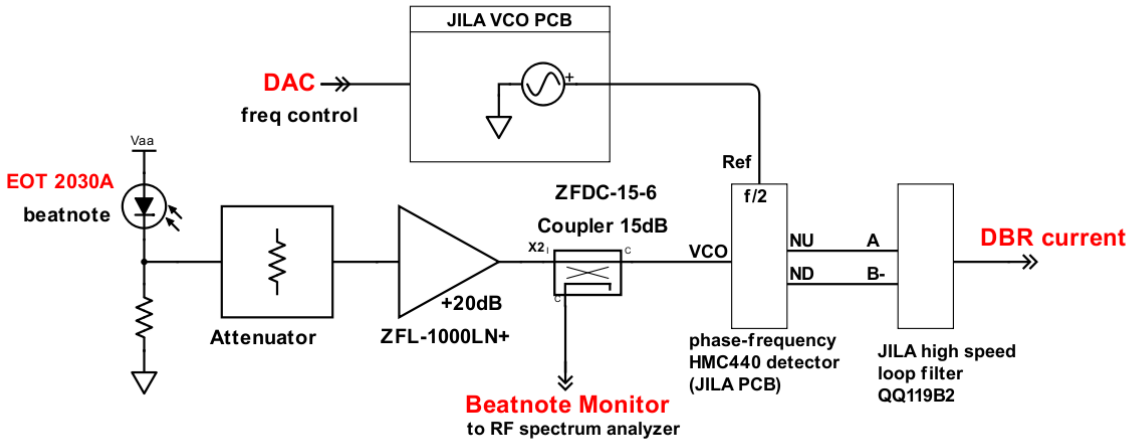


Figure 2.17: A typical electronic setup for a heterodyne beatnote offset lock. A DAC line from an FPGA card controls the reference frequency. Depending on the desired beatnote lock frequency, noise spectrum and power, additional RF filtering and attenuation and/or amplification might be necessary. This lock is fast, robust, has a large frequency-locking dynamic range (often limited by the PD), and enables one to establish phase coherence between two oscillators/lasers.

panels with added band-pass filtering (Roscolux R94). Failure to take these extra steps leads to $< 5\,\mathrm{s}$ atom lifetime.

Overall, the laser system stability is excellent, requiring only $\sim$ monthly periodic adjustments to achieve similar laser power and frequency stability. Most stability results from utilizing short steel 1 inch optical posts, secondary breadboards (thick, steel and vibration-damping) on top of the optical table, (mostly) steel opto-mechanics, a minimal number of and a minimal separation of optical elements, fiber coupling, laser curtains and panels (surrounding the optical table), having minimal heat sources underneath the table (most electronics are in the "cloud" above the optical table) and a stable lab environment ($\sim$ 0.5°C and 5% humidity stability). See Fig.2.19 for a closer look at the laser optics table. Most laser problems arise due to diode aging (laser lineshape broadening and more-frequent laser frequency mode hopping) and from RF noise (picked up from radiating antennas and electro-optic modulators). Some of our laser frequency diagnostic tools include: self-heterodyne laser linewidth measurement setup (see Fig. 2.18), heterodyne beatnote lock in-loop pickoff, grating-based commercial wavemeter, optical spectrum analyzer, optical cavity

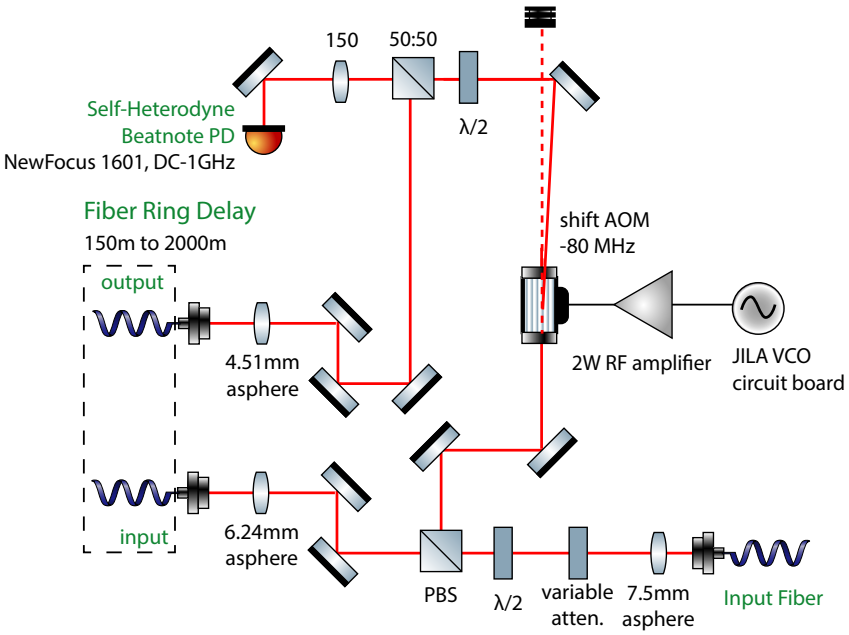


Figure 2.18: Self-heterodyne laser linewidth measurement setup. Laser light from an input fiber is split into a frequency-shifted path and a time-delayed path, before being recombined on a photodetector. We use an RF spectrum analyzer to measure the laser autocorrelation spectrum. An 80 MHz AOM, driven by low-noise electronics, is used to shift the lineshape center frequency to a higher value. The fiber delay length must be on order of or longer than the inverse of the laser linewidth we are trying to measure. We use fiber rings, often used in telecom optical time-domain reflectometers, with lengths spanning 150–2000 m (e.g. AFL FR1-SM-1000-FC-FC, a telecom singlemode 1 km patch with a 10 $\mu$m core, 125 $\mu$m cladding, and $\sim$ 2.5 dB/km loss near 800 nm).

and ultracold atom spectroscopy. The self-heterodyne setup is particularly valuable for DBR laser diagnostics; it allows us to directly extract the lineshape spectra of stable laser sources, even in instances where the coherence length is on the order of fiber delay length [69, 70].

### 2.3.2 MOT Load

The first MOT acts as a continuous cold atom source for a larger MOT in the second chamber, whose lifetime is much longer than that of the first MOT due to differential pumping. The first MOT (3D geometry) consists of a quadrupole field (coils wound directly on the Pyrex cell), three orthogonal shim coils (up to 5 G), and three retro-reflected laser cooling beams with a 1.4 cm Gaussian waist and circular polarization. We use an IR security camera and a Si amplified photodetector

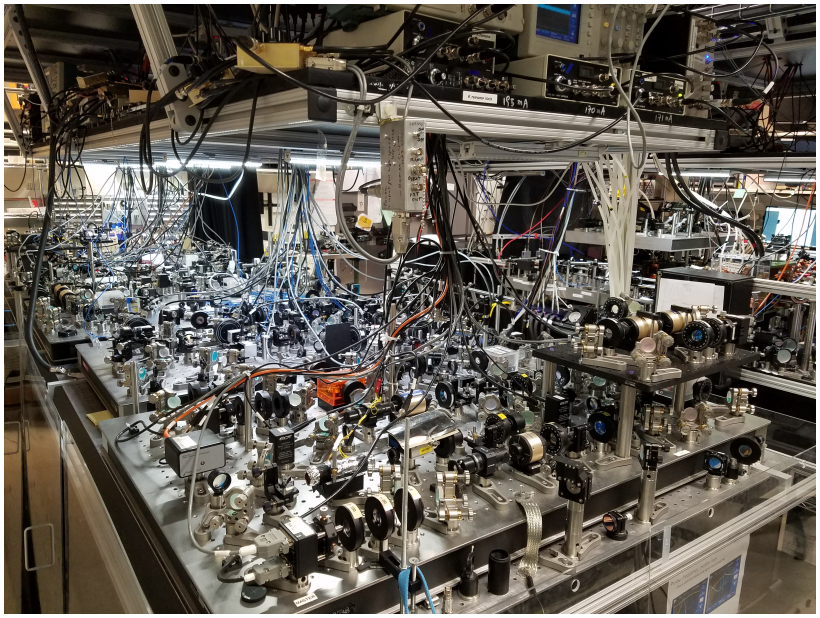

Figure 2.19: Optics for laser cooling: laser sources, amplifiers, spectroscopy, power and frequency control.

to measure MOT1 fluorescence. We use a relatively small quadrupole gradient ($\sim 7\,\mathrm{G/cm}$ for 1.7 A current) to produce a spatially-large MOT1. The MOT fill is described by $N(t) = N_0\left(1 - e^{-t/\tau}\right)$, where $N_0$ is the maximum number of atoms permitted and $\tau$ ($\sim 1\,\mathrm{s}$ for MOT1) is the MOT fill rate time constant. $N_0$ and $\tau$ values depend on the background collision rate, $^{39}$K vapor pressure, cooling beam intensities and their volume overlap, gradient field strength and laser detunings.

We continuously push atoms from MOT1 to MOT2 using a push beam, whose frequency is red detuned from the D2 $|4\,^2\mathrm{S}_{1/2}, \mathrm{F} = 1\rangle \rightarrow |4\,^2\mathrm{P}_{3/2}, \mathrm{F}' = 2\rangle$ transition [71] and has a linear polarization. The push beam has a 1 mm waist and is slightly converging, such that the focus is just past the MOT2 chamber. The second MOT (also 3D geometry) consists of a quadrupole field (coils mounted on a cart), 6 shim coils wound around chamber viewports (one top, one along the push beam direction, and two two-coil-pairs), and three retro-reflected D2 cooling beams with 0.8 in waists. Unlike for $^{40}$K isotope MOT2 setup [58], we do not implement a dark spot on the repump beam, as we require significantly higher repump power for $^{39}$K laser cooling .

The MOT2 fill rate and atom number are sensitive to the push beam alignment (with respect

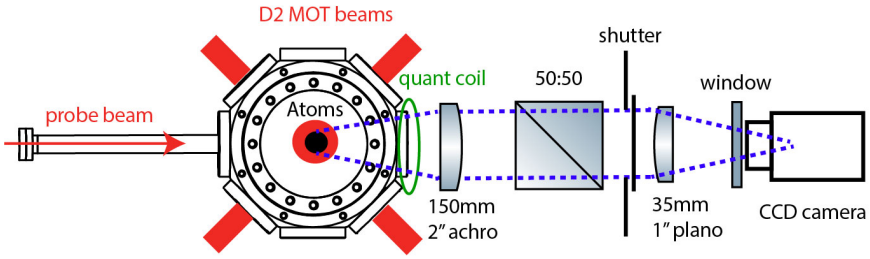


Figure 2.20: Second MOT imaging optics used for absorption (using a probe beam and a quantization coil) and fluorescence imaging (using D2 MOT beams and zero magnetic field). The 2" 50:50 beamsplitter is used for miscellaneous diagnostics: diverting part of the fluorescence signal or beam light (probe or push) onto a photodetector or an IR security camera.

to MOT1 and MOT2 cloud locations), quadrupole gradient, beam power and detunings. Optimizing MOT2 is an iterative process and we've spent a significant amount of time getting the desired conditions. We use a CCD camera (PCO Pixelfly QE) to image the MOT2 cloud (along the transfer tube direction, as shown in Fig. 2.20).

To extract the MOT2 atom number, we use absorption imaging: we turn off all MOT light, gradient and shims; turn on a few-G quantization field along the probe beam propagation direction; illuminate atoms with a $40\,\mu$s, $\sigma^+$ polarization, D2 $|4\,^2\mathrm{S}_{1/2}, \mathrm{F}=2\rangle \rightarrow |4\,^2\mathrm{P}_{3/2}, \mathrm{F}'=3\rangle$ transition resonant probe light, along with D2 repump light (using MOT beams). The atomic cloud attenuates (due to absorption) the probe beam intensity according to Beer's law:

$$I(x,y) = I_0 e^{-n(x,y)\sigma} = I_0 e^{-\mathrm{OD}(x,y)}, \tag{2.2}$$

where $I_0$ is the incoming probe beam intensity (assumed homogeneous), the probe beam propagates along $z$ direction, $n(x,y)$ is atom cloud column density (integrated along $z$), OD is the optical depth of the cloud and $\sigma$ is the absorption cross-section, whose on-resonance value is $\sigma_0 = 3\lambda^2/2\pi$ and whose off-resonance value is described by a Lorentzian with a FWHM width equal to the excited state national linewidth $\Gamma/2\pi = 6.035\,\mathrm{MHz}$ (assuming no power broadening of the transition, valid for $I \ll I_{\mathrm{sat}} = \pi\hbar c\Gamma/(3\lambda^3)$; the saturation intensity, $I_{\mathrm{sat}} = 1.75\,\mathrm{mWcm}^{-2}$ for $^{39}$K D2 transition) [66]. For absorption imaging (either in the MOT or science chambers), we always take three consecutive image frames: a shadow frame $I_S(x,y)$ with atoms and probe light, a light frame $I_L(x,y)$ without

atoms and with probe light, and a dark frame $I_D(x, y)$ without atoms nor probe light (captures CCD dark counts and background lab light). The OD 2D distribution is defined as:

$$\mathrm{OD}(x, y) = \ln\left(\frac{I_L(x, y) - I_D(x, y)}{I_S(x, y) - I_D(x, y)}\right). \tag{2.3}$$

For a Gaussian atom density distribution (e.g. a distribution of non-interacting thermal atoms in a harmonic trap), the atom number $N$ relates to the optical depth by

$$N = \frac{2\pi}{\sigma_0}\mathrm{OD}_{\mathrm{peak}}\sigma_x\sigma_y, \tag{2.4}$$

where $\mathrm{OD}_{\mathrm{peak}}$, $\sigma_x$ and $\sigma_y$ are fit the values for a 2D Gaussian distribution describing the OD profile: $\mathrm{OD}(x, y) = \mathrm{OD}_{\mathrm{peak}} \exp(-\frac{(x-x_0)^2}{2\sigma_x^2} - \frac{(y-y_0)^2}{2\sigma_y^2})$, where $(x_0, y_0)$ is the atom cloud center. The physical cloud sizes $\sigma_x$ and $\sigma_y$ are related to the CCD image sizes $\sigma_x^{\mathrm{CCD}}$ and $\sigma_y^{\mathrm{CCD}}$ by $\sigma_{x,y} = (\mathrm{pix}_{\mathrm{size}})\sigma_{x,y}^{\mathrm{CCD}}/M$, where $\mathrm{pix}_{\mathrm{size}}$ is the CCD pixel size (e.g. $6.45\,\mu$m for Pixelfly and $13\,\mu$m for Princeton Instruments camera, the primary camera used for the majority of science chamber imaging) and $M$ is magnification of the imaging system (often determined from measuring parabolic trajectory of a falling atom cloud). Since MOT clouds are rarely Gaussian (their shapes depend on many parameters), a more complicated analysis must be performed to accurately extract the MOT atom number from an in-situ absorption image.

Since the transfer tube (11 mm inner diameter) sets the maximal size of the probe beam, the field of view is limited and absorption imaging can be only used for a short time of flight (TOF) expansion durations, as depicted in Fig. 2.21. Therefore, we resort to fluorescence imaging for longer TOF imaging. The fluorescence imaging sequence goes as follows: we turn off MOT lights, gradient and shims; we allow the cloud to expand and fall; we illuminate atoms with resonant D2 repump and trap MOT2 beams (full power) for 0.5–3 ms and expose the camera. While fluorescence imaging is noisier (the signal depends on beam powers and background lab light) than absorption imaging and while it is more difficult to accurately extract the atom number (typically we work with arbitrary units which are proportional to $N$), fluorescence imaging works for hot/large MOT clouds and enables long cloud expansion for temperature extraction. For these reasons, we often resort to fluorescence imaging for MOT2 optimizations.

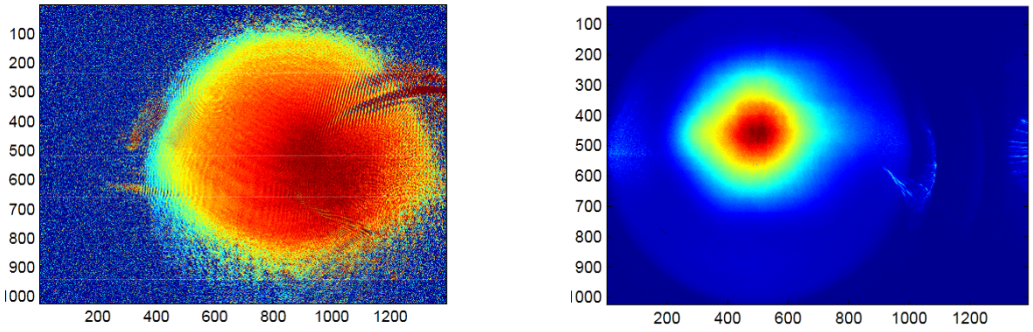


Figure 2.21: Absorption (left) and fluorescence (right) images of MOT2 atom clouds with similar conditions. The absorption image is taken with 0.7 magnification imaging system and short 3 ms TOF; the field of view is limited by the transfer tube clipping the probe beam. The fluorescence image is taken with a 0.2 magnification imaging system and has a much larger field of view.

With our modular laser frequency locking scheme and system stability, we are able to perform time-consuming multi-dimensional parameter optimization scans. For example, we performed a 3D scan on the push, trap and repump frequencies; Figure 2.22 shows their interdependence and the existence of a local maxima. The optimized laser beam frequencies and typical beam powers are summarized in Table 2.1. The MOT2 fill time constant is typically $\tau = 10$–$15\,\mathrm{s}$ and we use 20 s MOT2 fill duration, resulting in $N \sim 2 \times 10^9$ atoms and $T \sim 6\,\mathrm{mK}$. This fill time is much faster than 60 s we had for $^{40}$K isotope; we really despised that slow experimental cycle. Since the column density is very high, OD saturates at the cloud center to a value $\sim 4$ during absorption imaging. To extract atom number for such a high-density MOT, we take a probe lineshape and extrapolate $\mathrm{OD}_{\mathrm{peak}}$ from lineshape wings (e.g. typically $\mathrm{OD}_{\mathrm{peak}} \approx 8$ for a 3 ms TOF)by fixing the probe lineshape Lorentz width to be equal to the width measured with a low-OD cloud (typically 7–8 MHz, similar to the transition natural linewidth $\Gamma$).

Having an efficient load and a long lifetime in the quadrupole magnetic trap requires low temperatures on $\mathcal{O}(10$–$100\,\mu\mathrm{K})$ and good spatial mode-matching during load. Therefore, we strive to reduce the MOT cloud size in addition to its temperature. After loading MOT2, we perform the traditional D2 compressed-MOT (CMOT) stage [72] by abruptly increasing the MOT2 gradient to 11.3 G/cm and changing laser detunings: trap to $-8.8\,\Gamma$ and repump to $-2.7\,\Gamma$. After 20 ms, this

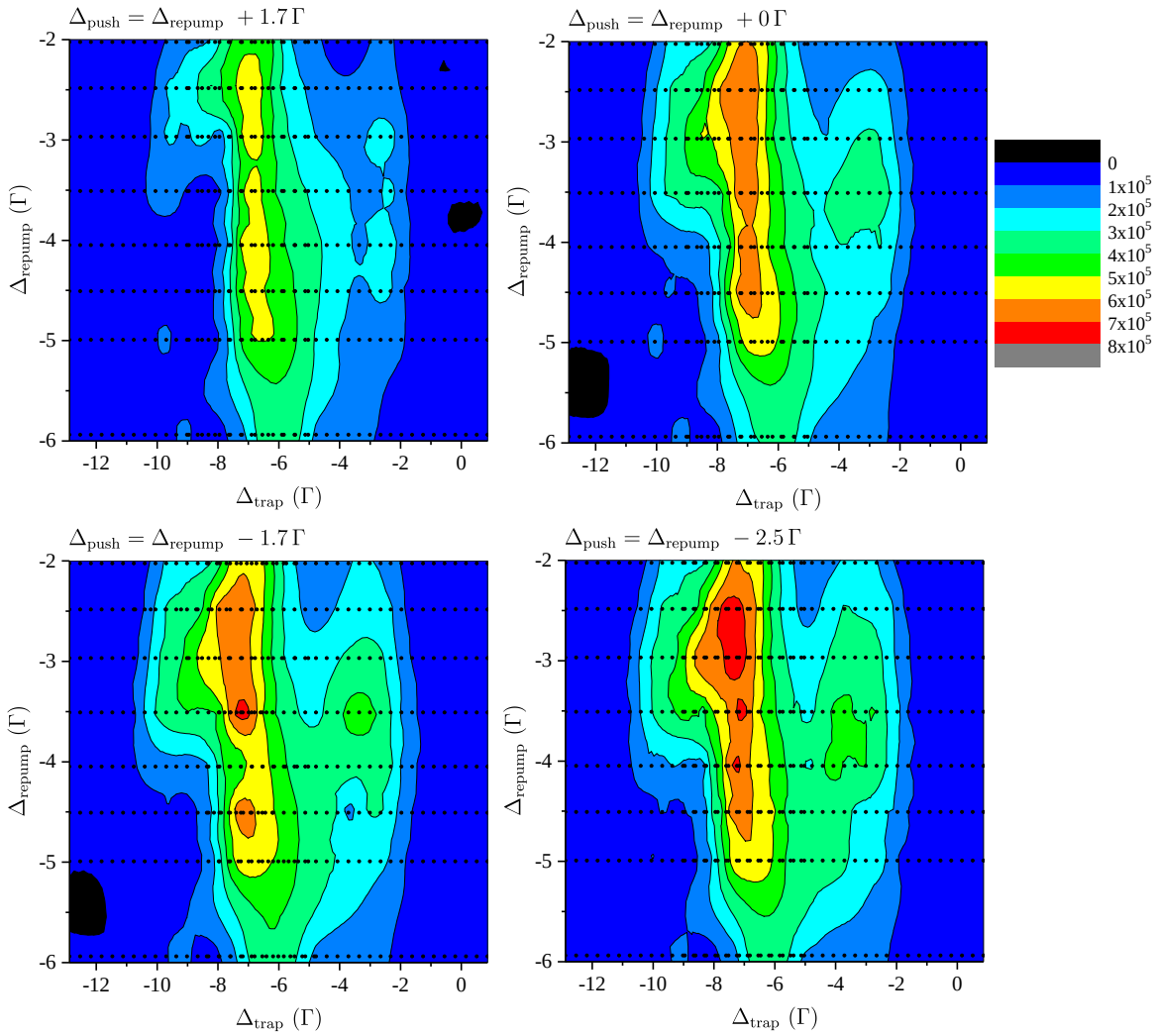


Figure 2.22: Contour plots demonstrating MOT2 laser frequency optimization. For each push beam detuning (linked to the repump frequency by an AOM frequency offset), we vary trap and repump frequencies, and record the fluorescence signal (imaging frame fit) which is proportional to the number of atoms captured in MOT2. We use a 15 s MOT2 fill duration. Here, TOF is 1 ms, $P_{\text{trap1}} = 210\,\text{mW}$, $P_{\text{repump1}} = 160\,\text{mW}$, $P_{\text{trap2}} = 170\,\text{mW}$, $P_{\text{repump2}} = 140\,\text{mW}$, $P_{\text{push}} = 8\,\text{mW}$, and 9.9 G/cm quadrupole gradient (31.1 A current). The maximal push beam detuning is limited by technical reasons relating to the required $\mathcal{O}(10\,\text{mW})$ push beam power and the use of an AOM for frequency shift from the repump light.

Table 2.1: Optimized MOT laser detunings and typical beam powers for 7.0 G/cm (strong direction) MOT2 quadrupole gradient (22.0 A current). A negative detuning corresponds to a transition red-detuned from the resonance.

| | Beam Waist (mm) | Power (mW) | Detuning ($\Gamma$) |
|---|---|---|---|
| MOT1 trap | 40 | 220 | $-7.6$ |
| MOT1 repump | 40 | 170 | $-3.4$ |
| MOT2 trap | 20 | 140 | $-7.6$ |
| MOT2 repump | 20 | 140 | $-3.4$ |
| push beam | 1 | 10 | $-5.1$ |

CMOT stage leads to $\sim 50\%$ reduction in cloud size and only $\sim 5\%$ atom number loss.

## 2.4 Sub-Doppler Laser Cooling

Due to the narrow hyperfine structure of the $4\,^2\mathrm{P}_{3/2}$ excited states, there is no efficient Sisyphus sub-Doppler cooling for potassium isotopes [73]. One must use either near-UV narrow-linewidth transitions [74] or gray molasses on the $|4\,^2\mathrm{S}_{1/2}\rangle \rightarrow |4\,^2\mathrm{P}_{1/2}\rangle$ 770 nm transition (D1) to reach sub-Doppler temperatures [75, 76]. We chose the latter due to a larger commercial availability of near-IR light and optics. A blue-detuned magneto-optical lattice [77] allows nearly-dark (gray) states for D1 transitions in potassium, enabling one to beat the Doppler limit $T_{\mathrm{Doppler}} = \hbar\Gamma/2k_{\mathrm{B}} = 145\,\mu\mathrm{K}$ and get close to the photon-recoil limit $T_{\mathrm{recoil}} = \hbar^2k^2/2mk_{\mathrm{B}} = 0.4\,\mu\mathrm{K}$, where $k = 2\pi/\lambda$.

### 2.4.1 D1 Laser System

We use two 770 nm 80 mW DBR laser diodes (Photodigm PH770DBR080T8) to generate $|4\,^2\mathrm{S}_{1/2}, \mathrm{F} = 2\rangle \rightarrow |4\,^2\mathrm{P}_{1/2}, \mathrm{F}' = 2\rangle$ D1 trap and $|4\,^2\mathrm{S}_{1/2}, \mathrm{F} = 1\rangle \rightarrow |4\,^2\mathrm{P}_{1/2}, \mathrm{F}' = 2\rangle$ D1 repump light, see Fig. 2.23. The D1 laser detunings are defined in Fig 2.13. We lock the D1 trap frequency using Doppler-free saturated absorption spectroscopy via a modified PDH locking technique, see Fig. 2.24. The probe beam is phase modulated (similarly to the D2 master lock), the pump beam intensity is chopped (to get rid of the Doppler background, see Fig. 2.25) and we generate a second-

derivative/harmonic of the PDH signal to provide lock peak detection. The amplitude modulation lock-in detection and the peak detector were necessary additions to prevent the D1 laser from unlocking during strong RF and microwave radiation (up to 25 W, $\sim 2$ m away from the D1 setup) from loop antennas we use to induce magnetic dipole transitions. Other methods, including mu-metal shielding, RF filtering, better grounding and shortening of routing cables, failed to resolve the unlocking issue. The new scheme made the D1 lock very robust.

The D1 trap frequency is changed using a double-pass AOM "cat's eye" configuration, allowing $\sim 50$ MHz ($8\,\Gamma$) dynamic range without optical re-alignment. The D1 repump frequency is locked to the D1 trap frequency via a heterodyne beatnote lock, similar to the heterodyne locks (Fig. 2.17) used in the D2 setup. We optimize the beatnote servo to establish phase coherence between the two lasers ($> 10$ dB narrow beatnote signal on top of a broad convoluted lineshape). This coherence enables Raman transitions ($\Lambda$-configuration) and observation of a narrow cooling feature (see Fig. 2.26), whose width is less than the excited state natural linewidth $\Gamma$.

The D1 trap and D1 repump light are combined on a 70:30 non-polarizing beam splitter before being amplified by the TA. Since the TA amplifies the two wavelengths in a nontrivial way, we use commercial and homebuilt optical cavities to sense the output power of each component (e.g. $\sim$ 1:8 repump:trap ratio). The D1 light is sent through a 10 m PM-SM fiber to the science optical table, delivering 130 mW. The D1 light (7 mm waist) is combined with the D2 MOT2 beams and is sent to the MOT2 vacuum chamber. The molasses lattice is formed by retro-reflected D1 light with circular polarization.

### 2.4.2 D1 Cooling and Quadrupole Trap Load

After the D2 CMOT stage, we perform a hybrid D1-D2 CMOT stage [78]: we instantaneously turn off the D2 trap light, turn on the D1 trap light (blue-detuned), change the D2 repump frequency (red-detuned) and reduce its power, and change the shim magnetic field values. We keep the quadrupole gradient unchanged at 11.3 G/cm. We optimized these parameters to minimize the cloud temperature, using a long-TOF fluorescence imaging. We find that the D1-D2 CMOT stage

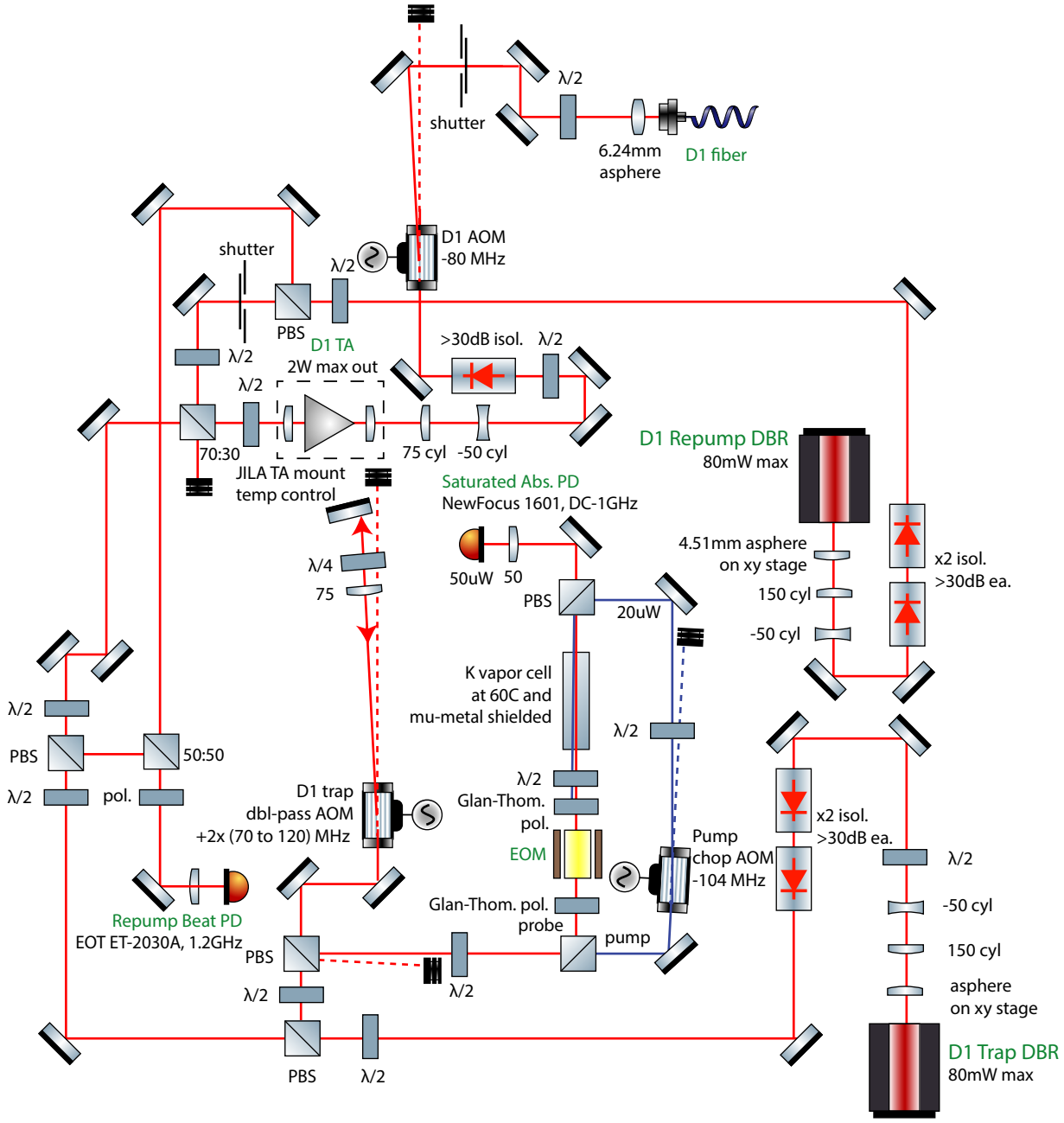


Figure 2.23: D1 laser system. The D1 trap laser frequency is locked to a saturated absorption spectroscopy setup. The D1 repump laser frequency is locked to the D1 trap via a heterodyne beatnote lock. The trap and repump light are combined before amplification and are sent to the science optical table via the same fiber.

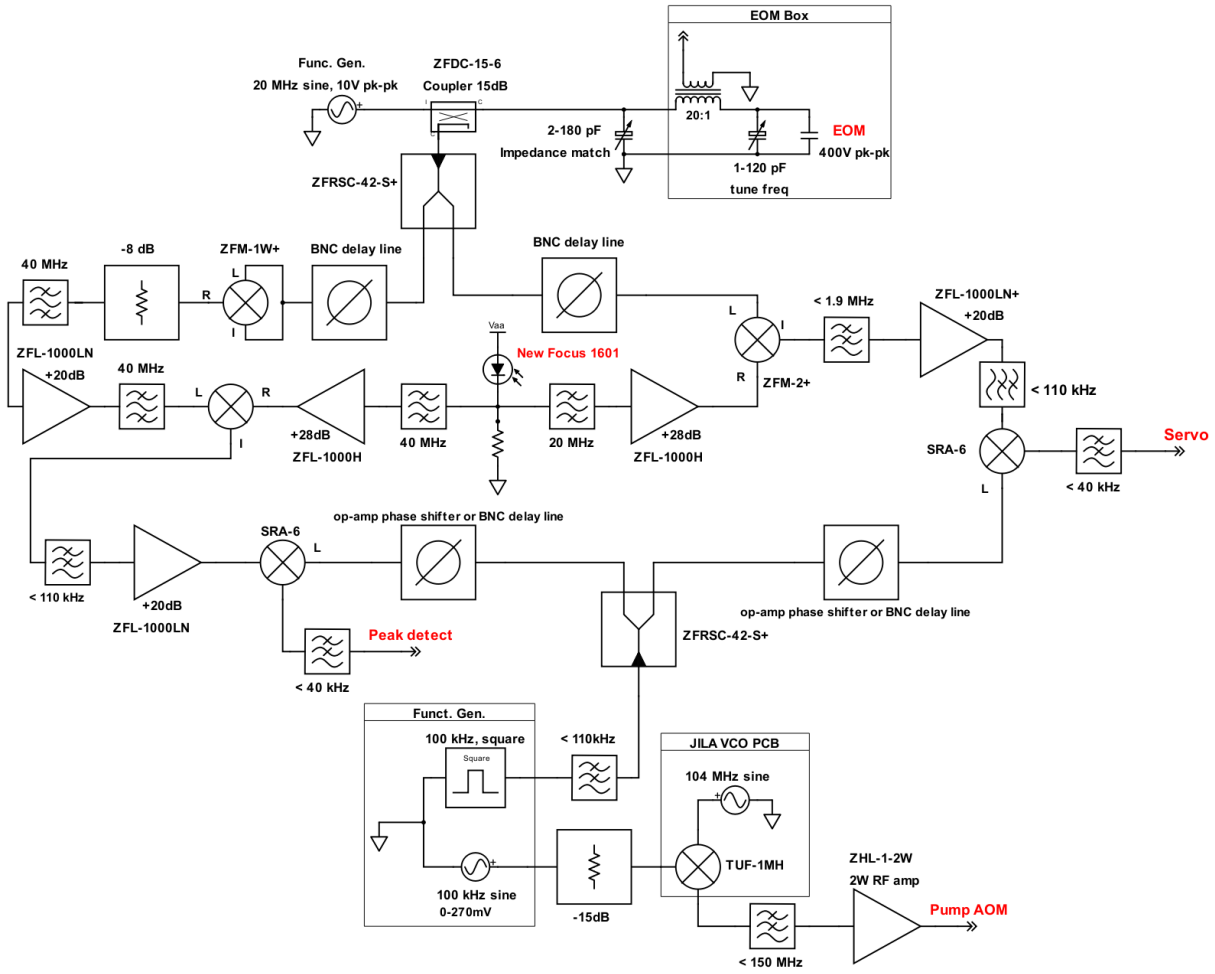


Figure 2.24: D1 frequency locking scheme via a modified PDH lock. A function generator drives a homebuilt resonant EOM tank circuit to phase modulate the probe beam. After passing through a saturated absorption spectroscopy, the probe beam is detected on a New Focus 1601 photodetector (see Fig. 2.23). We retrieve the first derivative (approximately speaking) of the absorption lineshape using the first harmonic (20 MHz) signal and send it to the servo (JILA high speed loop filter). We retrieve the (approximate) second derivative of the absorption lineshape using the second harmonic (40 MHz) signal and send it to the scope for peak detection. Additionally, we form AM lock-in detection to get rid of Doppler background and to make the PDH lock immune to background RF lab noise (10-1000 MHz stemming from RF antennas and/or other electro-optic modulators). We chop the pump beam intensity by mixing the 104 MHz RF drive with a 100 kHz sine wave before sending it to the pump beam AOM. We demodulate the 20 MHz and 40 MHz signals with the 100 kHz local oscillator (a sine wave after filtering the square wave of the function generator sync. output).

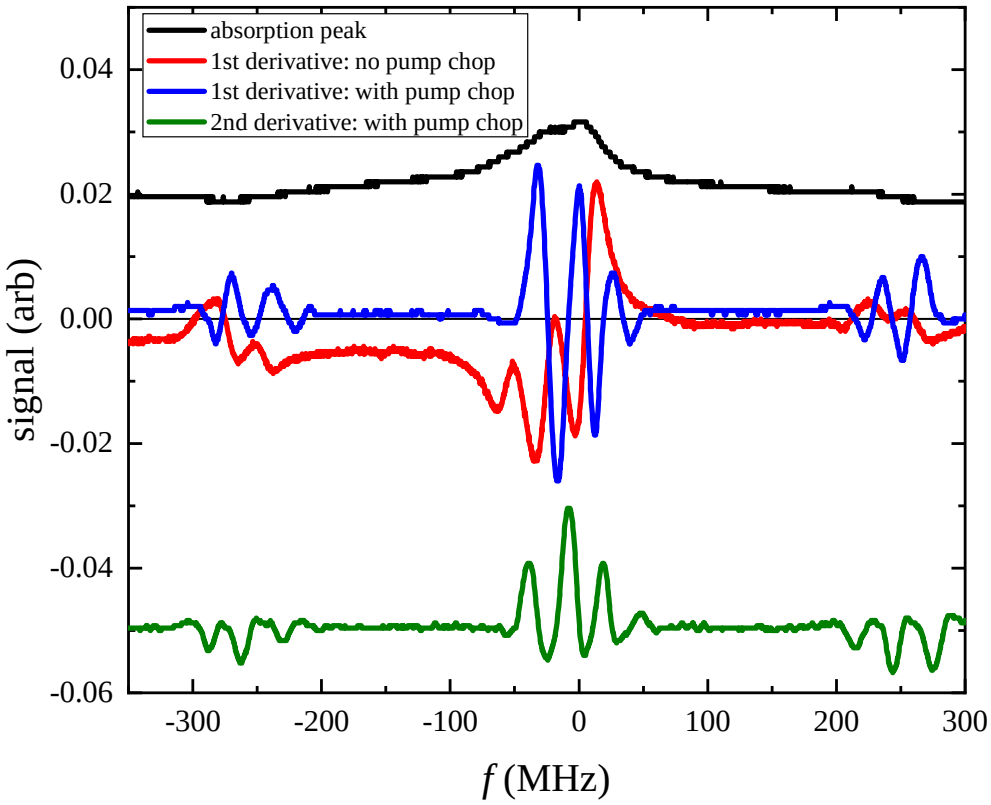


Figure 2.25: D1 spectroscopy signal: absorption peak with no phase modulation (black); first derivative (approximately speaking; the shape of the PDH lock demodulated signal depends on the lineshape width and the phase modulation frequency) with Doppler background and with probe phase modulation (red), using a similar setup as used for D2 laser lock in Fig. 2.16; first derivative without Doppler background and with probe phase modulation and pump chopping (blue), output from Fig. 2.24 circuit; second derivative without Doppler background and with probe phase modulation, pump chopping and second harmonic extraction (green), output from Fig. 2.24 circuit. Here, the frequency axis is calibrated using a wavemeter (while locking to individual spectral lines) and has an arbitrary offset. Each signal is scaled and shifted vertically for illustrative purposes.

prefers a low D2 repump power (a factor of 10–15 smaller than the MOT load and D2 CMOT values) and a near-resonant D2 repump frequency (red-detuned, at $-0.8\,\Gamma$); the stage is less sensitive to the D1 trap parameters (we use 120 mW power and blue-detune to $+2\,\Gamma$). This stage is kept on for 10 ms to reduce the cloud temperature to 220 $\mu$K at the expense of $\sim 10\%$ in atom number.

The D1 gray molasses capture efficiency depends mainly on the beam intensity and the initial cloud temperature. Since the D1-D2 CMOT stage pre-cools the atoms, we only require $> 100$ mW of D1 light to capture most atoms in the molasses. First, we turn off the D2 repump light, turn off the D1 trap light, turn off the quadrupole field, change the shim values, set the D1 frequencies and initiate opening of the D1 repump shutter (which was off during the D1-D2 CMOT; the shutter is before the 70:30 D1 trap-repump combiner, as shown in Fig. 2.23). Then, after 1 ms duration of dwell time, we turn on 130 mW of D1 light (containing trap and repump) and immediately begin linearly ramping down the D1 power to 13 mW in 8 ms. The final atom temperature relates to the final D1 beam intensity. We routinely reach 15 $\mu$K and have observed temperatures as low as 8 $\mu$K. Reaching such temperatures requires extensive optimization. We iteratively change the shim values (molasses are very sensitive to non-zero magnetic fields), the D1 beam alignment (need good optical lattices), the repump-to-trap power ratio (robust, around 1:3–1:10 is good) and the laser detuning. While the atom number and temperature after the D1 molasses stage depend weakly on the D1 trap parameters, the temperature is particularly sensitive to the Raman detuning (see Fig. 2.13 for definition) between the trap and repump light, as shown in Fig. 2.26. A 8 ms D1 gray molasses stage enables us to reach 15 $\mu$K at the expense of $\sim 30\%$ in atom number.

After the sub-Doppler cooling stage, we begin to load atoms into the quadrupole trap (formed by the same coils used for MOT2 gradient). Since we ultimately desire atoms only in the $|4\,^2\mathrm{S}_{1/2}, \mathrm{F} = 1, \mathrm{m_F} = -1\rangle$ state, we pump $|4\,^2\mathrm{S}_{1/2}, \mathrm{F} = 2\rangle$ atoms into the $|4\,^2\mathrm{S}_{1/2}, \mathrm{F} = 1\rangle$ state by turning off the D1 trap light 2.5 ms after turning off the D1 repump light. Since the D1 molasses dark states favor the $\mathrm{F} = 1$ manifold, we are able to predominantly populate the $\mathrm{F} = 1$ state with relative ease. Furthermore, since $|\mathrm{F} = 1, \mathrm{m_F} = -1\rangle$ is the only magnetically trappable $\mathrm{F} = 1$ state, one would like to pump all atoms there. We tried doing so with D1 and D2 pump light in separate

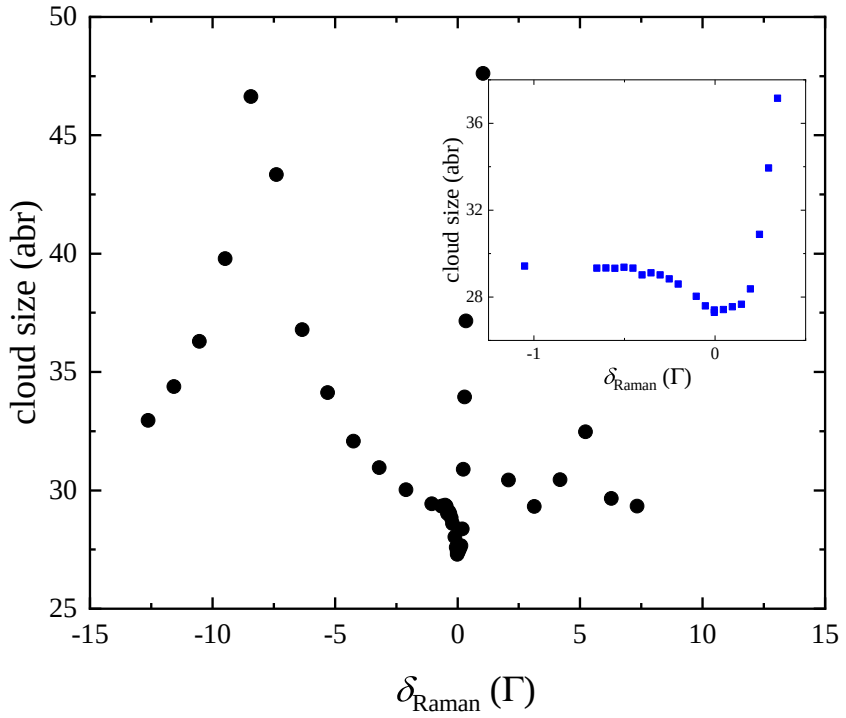


Figure 2.26: Cloud size vs Raman detuning for D1 gray molasses. Here we use a long TOF, hence the temperature is proportional to the cloud size. A feature with a width smaller than the transition natural linewidth Γ appears near zero detuning, as depicted in the inset zoom.

attempts. While successful, we noticed significant heating (up to 100 $\mu$K; related to the high pump intensity, which is required to efficiently pump such high-OD clouds) and abandoned this route. We prefer cold and pure $|\mathrm{F}=1,\mathrm{m_F}=-1\rangle$ samples with $\leq \frac{1}{3}$ QT load efficiency over hot clouds with greater atom number.

The QT load starts by creating a magnetic potential that mode-matches the spatial cloud distribution. Failure to do so will result in significant heating from the gained potential energy. After releasing atoms from D1 molasses, we suddenly turn on the QT and use shims to center it on the cloud. We find that a quadrupole trap with 30 G/cm gradient ($\sim \times 2$ the gradient needed to support against gravity) enables the best loading efficiency ($\sim 35\%$ of $|\mathrm{F}=1,\mathrm{m_F}=-1\rangle$ state) with minimal heating (25 $\mu$K), in agreement with Ref. [79] result, where the author derived the optimal QT load gradient for maximal phase-space density (PSD). After the initial load and a 20 ms dwell duration, the shims are ramped off and the QT is adiabatically compressed to 100 G/cm (300 A)

in 100 ms. While this step increases the cloud temperature to 80–100 $\mu$K, it also reduces the cloud size, necessary for an efficient cart transfer to the science cell through narrow vacuum components (1.5 cm inner diameter at the narrowest spots). Using 30 G/cm for cart transfer results in 50% less atoms reaching the science cell. We find that the efficiency saturates beyond 80 G/cm. Using 100 G/cm, the cart transfers $3 \times 10^8$ atoms in the $|\mathrm{F} = 1, \mathrm{m_F} = -1\rangle$ state to the science cell (54 cm away) in 3.5 s. We've measured the two-way transfer efficiency to be 77% (to the science cell and back to the MOT chamber; or 88% one-way, assuming symmetrical two-way loss). The atom lifetime in the cart QT is long in the MOT2 and the science chambers (60–70 s), mainly limited by the Majorana spin-flip loss [80].

Thermodynamic properties of non-interacting atoms in a quadrupole trap are extracted from a single-particle partition function:

$$Z_1 = \frac{64\sqrt{2}\pi^{5/2} m^{3/2} \left(k_\mathrm{b} T\right)^{9/2}}{(h\mu b)^3}, \tag{2.5}$$

where the external potential is given by Eq. 2.1 and we ignore gravity. A thermal cloud has spatial and momentum probability distributions described by:

$$P(x, y, z, p_x, p_y, p_z) = \frac{1}{Z_1} \exp\left(-\frac{E(x, y, z, p_x, p_y, p_z)}{k_\mathrm{B} T}\right), \tag{2.6}$$

$$P(x, y, z) = \frac{1}{32\pi} \left(\frac{\mu b}{k_\mathrm{B} T}\right)^3 \exp\left(-\frac{\mu b}{2k_\mathrm{B} T} \sqrt{x^2 + y^2 + 4z^2}\right), \tag{2.7}$$

$$P(p_x, p_y, p_z) = \frac{h^3}{\left(2\pi m k_\mathrm{B} T\right)^{3/2}} \exp\left(-\frac{p_x^2 + p_y^2 + p_z^2}{2m k_\mathrm{B} T}\right), \tag{2.8}$$

where $E$ is the total energy, $b$ is the gradient along the strong direction $z$, $\mu$ is the magnetic moment of the trapped spin state and the normalization is such that integration over all spatial and momentum dimensions results in unity probability. The rms cloud size $\bar{z} = \sqrt{\langle z^2 \rangle} = 2k_\mathrm{B} T/\mu b$, where $\langle z^2 \rangle = \int z^2 P(x, y, z) dx dy dz$; the rms sizes along $x$ and $y$ directions are twice as large. We often fit clouds released from the QT with a 2D Gaussian function; for in-situ imaging, we use a 0.65 correction factor for determining the rms size from a Gaussian width. Since atoms are presumed to be non-interacting, the rms momentum values are equal to $\sqrt{m k_\mathrm{B} T}$. The atom density distribution is $n(x, y, z) = N P(x, y, z)$. Similarly, many-atom properties can be retrieved from an $N$-particle

partition function $Z_N = (Z_1)^N/(N!)$. For example, we determine the expected temperature rise due to adiabatic compression of the trap to be $T_f/T_i = (b_f/b_i)^{2/3}$, where $b_i$ and $b_f$ are the initial and final gradient values. We find this by relating the cloud volume $V$, the heat capacity $C_V = \left(\frac{\partial U}{\partial T}\right)_V$ and the gas pressure $p = -\left(\frac{\partial b}{\partial V}\right)_T \left(\frac{\partial F}{\partial b}\right)_T$ ($p = Nk_BT/V$ for a non-interacting gas), where the internal energy $U = -\frac{d\ln(Z_N)}{d\beta}$, the Helmholtz free energy $F = -k_BT\ln(Z_N)$ and $\beta = (k_BT)^{-1}$. Similarly, one can obtain the scaling power 2/3 from dimensional analysis: relating PSD, density, $T$ and $b$, while acknowledging that the PSD remains constant during an adiabatic ramp. Our QT compression measurements agree to within 10% of the 2/3 scaling power.

After the cart transfer to the science cell, we transfer atoms to the science QT coils by ramping up the science QT (0 to 100 G/cm in 200 ms) while ramping down the cart QT (100 G/cm to 0 in 200 ms). We move the cart away after this swap. Since our next goal is to load the atoms into a small-waist optical trap, we further compress the magnetic trap to 199 G/cm (364 A). Typically, we end up with $3 \times 10^8$ atoms in the $|\mathrm{F} = 1, \mathrm{m_F} = -1\rangle$ state at a temperature 180 $\mu$K, a peak PSD $1.4 \times 10^{-6}$, a density-weighted density $\langle n \rangle = \frac{1}{N}\int n^2(\vec{x})d^3x = 1.9 \times 10^{10}\,\mathrm{cm}^{-3}$ and $\tau = 60$ s QT lifetime. While the trap has a modestly high trap frequency of 362 Hz, defined as $\mathrm{velocity_{rms}/size_{rms}}$, a small scattering length ($a = -46\,a_0$ for $B = 0$ G, assuming $T = 0$) leads to a low 1.3 Hz collision rate and a slow thermalization rate of 0.5 Hz (assuming we require $\approx$ 2.5–2.7 number of elastic two-body collisions for thermalization [81, 60, 82]).

## 2.5 All-Optical Evaporation

### 2.5.1 Optical Trap Load

Since efficient evaporative cooling requires a high thermalization rate, we need to increase our low elastic collision rate. We do so by transferring the atoms to an optical dipole trap (OT) and use a nearby ($\sim$ 34 G) Feshbach resonance to enhance elastic collisions. However, since the optical trap (OT) load efficiency also depends on thermalizing collisions, we need to be creative [83]. We employ an intense optical dipole beam with a 2.7 mK trap depth (resulting from a 25 W,

1064 nm, 28 $\mu$m $\times$ 28 $\mu$m waist beam) that significantly exceeds the collisional energy where the Ramsauer-Townsend minimum occurs (400 $\mu$K, see Fig. 2.7). This enables us to transfer 1–5% of atoms in the QT, whose cloud size is 600 $\mu$m $\times$ 1200 $\mu$m $\times$ 1200 $\mu$m, to the optical trap, consistent with the expected load efficiency estimates [84, 85, 83].

The OT load begins with the shims turning on to shift the QT center; the science cell has three shim pairs surrounding it, facing orthogonal directions. Then, the optical trap beam adiabatically ramps on to full power (20–25 W) in 200 ms. It takes 8 s to fill the OT potential, after which we ramp off the QT in 100 ms. While the PSD of the loaded cloud is nearly constant vs. dipole power, more atoms are loaded for higher powers. The number of atoms loaded into the OT saturates for powers $>$ 21 W and 8 s fill duration. The best OT load efficiencies occur when the focus of the dipole trap is *near* the QT center. This alignment is very sensitive, as alignment *to* the QT center leads to significant Majorana loss, as shown in Fig. 2.27. For alignment, we iterate between the OT beam tilt, OT focus location and the QT center (using shims). Additional complications resulting from thermal lensing (up to 1 mm in 10 s along the dipole beam propagation direction; compare this to the 2.3 mm Rayleigh range) make careful OT alignment crucial to get stable cloud conditions.

We typically load up to $5 \times 10^6$ atoms with a 300–400 $\mu$K temperature and $4 \times 10^{-5}$ peak PSD from a QT with 1–3 $\times$ $10^8$ atoms and 180–220 $\mu$K temperature. We estimate that a 25 W, 28 $\mu$m $\times$ 28 $\mu$m waist beam forms a potential with a $(\omega_x, \omega_y, \omega_z)/2\pi = (8700, 74, 8700)$ Hz trapping frequencies ($y$ along the beam), a 2.7 mK trap depth and a 1.4 $\mu$K/s heating rate (due to off-resonant scattering). Such a trap results in a cigar-shaped atom cloud with a large aspect ratio. Highly elongated clouds are difficult to analyze, as depicted in Fig. 2.29. While imaging along the dipole trap direction would help, thermal lensing from the high-power beam would lead to unnecessary imaging complications. Therefore, we decided to implement additional optical trapping beams that would shape the cloud at lower temperatures; see Sec. 4.2.2 for additional details on how we settled on the final optical trap configuration. The additional beams are: a vertical beam ("V beam") with a 140 $\mu$m $\times$ 140 $\mu$m waist and a horizontal sheet beam ("H2 beam") with a 80 $\mu$m $\times$ 810 $\mu$m waist, whose strong direction is along gravity and propagates at a 45° with respect to the 28 $\mu$m $\times$ 28 $\mu$m

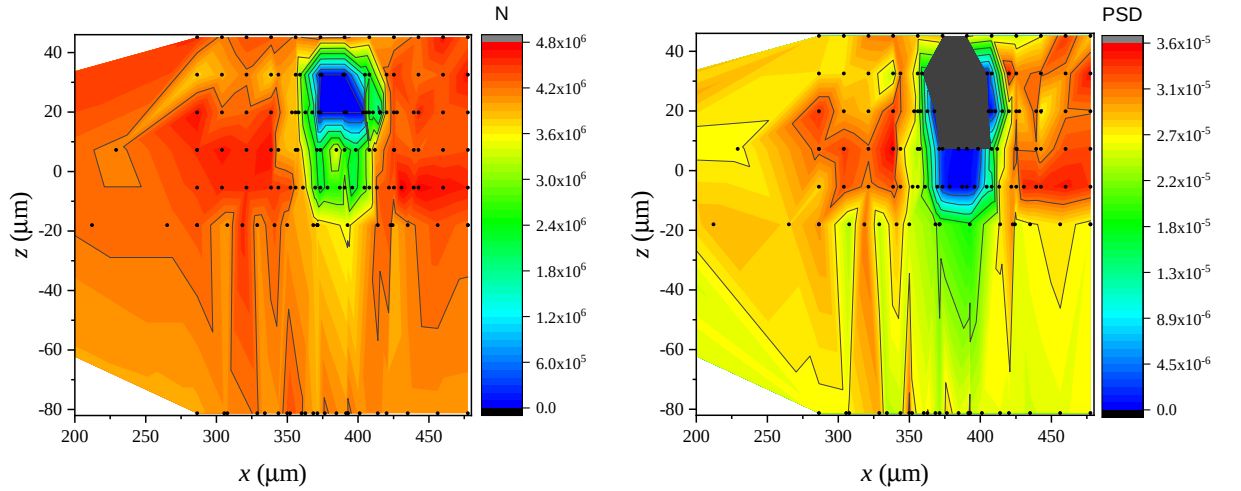


Figure 2.27: Sensitive alignment of the dipole beam is needed for an efficient OT load. The figures show that the largest number of loaded atoms (left) with the highest peak PSD (right) occur when the dipole beam is aligned near the QT trap center. At the center, significant Majorana spin-flip loss occurs (deep blue contour). Note an arbitrary offset of the axis values ($z$ is along gravity/strong QT direction, $x$ is horizontal). Ignore the gray region in the PSD plot, where we have insufficient data or have small atom signal that results in unreliable temperatures. Note the significant loss and heating below the Majorana hole, also shown in Fig. 2.28.

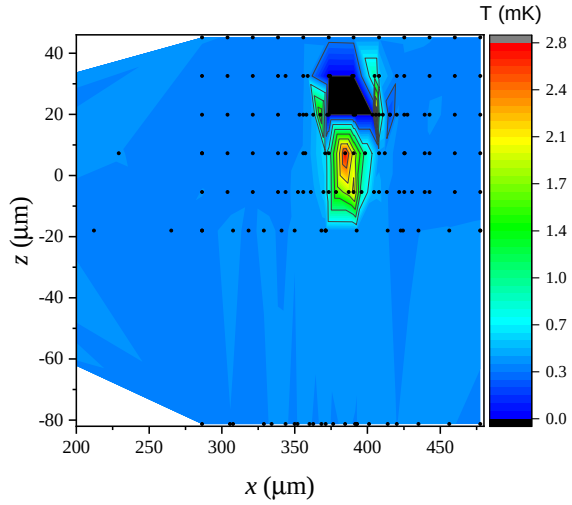


Figure 2.28: Atom temperature during optical trap load alignment.

waist beam ("H1 beam"). The H2 and V trap depths are 5.5 $\mu$K and 6.5 $\mu$K for their highest powers of 8 W and 1.5 W, respectively. Since the new potentials are only relevant at low temperatures, the H1 beam needs to perform most evaporation to cool atoms from $\sim 500\,\mu$K down to $< 500$ nK. The H1 beam requires a $10^3$–$10^4$ dynamic range in power control and small intensity noise at all levels.

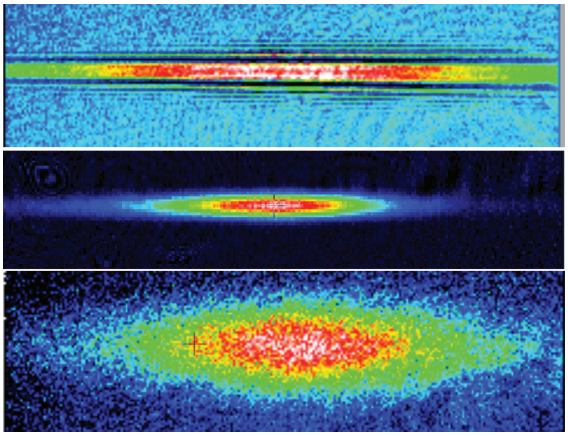

Figure 2.29: Atom cloud expansion after optical dipole trap load, with increasing TOF (top to bottom). The dipole trap propagates perpendicular to the imaging direction. The in-situ image (top) suffers from diffraction: the cloud size is smaller than the imaging resolution. The hot cloud expands significantly in a matter of a few ms (3 ms for bottom image). Imaging magnification is 0.7 and the horizontal field of view is 9.5 mm.

### 2.5.2 Optical Trap Laser Setup

Our optical dipole trap system has challenging requirements. We need high optical power (up to 25 W) delivered to the atoms, ability to accurately control the power with a $10^4$ dynamic range, minimal intensity noise and have great pointing stability ($\ll 28\,\mu$m, the H1 beam waist). To achieve these requirements, we decided on the Mephisto-Nufern laser-amplifier combination, whose properties were previously measured in select publications [86, 87]. We split and control the amplified light, then route it to the science cell via photonic-crystal fibers (PCFs), as shown in Fig. 2.30. After diligent engineering and overcoming multiple challenges, the dipole trap laser system became one of the most robust systems in our lab.

The seed laser (Coherent Mephisto S, 500 mW maximum output) is a monolithic non-planar ring oscillator (NPRO) that outputs coherent light ($<$ 1 kHz linewidth) with great beam quality ($\text{TEM}_{00}$, $M^2 < 1.1$; one of best Gaussian beams I've ever worked with) and low relative intensity noise (RIN) at $< -90$ dB/Hz. We run the laser at 24°C, 0.61 A and 1064.1 nm, operating in the middle of the measured mode-hop-free region. We collimate the output light (160 $\mu$m waist at the NPRO, 50 mW) to a 450 $\mu$m waist, pass it through an optical isolator, fiber couple (Thorlabs

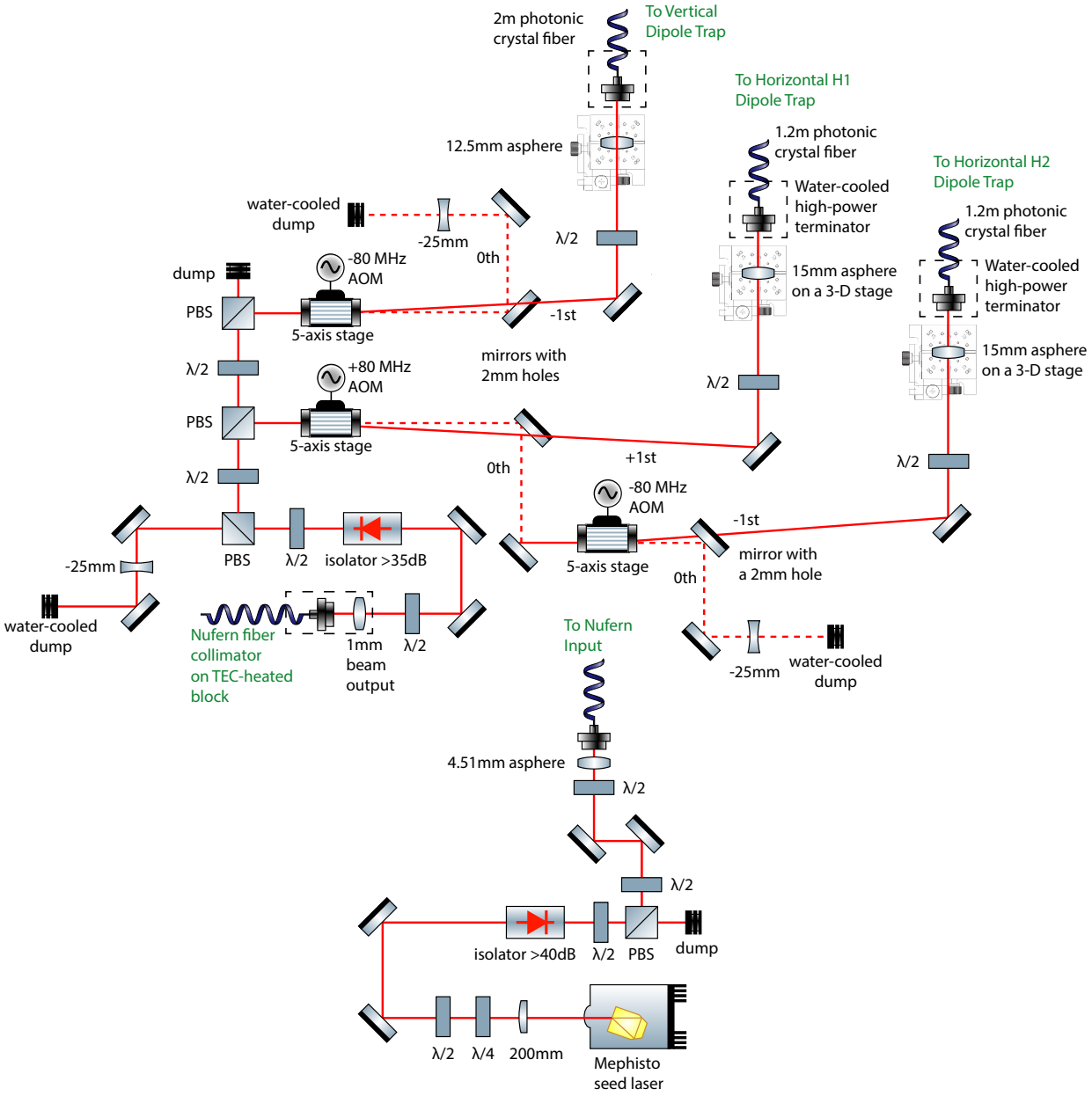


Figure 2.30: Optical setup for control of optical dipole traps. The Mephisto seeds the Nufern fiber amplifier, whose output is split into V, H1 and H2 beams. AOMs enable individual beam power control.

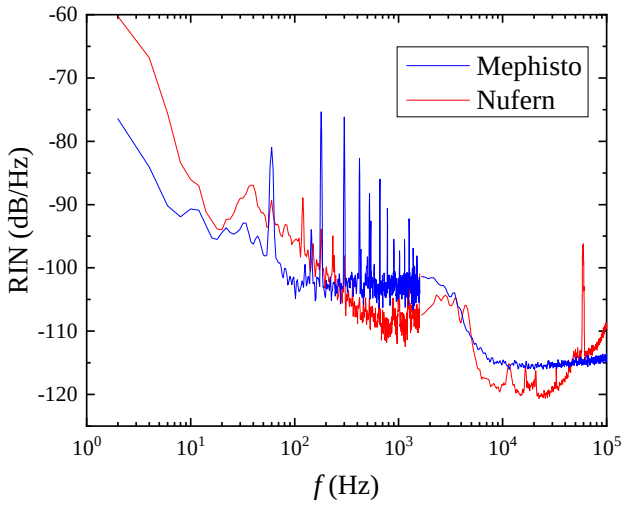


Figure 2.31: Measured relative intensity noise of a free-running (no feedback) Nufern fiber amplifier (full 50 W power) and a Mephisto seed laser. The FFT analyzer spectral resolution is changed from 128 Hz to 2 Hz below 1500 Hz frequency. At very high frequencies (beyond the shown) we see a noise peak at around 1 MHz resulting from relaxation oscillations from residual pump noise; we are unable to suppress this feature due to a faulty "noise eater" feedback circuit in the Mephisto.

2 m patch with a steel-steel jacket, using PM980XP Nufern fiber) and deliver 40 mW of PM light ($>$ 25 dB extinction ratio) to the Nufern amplifier input.

The Nufern fiber amplifier amplifies the seed light up to 50 W (for 15–50 mW input), while retaining the low RIN properties of the Mephisto laser, as shown in Fig. 2.31. Based on our previous experience, we took additional steps to ensure stable Nufern amplifier operation. The Nufern box is placed on a vibration-damping pad, water-cooled to 23°C (its crucial to a have stable temperature near 23°C) using a commercial chiller (Thermo Scientific Thermochill II, supplying 1.5 gallons/min) and the Nufern PCF output is tied down (without stress) and isolated using a rubberized sleeve. Additionally, we opted for a custom stainless steel collimator enclosure (much better than the standard aluminium part) with a custom 1 mm beam output diameter. We temperature-stabilize the collimator assembly using a TEC-heated aluminium block.

All dipole trap optics are contained in a large steel enclosure and all light is terminated by water-cooled beam dumps (Trap-IT ABD2CNP and Haas Laser Technologies BD25BW). It takes up to 1 hr for the temperature to stabilize within the laser box, leading to an iterative beam alignment

procedure. The enclosure also assists in preventing dust accumulation on the optics; we have burned some optics during the initial setup. We resort to mostly steel opto-mechanics, short beam height (3 in, set by the PCF 3-axis stage, Thorlabs MBT616D) and minimal number of components (thanks goes to a JILAn, Hans Green, for precisely machining holes in our mirrors) and their separation distances. We use high-power 1064 nm V-coated UV-grade fused silica optics (mostly from CVI) and minimize mechanical stress on the optics to ensure high polarization purity and high beam quality. We use large-aperture Tellurium Dioxide AOMs (Gooch & Housego AOMO 3080-199, mounted on good heat sinks) for intensity control; this leads to an improved beam pointing stability compared to when we use small aperture or flint glass AOMs.

The output from the Nufern amplifier is split into vertical and horizontal beam paths. The H2 beam results from the zeroth-order of the H1 beam intensity control AOM. AOM frequencies and orders are chosen to have a minimal chance of beam interference at the atoms. Each beam is fiber coupled into a PM-SM photonic-crystal fiber (NKT Photonics LMA-PM-15 fiber, Tratech Fiberoptics HP2.5 assembly) using one mirror, a 3-axis translation stage and a V-coated UV-grade fused silica asphere (TechSpec/Edmund Optics). The PCF has a high-power 1064 nm-AR-coated epoxyless/fused-endcap that expands the beam and protects the fiber core from dust, a mode stripping lantern that rejects the uncoupled light, and a copper assembly that we water-cool using 23°C water from a chiller.

While the large mode (12.6 $\mu$m mode diameter) PCF significantly reduces the stimulated Brillouin scattering (SBS), residual SBS back-reflections lead to an unstable Nufern operation. Using large optical isolation (an EOT Pavos 1045-1080 nm $>$ 30 dB isolator along with a Thorlabs IO-5-1064-VHP 1064 nm $>$ 35 dB isolator) resolved the back-reflection problem. However, beam quality degradation at high power (development of a hole in the beam center), resulting from self-focusing in the isolator material, lead to a terrible 60% PCF coupling efficiency, see Fig. 2.32. To circumvent the back-reflection and beam quality issues, we only use the $>$ 35 dB isolator, reduce the PCF length from 2 m to 1.2 m for H1 and H2 beams, and reduce the Nufern output power (from 50 W at 37 $A$ to 38 $W$ at 32 $A$). We reach 95% coupling efficiency and can get up to 32 W at the

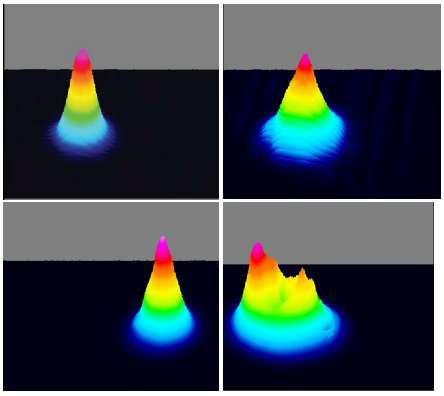

Figure 2.32: Nufern beam quality degradation at high power. At low operating power, the beam quality is great after an optical isolator (top left) and before PFC fiber (bottom left). However, at high operating power, self-focusing of the beam (top right) by the isolator material results in a beam with a hole at the PCF fiber input (bottom right). All images have a normalized beam peak intensity.

fiber output.

We deliver up to 2 W for V trap, 25 W for H1 trap and 8 W for H2 trap (after H1 trap ramps down during evaporation). Figures.2.33, 2.34 and 2.35 demonstrate how we shape and deliver the dipole light to the atoms. Similarly to the laser source side, we use high-power optics, high-quality opto-mechanics and short beam heights. We devote extra attention to wavefront error and use low distortion mirror mounts (e.g. Newport SU100W-F3K-127) when necessary. We use a high-resolution beam profile camera to verify beam quality at the focus (e.g. astigmatism and asymmetry), as depicted in Figs.2.36 and 2.37. The H1 and H2 beams are terminated by water-cooled beam dumps. We monitor long-term beam pointing stability using CCD cameras (Allied Vision MAKO G-125), allowing fast alignment troubleshooting.

A great beam pointing stability is crucial to get reproducible conditions and a low atom heating rate. We achieve a good long-term pointing stability by utilizing high-quality optics, low-expansion opto-mechanics and by surrounding the science optical table with curtains (improves the temperature stability and regulates the air flow). Additionally, we check the dynamic pointing stability. The expected atom heating rate due to pointing noise is $\langle dE/dt \rangle = \pi m \omega_{\mathrm{trap}}^4 S_x(\omega_{\mathrm{trap}})/2$, where $\langle dE/dt \rangle$ is time-averaged change rate of the total energy, $\omega_{\mathrm{trap}}$ is the trap frequency along

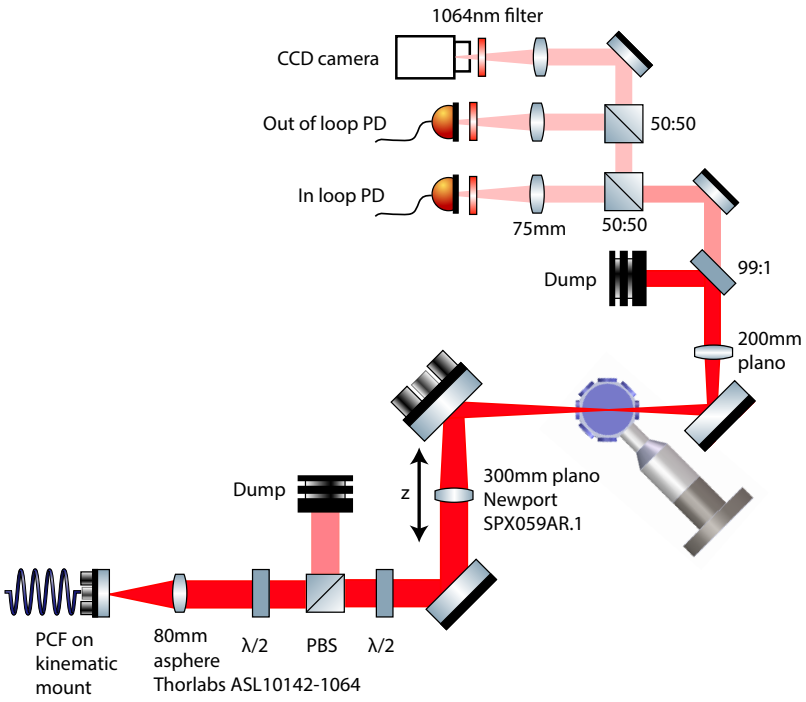


Figure 2.33: Optics for the horizontal dipole trap H1 (load beam) with a 28 $\mu$m × 28 $\mu$m waist and 25 W beam power. For illustrative purposes, we change the science cell orientation. The probing PDs and CCD cameras have 1064 nm band-pass filters.

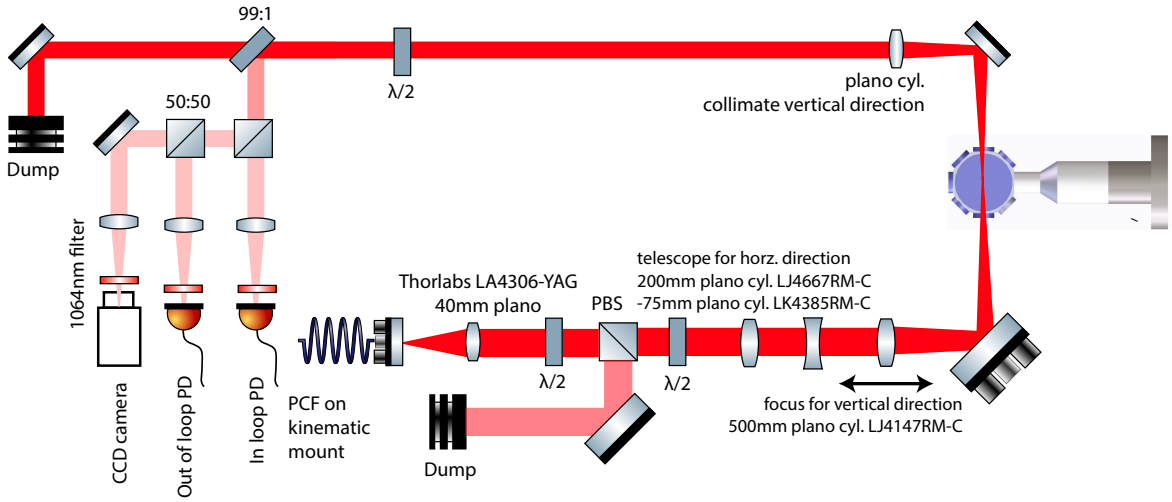


Figure 2.34: Optics for the horizontal dipole trap H2 with a 80 $\mu$m × 810 $\mu$m waist and 8 W beam power, where the strong direction is along gravity (termed vertical direction in the schematic). The beam has a vertical polarization (into the page) before entering the cell.

a particular direction (in this case $x$) and $S_x(\omega)$ is the one-sided power noise spectrum of the

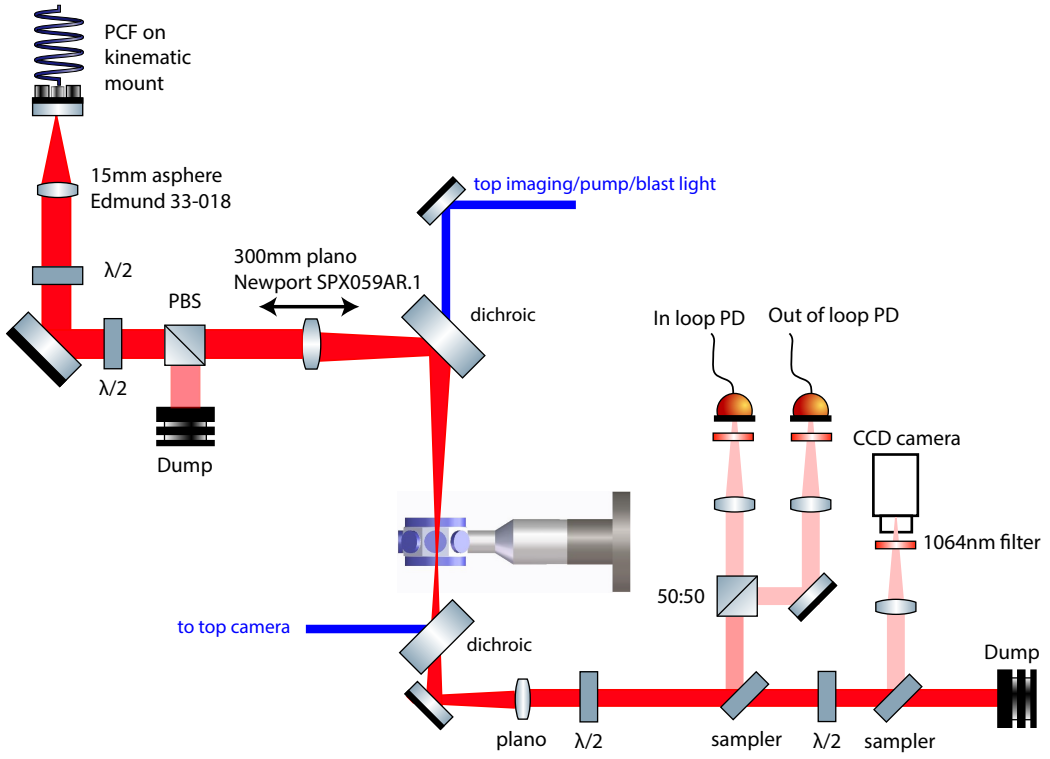


Figure 2.35: Optics for the vertical dipole trap with a 140 $\mu$m $\times$ 140 $\mu$m waist and 2 W beam power. The vertical dipole beam setup is located on a breadboard above the chamber. We use a periscope (formed by two dichroic mirrors) to pass the light through the science cell. The beam has a vertical polarization before the dichroic and a horizontal polarization (into the page) as it enters the science cell. The dichroic mirrors serve to deliver the 767 nm light used for imaging, pumping or blasting.

trap location along the $x$-direction; $\sqrt{S(\omega)} \propto x(\omega)$ and normalization $\int_0^\infty S(\omega)d\omega = \langle x^2 \rangle$, where $\langle x^2 \rangle$ is the time-averaged mean-square variation in the trap $x$ location [88]. We use a quadrant photodetector to probe the pointing instability and find that the low-noise of our setup would result in a negligible heating rate $\langle dT/dt \rangle = 4\pi^4 m f^4 S_x(f)/k_\mathrm{b}$. For example, we measure the pointing stability of the small-waist H1 trap (see Fig.2.38) and we estimate the heating rate to be $< 1$ nK/s for all frequencies below 1 kHz, except near 375–425 Hz where we estimate the heating rate to be as large as 100 nK/s (would be an unfortunate choice for the H1 trap frequency). Since the trap frequency decreases with evaporation and we expect low heating rates below 1 kHz, we are content with the pointing stability of our system.

We use a photodetector to monitor (using an out-of-loop PD) and servo (using an in-loop PD)

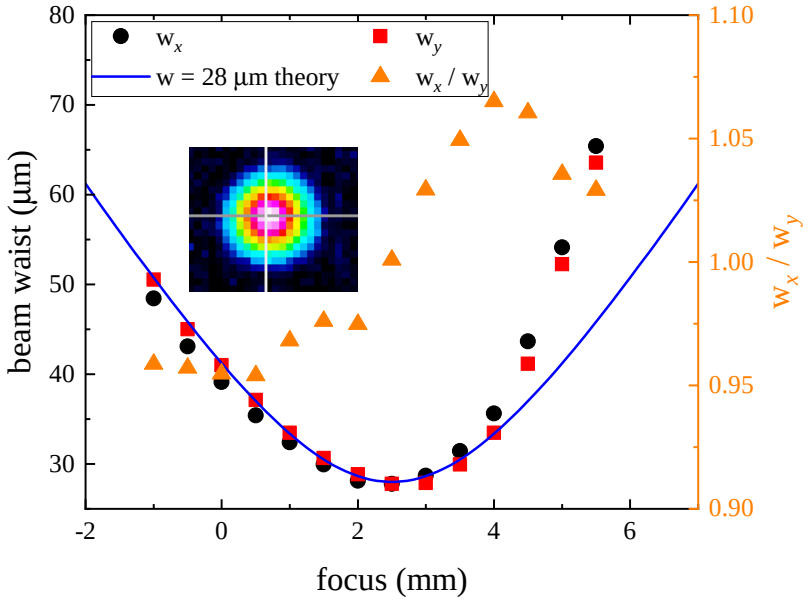


Figure 2.36: Beam waist and the spatial profile (inset image) of the H1 loading dipole beam near its focus. We record the spatial profile at different distances from the focus (located at 2.5 mm, an arbitrary $x$-axis offset), fit the distributions using a 2D Gaussian function and extract the beam waist along two orthogonal directions, rotating images if necessary. We notice a slight asymmetry and astigmatism in the H1 beam. The solid curve is a prediction for a $\mathrm{TEM}_{00}$ 28 $\mu$m waist beam propagation.

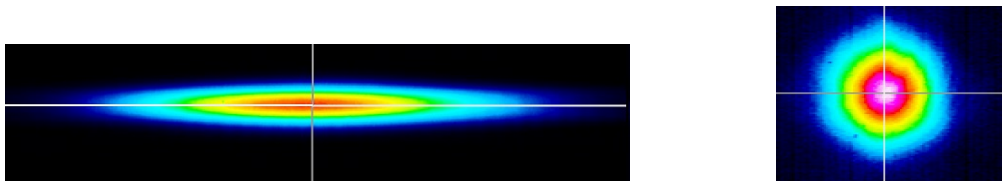

Figure 2.37: Spatial profiles of H2 (left) and V (right) dipole trap beams near their focus. Note the hexagonal structure in the V beam resulting from the photonic-crystal fiber core.

the optical power of each beam. Due to the need for a low-noise high-dynamic-range servo control of the H1 beam, I designed, modified and tested multiple servo components to engineer a low-noise feedback system. Extra emphasis was given to having low-noise across the full 10 Hz–20 kHz frequency span, determined by the expected trap frequencies for all dipole beam powers and configurations. For example, intensity noise at twice the trapping frequency $f_{\mathrm{trap}}$ leads to parametric heating rate $\Gamma = \pi^2 f_{\mathrm{trap}}^2 \mathrm{RIN}(2f_{\mathrm{trap}})$, defined as $\langle dE/dt \rangle = \Gamma \langle E \rangle$ [88]. For a desired $\Gamma^{-1} = 100\,\mathrm{s}$ time, RIN needs to be smaller than $-116\,\mathrm{dB/Hz}$ for $f_{\mathrm{trap}} = 20\,\mathrm{kHz}$, $-90\,\mathrm{dB/Hz}$ for $f_{\mathrm{trap}} = 1\,\mathrm{kHz}$

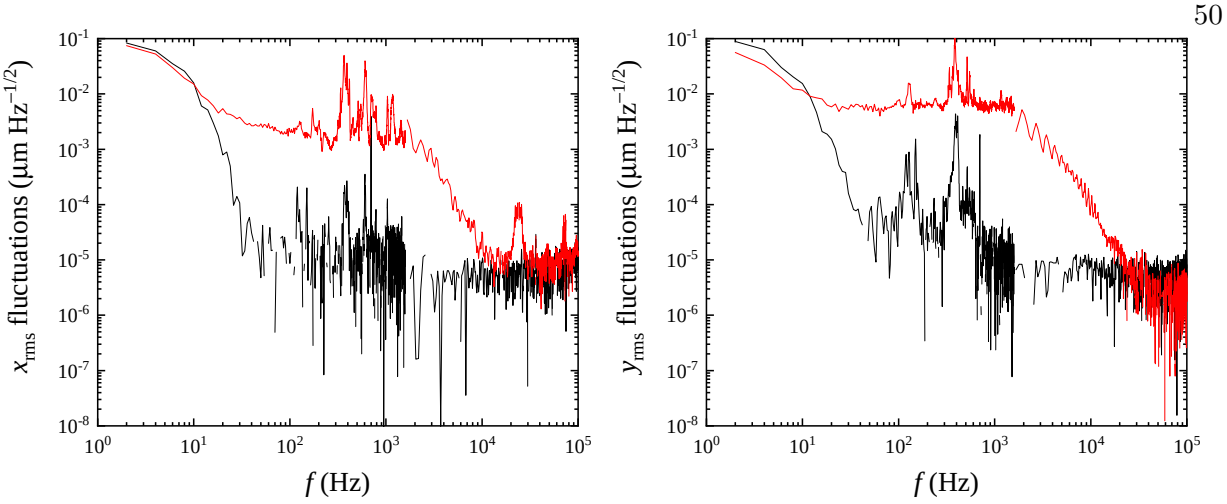


Figure 2.38: Pointing stability of the H1 horizontal beam at the focus. We measure the beam pointing stability in horizontal (left) and vertical (directions) using an FFT analyzer and a quadrant photodetector (QPD). We use a CCD camera to calibrate the QPD; the laser intensity noise is insignificant in this measurement. The black curves show steady-state pointing stability and the red curves show mechanical resonances, which we excite by tapping the breadboard on which the optics are located.

and $-70\,\mathrm{dB/Hz}$ for $f_{\mathrm{trap}} = 100\,\mathrm{Hz}$. Considering the RIN spectra of the free-running (no feedback) Mephisto and Nufern light (Fig. 2.31) and shot noise $\mathrm{RIN[dB/Hz]} = 10\log_{10}(2hc/\lambda P)$ of $P$ optical power (e.g. $P = 10\,\mu\mathrm{W}$ results in $-134\,\mathrm{dB/Hz}$), we should have no problem reaching the required noise levels with a low-noise servo system.

The workhorse of our low-noise intensity servo system is a photodetector I designed (Fig. 2.39). Its dark noise spectrum approaches the measurement noise floor of a low-noise FFT machine (see Fig. 2.40) and has a low RIN for many frequencies and power (see Fig. 2.41). It is based on a large InGaAs photodiode (2 mm Hamamatsu G12180-020A, required for ease of dipole trap alignment and long-term stability) with a good $\eta = 0.55\,\mathrm{A/W}$ photosensitivity at 1064 nm and 2 nA low dark current at $-5\,\mathrm{V}$ reverse bias (no cooling needed). The transimpedance amplifier (TIA) gain ($1500\,\mathrm{V/A}$) was chosen based on the required high-dynamic range in the H1 beam power. The Analog Devices AD8675 operational amplifier was chosen based on its low noise properties across low and high frequencies for the particular TIA gain.

A typical circuit diagram for dipole trap power control is shown in Fig. 2.42. We carefully

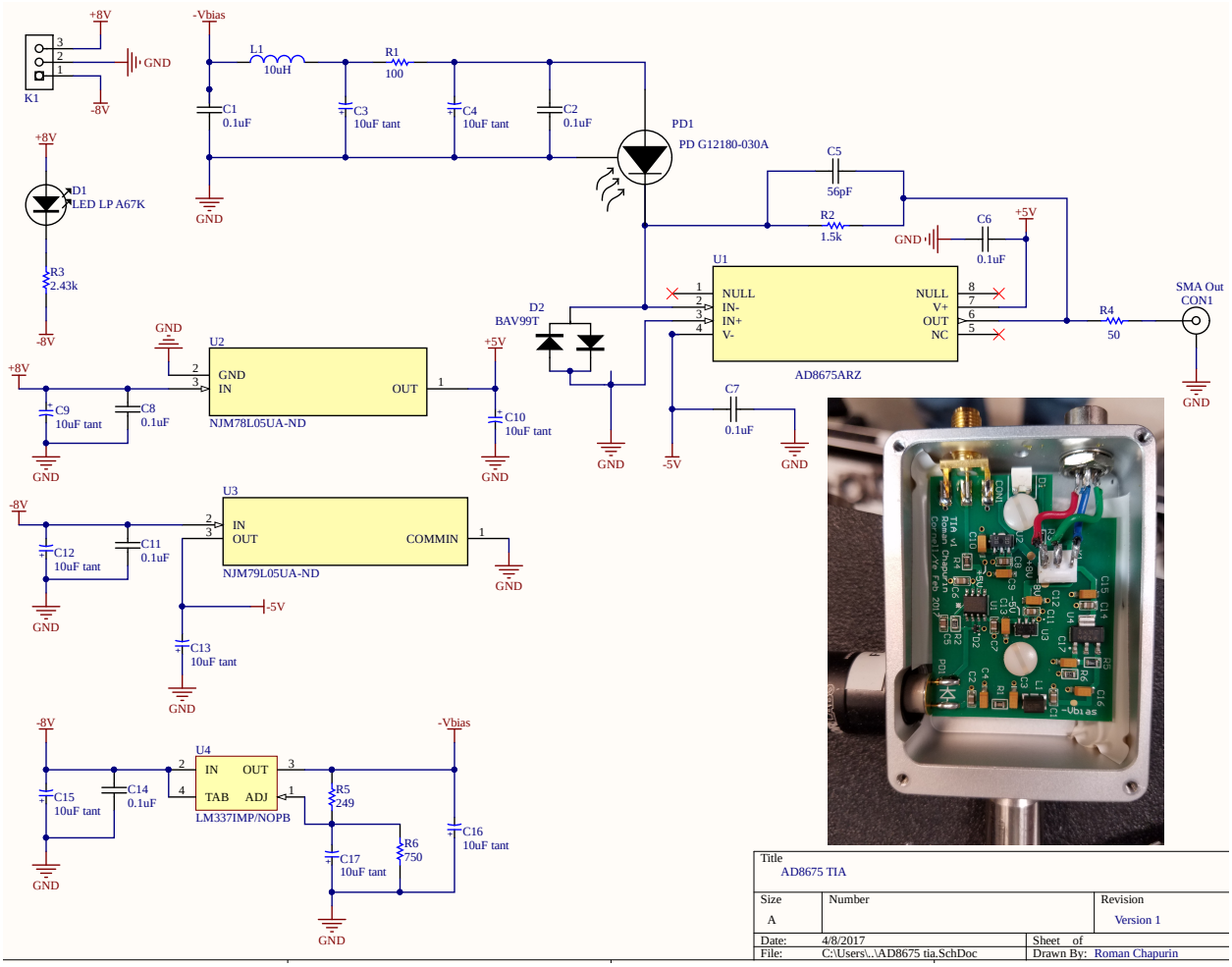


Figure 2.39: Circuit diagram for the low noise PD used for dipole trap control. The inset photo shows the resulting product PCB and the RF-shield box made by the JILA machine shop.

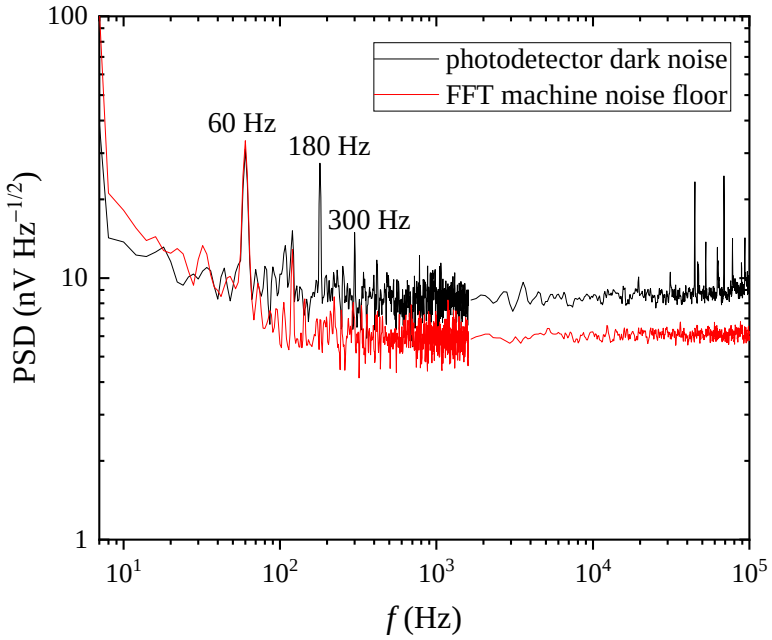


Figure 2.40: Measured dark noise of the dipole trap servo photodetector. Note: we regularly change the FFT analyzer spectral resolution from 128 Hz to 2 Hz below 1500 Hz frequency.

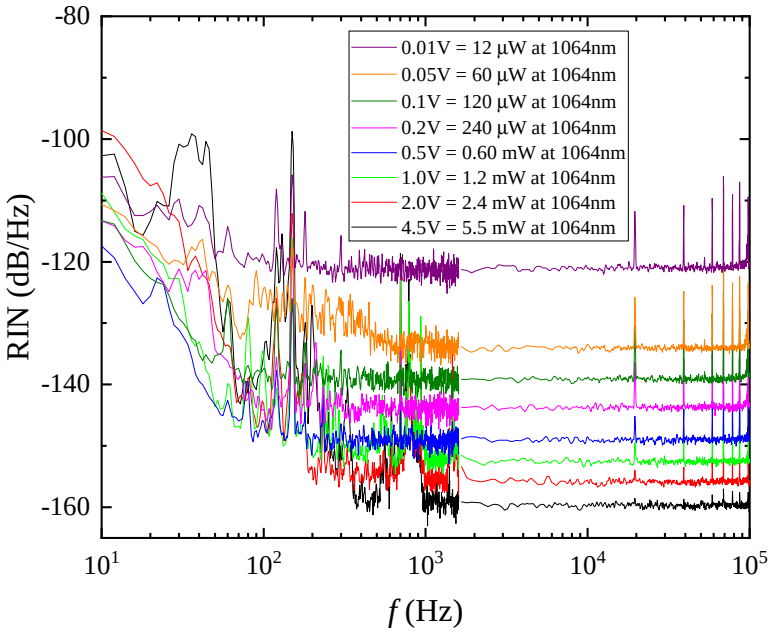


Figure 2.41: Measured RIN of the dipole trap servo photodetector using a thermal white noise source (flat spectrum) from an incandescent light bulb. We measure photodetector voltages and infer the input optical power from $\eta = 0.55\,\mathrm{A/W}$ photosensitivity at 1064 nm and from 1500 V/A TIA gain.

chose and modified electronic components to have a low-noise large-dynamic-range servo system. A commercial voltage controlled oscillator (VCO) on a JILA PCB provides an RF source; the RF amplitude is made constant using a Mini-Circuits RF power limiter. Power control is done using a variable gain amplifier (VGA) and a JILA AOM intensity servo, which senses the PD voltage and has a setpoint coming from an arbitrary waveform generator (AWG). The VGA output is amplified using an RF amplifier and sent to an AOM. For horizontal beams we achieve a low-noise high-dynamic-range ($\sim 10^4$, limited by the AOM transfer function) servo: we use a 16-bit resolution low-noise AWG (Agilent 33500B), a modified JILA servo (JILA PT004A4: has improvements to the voltage supplies and low-noise resistors; a bi-polar voltage output, used to increase the dynamic range; a differential PD input, to decrease measurement noise), and a large-dynamic-range linear-in-dB VGA (Agilent AD8330; we use a resistor network to convert/reduce the servo output voltage to match the VGA control voltage range). For the vertical trap, we use different components: a 14-bit Agilent 33220A for AWG, older (yet modified) JILA servo PT004A3, and a voltage variable attenuator (Mini-Circuits ZX73-2500+) for RF power control. Not shown in the figure: multiple frequency filtering stages, additional attenuation and amplification of RF signals and the high-quality RF shielded cables. We use MATLAB to upload the desired beam power profiles to the AWGs and trigger the AWGs with an FGPA card TTL line. Our low-noise servo system, along with great beam pointing stability, results in low heating rates (1–3 nK/s at low temperatures) and repeatable dipole trap conditions (typical shot-to-shot stabilities are 2–3% for $N$ and $< 4\%$ for $T$).

### 2.5.3 Evaporation in the Optical Dipole Trap

We use all-optical evaporation in order to reduce the temperature from 400 $\mu$K to 10–500 nK and increase the PSD from $4 \times 10^{-5}$ to near- or above-unity. We increase the elastic collision rate during evaporation by turning on a bias magnetic field, tuning it near the 34 G Feshbach resonance. We use the same coils for the bias as we have used for the science QT; an "H-bridge" relay configuration is used to change the current direction of one of the coils in the pair, see Fig. 2.43. Since the gas will depolarize in an absence of a bias magnetic field, we take extra precaution during

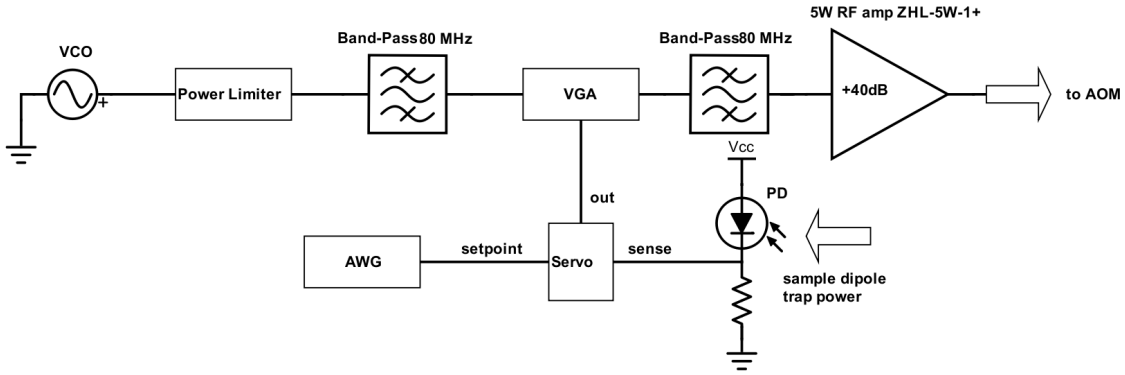


Figure 2.42: Dipole trap intensity servo circuit diagram.

QT-bias switching and monitor the $|\mathrm{F}=1,\mathrm{m_F}=-1\rangle$ spin purity. We begin by ramping off the 200 G/cm gradient field in 100 ms; at the same time, we ramp on (in 10 ms) a small bias field (a few Gauss) using a shim coil pair. Then, we use mechanical relays to change the coil current topology; this process takes 200 ms. Finally, we ramp on the main bias coils to 40 G in 10 ms, while simultaneously ramping off the shim coil field.

Due to great initial conditions (a high initial average density $\sim 5\times10^{12}\,\mathrm{cm}^{-3}$ and a high initial collision rate $\sim 5000\,\mathrm{s}^{-1}$ for a modest $100\,a_0$ scattering length), the H1 beam evaporation timescales are fast. To evaporate, we decrease the H1 beam power, following an exponential-decay profile. Evaporation in the single H1 beam enables efficient evaporation (a large PSD gain or a large reduction in $T$ for a small reduction in $N$, see Fig. 2.44) down to $\sim 10\,\mu$K; beyond that, the weak H1 trapping frequency becomes $< 15$ Hz and evaporation efficiency suffers. We optimize evaporation on the final PSD and vary the evaporation duration, the exponential time constant $\tau$ and the bias magnetic field value. We tried to optimize all these parameters for every factor of two reduction in the optical power (and hence in temperature), resulting in a 5-stage evaporation trajectory (see Fig. 2.45). In the end, however, we found that a single-stage exponential decrease of H1 beam power leads to a similarly efficient evaporation.

Our first successful attempt in reaching temperatures below 1 $\mu$K resulted from adding extra confinement along the H1 weak direction. We did so using a vertical sheet beam with a 28 $\mu$m $\times$

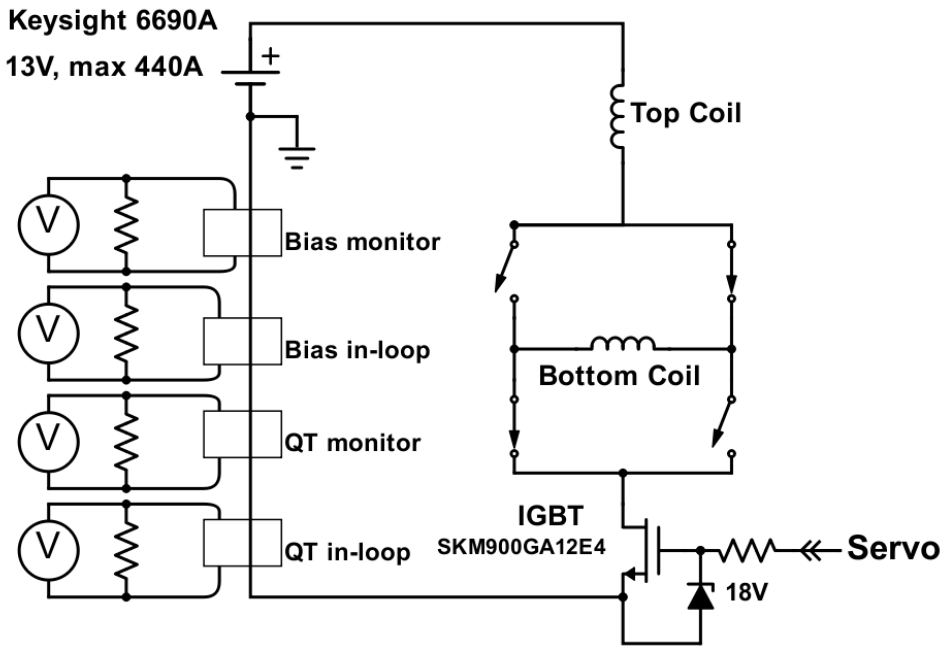


Figure 2.43: Circuit diagram for science coils control. The current is carried using 4/0 Gauge ultra flexible battery wire. We use mechanical relays (Kissling 29.511.11) to switch the current direction in the bottom main science coil, thereby switching between bias and quadrupole trap configurations. We use an IGBT (Semikron SKM900GA12E4) to control the current; a diode and a resistor protect the IGBT gate. We use two separate PI feedback servo systems (JILA coil servo JD013A2) for each configuration; we multiplex the servo output to the common IGBT gate using a MAX319 switch, see Fig.3.9. We sense the current using ultrastable fluxgate transducers (1:1500 Danisense DS600IDSA for in-loop, 1:1750 LEM IT 700-S for out-of-loop) along with high stability (0.2 ppm/C Vishay VPR221ZT) sense resistors (20 Ω for bias, mounted on a TEC-temperature-stabilized aluminium block; 10 Ω for QT, mounted to a heat sink). We are extra careful in avoiding ground loops.

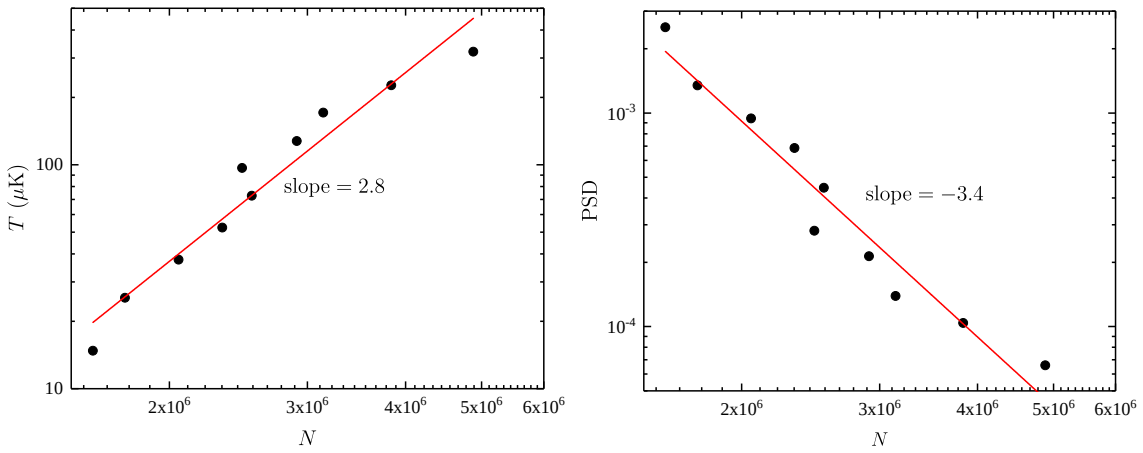


Figure 2.44: A typical evaporation trajectory using the H1 dipole beam. A large temperature decrease (left) and a large PSD increase (right) for a small number of atoms lost is evidence of efficient evaporation.

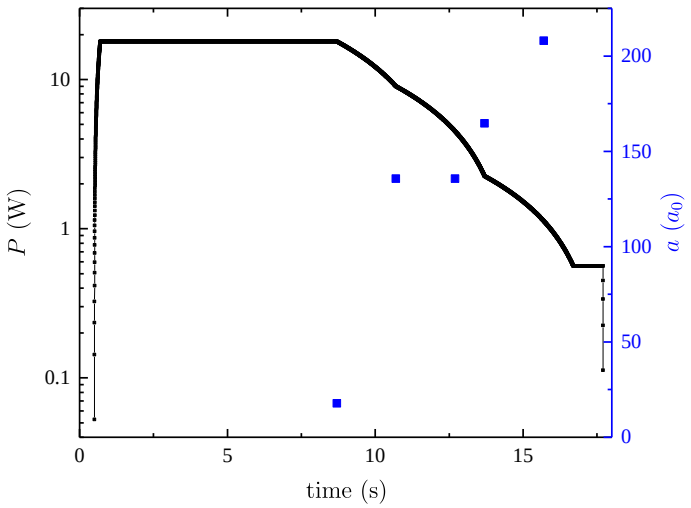


Figure 2.45: A five-stage evaporation trajectory used for reducing the atom temperature from 400 $\mu$K down to 10 $\mu$K, an extreme example of a dipole trap evaporation optimization. Shown is the optimized H1 optical power trajectory (black) along with the optimized scattering length for each stage (blue squares). In the end, the optimized H1 optical power trajectory can be approximated by a single exponential, as evidenced by the roughly straight slope between 8 s and 16 s in the plot. The initial 8 s represents the OT load from the QT trap.

800 $\mu$m waist (note that this is not the final V trap geometry). We achieved our first $^{39}$K BEC in the new lab using a roughly-spherical 300 Hz trap, resulting in $7 \times 10^4$ condensed atoms ($< 30\%$ in the thermal wings) and a temperature $\sim$ 500 nK, where the critical temperature $\sim$ 650 nK. Using this beam configuration, we were able to create BECs at will and with ease, see Fig. 2.46.

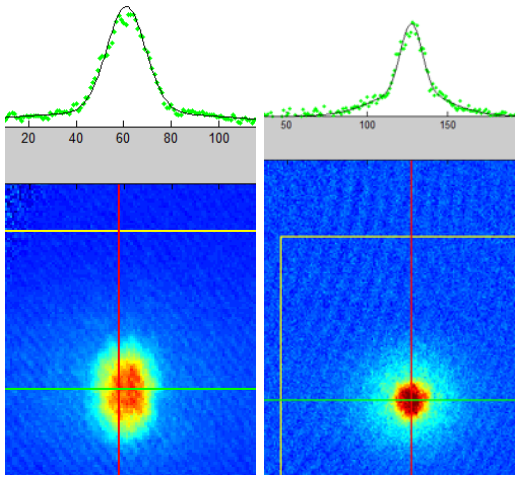


Figure 2.46: Example of BEC cloud distributions. Left: a BEC cloud with $> 80\%$ condensate fraction expanding from an asymmetric trap (12 ms TOF). Right: BEC atoms (expanding from a spherical trap, 8 ms TOF) in the presence of many thermal atoms, as evidenced by a pronounced peak (BEC) and thermal wings in the integrated OD distribution (top).

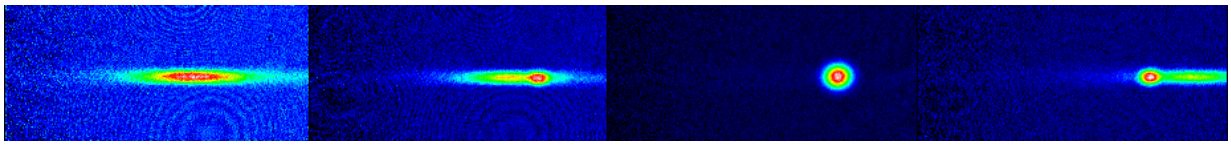

Figure 2.47: Alignment of our final optical dipole trap: the H2 sheet beam is aligned to the vertical beam. A good alignment corresponds to when all atoms fall into the intersection region of the two beams (second from the right image). Here, we use low-magnification ($M = 1$) imaging.

We use condensates for multiple troubleshooting purposes, including imaging objective alignment, thermometry calibration and trap frequency measurements. While working with BECs was fun, our science interests lay in few-body physics. Such experiments must be done with even-colder, yet thermal, dilute clouds. Therefore, our final trap configuration has a very weak confinement.

The final configuration consists of a vertical beam with a $140\,\mu\text{m} \times 140\,\mu\text{m}$ waist and a horizontal sheet beam with a $80\,\mu\text{m} \times 810\,\mu\text{m}$ (see Fig. 2.47). We transfer atoms from the H1 beam to the other two by ramping down the H1 beam to zero power. The optimized parameters (for loading the highest PSD cloud into H2 and V beams) of the H1 beam single-stage evaporation are: 5 s duration, $\tau = 0.4$ and $a = 150\,a_0$. With the initial H1 and V beam powers of 8 W and 1.5 W, respectively, we form a $(\omega_x, \omega_y, \omega_z)/2\pi = (190, 100, 85)$ Hz trap with a $9\,\mu$K depth. This results

in loading $3.5 \times 10^5$ atoms, 600 nK temperature and 0.3 peak PSD. From these great conditions, reaching degeneracy is trivial via a final single-stage evaporation in the H2 and V potential. For example, we can cool $2 \times 10^5$ atoms to a 100 nK temperature and 2 peak PSD (see Fig. 2.48) using evaporation parameters: 5 s duration, $\tau = 0.1$ , $a = 290\, a_0$, $(\omega_x, \omega_y, \omega_z)/2\pi = (145, 35, 22)$ Hz final trap frequency and 530 nK final deep trap. While reaching degeneracy became simple, preparation of non-degenerate samples at very low temperatures and with a sufficient atom number/signal is a non-trivial task; see Ch. 5 for a broader discussion.

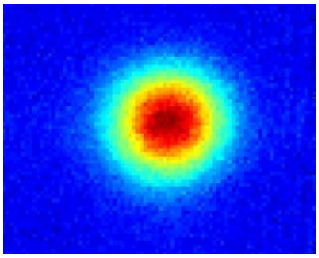

Figure 2.48: An image of cold cloud expanded (15 ms TOF) from our final optical dipole trap potential. We resort to a high-magnification ($M = 7$) imaging system to be able to resolve small-sized clouds, as the one shown here.

# Chapter 3

# Experimental Toolkit for State Manipulation and Readout

Performing precise measurements requires stable experimental conditions and a good understanding of state control and readout. In this chapter, I detail the RF system used for state purification and spectroscopy, along with the methods implemented which enable magnetic field control with a mG-level field stability. Then, I discuss our science cell imaging system and image analysis, expanding on the absorption imaging basics introduced in Sec. 2.3.2. A good understanding of imaging enables accurate determination of atom number and density. Lastly, I give an overview of the laboratory's computer and hardware control.

## 3.1 RF Control System

### 3.1.1 RF Circuitry

We utilize magnetic dipole transitions to go between hyperfine (Zeeman-split) states. We use RF antennas to drive an oscillating magnetic field perpendicular to the magnetic field bias generated by the mail coils, resulting in state transitions with selection rules $\Delta F = 0, \pm 1$ and $\Delta m_F = \pm 1$. Each antenna circuit (see Fig. 3.1) is composed of a resonant circuit, formed by a wire loop(s) and a series capacitor, and an impedance matching circuit. We use mostly non-magnetic components to avoid magnetization by the main magnetic field bias coils. Frequency tuning and impedance matching must be done in place, as antenna coupling to metal and dielectric components around the science cell changes circuit performance. We are careful to avoid optimizing on electronic circuit resonances; they are hard to distinguish from the true antenna resonance (formed by antenna loop

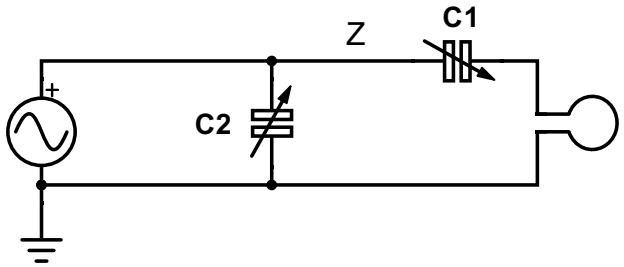


Figure 3.1: A typical circuit topology for RF antenna drive. We deliver RF power from the RF amplifier to the antenna circuit via a triple-shielded coax (MiniCircuits precision test cable 5–10 ft long, DC–18 GHz). Frequency tuning is mainly achieved by a trimmer capacitor C1 (Voltronics/Knowles NMA4M5HV; non-magnetic, 0.6–5 pF, PTFE dielectric, high-Q and high-V) that is placed in series with and close to the loop antenna. Impedance matching is done via tuning a variable capacitor C2 (Voltronics/Knowles TM56; 1–56 pF, air/glass, enclosed in an RF-shielded box or using TM42) and adjusting the length ($\lesssim \lambda/8$) of a $Z = 50\,\Omega$ transmission line (UT-085C; semi-rigid coax cable, non-magnetic *inner* and outer copper conductors) connecting C1 to C2. Note that coax cables add additional $\sim 30$ pF/ft shunt capacitance (not shown). If impedance matching is not achieved using this topology, one needs to determine (using a Smith Chart) whether one needs to implement an additional inductor, resistor, transmission line or a stub.

and C1), as they can still lead to radiation and can be sensed on a small-loop pickup antenna; they also can still induce RF transitions in atoms, albeit with smaller Rabi frequencies.

We use three separate antennas that enable select transitions (e.g. at 34 G, which is near the expected Feshbach resonance location of our interest): $|\mathrm{F}=1,\mathrm{m_F}=-1\rangle \rightarrow |\mathrm{F}=2,\mathrm{m_F}=-2\rangle$ (394.330 MHz), $|\mathrm{F}=1,\mathrm{m_F}=-1\rangle \rightarrow |\mathrm{F}=1,\mathrm{m_F}=0\rangle$ (24.623 MHz), and (using a common antenna) $|\mathrm{F}=1,\mathrm{m_F}=-1\rangle \rightarrow |\mathrm{F}=2,\mathrm{m_F}=0\rangle$ (446.827 MHz) and $|\mathrm{F}=1,\mathrm{m_F}=0\rangle \rightarrow |\mathrm{F}=2,\mathrm{m_F}=-1\rangle$ (446.841 MHz). We maximize radiation efficiency for each antenna by choosing the maximal amount of turns; the antenna-C1 resonator desired frequency limits the maximal loop inductance (and hence area) at the minimal C1 capacitance. The 390 MHz and 447 MHz antennas are single-loop, while the 25 MHz antenna is 6-loop; all are made from 16 AWG Cu wire and have $\approx 1$ inch inner diameter (large enough to fit around science cell side windows). Each antenna is matched such that the reflection coefficient $S_{11}$ is $\lesssim 10\%$ at the desired frequency; the resulting spectral FWHM widths and centers are: 20 MHz for 447 MHz, 20 MHz for 390 MHz, and 0.5 MHz for 25 MHz. While we need to re-tune the two latter antenna center frequencies for different magnetic fields, we do not need to do so for the 447 MHz antenna since $|\mathrm{F}=1,\mathrm{m_F}=-1\rangle \rightarrow |\mathrm{F}=2,\mathrm{m_F}=0\rangle$ and

$|\mathrm{F}=1,\mathrm{m_F}=0\rangle \rightarrow |\mathrm{F}=2,\mathrm{m_F}=-1\rangle$ transitions are relatively insensitive ($\sim 170\,\mathrm{kHz/G}$) around 34 G.

We can estimate loop antenna radiation efficiency $\eta_{\mathrm{rad}}$ by comparing radiative to resistive loss: $\eta_{\mathrm{rad}} = R_{\mathrm{rad}}/\left(R_{\mathrm{rad}} + R_{\mathrm{ohmic}}\right)$; $R_{\mathrm{ohmic}} = 2\pi r N/(S\sigma)$ is the ohmic resistance of the wire, where $N$ is the number of loops in the antenna, $r$ is loop radius, $S$ is the surface cross-section where the current is constrained to flow by the skin depth, $\sigma$ is the electrical conductivity; $R_{\mathrm{rad}} = R_0(8/3)\pi^3\left(\pi r^2 N/\lambda^2\right)^2$ is loop radiation resistance, where $R_0 = 120\pi\,\Omega$ is the impedance of free-space. Here, we assume the small-loop approximation (compared to the wavelength), such that the current distribution is uniform along the wire. We see that a loop with more turns, area or operating at a higher frequency is expected to have a higher radiation efficiency. For example, an antenna with 16 AWG Cu wire and $r = 0.5$ inch is estimated to be 20% efficient at 400 MHz and $\ll 1\%$ at 30 MHz. However, in practice there are extra unaccounted-for losses at higher frequencies and one needs to verify radiation efficiency of different frequency-band antennas using a vector network analyzer (VNA) along with a calibrated pickup antenna, to get $\eta_{\mathrm{rad}} = |S_{12}|^2/(1+|S_{11}|^2)$, or by comparison of Rabi frequencies in atom spectroscopy. We find that our low- and high-frequency antenna systems are just as efficient, resulting in similar Rabi $\pi$-pulse durations around 6–7 $\mu$s (time for full state transfer at full power).

These antenna circuits are much simpler than the antenna I designed for $^{40}$K microwave evaporation, which required a five-stub tuner for broadband 1.1–1.3 GHz match and extensive modeling. However, due to the required dynamic frequency and power control, fast switching and precise timing, the control circuitry for the new antennas is more complex. Figure 3.2 shows the overview of our RF system. The versatile frequency generator VFG-150 is the key component of our system, enabling fast frequency and amplitude (also phase, if needed) switching every 5 ns. For state manipulation we use this RF system to generate rectangular- and Gaussian-shaped amplitude pulses, at constant or chirped frequencies. We use a combination of RF spectrum analyzers, oscilloscopes, VNAs, pickup antennas, RF circulators, frequency mixers and atom spectroscopy to diagnose our RF antenna system.

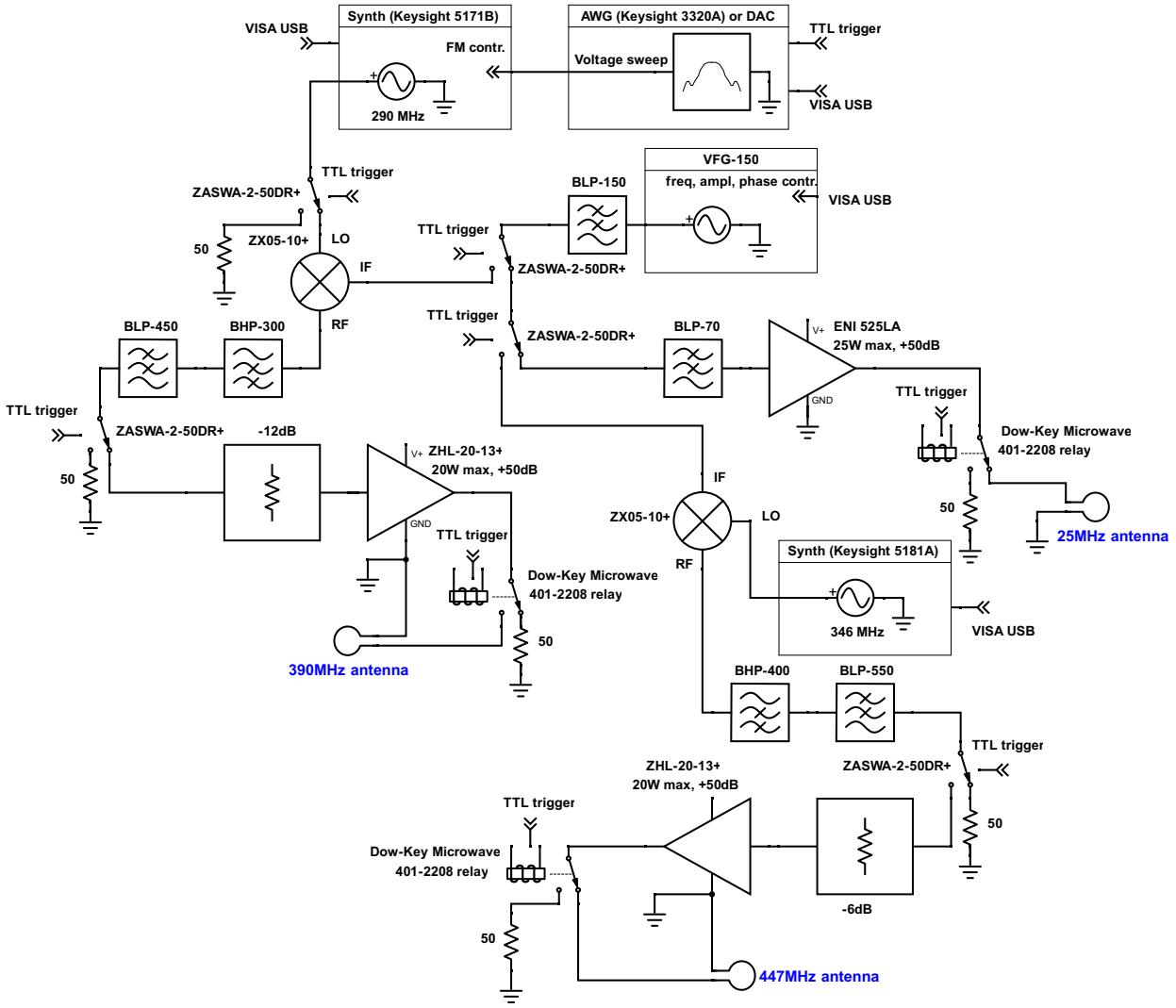


Figure 3.2: RF control system circuitry. We use a single versatile frequency generator VFG-150 to provide direct or mixed-up signals to the three RF antennas. We use the VFG to change the RF amplitude and center frequency; we use an external FPGA DAC or an arbitrary waveform generator (AWG) to sweep the frequency via frequency modulation (FM) ports. Fast RF solid-state switches (ZASWA-2-50DR+) are used for signal routing and pulse generation. To prevent noise leakage into antennas when the RF system is inactive, we use mechanical relays (401-2208) to isolate amplifier outputs. All frequency synthesizers are referenced to the lab's 10 MHz clock signal, which originates at NIST, travels to JILA via optical fiber and is split among and within labs via low-noise RF distribution amplifiers.

### 3.1.2 RF Transitions

We can estimate the effects the RF drive has on the atoms by solving a two-state problem, given by a Hamiltonian:

$$\mathbf{H} = \hbar \begin{pmatrix} \omega_1 & V_0 \cos(t\omega) \\ V_0 \cos(t\omega) & \omega_2, \end{pmatrix} \tag{3.1}$$

where $\hbar\omega_0 = \hbar(\omega_2 - \omega_1)$ is the energy splitting between the two Zeeman states in the presence of a magnetic field bias, $V_0$ is the coupling strength (proportional to the field strength times the dipole moment $\mu$) and $\omega$ is the angular drive frequency. System's response are solutions to the coupled equations [89, 90]:

$$\frac{dc_1(t)}{dt} = -\frac{i\Omega}{2} \exp(i\delta t) c_2(t) \tag{3.2}$$

$$\frac{dc_2(t)}{dt} = -\frac{i\Omega}{2} \exp(-i\delta t) c_1(t), \tag{3.3}$$

where $|c_1|^2$ and $|c_2|^2$ are probabilities of finding the system in states 1 and 2, $\delta = \omega - \omega_0$ is RF detuning from the transition, $\Omega = |\mu B_0/\hbar|$ is the Rabi frequency of the magnetic dipole transition, driven by a oscillating magnetic field of strength $B_0$, and where we've used the rotating wave approximation. For example, given the initial condition $|c_1(0)|^2 = 1$, the system undergoes Rabi flopping:

$$|c_2(t)|^2 = \frac{\Omega^2}{\delta^2 + \Omega^2} \sin^2\left(\frac{t}{2}\sqrt{\delta^2 + \Omega^2}\right). \tag{3.4}$$

On resonance, full state transfer occurs every multiple of $\tau_\pi \Omega = \pi$, where $\tau_\pi$ is referred to as the Rabi $\pi$-pulse duration. Note that while $\tau\Omega = 2\pi$ pulse retrieves the initial condition $|c_1|^2 = 1$, the resulting state is phase shifted ($-1$ prefactor) with respect to the original state and a $\tau\Omega = 4\pi$ pulse is required for the system to fully retrieve the original state. The off-resonant system response is best described by an effective Rabi frequency $\Omega_{\text{eff}} = \sqrt{\delta^2 + \Omega^2}$. When one needs to include dephasing and damping into the model, it is best to use Bloch equations instead of Eqs. 3.2 and 3.3 [91].

Similarly to the solution Eq. 3.4, which was solved using a time-independent $B_0$ and hence a constant $\Omega$, we can use Eqs. 3.2-3.3 or Bloch equations to calculate system's response to amplitude-

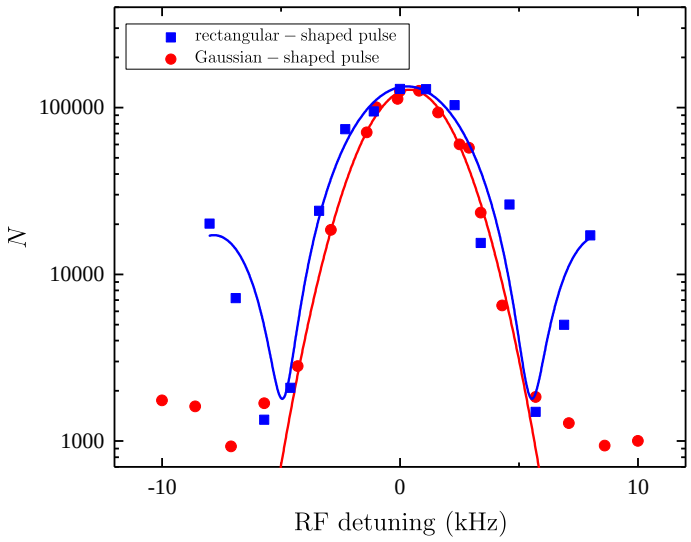


Figure 3.3: Spectral comparison of rectangular- (165 $\mu$s duration) vs. Gaussian-shaped ($\sigma = 67\,\mu$s, $6\sigma$ duration) RF pulses. For this measurement atom number imaging noise limited $N$ to $> 1000$ atoms. The solid curves are fits to the data, where center frequency (detuned from 446.560 MHz) and amplitude are the only free parameters. Here, the Gaussian fit does not incorporate finite-pulse duration.

shaped pulses. For example, we utilize Gaussian-shaped RF pulses when a large suppression of spectral sidebands is required, as in cases with nearby off-resonant transitions that we do not want to excite. Figure 3.3 illustrates this via comparison by two measured RF spectra, one taken with a rectangular-shaped pulse and the other with a Gaussian-shaped pulse. Note that even with significant suppression, spectral sidebands still exist in Gaussian-shaped RF pulses due to finite pulse durations. Further suppression can be achieved by the use of Blackman-shape pulses.

To test our RF system on the atoms, we need to utilize spin-selective imaging techniques. When performing RF transitions to the F = 2 state, we can directly diagnose RF transfer by imaging the final state, since the initial $|\mathrm{F} = 1, \mathrm{m_F} = -1\rangle$ state is dark to our imaging probe light (the D2 $|4\,^2\mathrm{S}_{1/2}, \mathrm{F} = 2\rangle \rightarrow |4\,^2\mathrm{P}_{3/2}, \mathrm{F}' = 3\rangle$ transition) in absence of repump light. When performing RF transitions within the F = 1 state, we utilize Stern-Gerlach–type technique to spatially separate spin components, imaging them using the D2 $|4\,^2\mathrm{S}_{1/2}, \mathrm{F} = 2\rangle \rightarrow |4\,^2\mathrm{P}_{3/2}, \mathrm{F}' = 3\rangle$ transition along with D2 repump (comes from an orthogonal direction as the probe, from top of the science cell). We can use a combination of the two techniques to enable imaging of all spin components simultaneously.

Figure 3.4 shows a typical measurement of Rabi flopping. All three antennas radiate sufficient RF power to result in $\tau_\pi = 6$–$7\,\mu$s $\pi$-pulse durations at highest amplifiers output power ($\sim 20\,$W). The Rabi flopping dephasing times are mainly dependent on transition sensitivity, pulse duration (spectral width is often Fourier-limited), magnetic field stability and magnetic field gradient across the atomic sample. Figure 3.5 shows Rabi flopping with spin-resolved imaging, where we use Stern-Gerlach technique along with repump light imaging to image all spin populations simultaneously. Such type of spin-dependent imaging is necessary for measuring high transfer efficiencies, as it is immune to the total atom number fluctuations (typically 2–5%). For example, we measure a 99% on-resonance transfer efficiency using such technique, as shown in Fig. 3.6.

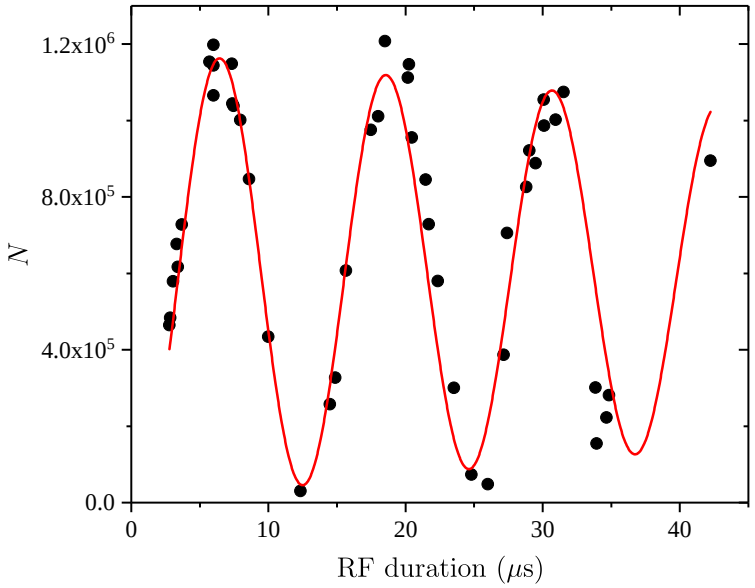


Figure 3.4: Typical timescales for Rabi flopping with our RF system. Here we use $|\mathrm{F}=1,\mathrm{m_F}=-1\rangle \rightarrow |\mathrm{F}=2,\mathrm{m_F}=-2\rangle$ RF on-resonant transition at 35.76 G and full RF power, resulting in $\tau_\pi = 6\,\mu$s $\pi$-pulse duration. We extract the $T_2 = 150\,\mu$s dephasing time by fitting Rabi oscillations to a function $0.5A\,(1-\exp(-(t-t_c)/T_2)\cos(2\pi f(t-t_c)))$, where $A$ is an amplitude prefactor, $t_c$ accounts for timing offsets, and $f$ is related to the Rabi frequency. The dephasing time for the $|\mathrm{F}=1,\mathrm{m_F}=-1\rangle \rightarrow |\mathrm{F}=2,\mathrm{m_F}=0\rangle$ transition is longer due to $\sim 10\times$ smaller magnetic field sensitivity. Note that the relaxation time $T_1$ is negligible in atomic systems for hyperfine (in our case $|\mathrm{F}=1\rangle$ and $|\mathrm{F}=2\rangle$) ground states.

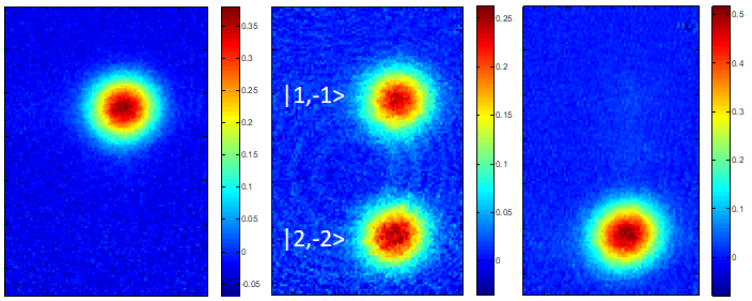


Figure 3.5: Spatially-resolved Rabi flopping between $|\mathrm{F}=1,\mathrm{m_F}=-1\rangle$ and $|\mathrm{F}=2,\mathrm{m_F}=-2\rangle$ spin states. From left to right: without RF transfer, $\pi/2$-pulse transition (equal populations) and $\pi$-pulse transition. Here, we use Stern-Gerlach technique along with optical repump light to image population in both spin states simultaneously. Note that the OD scale changes between images.

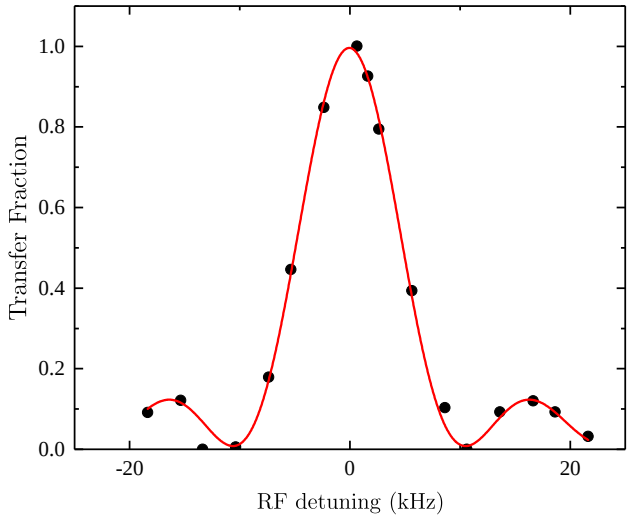


Figure 3.6: RF spectrum using $|\mathrm{F}=1,\mathrm{m_F}=-1\rangle \rightarrow |\mathrm{F}=2,\mathrm{m_F}=0\rangle$ transition with spin-resolved imaging (as in Fig. 3.5), measuring fractional population transfer to the final spin state. Here, we use a 82 $\mu$s rectangular $\pi$-pulse for spectroscopy. We fit data to Eq. 3.4, setting $\tau\Omega=\pi$, and extract the resonance center 446.5423 MHz (to give 35.881 G) and maximal transfer efficiency $A=0.99$.

## 3.2 Magnetic Field Stabilization

### 3.2.1 Lineshape Spectral Noise

Precision spectroscopy of few-body physics depends on having a precise magnetic field control and high field stability, since the induced interactions (via Feshbach resonances) and the hyperfine Zeeman splittings are sensitive to magnetic field noise. We perform RF spectroscopy to determine our field stability. Figures. 3.7 and 3.8 illustrate how $B$-field noise translates to spectral noise.

Prior to converting the apparatus to a $^{39}$K machine, and hence prior to adding many more electronic components (new noise sources) to the lab, the magnetic field stability was measured to be 10–15 mG with $^{40}$K RF spectroscopy. Such a high noise level was unacceptable for the kHz-level spectral sensitivity we desired in the new $^{39}$K machine. For example, magnetic field sensitivities at 34 G (near our Feshbach resonance of interest) for $|\mathrm{F}=1,\mathrm{m_F}=-1\rangle \rightarrow |\mathrm{F}=2,\mathrm{m_F}=-2\rangle$, $|\mathrm{F}=1,\mathrm{m_F}=-1\rangle \rightarrow |\mathrm{F}=1,\mathrm{m_F}=0\rangle$ and $|\mathrm{F}=1,\mathrm{m_F}=-1\rangle \rightarrow |\mathrm{F}=2,\mathrm{m_F}=0\rangle$ transitions are 1.85 kHz/mG, 0.73 kHz/mG and 0.17 kHz/mG, respectively. Similarly, considering that the Fourier-limited spectral width of Rabi $\pi$-pulses is $\Delta f_{\mathrm{FWHM}} = 0.80/\tau$, spectral noise arising from magnetic field noise would limit the maximal pulse durations. In fact, our initial RF spectroscopy with the $|1,-1\rangle \rightarrow |2,-2\rangle$ transition and 10 mG field noise was a failure due to having an unoptimized antenna system with a long 45 $\mu$s Rabi $\pi$-pulse duration. Only after solving antenna impedance matching issues and reducing noise down to mG-level, we were able to utilize the $|1,-1\rangle \rightarrow |2,-2\rangle$ transition.

### 3.2.2 Magnetic Field Control

In addition to RF spectroscopy, we use a set of magnetometers to monitor our magnetic field stability. We employ a NIST-calibrated AC magnetometer (MC910) to measure 60 Hz noise around the lab. Additionally, we utilize a three-axis high-sensitivity (0.1 mG) magnetometer (Bartington Instruments MAG690-1000) for general purposes (400 Hz 3 dB point). We check magnetometer calibration and frequency response using a large wound coil and a current source. Ultimately, we permanently affix the MAG690-1000 sensor $\sim$ 20 cm above the science coils (on top of the optical breadboard used for vertical optical dipole trap beam and vertical probe beam), $\sim$ 10 cm offset laterally (to provide sensitivity in all sensed $B$-field directions), to monitor the magnetic field during experimental sequences. We use an analog-to-digital converted (ADC, NI-USB 6003 multifunction I/O device) to record magnetic field values in all three directions during the last 150 ms of each experimental sequence: 100 ms before RF spectroscopy and imaging, and 50 ms afterward (when all coils are off). Using the two magnetometers, we determined that the sensed

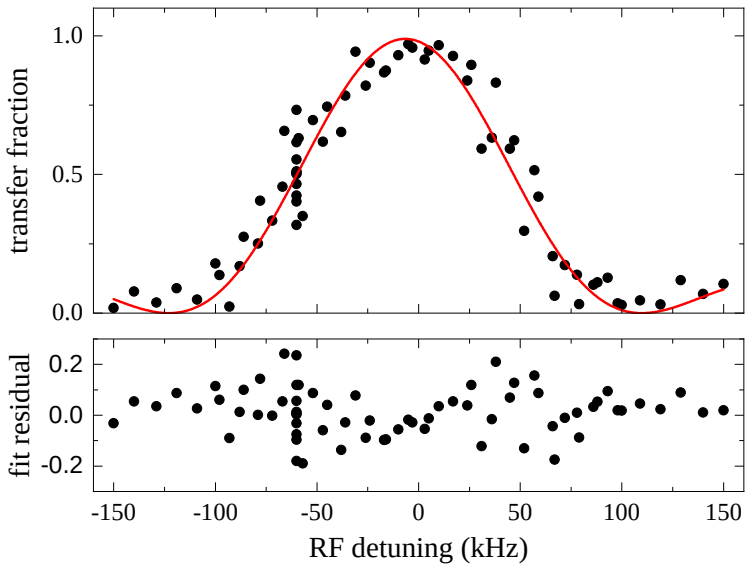


Figure 3.7: An example of $|1,-1\rangle \rightarrow |1,0\rangle$ lineshape spectral noise due to high magnetic field instability. Here, the RF $\pi$-pulse duration is 7.4 $\mu$s and spectroscopy is performed at 41.76 G, where the transition has 0.73 kHz/mG field sensitivity. We measure the transferred fraction (top) using Stern-Gerlach–type technique and fit the spectrum using Eq. 3.4. We extract noise properties from the resulting fit residuals (bottom). We extract 4% measurement noise from the spread near zero-detuning, where the transition is insensitive (small slope near the peak) to magnetic field noise; note that the atom number noise is irrelevant in this measurement as we record fractional spin populations. We extract 14 mG magnetic field noise from the spread on the side of the spectrum (we subtract out 4% measurement noise in quadrature), where the transition is most sensitive to magnetic field noise, as evidenced by a large spread in residuals.

noise (60 Hz field noise combined with the observed DC field drift) was consistent with the level of measured field stability using RF spectroscopy.

We took multiple measures to achieve few-mG magnetic field stability. Beginning with passive measures, the main bias coils are wound in a Helmholtz configuration, and are mounted on rigid non-magnetic G-11 glass/epoxy phenolic and water-cooled (with laminar flow). We use mainly non-magnetic components surrounding the science chamber, including optical breadboards, RF antenna circuitry (capacitors, coax cables and solder) and optical mounts. More generally, we are cautious about stray magnetic fields originating from various sources, minimizing or shielding them when possible. For example, we made sure that the science optical table was never magnetized throughout the years by avoiding magnetic optical posts and screws; we also accomplish a good table temperature stability by minimizing the amount of thermal sources underneath and on it, using

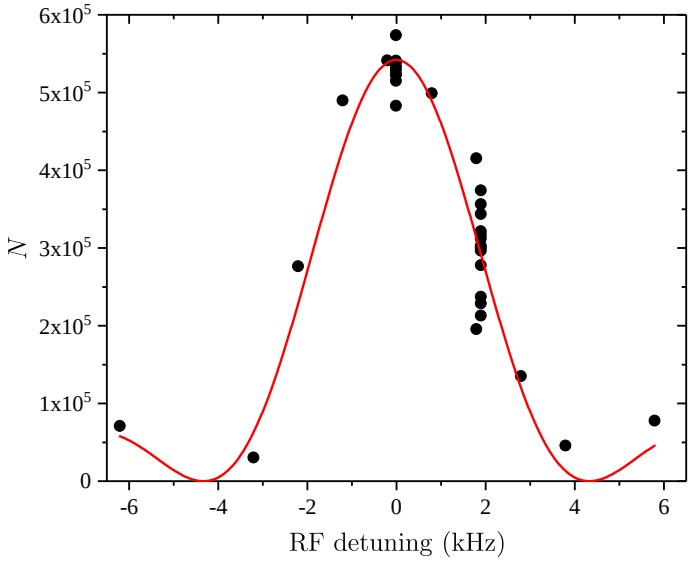


Figure 3.8: A typical $|1,-1\rangle \rightarrow |2,0\rangle$ spectrum after we took steps to minimize magnetic field noise. We take the spectrum with a 200 $\mu$s RF $\pi$-pulse duration near 34.67 G, where the transition has 0.16 kHz/mG field sensitivity. We determine the atom number noise to be 3.4%, using the standard deviation of the spread near the transition peak. We take the spread on the spectrum side, subtract out (in quadrature) the 3.4% atom number noise, convert noise to kHz units (using the slope of the fitted curve on the side of the transition, whose value is determined by the Fourier width) and finally use field sensitivity to determine magnetic field noise. In this spectrum, we deduce 1.4 mG field stability.

water-cooling when necessary. We put a mu-metal shield around the ion pump closest to the science chamber. We moved electronic equipment (especially those that contain transformers with large magnetic cores, e.g. shutters and power supplies) and AC power cables (60 Hz noise) away from the science cell. We even switched to plastic seating, restricted Vandy from carrying his steel multi-tool (leads to precisely 0.01(1) mG noise), correlated magnetic field noise with a nearby elevator (leads to $< 0.5$ mG noise, depending on the elevator floor location) and experimental cycles of nearby labs (negligible noise contributions), and performed field stability measurements at different times of day/night. All such measures were necessary, with each measure slightly improving the field stability.

We spent a significant amount of time actively stabilizing the current flowing through the main bias coils. Since the quadrupole trap operating current is 364 A, while the bias operating (near 34 G Feshbach resonance) current is $\sim 15$ A, we require either a feedback servo system that retains

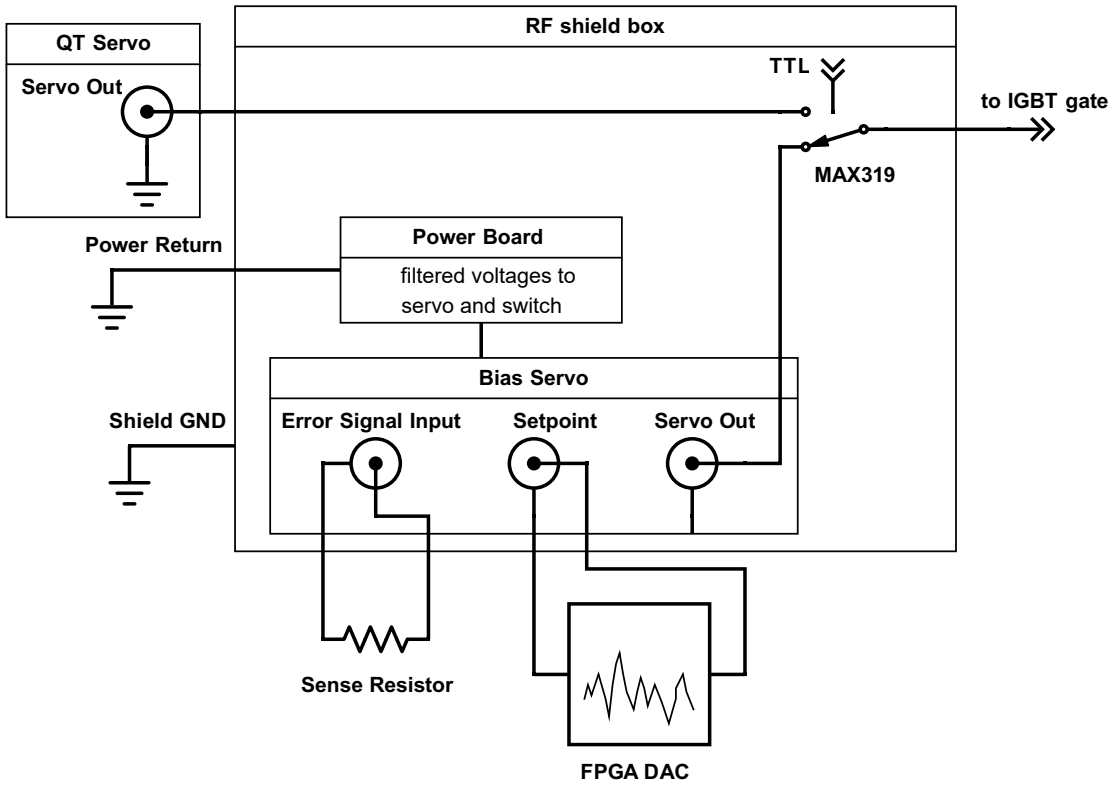


Figure 3.9: Circuit diagram for magnetic field servo. We use a switch to toggle between the quadrupole trap and the bias feedback loop circuits. We are careful in shielding signals and avoiding ground loops. Not shown: low-pass filters and RF chokes on multiple signals.

low-noise properties across a high dynamic range, or two separate servo systems, each optimized for a specific current range. We chose to go with the latter approach, implementing an additional servo that enables current control up to 40 A, see Fig. 3.9.

Both servo systems (quadrupole trap and bias) control the same IGBT gate but have separate sense transducers, as shown in Fig. 2.43. We switch between the two servo configurations using a MAX319 switch; this procedure is performed after optical dipole trap load. The bias servo sense resistors have higher resistance values and are temperature stabilized. Additionally, we increased the operating setpoint voltage (property of the servo circuit) by a factor of 10 to improve DAC (16-bit) step size from 40 mG to 4 mG. The servo circuit (JILA coil servo JD013A2) is modified to input differential setpoint and sense voltages, a lower-noise configuration. We chose a DAC channel with the lowest voltage noise: one located on the FPGA card rather than an external DAC. In

integrating the new servo system, we used short shielded electrical cabling, lots of RF low-pass $\mathcal{O}(1\,\mathrm{MHz})$ filters and RF chokes, high-quality electrical components, good RF shielding and proper electrical grounding practices.

The bias servo was tuned at the highest operating current (40 A) to give maximal feedback gain with lowest noise. We use an out of loop current transducer to look (on Keithley, FFT machine and RF spectrum analyzer) at servo stability during optimization procedure. In the end, we achieve current stabilities 12 ppm at 15 A and 6 ppm at 40 A, corresponding to $< 1$ mG field noise (if current noise is the main contributor). We use RF spectroscopy and determine, from multiple measurement with different transitions, conditions and on different days, that the total magnetic field noise is 1–3 mG. We check that the RF signal (used for spectroscopy) does not lead to rectification/shifts in the field value. In our observations, the typical magnetic field noise follows a standard Gaussian distribution. We find that the field stabilizes to within a few mG in a few ms (settling time) after an abrupt change in the setpoint value. Using a 60 Hz AC-line homebuilt setup to trigger RF spectroscopy on the 60 Hz waveform, we find that line noise contributes almost 1 mG to the total noise, a significant amount. However, due to timing complications arising from the 60 Hz sync, we do not generally utilize this setup. Finally, we check long-term magnetic field drift and find that on a day-to-day and weekly basis, magnetic field absolute value is remarkably stable, to within 2 mG.

We use two different techniques to conclude that the magnetic field inhomogeneity experienced by the atoms in the science cell is negligible. From the measured magnetic field profile (using an $xyz$-probe) of the main coils, at 37 G bias we estimate the magnetic field variation to be $\sim 0.1$ mG in the radial direction and $\sim 1$ mG in the axial direction over a 100 $\mu$m region, representing a typical size of cold cloud in a crossed dipole trap. Similarly, we estimate the radial magnetic field gradient from cloud lateral acceleration during free fall. We use three different spin state populations with differing magnetic moments ($|1,-1\rangle$, $|2,-2\rangle$, and $|2,0\rangle$) to place an upper limit of 4 mG/mm on the magnetic field gradient generated by the main coils at 36 G.

## 3.3 Imaging System

A good understanding of the imaging system is important for any ultracold laboratory that relies solely on atom images for data. For us, it is even more crucial to understand all imaging peculiarities since we are interested in measuring density-dependent loss rates in our few-body physics studies. We must accurately determine the imaging system magnification, atom number, cloud temperature and trap frequencies.

### 3.3.1 Side Imaging Specifications

The majority of our imaging is performed using the side imaging system. This system enables imaging small and/or cold clouds with a high-magnification configuration ($M = 6.7$) and hot and/or large clouds (e.g. like those in quadrupole trap and in H1 beam after dipole trap load) with a low-magnification ($M = 1$) configuration, see Fig. 3.10.

The commercial objective lens was chosen to achieve the best imaging resolution given the tight space constrains. We found that the $f = 75\,\text{mm}$ air-spaced achromatic doublet was our best option due small on- and off-axis aberrations. This objective enables diffraction-limited performance for on-axis or small off-axis imaging, resulting in $3.6\,\mu\text{m}$ (Airy disk radius) imaging resolution when considering aberrations, see Fig. 3.12. However, imaging off-axis beyond $\sim 1\,\text{mm}$ field of view, as in the cases imaging hot and/or elongated clouds expanding from quadrupole or H1 dipole traps, can lead to significant aberrations and image distortion, as depicted in Fig. 3.13.

We find that by decreasing the objective aperture via an iris, we are able to significantly reduce off-axis aberrations, at the expense of slightly worse imaging resolution. We see this effect in simulations of the modulation transfer function (MTF), point spread function (PSF) and wavefront error. We also verify this effect experimentally in a test setup. We image an effective point-source ($767\,\text{nm}$ light passing through a $1\,\mu\text{m}$ pin hole) and gather the effective PSF of the system for different focus positions, see Fig. 3.14.

Ultimately, we use information gathered directly from atom imaging to fine-tune our imaging

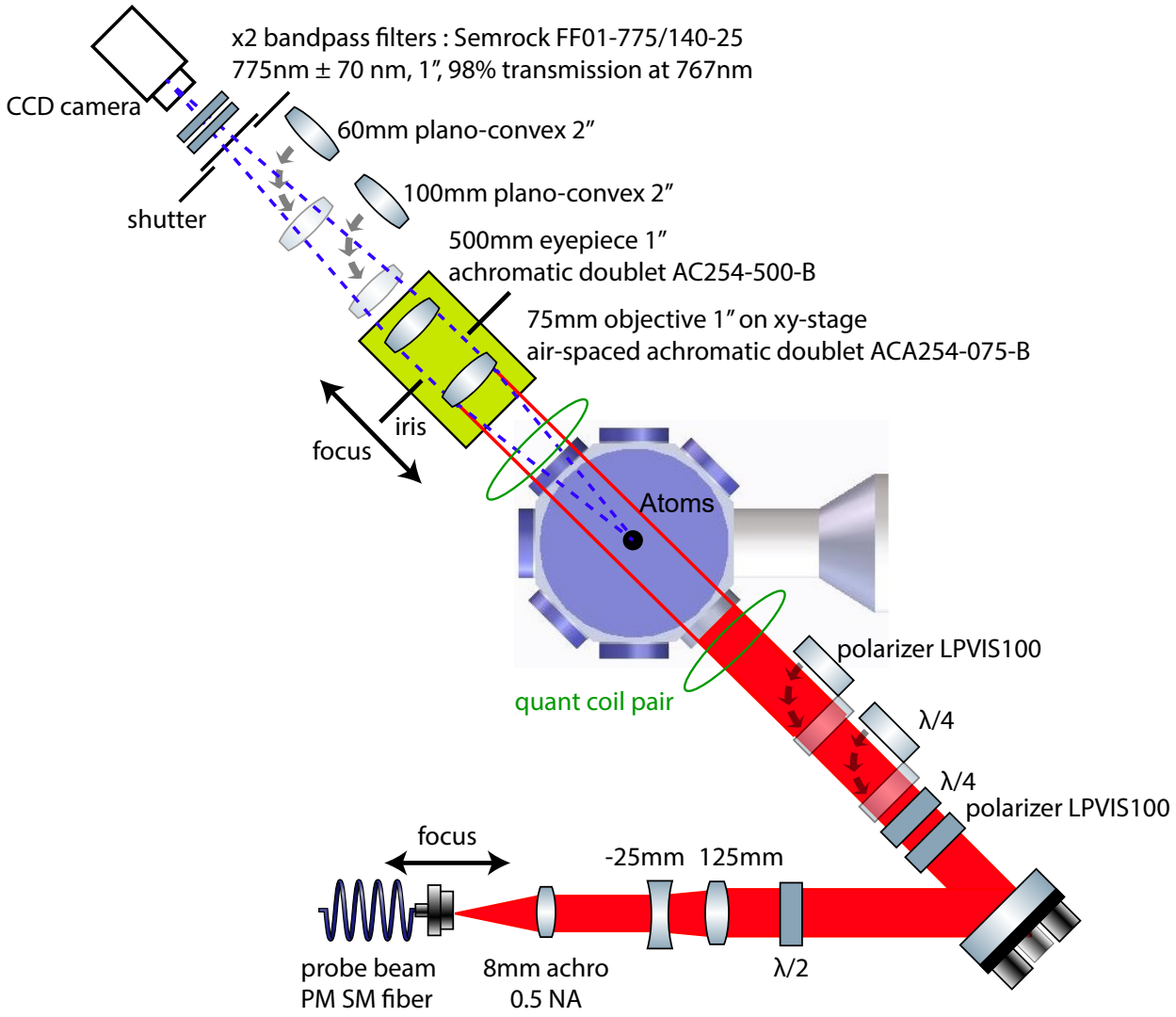


Figure 3.10: The main imaging system in the science chamber. A pair of coils provide a quantization magnetic field for the probe $\sigma^+$ or $\sigma^-$ transitions (or $\pi$ transitions when the extra $\lambda/4$ and polarizer are flipped in). The atoms are located 23.1 mm away from the 3.18 mm thick fused-silica side windows. We image atoms using two setups: a high-magnification ($M \approx 7$) setup with $f = 75$ mm objective and $f = 500$ mm eyepiece and a low-magnification ($M \approx 1$) setup with two additional lenses (on flipper mounts). The objective lens is 38 mm away from the window and is the limiting aperture of the imaging system (20 mm diameter clear aperture, 0.13 NA) when the iris is fully open. The eyepiece lens is approximately 55 mm behind the objective and is 481 mm (equal to the back focal length) away from the CCD. The 100 mm demagnification lens is approximately 160 mm behind the eyepiece, the 60 mm demagnification lens is approximately 240 mm following that and 100 mm in front of the CCD. Note that, due to the air-spaced nature of the objective, the achromatic pair is more prone to dust and imperfections; it took several cleaning (and outright replacement) of objective lenses to achieve acceptable optical quality and minimal image fringes.

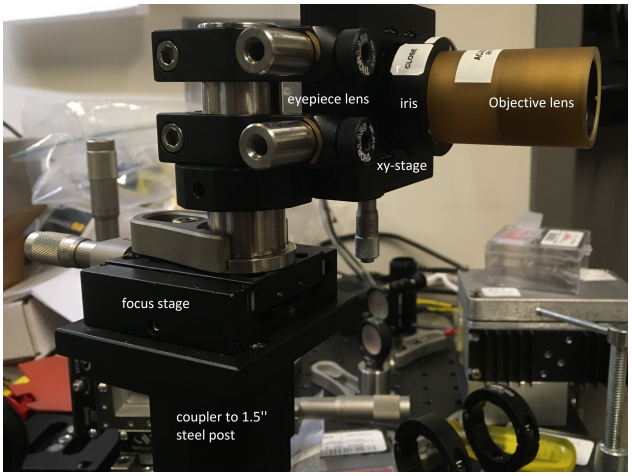


Figure 3.11: Mounting for the side imaging objective and eyepiece lenses. The objective lens tube is machined from Ultem/polyetherimide plastic to prevent eddy currents and magnetization from the science magnetic field coils (not shown).


Figure 3.12: Simulated (using Zemax/OpticStudio software) spot size diagrams for the side imaging objective lens, where we include the science cell window in the simulation. We simulate aberrations using geometrical rays (blue crosses) for on-axis imaging (left figure) and for 600 $\mu$m off-axis imaging (right figure), corresponding to a typical hot cloud size in a crossed dipole trap. The grid size is 10 $\mu$m $\times$ 10 $\mu$m and the diffraction limit (at 767 nm) is 3.5 $\mu$m (circles). We find that imaging aberrations are small, as evidenced by the small spread in the focused rays (0.9 $\mu$m RMS radius for on-axis and 1.8 $\mu$m RMS radius for off-axis) compared to the diffraction-limited size.

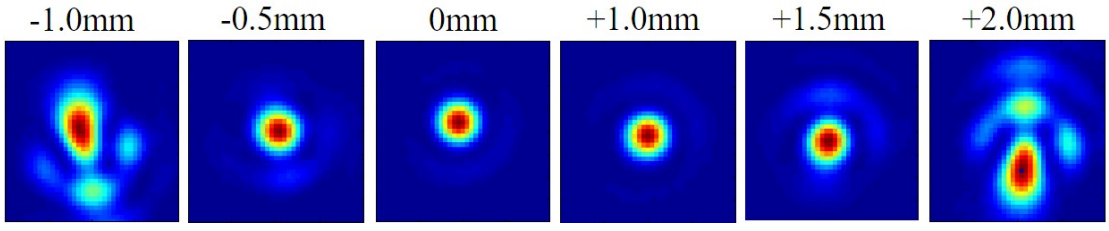


Figure 3.13: Measured point spread functions for different objective lens lateral positions. Off-axis aberrations lead to significant distortion away from the center position, defined as the position where the objective and the eyepiece lenses are concentric.

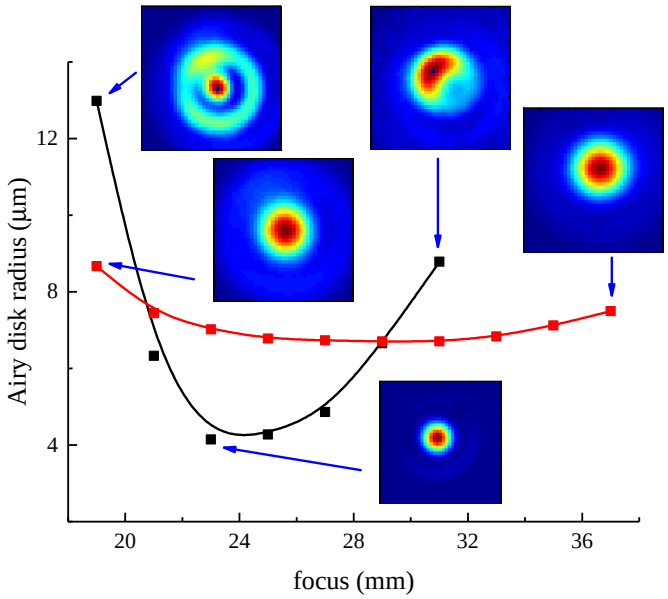


Figure 3.14: Reduction of aberrations via aperturing the objective. An unapertured objective lens (black points with spline), corresponding to 20 mm clear aperture diameter, has severe aberrations away from the focus. Reducing clear aperture diameter to 0.5 in via an iris following the objective lens leads to smaller aberrations, albeit at expense of imaging resolution. Note that, as in this case, we often fit the focused spots using a Gaussian distribution and deduce the Airy disk radius from the Gaussian width $\sigma$.

system. First, we optimize the focus position by using a dilute, cold (thermal or BEC) and small cloud, maximizing the detected OD with on-resonance imaging. Second, we check the level of astigmatism present using off-resonant imaging (see Fig. 3.15) and adjust the objective lateral position if need be. Last, we visually inspect the diffraction ring pattern in the PSF with on-resonant imaging of condensed clouds and verify the behavior at different focal spots. We iterate on the above techniques with smaller clouds to further increase optimization sensitivity, enabling us to focus the objective with sub-mm precision. We measure the imaging system magnification $M$ by dropping an atomic cloud (released from a trapping potential) and fitting its measured path to a parabolic function containing only $M$, the gravitational acceleration constant $g$ and the CCD pixel size. In absence of magnetic field gradients and significant image distortions, this technique enables an accurate demagnification of $M$.

Images are acquired with a low dark noise and a high quantum efficiency TEC-cooled (down

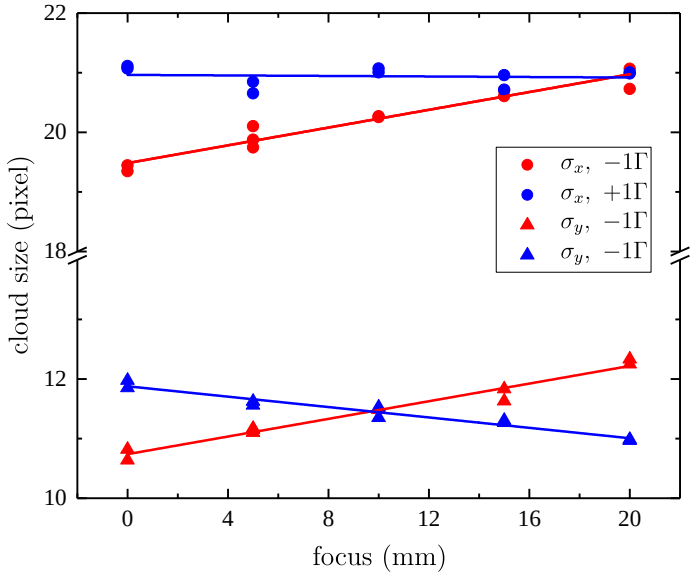


Figure 3.15: Measured astigmatism present in an unoptimized imaging system. We measure the size of dense clouds in two directions ($\sigma_x$ and $\sigma_y$) at different objective positions for off-resonant probe beam detunings $\pm 1\Gamma$. Since dense atom clouds lead to lensing, the focal spot in the two directions coincide with the crossings of the cloud sizes using blue- and red-detuned probe light. In this case, significant astigmatism is present, with the two focal spots occurring 1 cm apart.

to $-45$°C) CCD camera: Roper Scientific/Princeton Instruments NTE/CCD-512-EBFT camera with a back-illuminated E2V 57-10 CCD, 13 $\mu$m pixel size, $512 \times 512$ unmasked pixel array and a masked region that can be used for kinetics-mode imaging. We use shot noise statistics, resulting from white noise blackbody noise sources (dark noise or incandescent flashlight), to characterize CCD camera properties. We experimentally deduce [$e^-$/count] gain, electronic readout noise, electronic bias, dark noise rate, well capacity, quantum efficiency [counts/photon] and pixel gain inhomogeneity, see Figs. 3.16, 3.17 and 3.18. Overall, a good understanding of CCD properties and settings allows us to perform absorption imaging with only 100–300 photons per pixel (integrated over 20 $\mu$s, with an excellent signal-to-noise ratio. Our camera settings/properties are: 60 $\mu$s exposure, 16-bit resolution, 1 MHz readout rate (fast frame acquisition at an expense of a larger 7 counts/pixel read noise), high analog gain (measured 1.53 $e^-$/count), 223 counts electronic bias (set by a trimpot before the ADC), $\sim$ 80% quantum efficiency at 767 nm (measurement agrees with the spec sheet), continuous frame cleaning and $-40$°C operating temperature (resulting in

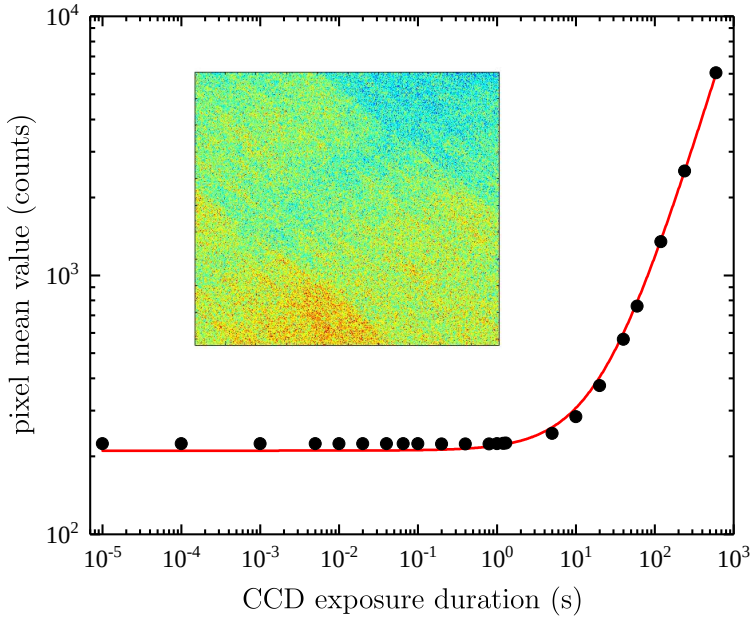


Figure 3.16: CCD camera dark-frame images at $-45°$C and with high-gain setting. We acquire images with different exposure durations for a capped CCD camera and extract the mean pixel value (digital count recorded by the ADC) in each image frame. The camera is biased (analog voltage addition to each pixel's value before the ADC) to give non-zero counts for short exposure durations, important for observing shot-noise statistics at low signal levels. Dark current (blackbody photons and/or leakage current) is present for long exposures. Due to pixel gain inhomogeneity and/or thermal/blackbody gradients, pattern noise is present in dark-frame images (inset). We use a linear fit (red curve) $A + B\tau$ to extract the bias voltage and the dark current rate.

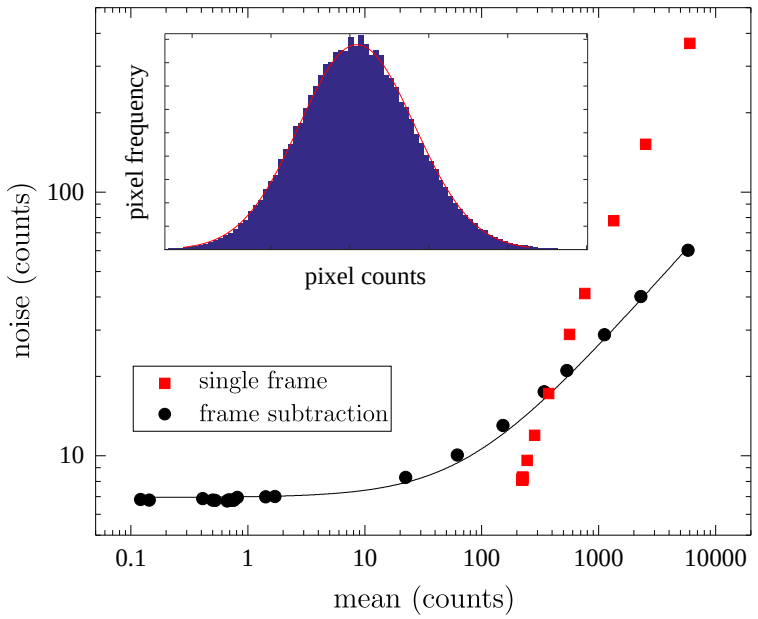


Figure 3.17: Characterizing CCD camera noise statistics using the photon-transfer technique [92]. For each exposure duration, we perform statistics (see histogram inset) to extract the mean pixel intensity value and the pixel intensity noise (the standard deviation of a normal distribution, assuming Gaussian random noise). Pattern noise/pixel count inhomogeneity in a single image frame, such as shown Fig. 3.16 inset, leads to large noise figures (red squares). We get rid of pattern noise by performing noise statistics (black circles) on a frame resulting from subtracting two image frames with the same exposure duration. Then, the total noise is dominated by the CCD read noise (e.g. resulting from ADC, high gain or fast readout) for small mean counts (small exposure durations) and by photon shot noise for large mean counts. We fit total noise to $\sqrt{(A\sqrt{\bar{y}})^2 + B^2}$ (solid curve) to extract the CCD gain $A^{-2}$ (measured in $e^-$/count) and the read noise $B$, where $\bar{y}$ is the mean pixel count. The accuracy of this technique relies on good frame subtraction and assumes that the photon noise results from random thermal sources.

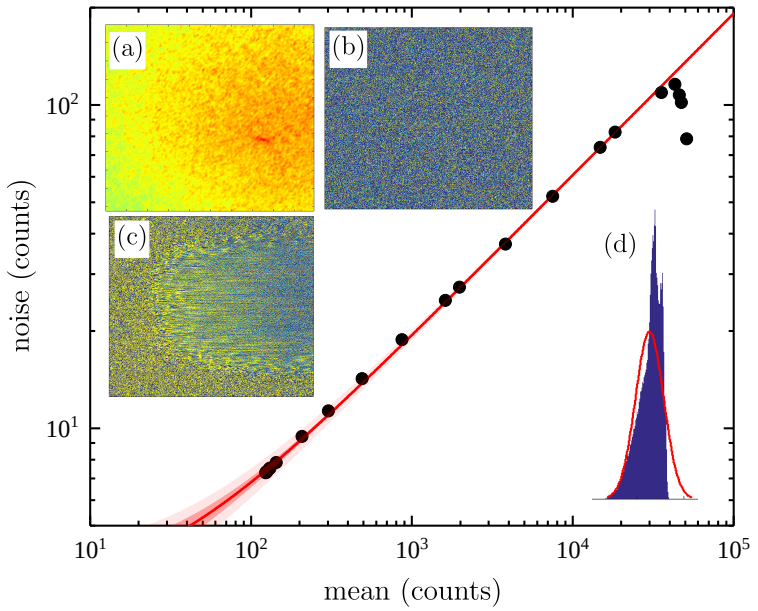


Figure 3.18: Measurement of the CCD pixel well capacity. We use a flashlight and a diffuser as the thermal light source (instead of the dark current) to provide a semi-uniform illumination (e.g. a single frame (a) inset) of the CCD chip. For low light levels, frame-subtracted images (e.g. (b) inset) display photon shot noise statistics, as demonstrated by an agreement ($\sqrt{\text{mean counts}}$ scaling and a similar CCD gain value) of the fitted curve (red line with 95% confidence intervals, fit up to $2 \times 10^4$ counts and extrapolated to higher values) with the fit used in Fig. 3.17. For high pixel counts, yet below the 16-bit ADC $2^{16}$ maximum count, we see CCD saturation (due to finite pixel well capacity) and blooming, as demonstrated in (c) inset by frame-subtracted image smearing, in (d) inset by histogram pixel value saturation and in the main plot by noise reduction at high count values.

15 $e^-$/pix/sec dark current).

### 3.3.2 Absorption Imaging Corrections

Absorption imaging basics introduced in Sec. 2.3.2 are often sufficient for estimating the atom number. However, to extract a more accurate atom number, one needs to consider multiple sources of systematic error [93]. For example, the effective absorption cross-section can be affected by technical systematics, which we limit by careful engineering and (iterative) tuning of system components. We use long enough TOF expansion durations to prevent limitations by finite imaging resolution, while short enough to prevent image distortion from off-axis aberrations. We verify that the quantization magnetic field is strong enough ($\gtrsim 3\,\mathrm{G}$) and stable during imaging by looking at probe spectral lineshape height at different $B$-field values, ensuring the maximal OD height is saturated. Since not all probe light is pure, the maximum measured OD statures to some value $\mathrm{OD}_{\mathrm{sat}}$ for even very dense clouds. We characterize the probe beam polarization purity (e.g. $\sigma^+$ or $\sigma^-$), directionality (with respect to the quantization field axis) and spectral purity (e.g. laser frequency noise sidebands) by imaging dense clouds on-resonance and take the saturated $e^{-\mathrm{OD}_{\mathrm{sat}}}$ value as a figure of merit; we often reach $< e^{-3.5}$. More quantitatively, the measured $\mathrm{OD}_{\mathrm{meas}}$ is smaller than the OD predicted by Lambert-Beer's law $\mathrm{OD}(x,y) = n(x,y)\sigma$ (see Sec. 2.3.2 and Eq. 2.3) by a factor [94]:

$$\mathrm{OD}_{\mathrm{meas}} = \ln\left(\frac{1 - e^{\mathrm{OD}_{\mathrm{sat}}}}{e^{\mathrm{OD}_{\mathrm{meas}}} - e^{\mathrm{OD}_{\mathrm{sat}}}}\right), \tag{3.5}$$

where $\mathrm{OD}_{\mathrm{mod}}$ is the modified OD definition due to impure probe light. We typically image clouds with $\mathrm{OD}_{\mathrm{meas}} \lesssim 1$ and this correction factor is $\lesssim 5\%$. Additionally, we check the affect of the probe beam spectral laser noise on the probe lineshape (see Fig. 3.19), tweaking frequency lock servo settings or outright replacing laser diodes (master or trap DBR) with new ones if needed. Lastly, we spent significant time minimizing interference fringes in the image frames resulting from optical imperfections (e.g. dust, scratches and etaloning) and vibrations to achieve nearly perfect image frame subtraction in absence of atoms (i.e. homogeneous background OD frame).

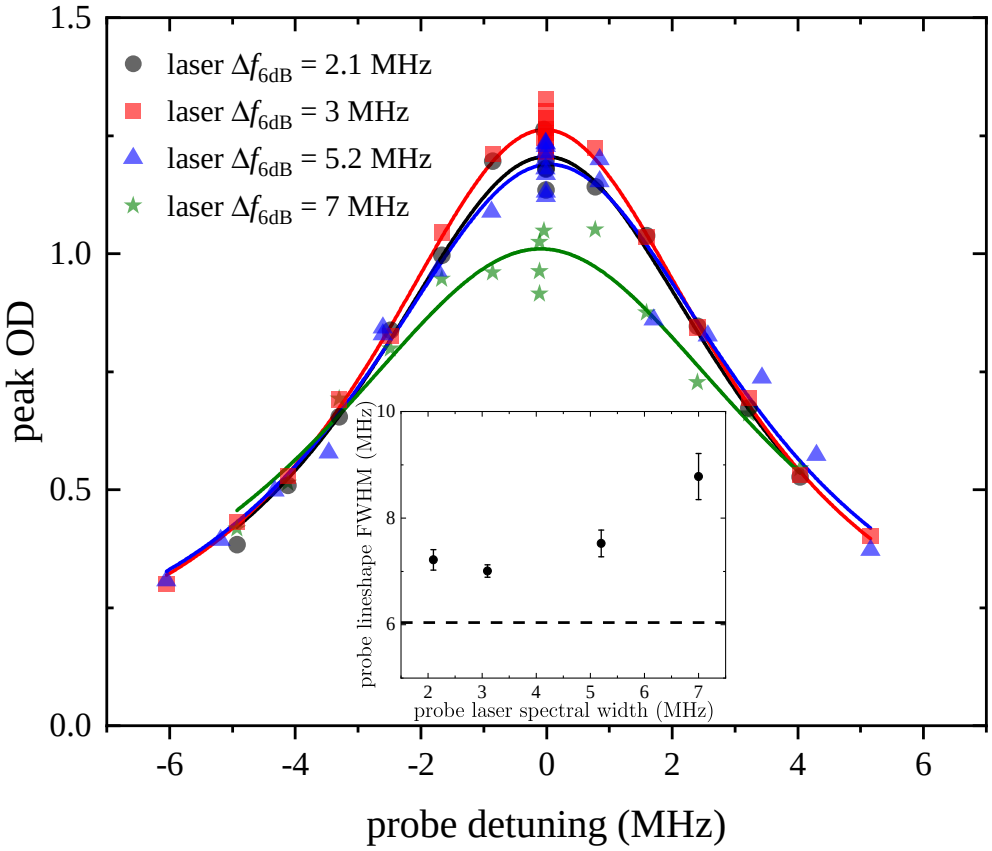


Figure 3.19: The effect of probe beam laser noise on the probe lineshape. We intentionally broaden the laser linewidth by tweaking frequency lock servo settings and measure the spectral width (full-width 6 dB points) using the self-heterodyne setup. The narrowest laser linewidths of a locked laser approach the linewidth of an unlocked laser. New laser DBR diodes have narrow linewidths (measured $< 1$ MHz for 3 dB points, $< 2$ MHz for 6 dB points) and broaden with age ($\mathcal{O}(2\,\text{yrs})$). We take a probe lineshape for each servo setting and extract the FWHM $\gamma$ from a Lorentz fit $A\gamma/\left(4(f-f_0)^2+\gamma^2\right)$, where $A$ is an amplitude prefactor and $f-f_0$ is the probe detuning. The inset shows that while the probe lineshape is broadened for spectrally-broad probes, lineshape width saturates to small values for spectrally-narrowest probes. Note that due to some other systematic effects, the probe lineshape FWHM is large than the natural linewidth $\Gamma/2\pi = 6.035$ MHz (dashed) of the D2 atomic transition.

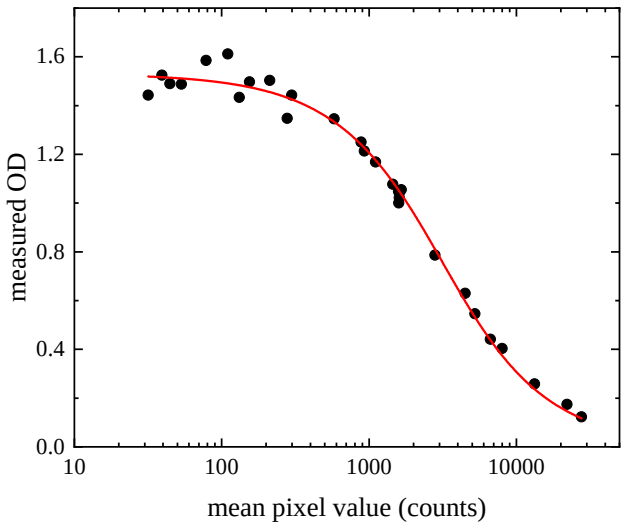


Figure 3.20: An example of OD saturation due to a high intensity probe. We measure the peak OD of similar atomic clouds using different probe beam powers, changed by a combination of an AOM (RF power) and ND filters. We take $(1/N_{\mathrm{pix}})\int_A I_L(x,y) - I_D(x,y)dxdy$ (light and dark frames integrated over $40\,\mu$s probe pulse duration) as the mean intensity (measured in units of ADC counts per pixel), where we take the average over a region $A$ with $N_{\mathrm{pix}}$ pixels that contains the atom cloud in the shadow frame $I_S(x,y)$. We fit to Eq. 3.7 and extract $I_{\mathrm{sat}} = 2200$ counts and $\mathrm{OD}_{\mathrm{true}} = 1.53$. Note that here we used a probe with a $40\,\mu$s duration, which is too long to extract an accurate $I_{\mathrm{sat}}$ value. Using a numerical fit that includes photon-recoil-related corrections, we obtain $I_{\mathrm{sat}} = 3600$ counts.

In addition to technical systematic effects, the measured optical depth is affected by transition saturation. Taking into account the transition saturation, described by saturation intensity $I_{\mathrm{sat}}$, and the saturation due to impure probe light, the "true" OD becomes [94, 95]:

$$\mathrm{OD}_{\mathrm{true}} = \mathrm{OD}_{\mathrm{mod}} + \left(1 + e^{-\mathrm{OD}_{\mathrm{mod}}}\right)\frac{I_{\mathrm{in}}}{I_{\mathrm{sat}}}, \tag{3.6}$$

where $I_{\mathrm{in}}$ is the incoming beam intensity. For $\mathrm{OD}_{\mathrm{sat}} \gg \mathrm{OD}_{\mathrm{meas}}$, $\mathrm{OD}_{\mathrm{mod}} \approx \mathrm{OD}_{\mathrm{meas}}$ and

$$\mathrm{OD}_{\mathrm{meas}} \approx \mathrm{OD}_{\mathrm{true}} - \frac{I_{\mathrm{in}}}{I_{\mathrm{sat}}} + W\left(\exp\left(\frac{I_{\mathrm{in}}}{I_{\mathrm{sat}}} - \mathrm{OD}_{\mathrm{true}}\right)\frac{I_{\mathrm{in}}}{I_{\mathrm{sat}}}\right), \tag{3.7}$$

where $W(x)$ is the Lambert W function. We measure $\mathrm{OD}_{\mathrm{meas}}$ for multiple probe intensities $I_{\mathrm{in}}$ and experimentally extract $I_{\mathrm{sat}}$ from the fit to Eq. 3.7, as depicted in Fig. 3.20.

While Eq. 3.7 is sufficient in certain probing regimes, further corrections require understanding how the measured optical depth is affected by the finite recoil momentum $h/\lambda$ that each photon imparts on the atom during the imaging process [93, 96]. Each atom gets a momentum kick in

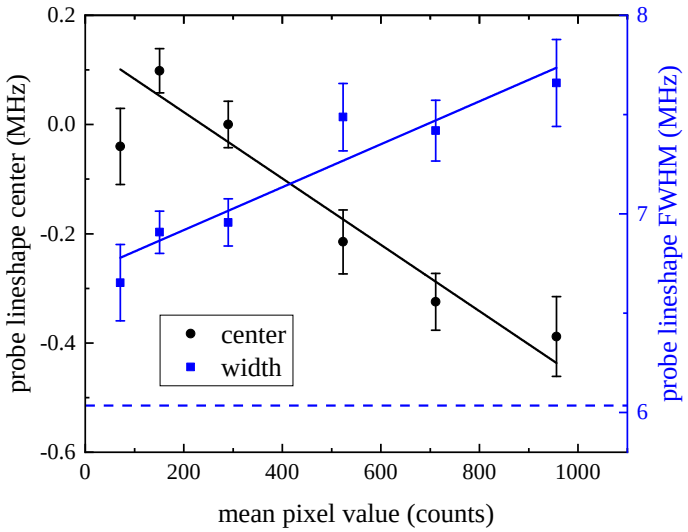


Figure 3.21: Doppler shift and broadening of a probe lineshape at high probe intensities. We analyze probe lineshapes (similar as in Fig. 3.19) taken at different probe pulse powers and a fixed 20 $\mu$s probe pulse duration. The mean pixel value (the time-integrated intensity) is proportional to the number of photons scattered by each atom during the absorption imaging process. The atom cloud accelerates away from the probe beam due to finite photon recoil momentum. Higher number of scattering events leads to larger Doppler shifts in the probe lineshape center (black circles) and larger lineshape widths (blue squares). The solid curves are linear fits and dashed line represents the atomic transition natural linewidth $\Gamma/2\pi = 6.035$ MHz.

the direction of the probe beam (resulting in linear acceleration) due to absorption and performs a random walk due to subsequent photon re-emission. The latter process leads to diffusive cloud size increase in the direction transverse to the probe beam propagation direction and can be limited by using short probe pulse durations. The prior process can lead to a Doppler shift from the resonance (thereby changing the scattering cross-section), cloud distortion in the direction along the probe beam propagation (atoms in the front of the cloud can initially scatter more photons than atoms in the back of the cloud), and cloud movement away from the imaging focus. Figure 3.21 shows our measurement of such effects.

To extract accurate OD values, and hence accurate atom numbers, we take multiple measures. We model [93, 96] the aforementioned effects and determine that Eq. 3.7 requires photon-recoil-related corrections for long probe pulse durations and strong probe pulse intensities, as depicted in see Fig. 3.22. We use such a model to fit saturation data to extract accurate $I_{\mathrm{sat}}$ values. However,

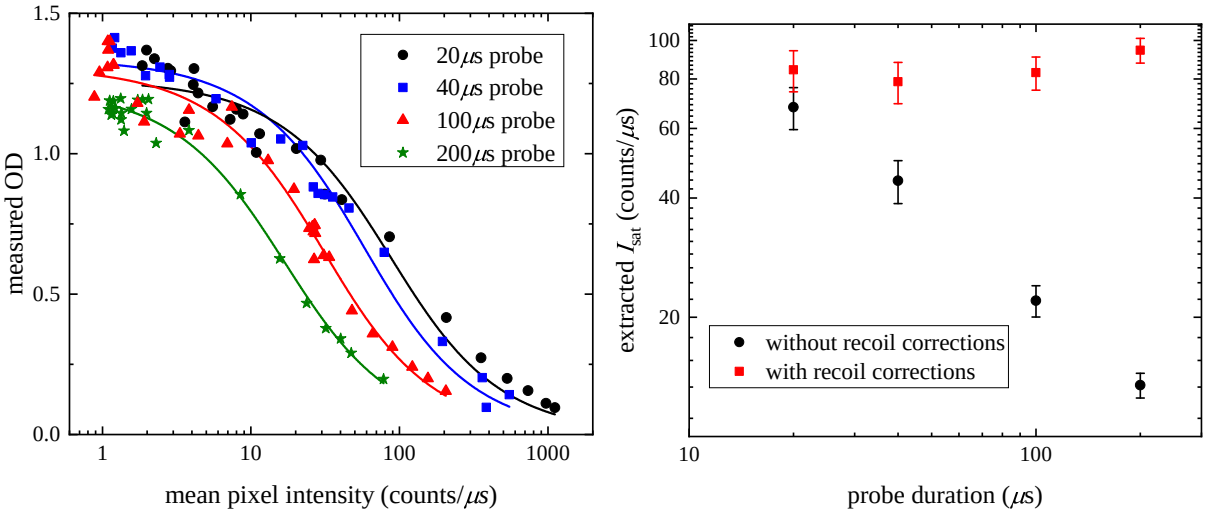


Figure 3.22: Probe pulse duration affect on the measurement of $I_{\text{sat}}$. We perform measurements (left figure) similar to Fig. 3.20, except we normalize the $x$-axis by the probe beam duration to get the mean pixel intensity, necessary for data comparison with different probe pulse durations. We fit (right figure) the data using two different methods: without recoil corrections (Eq. 3.7) and with recoil corrections (numerical model). While the two methods agree only at small probe pulse durations, the finite photon recoil momentum model gives consistent $I_{\text{sat}}$ values for all pulse durations. These results demonstrate the need for a more complex model or the need to image with short probe pulse durations to accurately determine $I_{\text{sat}}$ values.

we do not use the model for OD corrections. Instead, we suppress systematic effects associated with finite photon recoil momentum by limiting the probe pulse duration to 10–20 $\mu$s and the probe pulse intensity to $(I/I_{\text{sat}})^{-1} = 10$–$20$. However, we still include (small) OD corrections due to transition saturation by performing a pixel-by-pixel correction using a re-written version of Eq. 3.6:

$$\text{OD}_{\text{true}}(x,y) = \ln\left(\frac{I_L(x,y) - I_D(x,y)}{I_S(x,y) - I_D(x,y)}\right) + \frac{I_L(x,y) - I_S(x,y)}{I_{\text{sat}}}, \tag{3.8}$$

substituting $I_{\text{in}} = I_L(x,y) - I_D(x,y)$, $I_{\text{out}} = I_S(x,y) - I_D(x,y)$ and $\text{OD}_{\text{mod}} \approx \text{OD}_{\text{meas}} = \ln(I_{\text{in}}/I_{\text{out}})$. For the best signal-to-noise ratio and the small systematic uncertainties, we typically work with $I_{\text{in}} = 120\,\text{counts/pixel}$, $I_{\text{sat}} \sim 1900\,\text{counts/pixel}$ (high CCD gain $1.53\,e^-/\text{count}$), $20\,\mu$s probe pulse duration and $\text{OD}_{\text{meas}} \sim 0.6$. The CCD camera noise floor ($\sigma = 7\,\text{counts/pixel}$ readout noise for high gain, see Fig. 3.17) prevents us from using smaller probe beam intensities, as depicted in Fig. 3.23. Furthermore, we always utilize optical cycling transitions (e.g. $|\text{F} = 2, \text{m}_\text{F} = -2\rangle \rightarrow$

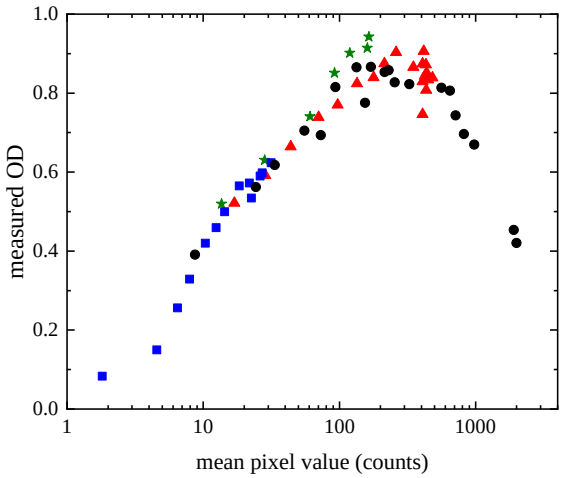


Figure 3.23: CCD camera noise affect on absorption imaging. We perform similar measurement as in Fig. 3.20, except we use the medium gain CCD camera setting ($3.03\,e^-$/count gain and 4 counts/pixel read noise) and lower probe pulse powers. Due to bad SNR at very low powers, the measured OD decreases as the cloud image becomes unresolvable. Different colors represent different optical settings (e.g. diverting more power to the probe beam and different ND filters/attenuators) that enabled the high dynamic range in the mean pixel value.

$|\mathrm{F}' = 3, \mathrm{m}_{\mathrm{F}'} = -3\rangle$) for imaging when an accurate measurement of the atom number is required, since non-cycling optical transitions have imaging peculiarities in addition to those listed above. Lastly, since we always measure probe lineshape widths $> \Gamma/2\pi = 6.035\,\mathrm{MHz}$, we correct OD for lineshape broadening. We extrapolate the lineshape FWHM width $\Delta f$ to zero probe intensity (using a fit similar to the one in Fig. 3.21) and correct OD by $\Delta f/6.035\,\mathrm{MHz}$ (typically $\sim 10\%$ correction).

### 3.3.3 Extracting Atomic Density

In addition to accurately measuring the atom number, we need to accurately measure the atom temperature and trapping frequencies to correctly determine the atom density. We measure the temperature using standard thermometry techniques involving atom cloud expansion [94]. The uncertainty in the measured temperatures is mainly determined by imaging peculiarities (e.g. magnification, resolution, astigmatism) or the uncertainty in the trapping frequencies.

We measure the trapping frequencies of our optical dipole trap using several different methods:

we can induce a sloshing motion, induce a breathing motion, parametrically heat the gas, measure the optical trap curvature by looking at the gravitational sag as a function of optical power, or from thermometry. While we've utilized all methods to check the consistency of our results, we found the sloshing method to be the most precise. To measure the trapping frequency along gravity, we drop the cloud for a short duration and recapture it in the same potential; the induced sloshing motion is equal to the trapping frequency. To measure the trapping frequency in the other directions, we use magnetic field gradients to induce sloshing by displacing the cloud from the optical trap center and subsequently turning off the gradient field. To accurately measure trapping frequencies, we are careful in probing only the harmonic region of the trap. We use small clouds (e.g. cold thermal clouds or BECs) and systematically check the sloshing frequency as a function of the induced perturbation (e.g. displacement from the trap center). Lastly, we verify the trapping frequencies by looking at the expansion of thermal clouds: the cloud size is predominately determined by the trap frequencies and temperature during short expansion durations. Precise knowledge of atom number and temperature, the trapping potential and imaging, enables accurate determination of atom density to within 20% (see Sec. 5.3 for further details).

### 3.3.4 Top Imaging Specifications

The side imaging enabled accurate determination of atom number, temperature and density for most measurements presented in this thesis. Due to the amount of effort required in calibrating an imaging system, we abandoned our initial efforts in using the top imaging system, where the probe beam propagates along the main field direction. However, after precise measurements of cold dilute atomic and molecular samples in our Efimov (Ch. 5) and dimer spectroscopy (Ch. 4) studies, we realize the need for a better imaging system from the top, as our side imaging suffers from multiple limitations.

With the side imaging, we cannot perform accurate in-situ imaging of the smallest clouds due to a relatively low (3.6 $\mu$m Airy disk radius) imaging resolution. The required cloud expansion results in smaller OD signals and a reduced signal-to-noise ratio (SNR). We cannot increase the

image frame SNR by increasing the probe intensity due to effects discussed in Sec. 3.3.2 and we resort to using a small number of photons during the absorption imaging process. Due to a relatively small CCD camera gain, we end up detecting only $\sim 50$ counts/pixel (for 1 OD cloud and $I_{\text{in}} = 120$ counts/pixel), a small value compared the $\sigma = 7$ counts/pixel CCD camera noise floor. Furthermore, since the magnetic field bias direction is orthogonal to the side probe propagation, we resort to two options for side imaging: we use $\pi$ transitions at the expense of 50% in the OD signal or we use $\sigma^{\pm}$ transitions along with a magnetic field parallel to the probe beam propagation direction generated by separate quantization coils. We often resort for the latter option at the expense of requiring a minimal expansion time $\mathcal{O}(1\,\text{ms})$, associated with the main coils turn off time and the quantization coils turn on time.

We plan to use a high-resolution top imaging system and an electron multiplying CCD camera in our future studies. The camera (Princeton Instruments ProEM 512B, CCD97-B detector with a $512 \times 512$ pixel array, $16\,\mu$m pixel size and $\sim 75\%$ QE) has a low-noise 1–1000 electron multiplier gain and can be cooled down to $-70°$C (0.02). Such high gain enables a better usage of the 16-bit ADC and results in a higher SNR for low probe intensity imaging. We measure the top imaging camera to be less noisy than the side imaging camera for similar camera settings: a higher gain ($1.0\,e^-$/count compared to $1.53\,e^-$/count) with similar read noises (7 counts/pixel).

We make a custom high-resolution objective for top imaging using a combination of commercially available lenses. We are limited to using only a few optical elements due to the space constraint imposed by the moving cart coils. Furthermore, the numerical aperture of the 0.75 NA window is limited to $\sim 0.5$ NA by the presence of the surrounding $\sim 1.7$ in shim and gradient coils. Based on the aforementioned constraints and some preliminary Zemax simulations, we chose to use an aspheric lens (Thorlabs AL4532-B, $f = 32$ mm, 0.61 NA, 24.2 mm working distance and 45 mm outer diameter) as the primary imaging lens in the custom objective. Due to further space constraints associated with lens mounting and clearances, we reduce (JILA instrument shop) the asphere diameter to a 30 mm outer diameter (26.2 mm clear aperture and 0.38 NA). While the lens is diffraction-limited in free-space, the science window introduces significant spherical aberrations

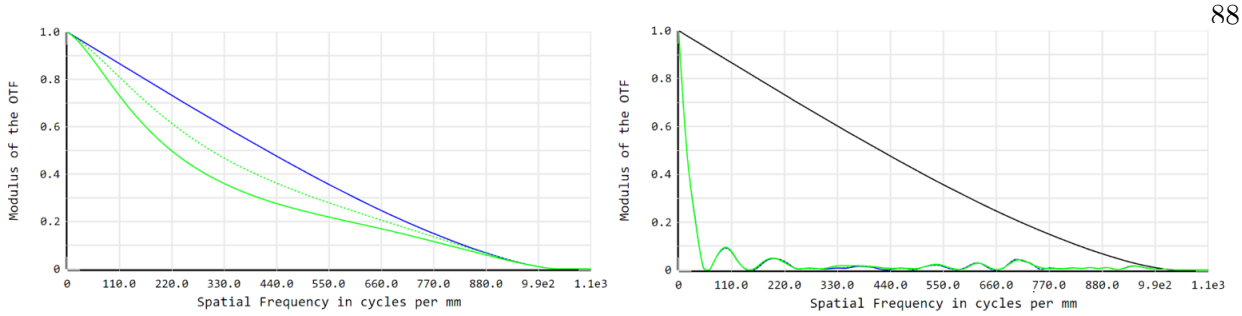


Figure 3.24: MTF (modulation transfer function) of the top imaging asphere (Thorlabs AL4532-B, $f = 32\,\text{mm}$, 0.61 NA) without (left) and with (right) the science cell window. The diffraction limit (1.1 $\mu$m Airy disk radius at 767 nm) of the chosen (apertured) 0.38 NA is represented by black curves, on-axis imaging rays MTF by blue curves, 100 $\mu$m off-axis sagittal rays by dashed green curves and 100 $\mu$m off-axis tangential rays by solid green curves. Without the science cell window, the imaging system is expected to be diffraction-limited on-axis (note the blue and black curves overlap) and nearly diffraction-limited off-axis. However, with the window, the imaging system is far from diffraction limit. The 6.35 mm thick fused silica window, located 10.5 mm away from the atoms, introduces significant spherical aberrations (0.9 $\lambda$ rms wavefront error contribution), resulting in a $\sim 28\,\mu$m spot size radius.

(see Fig. 3.24) and we cannot use the asphere on its own. We simulate various configurations with additional one or two compensating lenses to see how we can reduce spherical aberrations. While a custom meniscus lens would be the best solution, addition of a single plano-convex lens (see Fig. 3.25) would lead to satisfactory performance. The custom objective is expected to be diffraction limited (1.1 $\mu$m Airy disk radius) for on-axis imaging and nearly diffraction-limited for off-axis, as depicted in Fig. 3.26.

The objective lenses are placed in a custom machined lens tube. We perform tolerance analysis prior to machining to determine which dimensions require the highest precision. The lens tube and the mounting arm (made necessary long to provide sufficient cart coils clearance) are made from plastic (Ultem and G11, respectively) to prevent vibrations from magnetic field sweeps. A pair of goniometers and an $xyz$-stage provide the necessary degrees of freedom for objective assembly movement. We perform vibration analysis (using an accelerometer) and verify mechanical stability of the objective assembly. The high-resolution top imaging system is ready to be implemented into our system and will provide a new invaluable tool for precise imaging of dilute and small atomic and molecular clouds.

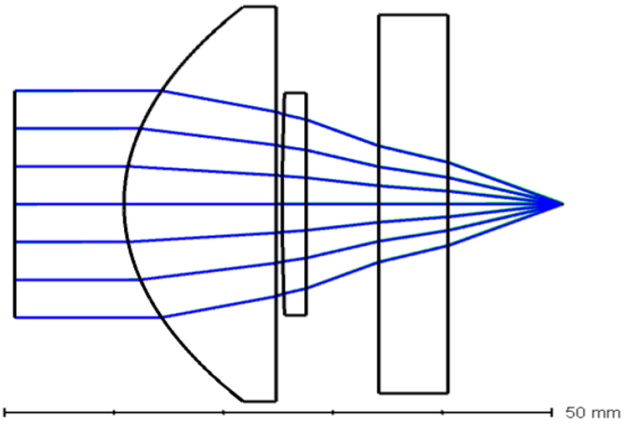


Figure 3.25: Top imaging objective lens configuration. Rays propagating from right to left: atoms, 10.5 mm space in the vacuum chamber, 6.35 mm thick fused silica window, 6.6 mm space outside the vacuum chamber, 2.2 mm thick plano-convex lens (Thorlabs LA1978-B), 0.57 mm space between the lenses, and 13.9 mm thick asphere. The exit pupil diameter is 26.2 mm. We vary separation distances and the clear aperture diameter during imaging system optimization on the rms wavefront error.

## 3.4 Computer Control

Figure 3.27 shows an overview of our lab's computer and hardware control. Most of the experiment is controlled via two FGPA cards (NI PCIe-7852R LX50), which have on-board 40 MHz clocks, analog and digital lines. Synchronization of all experimental sequence timings to FPGA clocks (instead of using computer time) leads simplification and robustness of the machine. The two FGPA board timings are synchronized by triggering the FPGA2 clock with an FPGA1 TTL at the beginning of every experimental sequence. We periodically compare the two FPGA clock frequencies and adjust them when necessary (artificially, by adjusting the FPGA2 board clock cycle definition in the Matlab control code); typically the two clocks differ only by a few $\mu$s/min. Currently there is no easy way to synchronize the two FPGA clocks to the stable 10 MHz signal that is distributed throughout JILA and referenced to NIST.

We use LabView software to program, compile and communicate with the FPGA boards. Fortunately, due to the modularity of our control program (credit to Yoav Sagi), we rarely $\mathcal{O}$(yrs) reprogram or recompile the FPGA boards. For each experimental sequence, we generate all com-

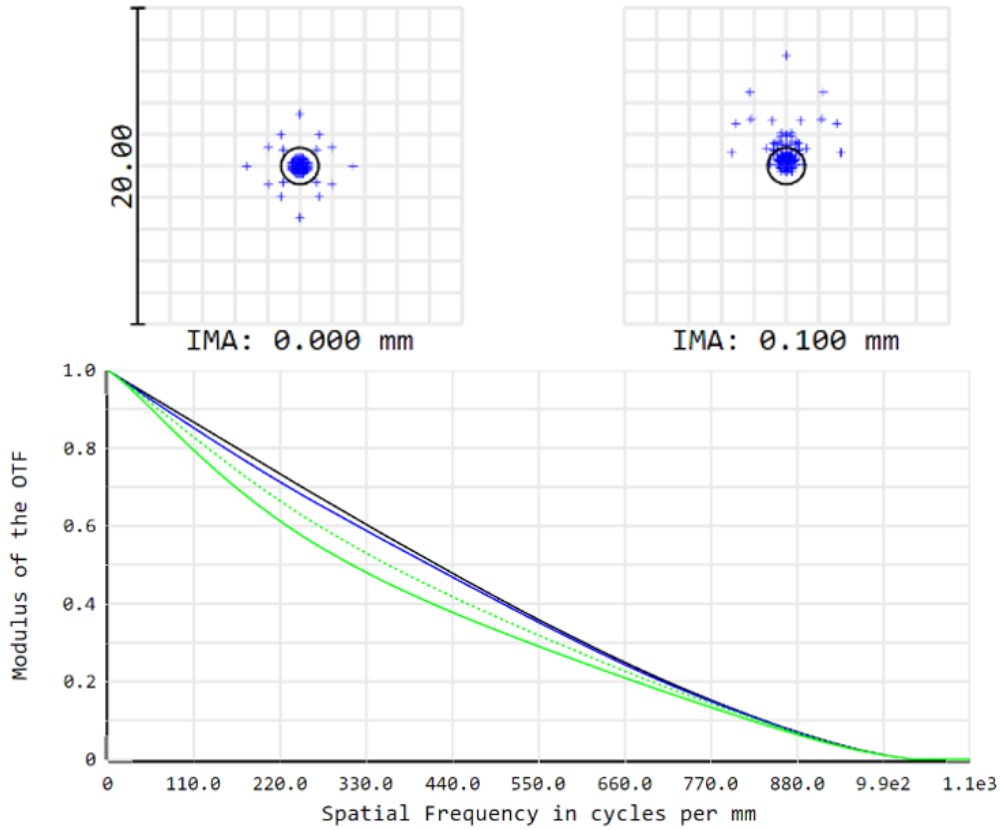


Figure 3.26: Expected performance of the high-resolution objective in the top imaging system. We simulate geometrical ray spot sizes (blue crosses) for on-axis imaging (top left figure) and for 100 $\mu$m off-axis imaging (top right figure), where the circles represent the diffraction limit. The bottom figure shows the simulated MTF, similar to Fig. 3.24. The objective is diffraction limited (black curve) for on-axis imaging (blue curve), with 0.025 $\lambda$ rms wavefront error, and nearly diffraction-limited for off-axis (green curves), with 0.146 $\lambda$ rms wavefront error. The leading residual aberration term is the 22$^{\text{nd}}$ Zernike polynomial.

mand lists (channel timings and settings) in Matlab, re-interpret them using LabView, and upload the command lists to the FPGA cards. Once triggered, the FPGA cards will independently execute the uploaded commands. LabView interface queries FPGA on-board clocks during their execution and we can send semi-synchronized (e.g. GPIB) commands to various instruments. The control code is modular and is based on simple hardware commands: digital line state and timing; analog line voltage and timing; analog line linear voltage ramp (resource efficient high-resolution steps) with beginning voltage, end voltage and timings; GPIB command and timing. Furthermore, we have an ability to do real-time on-board logic. For example, we can make all FPGA channels wait

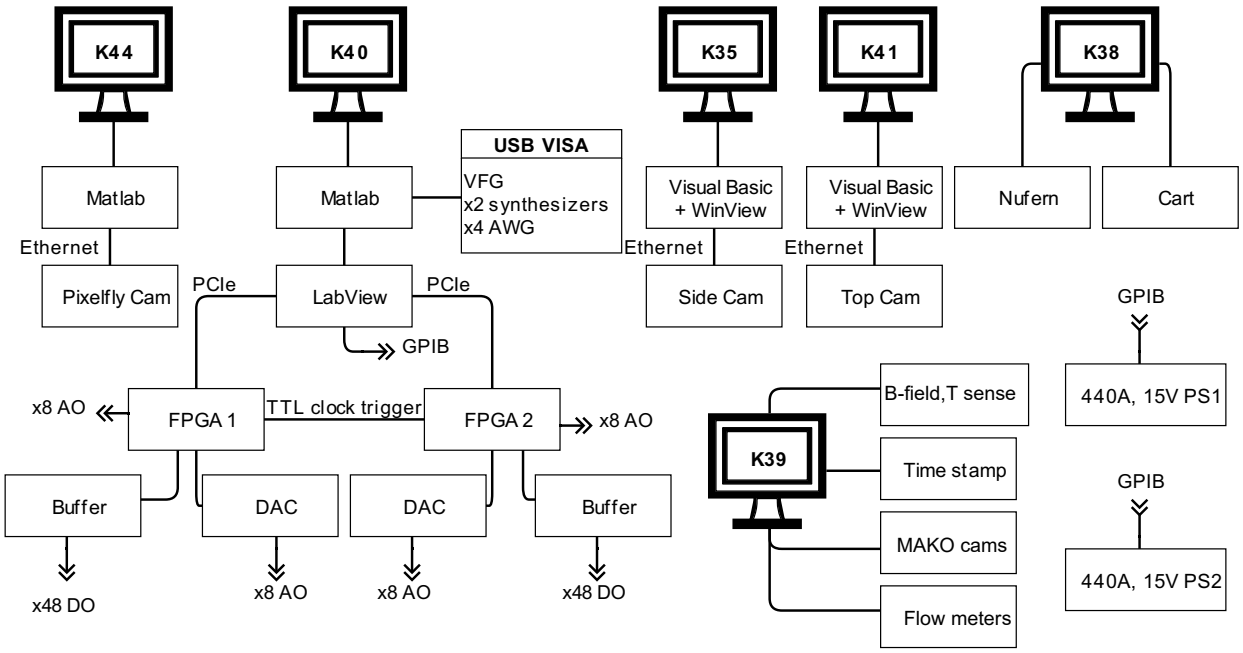


Figure 3.27: An overview of computer and hardware control. The main computer "K-40" programs FGPA cards and controls the majority of the experiment via analog output (AO), digital output (DO), GPIB, and USB lines. "K-40" control includes: magnetic coil power supplies (PS), synthesizers and VFG for RF antennas, and AWGs for optical dipole trap control. The "K-39" is used for sensing and recording laboratory conditions every experimental cycle, including: magnetic field near the chamber, the main coils and the science optical table temperatures, water cooling flow rates, optical trap alignment ($\times 3$ MAKO cameras), and the absolute time when experiment was run (an Arduino clock synchronized to NIST time). Note, two separate sensors (Colorado Sensors HT6130, not shown) record laboratory's temperature and humidity every 5 minutes; we have records dating back to 2013. The other computers are used for interfacing with imaging cameras, a cart motion controller and a Nufern laser amplifier. "K-44" computer is used as the main computer for image analysis. All lab instruments are triggered by FPGA TTL lines.

for an external trigger before proceeding, useful in instances such as triggering on the MOT fill level or synchronization to the 60 Hz line. Since FPGA cards also have digital and analog input capability, we did attempt to implement on-board digital PID loops for laser (e.g. locking to spectroscopy signals) and coil control (e.g. using a nonlinear gain profile to extend ppm-level field stability over a large dynamic range; hard to achieve with analog circuits). While somewhat successful, digital PID loops used too many on-board resources and were not as fast or as low-noise as our JILA analog PID loops. We abandoned any further attempts to implement digital PID loops on our main FPGA cards.

The FPGA digital output lines pass through buffers (Avago Technologies HCPL-0723 optocouplers) before being distributed around the lab. The 16 FPGA analog lines is not a sufficient amount and we resort to using two additional DACs (AD5360, 16-bit, 8 channel), sacrificing one digital port (8 digital lines) to program each DAC. The external DAC clocks are synchronized to FPGA clocks. Due to FPGA on-board resource overhead, we end up with a total of 96 digital (TTL) lines and 32 analog lines from two FPGA cards. While not currently implemented, we have previously used FPGAs to interface with high-resolution DACs (AD5191, 1ppm 20-bit) and ADCs (AD7767, 3ppm 24-bit).

We have five additional computers (see Fig. 3.27) for recording experimental conditions, data and image analysis, and for interfacing with various hardware. All laboratory instruments are triggered by the two FPGA cards.

# Chapter 4

## Precise Characterization of a Feshbach Resonance

Fano-Feshbach resonances offer an unparalleled ability to control interactions in quantum systems, and understanding their properties is essential. This chapter reviews our characterization of a Feshbach resonance with unprecedented precision. I begin with a short overview of different methods used in measuring Feshbach resonance properties and describe the advantage of using dimer dissociation spectroscopy. I then detail how we prepare pure molecular samples used in studies throughout this chapter. In the first study, I discuss how we use precision RF spectroscopy of dimer binding energies to locate the Feshbach resonance location $B_0$. The second study details molecular lifetime measurement and the observation of an unexpected lifetime maximum at a high binding energy.

### 4.1 Methods for Characterizing Feshbach Resonances

Most experimental studies rely on atom-loss measurements for locating Feshbach resonances [19]. In such studies, one records the atom-loss fraction (for a specific hold time) at different magnetic fields. Since the inelastic collision rate is presumed to be maximal at the resonance, the $B$-field value of maximal loss is taken to be the resonance position $B_0$. A complementary method, stemming from the two- and three-body nature of inelastic loss, relies on locating the maximal heating rate in a gas with inhomogeneous density. While these methods are easy to implement, imprecise knowledge of important details limits their validity and results only in rough estimations of resonance locations. For instance, the presence of Efimov physics and two-body bound states is

expected to complicate loss dynamics close to the resonance.

To demonstrate problems associated with these simplest methods, we used them to roughly locate our Feshbach resonance $B_0 \sim 34\,\mathrm{G}$. We prepared a sample of $5\times10^5$ atoms in the $|\mathrm{F}=1, \mathrm{m_F}=-1\rangle$ hyperfine state and temperature of 700 nK in a single-beam optical trap. The trap depth was raised by a factor of two to limit loss associated with evaporation. The initial magnetic field is $B = 41.8\,\mathrm{G}$, corresponding to a scattering length $a \sim 115\,a_0$. In the first experiment, we ramp the magnetic field to a new value in 2 ms and hold additional 20 ms before imaging. Due to enhanced three-body loss, significant atom loss and heating are prevalent near $B_0$, as shown in Fig. 4.1a. We fit the atom loss feature with a Gaussian function and extract its center to be at 32.8(1) G. In the second experiment, we ramp the magnetic field to a new value in 2 ms and vary the hold duration to take a lifetime measurement at each field. A fit to an exponential with a floating offset is sufficient to capture the decay dynamics. Fig. 4.1b shows the resulting lifetimes at different fields. A lack of a sharp signal in both of these measurements (related to the resonance width $\Delta B$) and the asymmetry of the loss features (three-body loss is inherently asymmetric about $B_0$ and is complicated by Efimov features) lead to only a rough measurement of $B_0$.

Methods based on elastic properties are considered better and more sensitive for locating Feshbach resonance centers. For example, measurements using the anisotropic expansion of an interacting gas [32, 21] and cross-thermalization methods [97] allowed several groups to significantly improve on prior results. Methods using RF spectroscopy to measure mean-field related frequency shifts enable one to extract the amplitude and sign of the elastic scattering length $a$ near $B_0$ [98]. While these methods are better than those based on inelastic properties, systematic shifts at high temperatures [99] and beyond-mean-field effects at high $na^3$ [100] limit their applicability. Furthermore, examples of inconsistent results, such as in Refs. 32 and 21, obtained by the same method, are troublesome.

The most accurate methods for characterizing Feshbach resonances rely on measuring the Feshbach dimer state. This molecular state intersects the free-atom continuum at $B_0$ and its

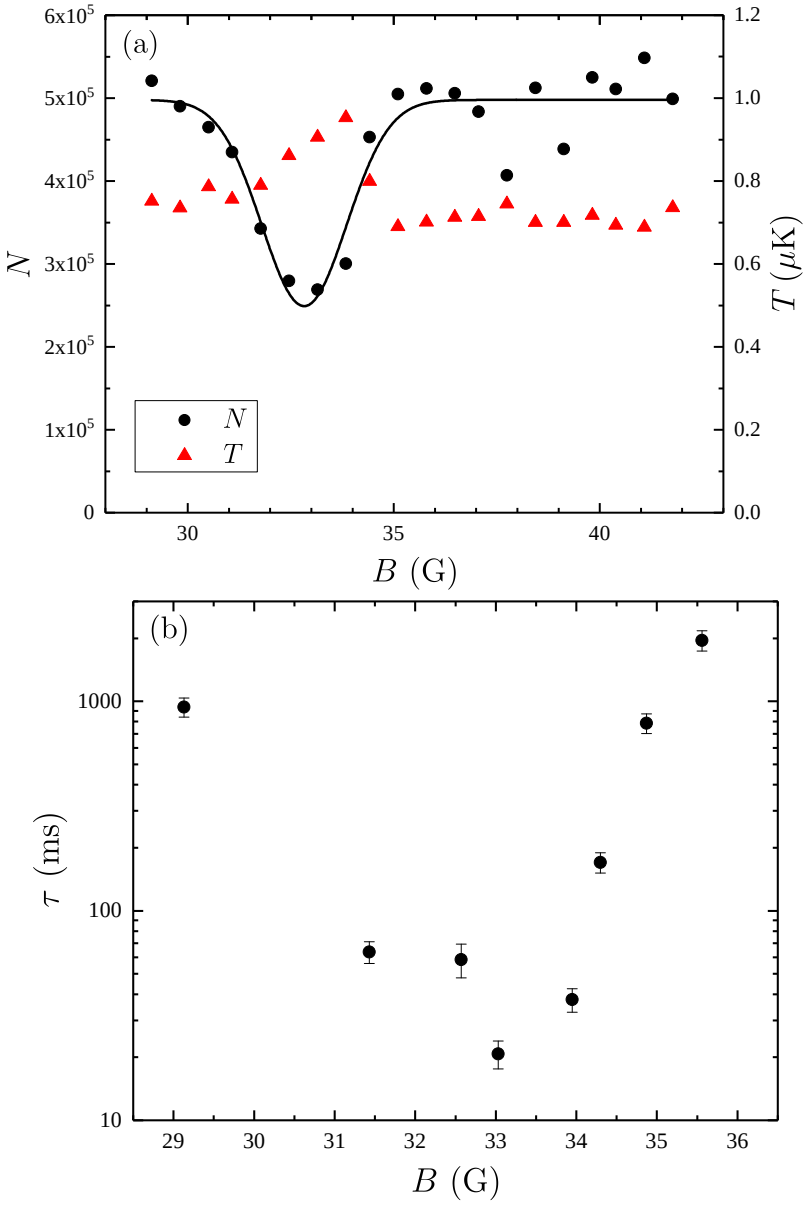


Figure 4.1: A rough measurement of the Feshbach resonance center $B_0$ using two different methods. In both methods we start with a weakly interacting gas and ramp the magnetic field from 41.8 G (115 $a_0$) to a $B$ value of interest in 2 ms. In the first method (a), we hold the sample at varied $B$ for 20 ms and observe significant atom loss and heating near the expected $B_0$. Using a Gaussian fit to atom number, we can roughly extract $B_0 \sim 33$ G. In the second method (b), we observe a reduction in the atom lifetime near the expected $B_0$. Both methods are crude for the extraction of $B_0$.

binding energy is approximated by a simple universal expression

$$E_b = \frac{\hbar^2}{ma^2}, \tag{4.1}$$

where $a > 0$. There are three methods based on Feshbach dimers for extracting $B_0$: magnetic sweep across the Feshbach resonance, the crudest; dimer association, a better method; dimer dissociation, the most precise method. The simplest, yet coarse, method involves measuring the onset of the molecular state by magneto-association of dimers. In this thesis, I use the term "magneto-association" to refer to ramping the scattering length from $a < 0$ to $a > 0$, such that some atoms are adiabatically swept into the molecular state. During this association process, one observes a dip in the atom number near $B_0$ [101]. While we do utilize magneto-association in our work, we only do so for purposes of populating the molecular state and not for the purpose of extracting an accurate $B_0$ value. Precise methods for extracting $B_0$ rely on direct measurements of dimer binding energies. In our work, we use magneto-association to prepare a molecular sample and use RF dissociation spectroscopy to probe dimer binding energies. Spectroscopic methods based on molecular association, such as Ramsey interferometry [102, 103] and magnetic-field modulation spectroscopy [104, 105, 106, 107, 108, 40, 99], also enable determination of $E_b$ values. However, due to the complex interdependence between conditions (e.g. atom temperature, phase space density and mean-field energy) and the signal (e.g. its contrast, center and spectral width), limits the accuracy of molecular association spectroscopy method. Hence, we resort to RF dissociation spectroscopy.

RF dissociation spectroscopy overcomes many limitations present in association spectroscopy and enables accurate determination of molecular binding energies [109]. Unlike in other methods, the signal contrast is only limited by the number of molecules in the sample (in the absence of unpaired atoms) and does not depend on the density, phase space density or collisional processes. Additionally, temperature-dependent shifts are absent and mean-field related shifts can be negligible in a low density gas. The spectral resolution is only limited by molecular lifetimes and the magnetic field stability. Precise dissociation spectroscopy enabled accurate characterization of Feshbach

resonances for many species [101, 110, 13, 20, 111, 112]. Recent work of Ref 20 measured a Feshbach resonance location in $^6$Li with an unprecedented precision. Our measurement in $^{39}$K attempts to do even better.

## 4.2 Magneto-Association of Feshbach Molecules

### 4.2.1 Populating the Dimer State

We use magneto-association method [101, 113] to create a macroscopic population of Feshbach dimers for use in our $E_b$ measurements. This technique enables high atom-dimer conversion efficiencies, reaching 50% for Bose gases [114], 90% for Fermi gases [114] and 50% for quantum mixtures (90% in a 3-D lattice [115]). While other methods [116] can also be efficient, historically, the magneto-association method has resulting in largest molecular populations. We need $10^3$–$10^4$ Feshbach dimers to provide an adequate signal for precision $E_b$ spectroscopy. We carefully consider our initial conditions and experimental procedures during magneto-association to produce the maximum molecular population. For example, while the atom-dimer conversion efficiency increases with the phase space density, the atom loss also increases with the phase space density, thereby we need to find a balance.

The general scheme of magneto-association relies on adiabatic transfer of atoms in the monomer (unpaired) state into the Feshbach dimer state via a Landau-Zener–type process, as depicted in Fig. 4.2. There are several important timescales that one must consider during this process. When changing from $a > 0$ to $a < 0$, using the fastest possible ramp rate $\dot{B}$ (in units of G/s) is important in order to limit the duration the gas spends at high $a$ values, where inelastic losses are high. The three-body loss rate $L_3$, scaling as $a^4$, and the two-body loss rate $L_2$ (present since the $|\mathrm{F} = 1, \mathrm{m_F} = -1\rangle$ state is not the absolute ground state at non-zero magnetic field), scaling as $a^2$ can limit the sample's lifetime to millisecond timescales even at modest atomic densities of $n \sim 10^{11}\,\mathrm{cm}^{-3}$ (note that $L_3$ and $L_2$ values are capped by finite $n$ or $T$ at unitarity, deviating from their respective $a^4$ and $a^2$ scaling). More concretely, $L_2$ and $L_3$ lead to loss of the form (also

see Ch. 5):

$$\frac{1}{N}\frac{dN}{dt} = -L_2\langle n\rangle - L_3\langle n^2\rangle, \tag{4.2}$$

where $\langle n\rangle = \frac{1}{N}\int n^2(\vec{x})d^3x$ and $\langle n^2\rangle = \frac{1}{N}\int n^3(\vec{x})d^3x$. While performing magneto-association at higher temperatures (see Sec. 5.2 and Fig. 4.3) and lower densities can help limit inelastic loss, molecular association efficiency favors high phase-space density [114]; leading to contradicting requirements for conditions. Additionally, the association probability depends on the Feshbach resonance parameters $a_{\mathrm{bg}}$ and $\Delta B$, the ramp rate $\dot{B}$ and density $n$:

$$P = P_{\max}\left(1 - \exp\left(-\frac{\alpha n\hbar}{m}\left|\frac{a_{\mathrm{bg}}\Delta B}{\dot{B}}\right|\right)\right), \tag{4.3}$$

where $P_{\max}$ is the maximum association efficiency possible and $\alpha$ is a dimensionless resonance-dependent parameter [114, 19]. Overall, for $a > 0$ to $a < 0$ sweep, one desires a fast magnetic field ramp to limit inelastic loss; for $a < 0$ to $a > 0$ sweep, one desires a slow magnetic field ramp to efficiently/adiabatically transfer atomic population to the dimer state via a Landau-Zener–type process.

We begin with a thermal sample with few-$10^5$ atoms, temperature around 300 nK and $a \sim 300\,a_0$. In order to get the desired final molecule density, temperature and number, we vary the initial atom number and temperature by changing the parameters of the last evaporation stage. While the initial phase space density is chosen to be $\mathcal{O}(1)$ to ensure a high atom-dimer conversion efficiency, we verify that the condensate fraction is small or vanishing. A large condensate fraction would result in high number loss and heating upon the preliminary ramp to negative $a$ values, before the magneto-association ramp [117]. Prior to jumping across $|a| \to \infty$, we perform a preliminary ramp to $B = 35.76\,\mathrm{G}$ $(480\,a_0)$, a convenient value for our spin-purification procedure: we get rid of $|\mathrm{F} = 1, \mathrm{m_F} = 0\rangle$ atoms that contaminate our dimer spectroscopy at low $E_b$ values. Performing the purification procedure after association would add extra time and result in a larger loss of molecules; further details are discussed in Sec. 4.4.

To magneto-associate dimers, we first ramp the magnetic field from $B = 35.76\,\mathrm{G}$ $(a = 480\,a_0)$ to $B = 19.8\,\mathrm{G}$ $(a = -90\,a_0)$ in 1 ms (see Fig. 4.2). We can get an idea of timescales required for

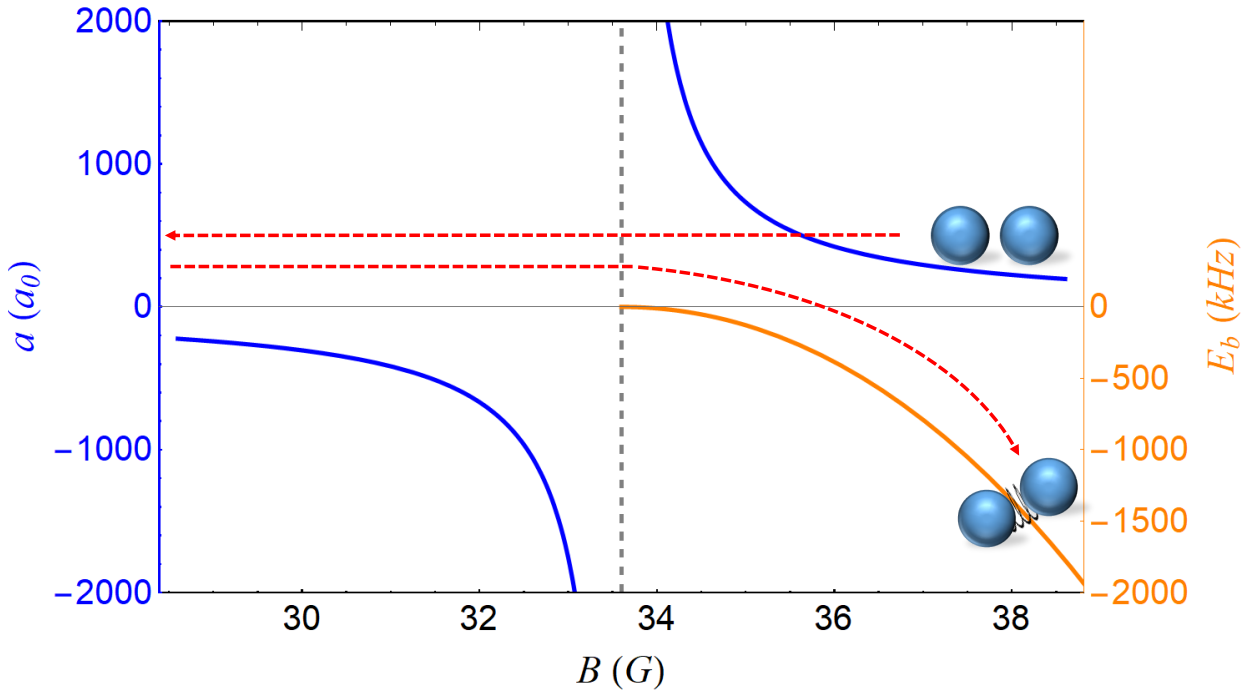


Figure 4.2: Illustration of magneto-association of Feshbach dimers near the $B_0 = 34\,\mathrm{G}$ resonance (dashed vertical line) in $^{39}$K hyperfine state $|\mathrm{F} = 1, \mathrm{m_F} = -1\rangle$. Two unpaired atoms are adiabatically transferred to the molecular state by magnetic field ramps (dashed red arrows).

our conditions by solving the coupled-equations describing three-body atom loss and heating (we focus on the $L_3$ part of Eq. 4.2) [118]:

$$\frac{1}{N}\frac{dN}{dt} = -L_3\langle n^2\rangle, \tag{4.4}$$

$$\frac{1}{T}\frac{dT}{dt} = \frac{1}{3}L_3\langle n^2\rangle, \tag{4.5}$$

where now we introduce a time-dependent three-body loss coefficient $L_3 = L_3\left(T\left(t\right), a\left(t\right)\right)$ (taken from the finite-temperature theory of Ch. 5) and time-dependent scattering length $a\left(t\right) = a\left(B\left(t\right)\right)$. For example, typical initial conditions of $3\times10^5$ atoms, $T = 250\,\mathrm{nK}$ and a mean trapping frequency of 57 Hz, using a 10 ms magnetic field ramp leads to significant atom loss and heating, as depicted in Fig. 4.3. However, using a 1 ms magnetic field ramp instead of a 10 ms ramp would increase the final atom number by almost 50% and lead to negligible heating. While ramps durations $\ll 1\,\mathrm{ms}$ would be desirable, the inductance of our Feshbach coils limits large $B$–field jumps to a $\sim 0.5\,\mathrm{ms}$ timescale. We also use such estimates to get an idea of the three-body loss timescales during the magneto-association ramp (from $a < 0$ to $a > 0$), where the ramp must be performed slow enough according to the adiabaticity criterion in the Landau-Zener–type process (Eq. 4.3).

After jumping to $a < 0$, we subsequently populate the dimer state by ramping back to $B = 35.76\,\mathrm{G}$ ($a = 480\,a_0$), a specific value chosen for atom-cleaning procedure described in 4.4. We can use the Laundau-Zener formula Eq. 4.3 to estimate how slow we need to perform the molecular-association ramp to be adiabatic. Using a typical density of $\langle n\rangle = 8\times10^{11}\,\mathrm{cm}^{-3}$, $\Delta B = 55\,\mathrm{G}$, $a_{\mathrm{bg}} = -19.7\,a_0$ and $\alpha = 276$ (where we took $\alpha$ value from $^{85}$Rb [114], as we don't know the value for $^{39}$K), we predict that an inverse ramp rate of $\dot{B}^{-1} = 55\,\mu\mathrm{s/G}$ would result in $P/P_{\mathrm{max}} = 67\%$ efficiency. We confirm the Landau-Zener model for Feshbach association by comparing predictions to experimental data. We look at the number of molecules produced as we vary the inverse ramp rate $\dot{B}^{-1}$, keeping the starting and final magnetic field values unchanged. Fig. 4.5 shows a good agreement between theory and the data for fast ramps. However, ramps with $\dot{B}^{-1} > 500\,\mu\mathrm{s/G}$, corresponding to ramp durations $> 7.4\,\mathrm{ms}$, are affected by loss processes not accounted for by Eq. 4.5 (e.g. atom-dimer and dimer-dimer inelastic collisions, loss from dimer spin relaxation) and

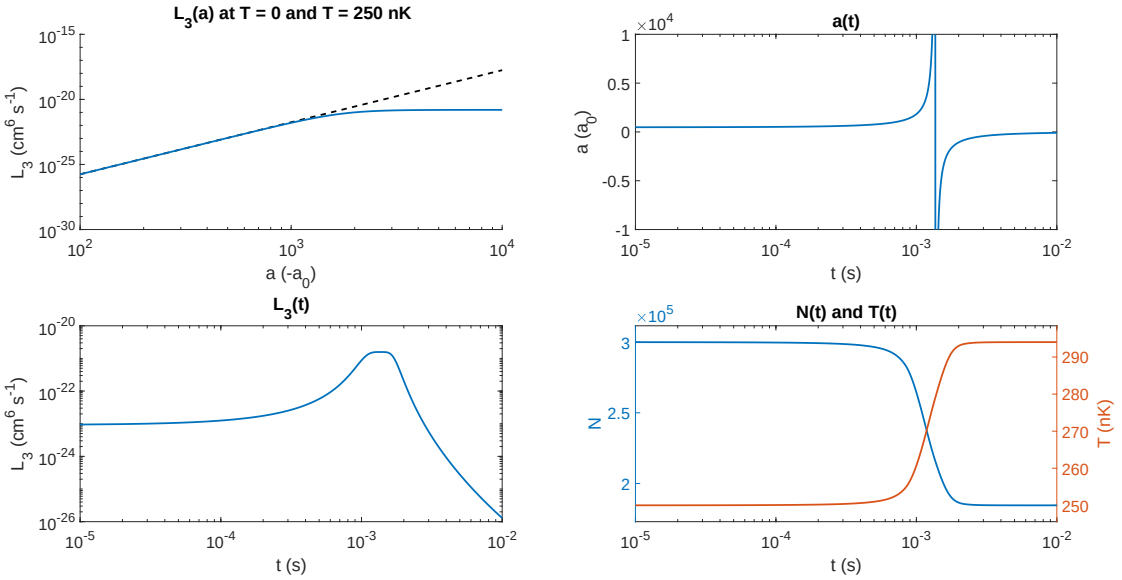


Figure 4.3: Estimating the impact of three-body loss on the atom population and temperature during a 10 ms $B$–field ramp from $B = 35.76$ G to $B = 19.8$ G. Here, we ignore the Efimov structure in $L_3$, which modulates the $a^4$ scaling, see Ch. 5. The top-left figure shows that $L_3$ saturates at high scattering lengths due to finite-temperature effects (note we us an artificial scenario: thermal Bose cloud with $T = 0$). Top-right and bottom-left figures show instantaneous $a\,(t)$ and $L_3\,(t)$, respectively. The bottom-right figure shows the predicted atom decay and heating during the $B$–field ramp, as predicted by solving coupled-equations in Eq 4.5.

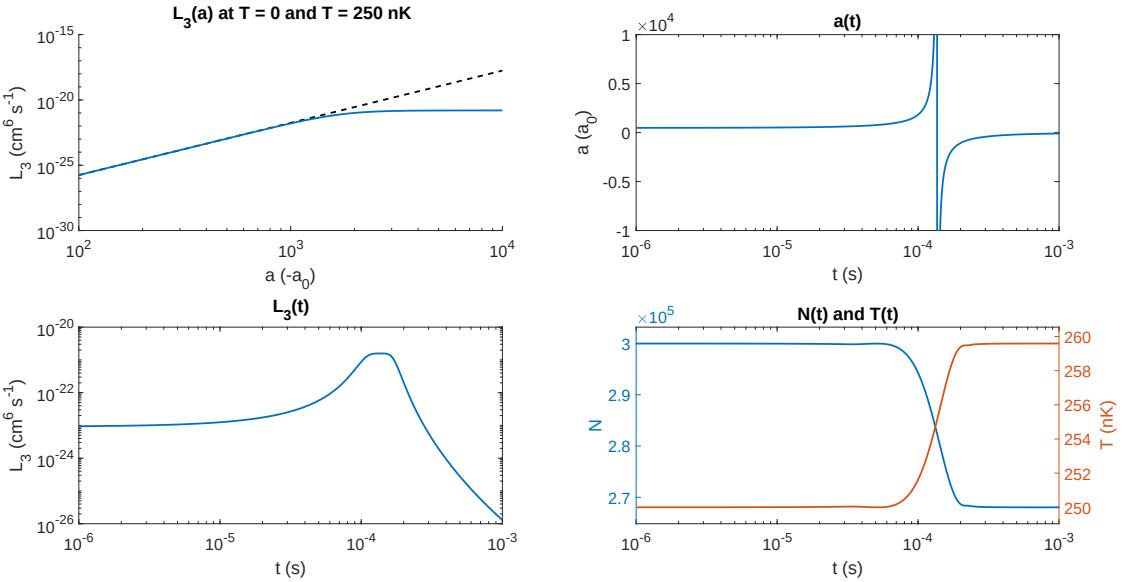


Figure 4.4: Estimating the impact of three-body loss on the atom population and temperature during a 1 ms $B$–field ramp from $B = 35.76$ G to $B = 19.8$ G, similarly to Fig. 4.3. Atom loss and heating associated with three-body loss is significantly smaller for 1 ms ramp than for 10 ms $B$–field ramp.

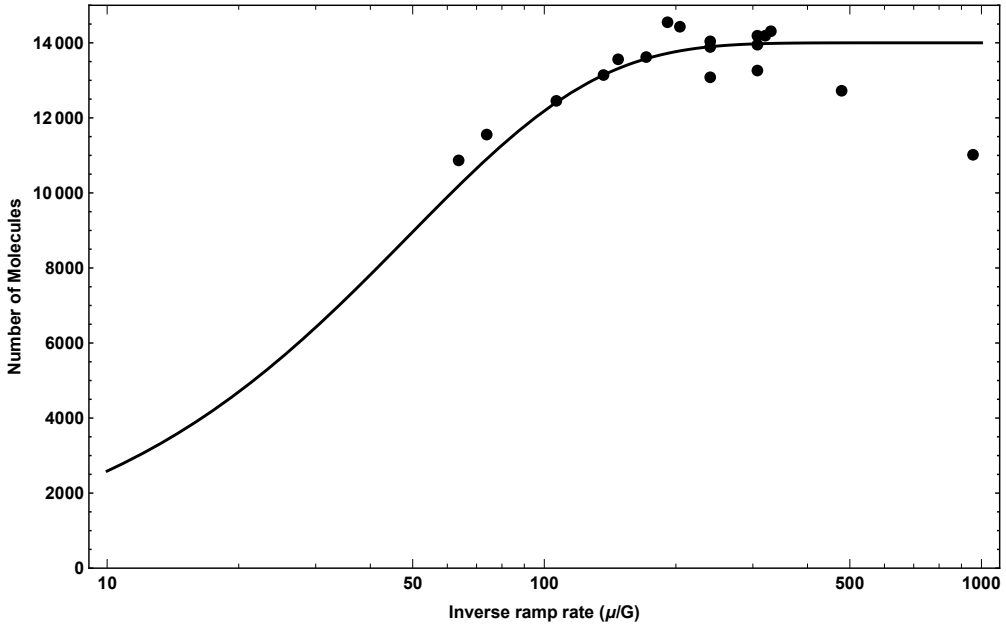


Figure 4.5: Comparing experimental data (points) to predictions of Landau-Zener–type process (Eq. 4.3) for magneto-association of Feshbach dimers. The conversion efficiency at large inverse ramp rates $\dot{B}^{-1}$ is affected by atom-dimer, dimer-dimer and dimer spin relaxation loss processes.

strong deviations from the simple model are expected.

### 4.2.2 Optimizing Molecular Number and Preliminary Detection Schemes

Due to short molecular lifetimes and low signal, detection of Feshbach molecules is no easy task. Our first attempts to create and directly detect Feshbach dimers resulted in a poor signal of only $\sim 200$ molecules and 50 mOD. To get a sufficient signal for precision RF spectroscopy, we had an iterative process of switching between different detection methods and improving the molecular number.

The biggest improvement in molecule number resulted from altering our optical trap configuration. We saw our first molecular signal in a crossed-dipole trap with the horizontal beam waist of $28\,\mu\text{m} \times 28\,\mu\text{m}$ and the vertical beam waist of $28\,\mu\text{m} \times 220\,\mu\text{m}$, forming a spherical potential with a trapping frequency of $2\pi \times 432\,\text{Hz}$. This configuration enabled reaching PSD $= 1$ with $N = 7 \times 10^4$ atoms at $T = 700\,\text{nK}$, corresponding to $n_{\text{peak}} = 4 \times 10^{13}\,\text{cm}^{-3}$. Such a high density results in very fast timescales for three-body loss and leads to a significant number loss and heating

(to $T = 1.3\,\mu$K), even for our fastest ramp speeds. Additionally, high density atomic samples result in short molecular lifetimes, limited by inelastic atom-dimer collisions, rendering RF dissociation spectroscopy useless since it requires moderate interrogation times even at full 20 W RF power.

We significantly increased our molecule number by reducing atom density. In our first attempt to do so, we used only a horizontal beam (waist $28\,\mu\text{m} \times 28\,\mu\text{m}$ and trapping frequencies $(\omega_x, \omega_y, \omega_z) = 2\pi \times (3, 306, 306)$ Hz) to prepare an atomic sample with $n_{\text{peak}} = 4 \times 10^{12}\,\text{cm}^{-3}$. While this configuration successfully created $\sim 10^4$ molecules, the signal was poor due to a small optical density along the imaging direction $y$. The next iteration included a $28\,\mu\text{m} \times 28\,\mu\text{m}$ horizontal beam with a $140\,\mu\text{m} \times 800\,\mu\text{m}$ vertical beam, resulting in an atomic density $n_{\text{peak}} = 1 \times 10^{13}\,\text{cm}^{-3}$ and 5000 molecules. We settled on the final optical trap configuration: horizontal sheet beam with a waist of $80\,\mu\text{m} \times 810\,\mu\text{m}$ and a vertical beam with a waist of $140\,\mu\text{m} \times 140\,\mu\text{m}$ (e.g. with typical trapping frequencies $(\omega_x, \omega_y, \omega_z) = 2\pi \times (30, 30, 120)$ Hz), which turn on as the loading beam $28\,\mu\text{m} \times 28\,\mu\text{m}$ is ramped off during the evaporation. With the new trap we are able to associate $\sim 2 \times 10^4$ molecules, with 10–20% association efficiencies, from an atomic gas of $n_{\text{peak}} = 4 \times 10^{12}\,\text{cm}^{-3}$ and have a good signal for spectroscopy. We can vary the molecular number, temperature and density by changing evaporation parameters prior to the magneto-association procedure.

Our first signature of molecules was an observed dip in atomic number near $B_0$ as we performed the magneto-association procedure, as depicted in Fig. 4.6. The magnetic field is ramped from $B > B_0$, where $a > 0$, to a varied $B$–field value and then back to a final value $B > B_0$ where the sample is held before imaged. Both ramps are performed with fixed speeds for consistency, relating to Landau-Zener and three-body loss timescales. In such scenario, a fraction of the atomic population is transferred to the dimer state when the varied $B$–field value crosses $B_0$. The final $B$–field is chosen such that the atomic lifetime without such ramps is on order of seconds, easily achieved with $a < +500\,a_0$ even with moderate densities. Finally, after a hold time at the final field, the magnetic field is ramped to a low value, thereby dissociating molecules, and the remainder population (consisting of atoms and dissociated molecules) is imaged. There are two decay timescales: a fast decay $\mathcal{O}(1\,\text{ms})$, resulting from spontaneous dimer decay, atom-dimer and

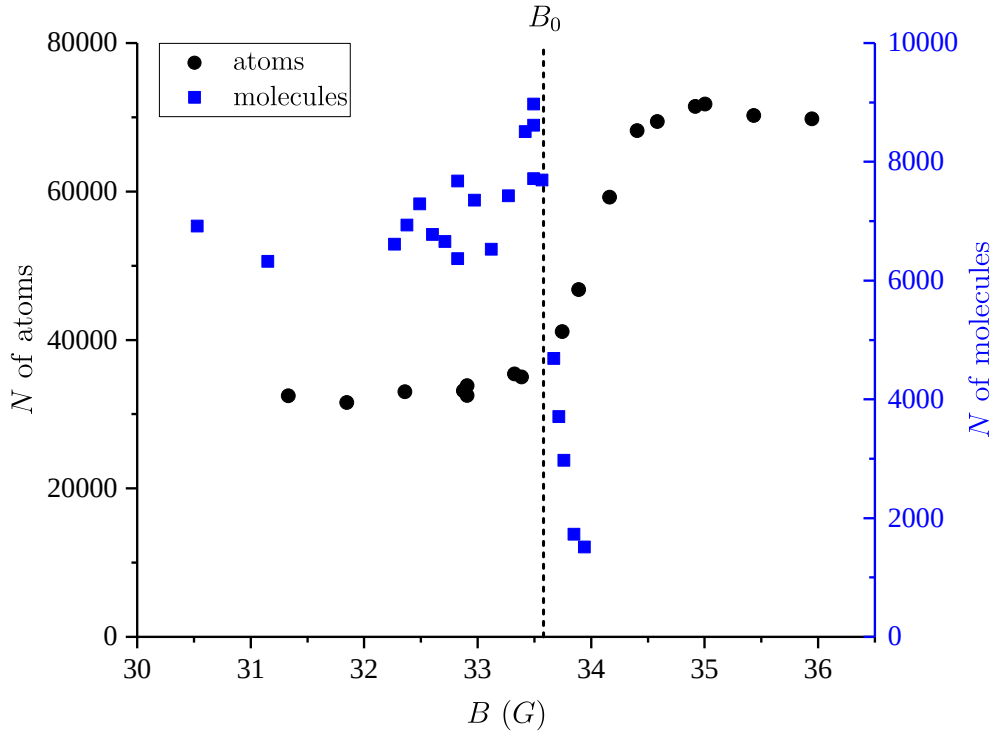


Figure 4.6: Atom number dip (dots) near a nominal $B_0$ (dashed) is evidence of molecular formation during the magneto-association process, supported by direct detection of molecular population (squares) via RF spectroscopy.

dimer-dimer inelastic collisions; a slow decay $\mathcal{O}$(s) dictated by monomer lifetime. After waiting a sufficient time for the fast decay to cease, one sees a dip in atomic number as the varied $B$–field value becomes $< B_0$, a signature of the molecular state. We later confirmed the conclusion from the indirect technique with the direct detection (using RF dissociation) of molecules, shown as blue squares Fig. 4.6. Initially, the indirect technique proved to be easier for detecting molecules than via direct spectroscopic techniques, where variables such as RF duration, power, and frequency must be properly chosen.

RF association of molecules is another useful technique that helped us figure out the correct parameters for RF dissociation spectroscopy. Specifically, it helped us to roughly map out the molecular binding energies, and hence RF frequencies at various magnetic field values. Unlike in RF dissociation spectroscopy, one does not need to worry too much about the RF pulse duration for RF association spectroscopy, even for short molecular lifetimes, as the baseline signal comes

from atomic population. The association technique is of most use when dealing with Feshbach resonances of narrow and intermediate width (see Sec. 4.5.3), where the universal relation Eq. 4.1 cannot accurately predict $E_b$. We start with a monomer gas in the $|\mathrm{F}=1,\mathrm{m_F}=-1\rangle$ state and use an auxiliary coil to apply field modulation in parallel direction as the field created by the main Feshbach coils. We modulate the field for 10 ms at fixed modulation frequency fixed while varying the magnetic field of the main coils. Molecules are associated when $E_b(B) = hf_{\mathrm{mod}}$ and are quickly lost due to spontaneous decay and inelastic atom-dimer collisions, resulting in a dip in the imaged atom population at a particular magnetic field, as depicted in Fig. 4.7a. We also take RF-association spectra at two different magnetic fields, as depicted in Fig. 4.7b, allowing us to extract $E_b$. While this technique is able to retrieve $E_b$ values in rough agreement with the values predicted by the coupled-channel theory and provide guidance for RF dissociation spectroscopy, this technique suffers from a non-trivial asymmetric lineshape (associated with the non-symmetric modulation in $a$), systematic temperature shifts (resulting from a thermal distribution of the monomer gas) and a complicated relationship between signal contrast, feature width, modulation amplitude and temperature.

## 4.3 RF Dissociation Spectroscopy

### 4.3.1 Understanding Molecular Dissociation Spectra

The RF dissociation spectroscopy of Feshbach dimers is a well-understood technique [109] and is relatively immune to systematic shifts (e.g. from finite-temperature and photon momentum recoil), enabling us to precisely measure $E_b$ values. With a sufficiently low molecular density ($n_{\mathrm{mol}}a^3 \ll 1$), our pure molecular gas (see Sec. 4.4 on how we achieve this) can be described as an ensemble of two-atom states, initially in the bound state $|\psi_{\mathrm{mol}}\rangle$. The state $|\psi_{\mathrm{mol}}\rangle$ has an energy that is $E_b$ less than the energy of two non-interacting atoms in the $|\mathrm{F}=1,\mathrm{m_F}=-1\rangle$ hyperfine state (see Fig. 4.8a) and has a spatial extent $\mathcal{O}(a)$, described by the wavefunction $\langle r\,|\,\psi_{\mathrm{mol}}\rangle = \sqrt{\frac{2}{a}}e^{-r/a}$. We use an RF pulse to break the pair by transferring one its atoms to the $|\mathrm{F}=2,\mathrm{m_F}=0\rangle$ state (see

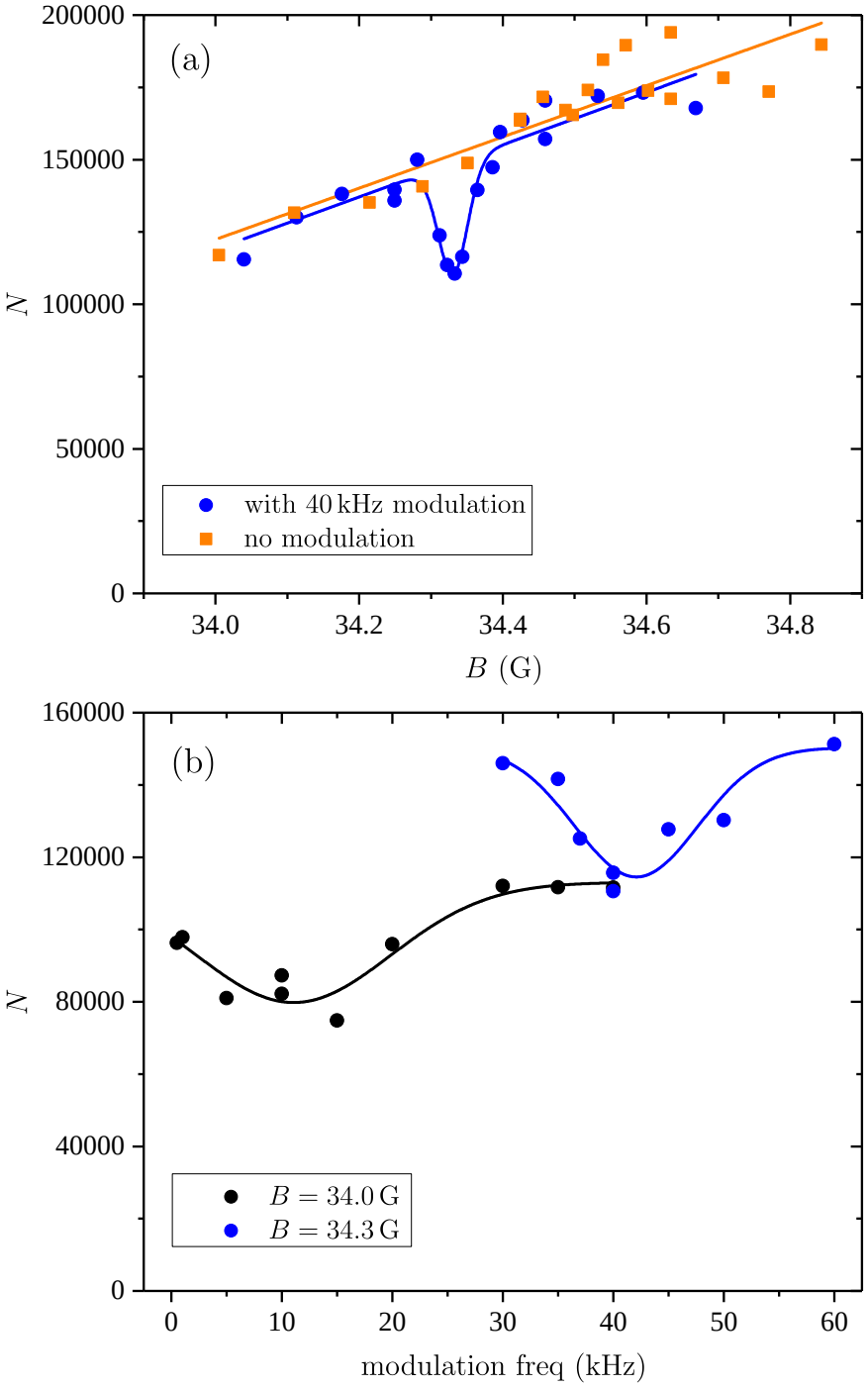


Figure 4.7: RF association of molecules by field modulation. (a) Field modulation with a fixed frequency of 40 kHz, peak amplitude of 115 mG and 10 ms modulation duration. A dip in the total number occurs when $E_b(B) = hf_{\mathrm{mod}}$, occurring at $B = 34.3$ G when fitted with a sloped Gaussian function, where the slope arises from increased three-body loss near $B_0$. This result is close to the value $E_b(34.3\,\mathrm{G}) = 41.8$ kHz we later obtained using RF dissociation spectroscopy. (b) RF association spectra at two different fields, with modulation peak amplitude of 250 mG and 10 ms duration. We extract $E_b(34.0\,\mathrm{G}) = 11(1)$ kHz and $E_b(34.3\,\mathrm{G}) = 42(1)$ kHz from Gaussian fits, while coupled-channel predicts $E_b(34.0\,\mathrm{G}) = 15.2$ kHz and $E_b(34.3\,\mathrm{G}) = 46.5$ kHz.

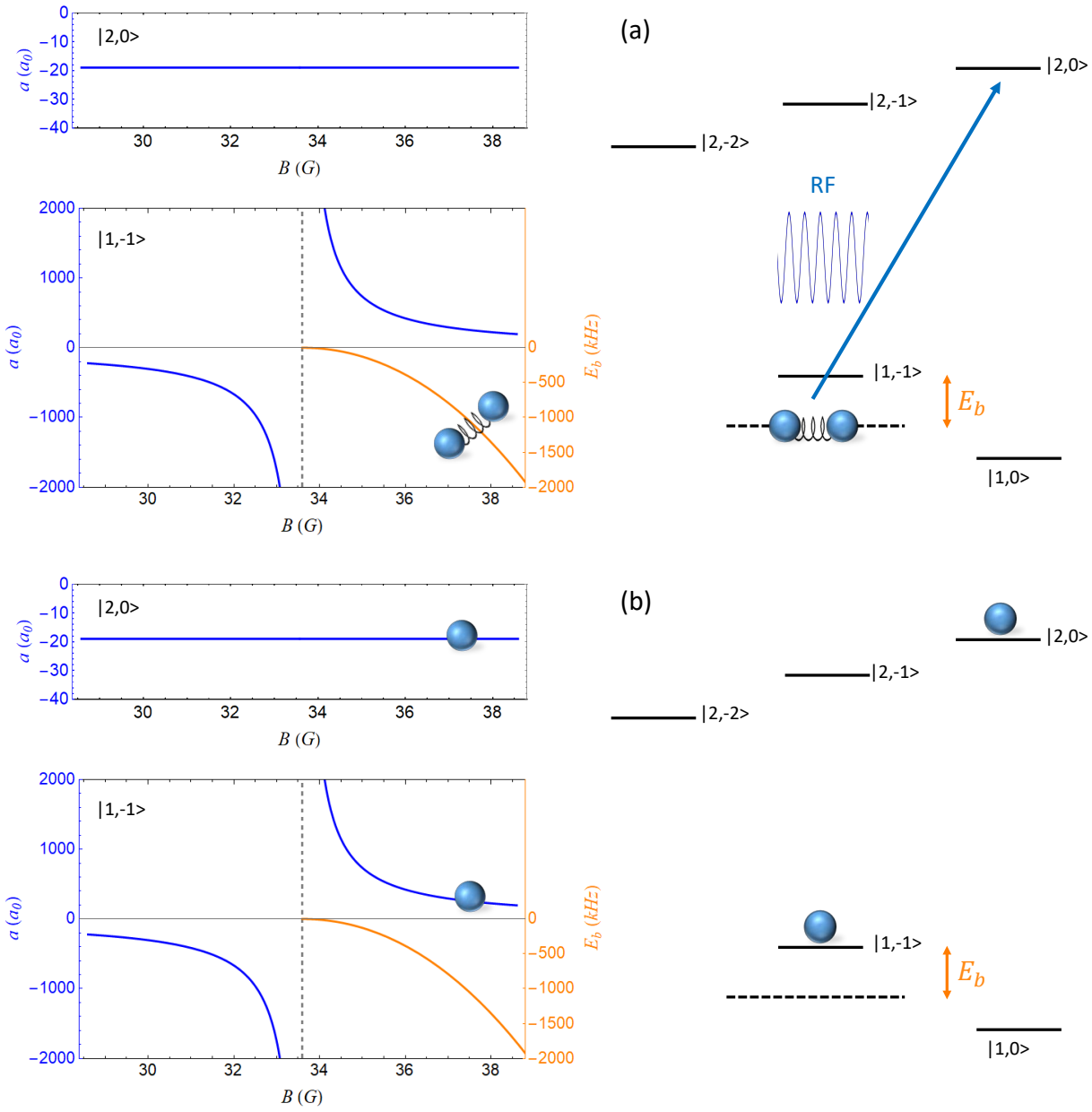


Figure 4.8: Initial (a) and final (b) states in the dimer dissociation procedure. The initial state is a molecular state with binding energy $E_b$. The final state has one atom in the $|\mathrm{F}=2,\mathrm{m_F}=0\rangle$ hyperfine state and the other in $|\mathrm{F}=1,\mathrm{m_F}=-1\rangle$.

Fig. 4.8b), when RF photon energy $E_{\rm RF} \geq E_{\Delta \rm m} + E_b$, where $E_{\Delta \rm m} = \left(E_{|\rm F=2,m_F=0\rangle} - E_{|\rm F=1,m_F=-1\rangle}\right)$ is the Zeeman energy difference of the two undressed states (for us $E_{\Delta \rm m} = 446$–$447\,\rm MHz$ in the vicinity of $B_0$). Since our final state scattering length $a_f = -19\,a_0 < 0$, the final state cannot support any bound states and must be a superposition of scattering states $|\psi_K\rangle$, described by the wavefunction $\langle r\,|\,\psi_K\rangle = \sqrt{\frac{m}{\pi k \hbar^2}}\sin(kr + \delta_f)$, where $\delta_f$ is the scattering phase shift in the final channel and $\hbar^2 k^2/m$ is the excess energy given to the pair by the RF photon when $E_{\rm RF} > E_{\Delta \rm m} + E_b$. Assuming the photon imparts a negligible momentum on the atoms (true for RF frequencies), $a \gg \bar{a} = 61.65\,a_0$ (the mean scattering length of the van der Waals potential), RF detuning energy $\Delta E_{\rm RF} = E_{\rm RF} - E_{\Delta \rm m} \gg \hbar^2/m\bar{a}^2$, the molecular decay is negligible for the duration of the RF pulse and $a^2 \gg a_f^2$, we can solve for the dissociation rate of this bound-free transition [109]:

$$\Gamma = \frac{2\pi}{\hbar}\left|\left\langle \psi_K \left| \frac{\hbar\hat{\Omega}}{2} \right| \psi_{\rm mol} \right\rangle\right|^2 = \frac{h\Omega^2}{2}\left|\langle \psi_K\,|\,\psi_{\rm mol}\rangle\right|^2, \tag{4.6}$$

where $\Omega$ is the atom-atom bare Rabi frequency (in Eq. 4.6 we also assume RF power is small compared to $\Omega$) and $|\langle \psi_K\,|\,\psi_{\rm mol}\rangle|^2 = F(\Delta E_{\rm RF})$ is the Franck-Condon factor (per unit energy)

$$F(\Delta E_{\rm RF}) = \frac{2}{\pi}\left(1 - \frac{a_f}{a}\right)^2 \frac{\sqrt{\Delta E_{\rm RF} - E_b}\sqrt{E_b}}{\left(\Delta E_{\rm RF}\right)^2}, \tag{4.7}$$

that determines the shape of the dissociation spectra. Since there are no final bound states for $a_f < 0$, normalization leads to $\int_0^\infty F(\Delta E_{\rm RF})\,d\Delta E_{\rm RF} = 1$ for all spectra. Transitions are forbidden for RF detunings $\Delta E_{\rm RF} < E_b$ and have maximum rate at $\Delta E_{\rm RF} = \frac{4}{3}E_b$, as shown in Fig. 4.9. The maximum amplitude of the Franck-Condon factor and the sharpness of the feature near $E_b$ depend on the absolute value of $E_b$.

The real dissociation spectrum involves counting the number of molecules dissociated for a particular RF detuning and pulse duration $\tau$:

$$\begin{aligned} N_{\rm mol}(\Delta E_{\rm RF}, \tau) &= \tau\Gamma(\Delta E_{\rm RF}) \\ &= \tau\frac{h\Omega^2}{2}F(\Delta E_{\rm RF}), \end{aligned} \tag{4.8}$$

where $\tau\Omega^2$ is proportional to the irradiating pulse energy. We check the relations $N_{\rm mol} \propto F(\Delta E_{\rm RF}$ (see Fig. 4.10a and 4.10b) and $N_{\rm mol} \propto \tau\Omega^2$ (see Fig. 4.10c), by taking dissociation spectra at con-

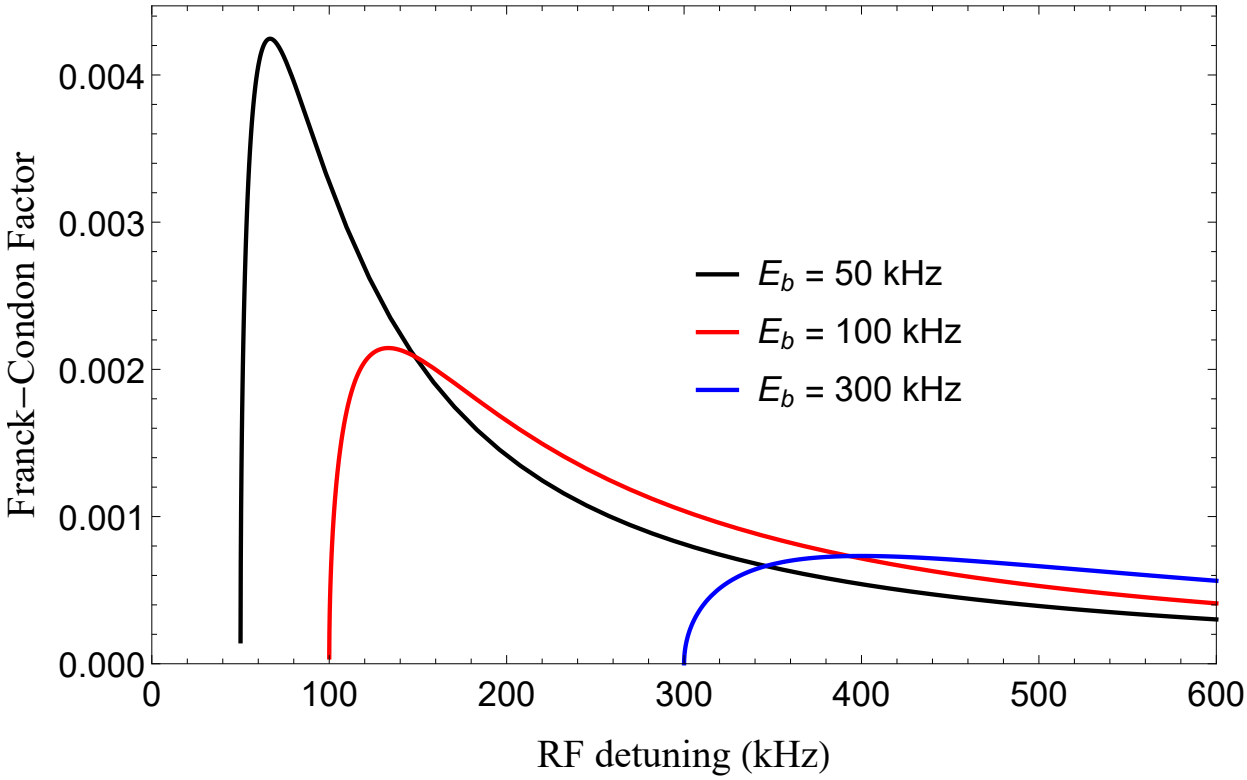


Figure 4.9: Franck-Condon factor at different binding energies as a function of RF detuning.

stant RF detuning and constant pulse energy, respectively. Additionally, we verify the dependence of the dissociated cloud spatial size (meaning high $\hbar^2k^2/m$ energy, probed with a long TOF or long RF duration) on the RF photon detuning $\Delta E_{\mathrm{RF}} > E_b$ and observe that the size increase is significant for large detunings at large $E_b$ values, such as shown in Fig. 4.10a. Lastly, we check how the shape of the spectrum is affected by RF pulses with finite durations. We notice that the molecular spectra with small $E_b$ values are Fourier-limited when using short RF pulses, as depicted in Fig. 4.10d. To circumvent this problem, we use longest RF pulses permissible by finite molecular lifetimes and fit our spectra to a function that is a convolution of Eq. 4.7 and the Fourier transform of the (Gaussian or rectangular) RF pulse.

### 4.3.2 High RF Power Effects

Since Eq. 4.8 was derived using weak coupling, there are several high RF power (compared to $\Omega$) effects that can distort the expected spectrum. The first effect is the saturation of lineshapes at high power. As the RF pulse amplitude is increased, the lineshape tail starts to deviate from the predicted spectrum and eventually becomes flat at highest powers, as depicted in Fig. 4.11a. Additionally, for high RF powers we need to add a significant amplitude/$y$-axis offset to the fit function since the spectral signal is no longer zero for $E < E_b$. The physical origin of this offset will be discussed shortly. Another way to visualize the saturation effect is by comparing lineshape amplitudes at the peak ($\Delta E_{\mathrm{RF}} = (4/3)\, E_b$) versus the tail (for instance, $\Delta E_{\mathrm{RF}} = (8/3)\, E_b$) as one varies the RF power. The lineshape peak and tail differ at low RF power and have the same amplitude at high RF power, as shown in Fig. 4.11b. We ensure that we are far from the saturation regime by performing such saturation checks for each $E_b$ and by verifying the measured spectra fits well to Eq. 4.8. Typically, a 30–50% molecular dissociation fraction satisfies low-saturation condition while retaining a good signal to noise ratio.

The second effect associated with high RF powers is atom-molecule Rabi flopping at small $E_b$. This effect occurs when the Franck-Condon factor is large and its integral is mainly concentrated within a small spectral region, being smaller than (or comparable to) the Fourier width of the RF

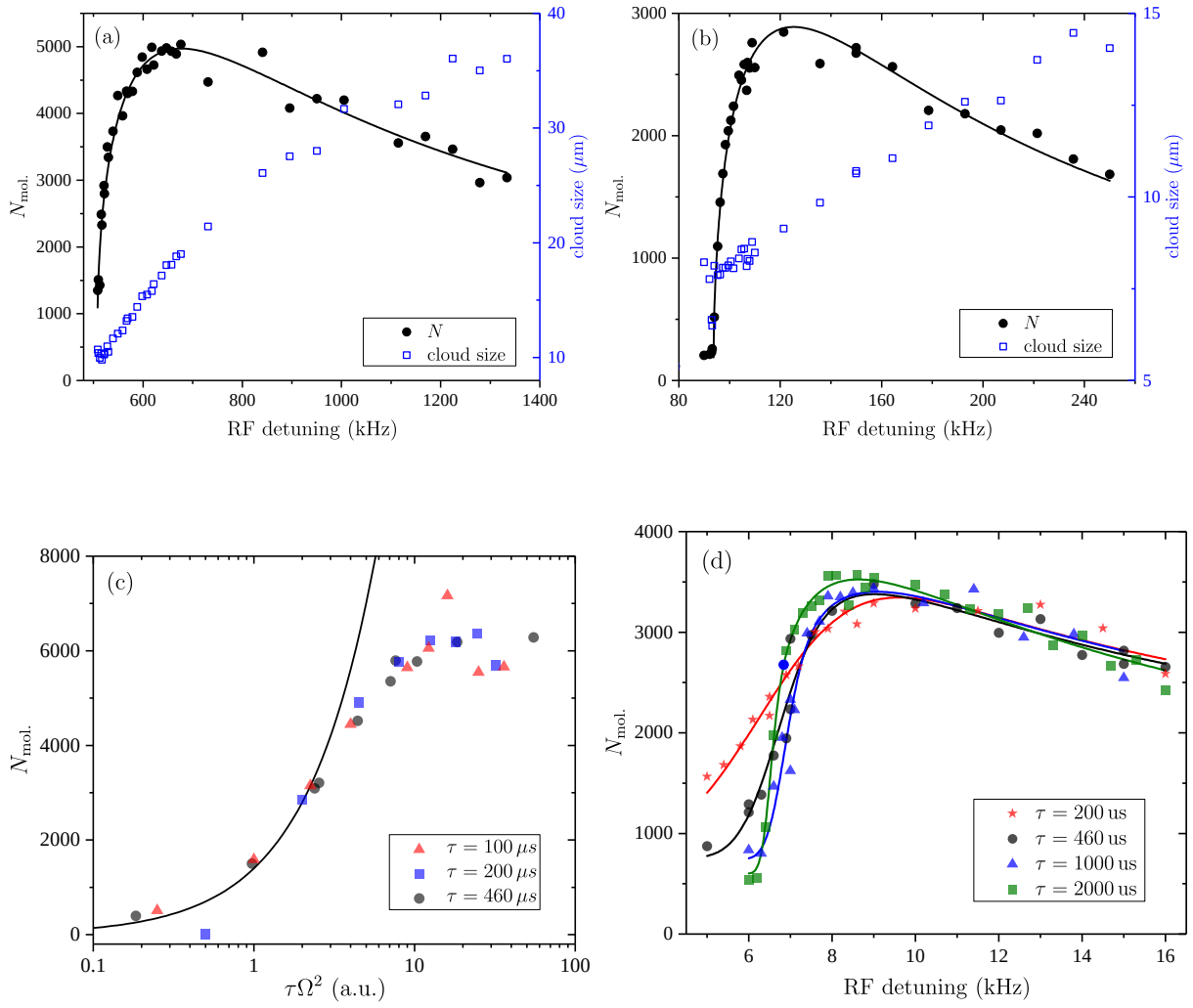


Figure 4.10: Experimental checks on the dimer dissociation spectra. (a) Dissociation spectrum for $E_b = 508\,\mathrm{kHz}$. Note that the imaged (with a finite TOF) cloud size is increases with the RF detuning $> E_b$, suggesting added energy to atoms by the RF photon. (b) Dissociation spectrum for $E_b = 95\,\mathrm{kHz}$. (c) We probe $E_b = 95\,\mathrm{kHz}$ molecules with a fixed RF detuning of $+250\,\mathrm{kHz}$, while varying RF pulse duration and power, to verify the relation $N_{\mathrm{mol}} \propto \tau\Omega^2$ (solid curve, assuming no RF saturation). All data coinciding, as $\tau\Omega^2$ is varied by a factor $\sim 10^3$, is evidence that this relation holds. (d) The dissociation spectrum at low $E_b$ value, in this case $E_b = 6.5\,\mathrm{kHz}$, are Fourier-limited when the RF pulse durations are short, smearing the sharp feature near $E_b$. This effect is significant for a $\tau = 200\,\mu\mathrm{s}$ rectangular pulse. We fit our data to functions (solid curves) involving a convolution of the RF pulse spectra (Gaussian or sinc functions) with that of Eq. 4.7. We keep $\tau\Omega^2$ constant by reducing RF power for longer pulse durations.

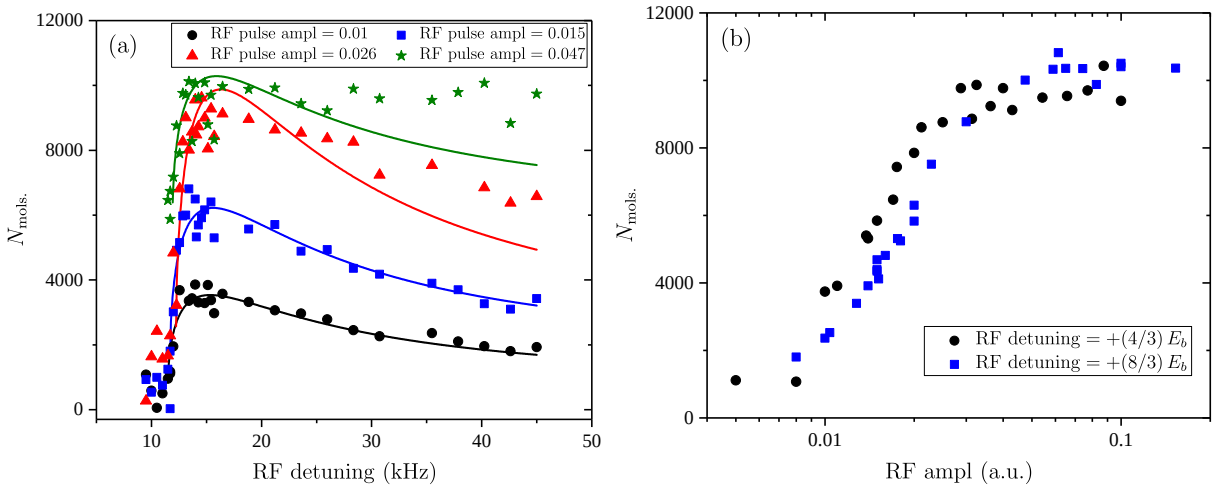


Figure 4.11: Demonstration of the dimer spectrum saturation at high RF power with $E_b = 11.5\,\mathrm{kHz}$. (a) As the RF pulse amplitude is increased, significant deviations from Eq. 4.8 are evident in the measured spectra. (b) Measuring spectrum saturation at two RF detunings.

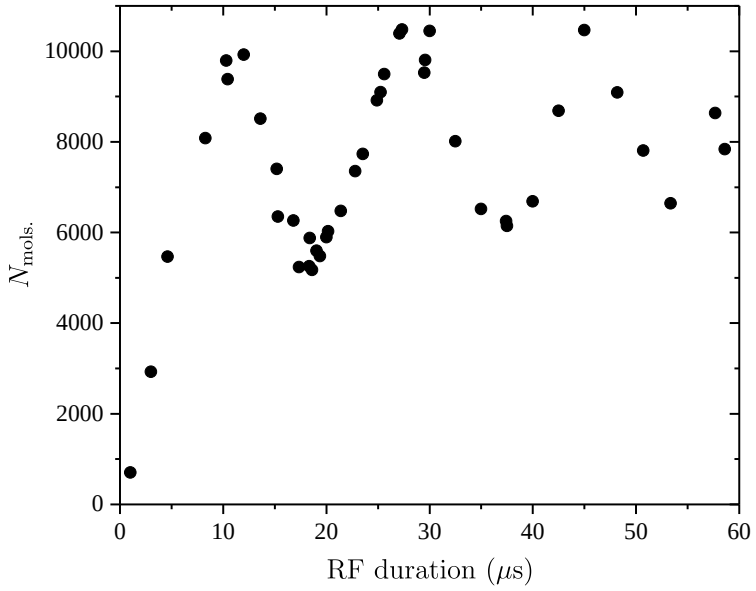


Figure 4.12: Atom-molecule Rabi flopping for $E_b = 11.5\,\mathrm{kHz}$ molecules. The dissociated molecules can be re-associated with a high-power RF field. We record the number of dissociated molecules $N$ as we vary the RF pulse energy $\tau\Omega^2$ by scanning the RF pulse duration at the highest RF power of 20 W. This measurement was performed with a pure molecular sample.

pulse. In such scenario, the dissociated molecules (atoms) can be coherently transferred back to the molecular state. To see this effect clearly, we prepared a pure molecular sample with $E_b = 11.5\,\mathrm{kHz}$ and scanned the RF duration at maximum RF power. For RF detunings close to the peak at $\Delta E_{\mathrm{RF}} = (4/3)\,E_b$ ($E_b$ works too), we see clear coherent oscillations in the molecular population as the RF pulse energy $\tau\Omega^2$ is varied (see Fig. 4.12). To prevent this effect from affecting our molecular lineshapes, we use long RF pulses for small $E_b$ spectra, ensuring that the integrated Franck-Condon area $\int_{E_{\mathrm{RF}}-\delta/2}^{E_{\mathrm{RF}}+\delta/2} F(\Delta E_{\mathrm{RF}})\; d\Delta E_{\mathrm{RF}} \ll 1$, where $\delta$ corresponds to the spectral width of the RF pulse.

The last high-power effect is a two-photon transition, appearing as a second peak in the molecular dissociation spectrum at $E_b/2$. The two-photon transition corresponds to both atoms in the dimer being driven to the final $|\mathrm{F} = 2, \mathrm{m_F} = 0\rangle$ state during the dissociation process, in contrast to only one atom being transferred to the $|\mathrm{F} = 2, \mathrm{m_F} = 0\rangle$ in the one-photon case (as depicted in Fig. 4.8). Due to energy conservation, the two-photon feature occurs at $E_b/2$. The molecular dissociation spectrum of such transition is described by the square of the one-photon Franck-Condon factor (Eq. 4.7), as depicted in Fig. 4.13a. Additionally, as expected, the two-photon transition is twice more sensitive to the RF power and becomes visible at a higher RF power threshold than the one-photon transition (see Fig. 4.13b). We do not observe the two-photon transition when probing molecules with high $E_b$, where small Franck-Condon factors would require very high RF power, beyond 20 W we have available, for us to see it. At low $E_b$ values, the two photon transition is easier to drive and distorts our one-photon feature even at moderate powers, requiring us to fit molecular spectra with an offset added to Eq. 4.7, as shown discussed earlier. We try to limit such systematic effects by dissociating a smaller fraction of molecules for smaller $E_b$ spectra, at the expense of signal to noise ratio.

While some evidence of a two-photon transition was previously seen in RF association of Feshbach dimers [40, 107, 38], to my best knowledge, it was not previously studied in the RF dissociation case. Due to some unique properties, the two-photon transition can be more advantageous than the one-photon transition in some instances. First, since both atoms are transferred to the same final state, the observed signal is twice higher. Second, due to square nature of the one-photon

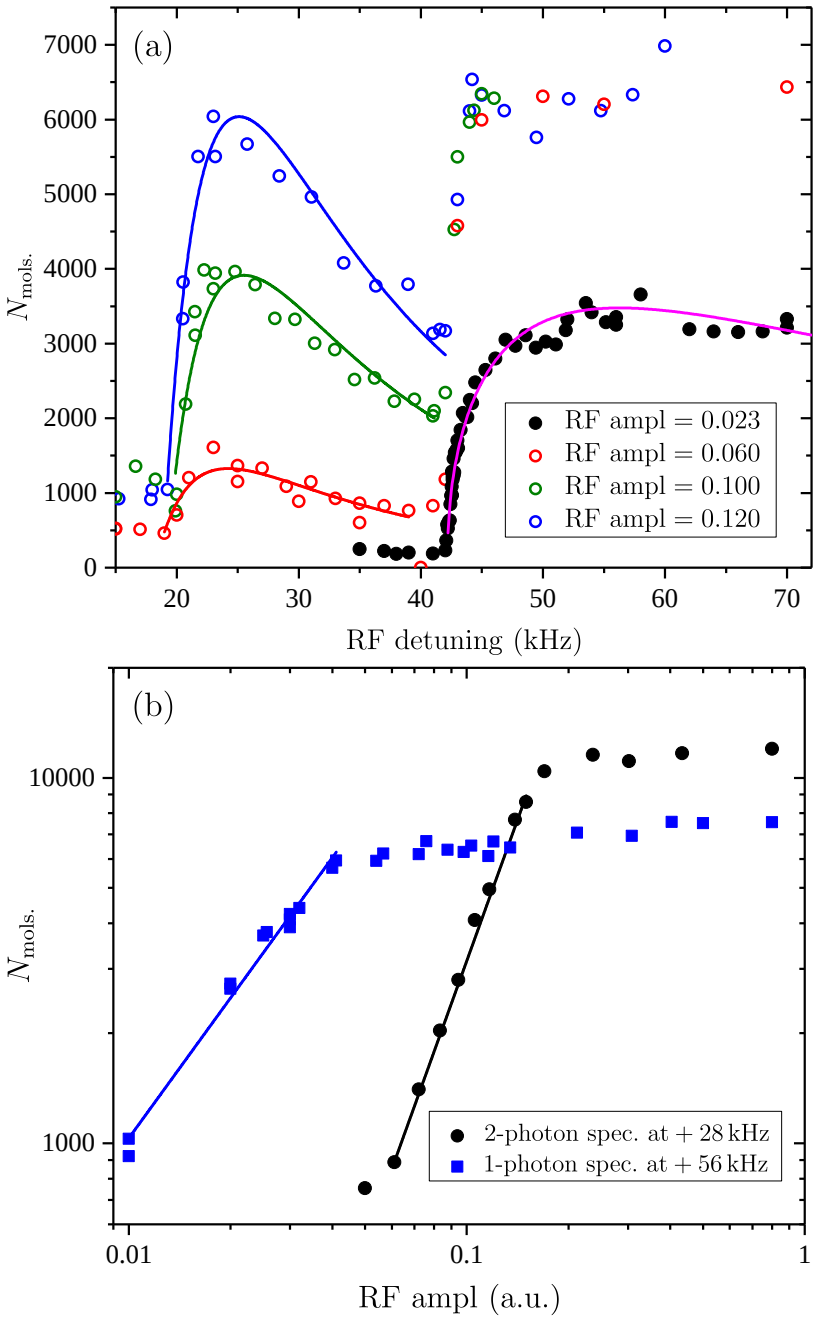


Figure 4.13: Appearance of a two-photon transition in the molecular dissociation spectrum at high RF powers. These measurements were performed with pure molecular samples. (a) As RF power is increased, the two-photon transition becomes more evident near $E_b/2$, where $E_b = 42\,\mathrm{kHz}$ was measured using low RF powers (solid black points). Note that the one-photon (regular) dissociation spectrum is saturated for most of RF powers used in these measurements. Two-photon transitions are fitted with the square of the one-photon spectrum (described by Eq. 4.7). (b) RF power dependence of the one- versus the two-photon transition, measured with fixed RF duration at the two detunings $(4/3)\,E_b$ and $(4/3)\,E_b/2$, corresponding to the peak locations of each feature. Note that the two-photon transition starts at higher RF power, has a stronger RF power dependence and detects twice more number of atoms (in the saturated region) than the one-photon transition. We fit select data to a line on a log-log plot and observe the two slopes differing by a factor of 2.0, another evidence of a two-photon transition.

Franck-Condon factor (Eq. 4.7), the transition is sharper near the dissociation threshold at $E_b/2$ than near the threshold at $E_b$. Third, one can use RF photons of two different frequencies to drive this transition. By using both positive and negative RF detunings for the two RF fields, one can shift the two-photon feature to higher RF detunings, away from the (free-free) atom transition, allowing one to probe very small binding energies. Last, one can compare one- and two-photon transition spectra to extract energy shifts resulting from dimer-dimer and atom-dimer interactions.

## 4.4 Creating a Pure Molecular Sample

### 4.4.1 The Affect of Residual Unpaired Atoms on Molecular Dissociation Spectra

Since the magneto-association process is not perfect, a significant portion ($> 80\%$) of atoms remain in the unpaired state. RF pulses used for molecular dissociation will also off-resonantly drive the atomic transition $|\mathrm{F} = 1, \mathrm{m_F} = -1\rangle \rightarrow |\mathrm{F} = 2, \mathrm{m_F} = 0\rangle$. With relatively small Franck-Condon factors, molecular dissociation transitions require significantly more RF power than atomic transitions. Therefore, atomic transitions are strongly driven (multi-$\pi$ Rabi flopping) during dissociation and contribute to the molecular signal, as shown in Fig. 4.14. For very small detunings, such as in measurements of small $E_b$ spectra, the atomic contribution can be significant and will distort the measured spectrum. For instance, for $E_b = 15\,\mathrm{kHz}$, we estimate that $\sim 20\%$ of atoms can be off-resonantly excited near the molecular threshold, as shown in Fig. 4.15a. Considering that we only dissociate $\sim 50\%$ of molecules and that magneto-association of molecules is $< 20\%$ efficient, a 20% excitation of unpaired atoms would completely wash out the molecular signal. While we can suppress the sidebands of atomic transitions by using longer RF pulses, as depicted in Fig. 4.15b, finite molecular lifetimes will limit the maximum duration of our pulses.

Before detailing what affects molecular lifetimes, I will discuss an additional spectroscopic complication arising from unpaired atoms in the $|\mathrm{F} = 1, \mathrm{m_F} = 0\rangle$ hyperfine state. We first noticed the presence of $|\mathrm{F} = 1, \mathrm{m_F} = 0\rangle$ atoms during measurements of molecular spectra with small $E_b$ values, where we see a large distortion of the molecular signal near 13.5 kHz RF detuning from

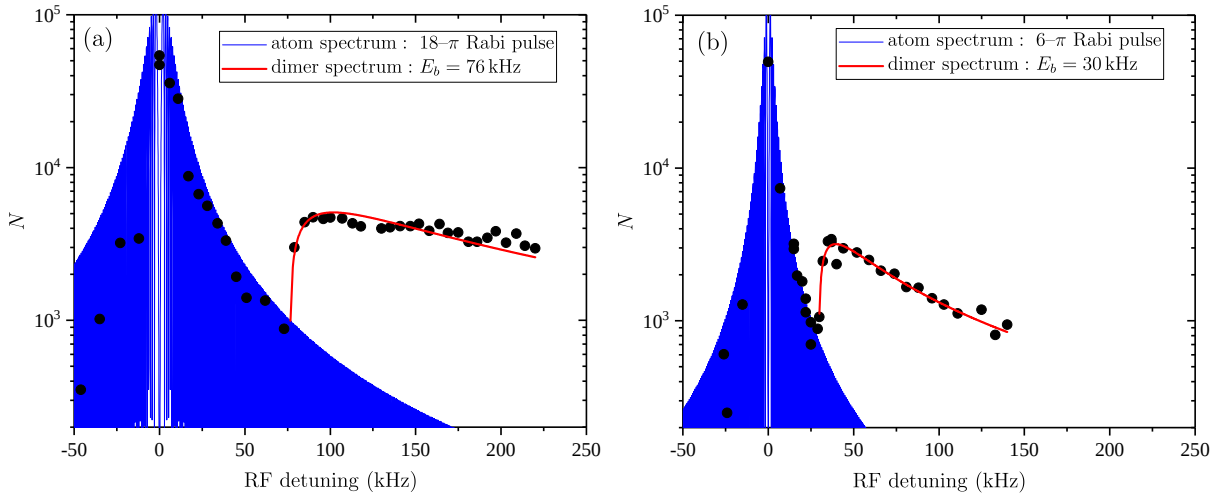


Figure 4.14: Measured molecular spectra with the presence of (monomer) atomic population. Off-resonant drive of the atomic transition contaminates the dissociation signal for small $E_b$. The atomic population was measured to be $1.6 \times 10^5$ using a $\pi$–pulse with zero RF detuning. We dissociate $\sim 50\%$ of molecules to ensure that the saturation effects are negligible. (a) Dissociation spectrum of $E_b = 76\,\mathrm{kHz}$ molecules. The RF power and duration ($1500\,\mu\mathrm{s}$) correspond to a $\Omega\tau = 18$–$\pi$ pulse for the atomic transition (on-resonance). The Rabi pulse spectral sidebands are too fine to resolve on this scale. (b) Dissociation spectrum of molecules with $E_b = 30\,\mathrm{kHz}$. The RF power and duration ($1500\,\mu\mathrm{s}$) correspond to a $\Omega\tau = 6$–$\pi$ pulse.

the $|\mathrm{F} = 1, \mathrm{m_F} = -1\rangle \rightarrow |\mathrm{F} = 2, \mathrm{m_F} = 0\rangle$ atomic transition, as depicted in Fig. 4.16. This feature coincides with the $|\mathrm{F} = 1, \mathrm{m_F} = 0\rangle \rightarrow |\mathrm{F} = 2, \mathrm{m_F} = -1\rangle$ atomic transition, proving the presence of atoms in the $|\mathrm{F} = 1, \mathrm{m_F} = 0\rangle$ state. We haven't detected this impurity beforehand, as its population composes a small fraction ($\sim 10\%$) of the total atomic population (mostly in the $|\mathrm{F} = 1, \mathrm{m_F} = -1\rangle$ state) and because the $|\mathrm{F} = 1, \mathrm{m_F} = 0\rangle \rightarrow |\mathrm{F} = 2, \mathrm{m_F} = -1\rangle$ transition is spectroscopically very close to the main $|\mathrm{F} = 1, \mathrm{m_F} = -1\rangle \rightarrow |\mathrm{F} = 2, \mathrm{m_F} = 0\rangle$ transition. Since $|\mathrm{F} = 1, \mathrm{m_F} = 0\rangle$ atoms are not magnetically trappable in the QT, we were puzzled by their presence.

The impurity population impeded our dimer spectroscopy measurements and we tried to understand its mysterious origin. To better detect the impure population, we combined RF spectroscopy with spatial spin separation, as shown in Fig. 4.17. This Stern-Gerlach–type technique enabled us to measure the atomic fraction in the $|\mathrm{F} = 1, \mathrm{m_F} = 0\rangle$ state at different stages of our experiment. We traced down the source to be spin-changing collisions are high temperatures. We

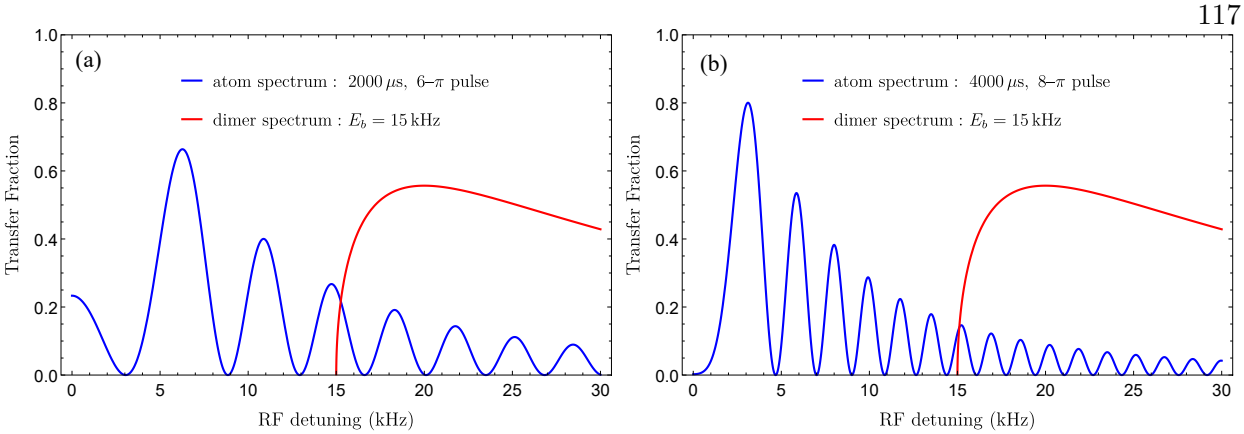


Figure 4.15: Predicted atom contamination of the molecular spectrum at small $E_b$, here $E_b = 15\,\mathrm{kHz}$. The RF pulse energy $\tau\Omega^2$ is chosen to dissociate 50% of molecules and is predicted by extrapolating measurements at high $E_b$ (while compensating for the differing Franck-Condon factors). (a) An RF pulse with energy $\tau\Omega^2$ and duration $\tau = 2000\,\mu\mathrm{s}$ will dissociate 50% of molecules and corresponds to a 5.7–$\pi$ pulse for atoms. A significant distortion of the molecular spectrum is expected by atom signal. (b) Distortion can be significantly reduced by using a longer RF pulse. An RF pulse with a duration $\tau = 4000\,\mu\mathrm{s}$, yet the same energy $\tau\Omega^2$, will also dissociate 50% of molecules. Such a pulse is equivalent to a 8.0–$\pi$ pulse for atoms.

notice that, after loading the optical trap and switching off the quadrupole trap, a pure sample of $|\mathrm{F}=1,\mathrm{m_F}=-1\rangle$ atoms at $T \approx 400\,\mu\mathrm{K}$ decays ($\tau \sim 5\,\mathrm{s}$) and gives rise to a population of $|\mathrm{F}=1,\mathrm{m_F}=0\rangle$ atoms, which becomes as large as $\sim 10\%$ of the remaining total population in 1 s and $\sim 20\%$ in 2.5 s. Such behavior is not present at low temperatures ($T \lesssim 1\,\mu\mathrm{K}$), where both $|\mathrm{F}=1,\mathrm{m_F}=-1\rangle$ and $|\mathrm{F}=1,\mathrm{m_F}=0\rangle$ populations decay with the same time constant. We don't detect any other spin states, including those in the $|\mathrm{F}=2\rangle$ state, besides the two mentioned. Since we were unable to minimize the impurity population fraction by changing evaporation parameters, we decided to use RF and optical pulses to blast away $|\mathrm{F}=1,\mathrm{m_F}=0\rangle$ atoms; this procedure is discussed in Sec. 4.4.2.

Molecular lifetimes are affected by three different phenomena. First is the spontaneous dissociation of Feshbach dimers due to spin relaxation [119, 120]. This one-body–type (exponential) decay dominates the total loss at small $a$ and decreases with increasing $a$ (see Sec. 4.6 for more details). The second decay type is due to dimer-dimer inelastic collisions. Ignoring interference effects,

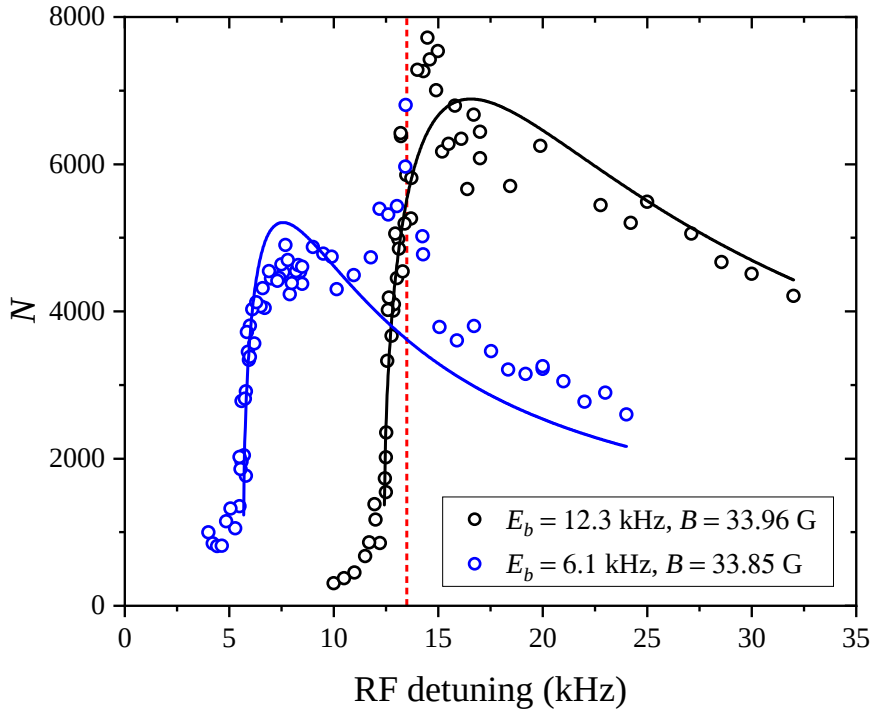


Figure 4.16: Distortion of molecular spectra by presence of $|\mathrm{F}=1,\mathrm{m_F}=0\rangle$ residual atoms. An additional feature in $E_b = 6.1\,\mathrm{kHz}$ and $E_b = 12.3\,\mathrm{kHz}$ molecular spectra near RF detuning of 13.5 kHz coincides with the predicted $|\mathrm{F}=1,\mathrm{m_F}=0\rangle \rightarrow |\mathrm{F}=2,\mathrm{m_F}=-1\rangle$ transition (vertical dashed) at those magnetic fields. RF detuning is with respect to the $|\mathrm{F}=1,\mathrm{m_F}=-1\rangle \rightarrow |\mathrm{F}=2,\mathrm{m_F}=0\rangle$ transition, whose center frequency is 446.853 MHz for $E_b = 6.1\,\mathrm{kHz}$ lineshape and 446.834 MHz for $E_b = 12.3\,\mathrm{kHz}$ lineshape.

such as those arising from Efimov physics, the dimer number loss is described by [121, 122, 123, 124]

$$\frac{dN_\mathrm{D}}{dt} = -2\beta_\mathrm{DD}\langle n_\mathrm{D}\rangle_\mathrm{D} N_\mathrm{D} \tag{4.9}$$

$$\beta_\mathrm{DD} = C_\mathrm{DD}\frac{\hbar}{m}a\left(\frac{a}{a_0}\right)^{\nu}, \tag{4.10}$$

where $\beta_\mathrm{DD}$ is the dimer-dimer inelastic relaxation rate, the dimer density-weighted density is $\langle n_\mathrm{D}\rangle_\mathrm{D} = \frac{1}{N_\mathrm{D}}\int n_\mathrm{D}^2(\vec{x})d^3x = \left(m\bar{\omega}^2/\left(2\pi k_\mathrm{B}T\right)\right)^{3/2} N_\mathrm{D}$, the dimensionless constant $C_\mathrm{DD} = 0.73(4)$ and the power $\nu = 0.34(12)$, were both measured in our unpublished work (note that for Bosons $\nu$ is predicted to be 0 [121, 122], such that $\beta_\mathrm{DD} \propto a$). In the presence of Efimov physics, the factor $C_\mathrm{DD}$ would depend on $a$ and result in interference features. While we measure the loss rate ($\beta_\mathrm{DD} = 7\times10^{-10}\,\mathrm{cm^3s^{-1}}$ near $a = 1000\,a_0$ and $\beta_\mathrm{DD} = 9\times10^{-9}\,\mathrm{cm^3s^{-1}}$ near $a = 7000\,a_0$) be an order of magnitude larger than observed in Cesium [123], our extracted values are close to their

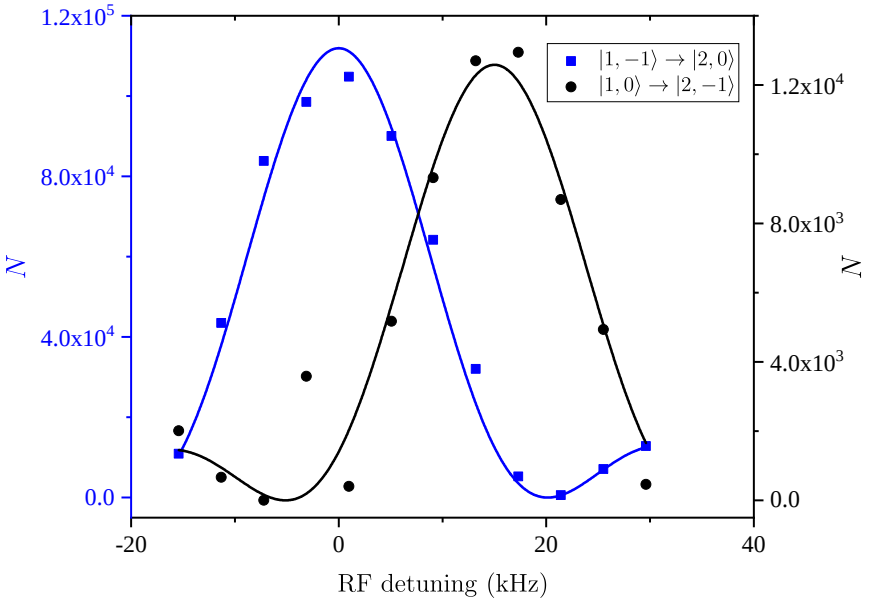


Figure 4.17: Spin composition of our atomic cloud after molecular association. Using Stern-Gerlach–type technique and a 43 $\mu$s RF pulse, we are able to spatially separate different spin components and detect a small impurity of $|\mathrm{F}=1,\mathrm{m_F}=0\rangle$ atoms. Not the different $y$-scales.

$C_{\mathrm{DD}} \sim 3$ and $\nu = 0$ (fixed and observed). We suspect that some discrepancy in the values is due to $|\mathrm{F}=1,\mathrm{m_F}=-1\rangle$ not being the absolute ground state. The last type of loss that limits molecular lifetimes arises from atom-dimer inelastic collisions. Since this loss is of more-than-two-body nature (three-body), it is strongly affected by Efimov physics and is described by [121, 31]

$$\frac{dn_{\mathrm{A}}}{dt} = \frac{dn_{\mathrm{D}}}{dt} = -\beta_{\mathrm{AD}}\langle n_{\mathrm{A}}\rangle_{\mathrm{A}}\langle n_{\mathrm{D}}\rangle_{\mathrm{A}} \tag{4.11}$$

$$\frac{dN_{\mathrm{D}}}{dt} = -\frac{8}{\sqrt{27}}\beta_{\mathrm{AD}}\langle n_{\mathrm{A}}\rangle_{\mathrm{A}} N_{\mathrm{D}}$$

$$\beta_{\mathrm{AD}} = \frac{\hbar a}{m}\frac{20.3\sinh(2\eta_*)}{\sin^2(s_0\ln(a/a_*)) + \sinh^2(\eta_*)} \tag{4.12}$$

where $\beta_{\mathrm{AD}}$ is the atom-dimer inelastic relaxation rate, the constant $s_0 \approx 1.00624$ fixes Efimov series spacing $e^{\pi/s_0} \approx 22.7$ (see Ch. 5), $a_*$ determines the location of the atom-dimer Efimov resonance, where the dimer energy is degenerate with an Efimov state, and the dimensionless inelasticity parameter $\eta_*$ characterizes the resonance width. Our unpublished measurements give $a_* = 780\,a_0$ and $\eta_* = 0.21$. Due to differing polarizabilities, the overlap of molecular and atomic clouds is not unity and results in $\langle n_{\mathrm{D}}\rangle_{\mathrm{A}} = \frac{1}{N_{\mathrm{D}}}\int n_{\mathrm{D}}(\vec{x})n_{\mathrm{A}}(\vec{x})d^3x = \frac{8}{\sqrt{27}}\langle n_{\mathrm{A}}\rangle_{\mathrm{A}}$, where atom density-weighted

density $\langle n_{\rm A}\rangle_{\rm A} = \frac{1}{N_{\rm A}}\int n_{\rm A}^2(\vec{x})d^3x = \left(m\bar{\omega}^2/\left(4\pi k_{\rm B}T\right)\right)^{3/2} N_{\rm A}$.

Overall, the total molecular loss is given by

$$\frac{1}{N_{\rm D}}\frac{dN_{\rm D}}{dt} = -\frac{1}{\tau_{\rm 1b}} - 2\beta_{\rm DD}\langle n_{\rm D}\rangle_{\rm D} - \frac{8}{\sqrt{27}}\beta_{\rm AD}\langle n_{\rm A}\rangle_{\rm A}, \tag{4.13}$$

where $\tau_{\rm 1b}$ is the $a$–dependent one-body decay time constant, described in detail in Sec. 4.6. Assuming the three terms in Eq. 4.13 barely deplete atomic and molecular populations (a valid assumption for short timescales), each term becomes time-independent and results in an exponential decay of $N_{\rm D}$. We can estimate the contribution of each loss term at different scattering lengths for typical mean densities $\langle n_{\rm D}\rangle_{\rm D} = 1\times10^{10}\,{\rm cm}^{-3}$ and $\langle n_{\rm A}\rangle_{\rm A} = 1.4\times10^{11}\,{\rm cm}^{-3}$ (measured after the magneto-association procedure). While at low scattering lengths the molecular loss is primarily due to spontaneous dimer decay, atom-dimer inelastic collisions dominate the loss at high scattering lengths, as depicted in Fig. 4.18. High loss rates at large $a$ present complications for dimer spectroscopy at small $E_b$. Population decay leads to a spectral broadening of the dimer signal. For instance, an exponential decay with $\tau = 0.15\,{\rm ms}$ is equivalent to a Lorentzian function with a $\Delta f_{\rm FWHM} = 1\,{\rm kHz}$ in the Fourier domain, where $\Delta f_{\rm FWHM} = 1/\left(2\pi\tau\right)$. Additionally, fast decay of molecular signal would prevent the use of long RF pulses, which are advantageous for obtaining uncontaminated (by atomic signal) dimer spectra. To circumvent these problems, we extend our molecular lifetimes at high $a$ values by getting rid of all unpaired atoms.

### 4.4.2 Blasting Residual Unpaired Atoms from the Trap

To extend molecular lifetimes and reduce dimer spectra distortion, we get rid of all unpaired atoms. The full cleanup procedure, along with the probing RF and optical pulses, is shown in Fig. 4.19. We first remove $|{\rm F}=1,{\rm m_F}=0\rangle$ atoms before the molecular-association procedure. Since dimer lifetime is short, performing this state cleanup afterward would lead to an unnecessary dimer loss. We begin by changing the $B$–field value to 35.76 G and wait 2 ms for the field to stabilize to within $\sim 1\,{\rm mG}$. We use a rectangular RF pulse, coming from the same antenna used for the $|{\rm F}=1,{\rm m_F}=-1\rangle \rightarrow |{\rm F}=2,{\rm m_F}=0\rangle$ transition, to transfer $|{\rm F}=1,{\rm m_F}=0\rangle$

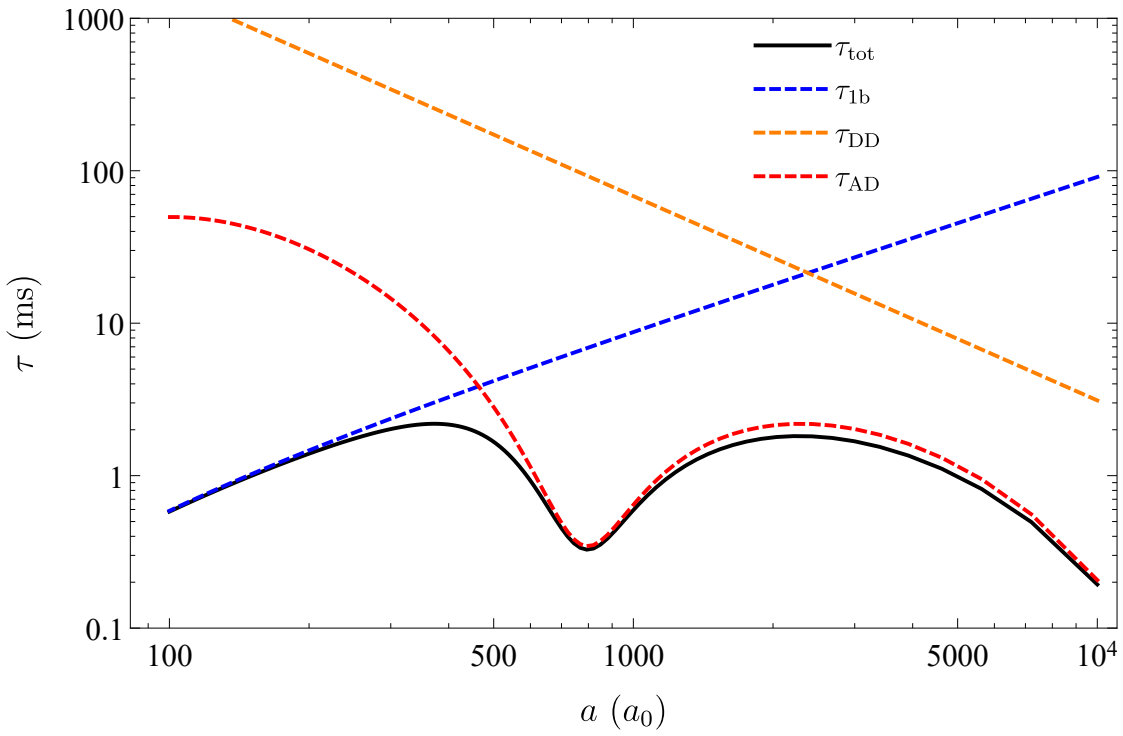


Figure 4.18: Molecular lifetime estimate for typical dimer and atomic densities of $\langle n_{\mathrm{D}} \rangle_{\mathrm{D}} = 1 \times 10^{10}\,\mathrm{cm}^{-3}$ and $\langle n_{\mathrm{A}} \rangle_{\mathrm{A}} = 1.4 \times 10^{11}\,\mathrm{cm}^{-3}$. Different processes limit the total molecular lifetime (black solid) at different scattering lengths, as predicted by Eq. 4.13. While spontaneous 1–body decay (blue dashed) is the primary loss mechanism at small $a$, atom-dimer inelastic collisions (red dashed) lead to most loss at high $a$. For this particular molecular density, the dimer-dimer inelastic loss is negligible compared to the other two mechanisms.

atoms to the $|\mathrm{F}=2,\mathrm{m_F}=-1\rangle$ state, where optical light can blast them from the trap. Since the $|\mathrm{F}=1,\mathrm{m_F}=0\rangle \rightarrow |\mathrm{F}=2,\mathrm{m_F}=-1\rangle$ transition is only 13.2 kHz detuned from the $|\mathrm{F}=1,\mathrm{m_F}=-1\rangle \rightarrow |\mathrm{F}=2,\mathrm{m_F}=0\rangle$ transition at 35.76 G, we use a 269 $\mu$s pulse that only excites 2% of $|\mathrm{F}=1,\mathrm{m_F}=-1\rangle$ population. Such an excitation is unfavorable, as it would deplete the $|\mathrm{F}=1,\mathrm{m_F}=-1\rangle$ population used for molecular association and because it is difficult to blast away $|\mathrm{F}=2,\mathrm{m_F}=0\rangle$ atoms with D2 transitions, where any chosen excited state would have a $>30\%$ chance to decay into $|\mathrm{F}=1\rangle$ states. Field stability/drift prevents us from using a longer RF pulse, as a 269 $\mu$s pulse already corresponds to $\Delta f_{\mathrm{FWHM}} = 590$ Hz, or equivalently 4 mG at 140 Hz/mG transition sensitivity.

We use a 100 $\mu$s optical pulse, coming from top (parallel to the Feshbach field $\vec{B}$, see Fig. 2.35) and $\sigma^-$ polarization, to blast the atoms transferred to the $|\mathrm{F}=2,\mathrm{m_F}=-1\rangle$ state. We chose the D2 $|\mathrm{F}=2,\mathrm{m_F}=-1\rangle \rightarrow |\mathrm{F}'=3,\mathrm{m_{F'}}=-2\rangle$ transition, since the branching ratios favor the excited state decay predominantly into the F = 2 states: 21% to $|\mathrm{F}=2,\mathrm{m_F}=-1\rangle$, 65% to $|\mathrm{F}=2,\mathrm{m_F}=-2\rangle$ and 14% to $|\mathrm{F}=1,\mathrm{m_F}=-1\rangle$. If we had chosen the D2 $|\mathrm{F}=2,\mathrm{m_F}=-1\rangle \rightarrow |\mathrm{F}'=2,\mathrm{m_{F'}}=-2\rangle$ transition instead, more atoms would decay into the initial $|\mathrm{F}=2,\mathrm{m_F}=-1\rangle$ state, but at an expense of decaying into and contaminating the $|\mathrm{F}=1,\mathrm{m_F}=-1\rangle$ population: 56% to $|\mathrm{F}=2,\mathrm{m_F}=-1\rangle$, 1.5% to $|\mathrm{F}=2,\mathrm{m_F}=-2\rangle$ and 42.5% to $|\mathrm{F}=1,\mathrm{m_F}=-1\rangle$. Since the blast $|\mathrm{F}=2,\mathrm{m_F}=-1\rangle \rightarrow |\mathrm{F}'=3,\mathrm{m_{F'}}=-2\rangle$ is not a cycling transition, $>80\%$ of the initial $|\mathrm{F}=2,\mathrm{m_F}=-1\rangle$ population quickly ends up in the $|\mathrm{F}=2,\mathrm{m_F}=-1\rangle$ state, without scattering enough photons to completely blast away those atoms. Therefore, we use a second 100 $\mu$s blast pulse, using the $|\mathrm{F}=2,\mathrm{m_F}=-2\rangle \rightarrow |\mathrm{F}'=3,\mathrm{m_{F'}}=-3\rangle$ cycling transition that is +28 MHz detuned from the first pulse frequency, to efficiently blast away all atoms that were initially in the $|\mathrm{F}=2,\mathrm{m_F}=-1\rangle$ state.

After the initial impurity $|\mathrm{F}=1,\mathrm{m_F}=0\rangle$ cleanup, we perform magneto-association of Feshbach dimers and return the field to $B = 35.76$ G, where $a = 480\,a_0$ and $E_b = 508$ kHz. We remove the unpaired $|\mathrm{F}=1,\mathrm{m_F}=-1\rangle$ atoms at this particular field, because here $E_b$ is large enough that are molecules unperturbed when we address atoms and because here the molecular lifetime is relatively long. The dimer lifetime is primarily limited by spontaneous dissociation at this field, as

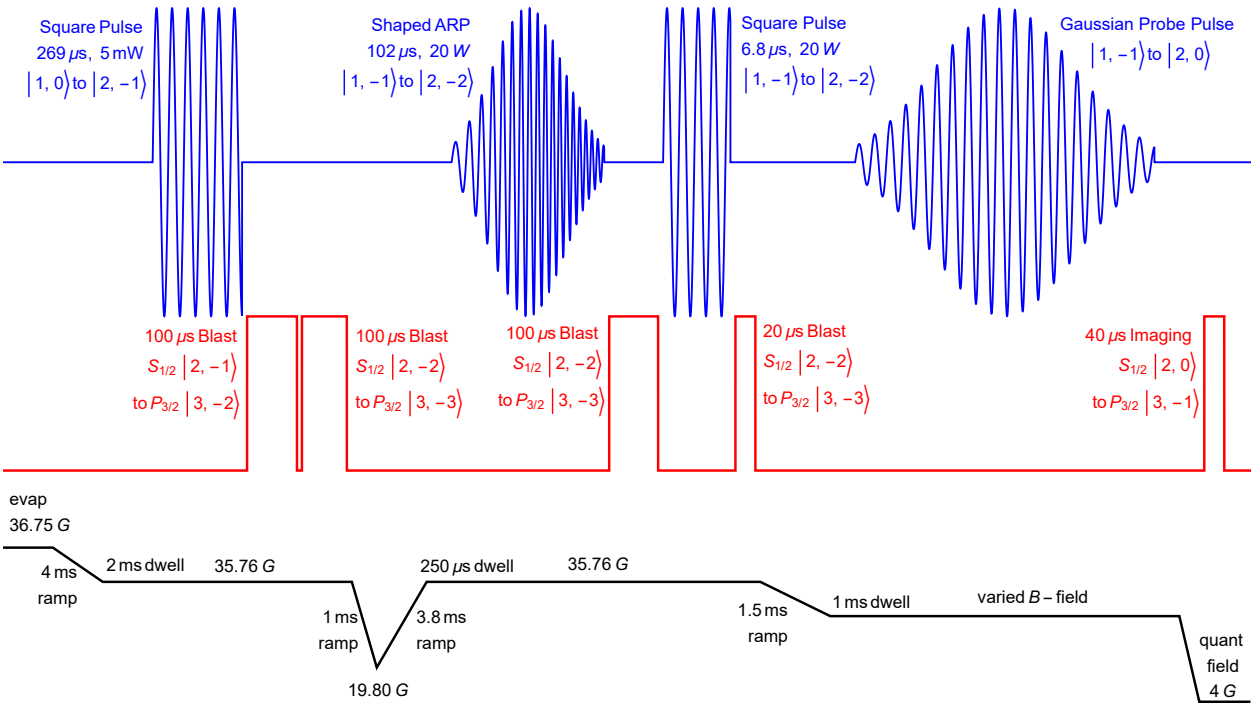


Figure 4.19: Procedure for preparing and probing a pure molecular sample. Besides the last RF and optical pulses, all other pulses are for purposes of getting rid of all unpaired atoms in $|\mathrm{F}=1,\mathrm{m_F}=-1\rangle$ and $|\mathrm{F}=1,\mathrm{m_F}=0\rangle$ states. The fast ramp to and from $B=19.80\,\mathrm{G}$ corresponds to the molecular-association procedure. Note, the axis and the time separations between events are not to scale.

evidenced by an observed lifetime of $\tau = 3.0\,\mathrm{ms}$ compared to the predicted value (see Eq. 4.33) of 4 ms.

Since we desire a complete removal of unpaired $|\mathrm{F} = 1, \mathrm{m_F} = -1\rangle$ atoms, we need to transfer them to the $|\mathrm{F} = 2, \mathrm{m_F} = -2\rangle$ state, where the $|\mathrm{F} = 2, \mathrm{m_F} = -2\rangle \rightarrow |\mathrm{F}' = 3, \mathrm{m_{F'}} = -3\rangle$ cycling transition can efficiently blast them away. Initially, we tried using rectangular RF $\pi$–pulses to achieve this transfer. While such pulses can be 99% efficient when first optimized, field drift makes the transition only $\sim 95\%$ efficient (without re-optimizing) on a day-to-day basis. Additionally, due to fast molecular decay, we perform this RF transfer immediately after the magneto-association $B$–field jump, when the field has not fully settled to its new value. We can estimate the required tolerance on the $B$–field stability from the ratio of the effective $\Omega_{\mathrm{eff}} = \sqrt{\Omega^2 + \delta^2}$ and on-resonance $\Omega$ Rabi frequencies, setting the detuning $\delta$ equal to the product of deviation $\delta B$ and transition sensitivity $\Delta\mu = 1.8\,\mathrm{kHz/mG}$. Assuming we desire 99% RF $\pi$–pulse transfer efficiency, this results in stringent requirements: $\delta B = 11\,\mathrm{mG}$ for a $7\,\mu$s pulse and $\delta B = 4\,\mathrm{mG}$ for a $20\,\mu$s pulse.

An alternative is to use an adiabatic rapid passage (ARP), which is less sensitive to the magnetic field noise. Due to short dimer lifetimes, we require a short-duration ARP, and therefore a high Rabi frequency $\Omega$. However, since the frequency sweep range must be large compared to $\Omega$ for a high transfer efficiency, we cannot utilize this "standard" ARP for our purposes, where the molecular transition is only 500 kHz away. To circumvent this problem, we dynamically change $\Omega$ (an ARP pulse with a Gaussian-shaped amplitude profile, as shown in Fig. 4.20) during the RF frequency sweep. As a result, the dressed state energies approach (see Fig. 4.21) the undressed state values much faster (at detunings away from the resonance) than if one were to use a standard ARP technique, where $\Omega$ is constant. This "shaped" ARP enables us to perform the state transfer quickly (in $102\,\mu$s) and within a small frequency span ($\pm 150\,\mathrm{kHz}$ around the resonance at 391 MHz, $\Omega = 140\,\mathrm{kHz}$). We achieve transfer efficiencies exceeding 99% and rarely require re-optimization using this shaped ARP technique.

Immediately ($10\,\mu$s) after the RF transfer pulse, we blast $|\mathrm{F} = 2, \mathrm{m_F} = -2\rangle$ atoms from the trap. Since the cloud of unpaired atoms is optically dense and because dimers are relatively sensitive

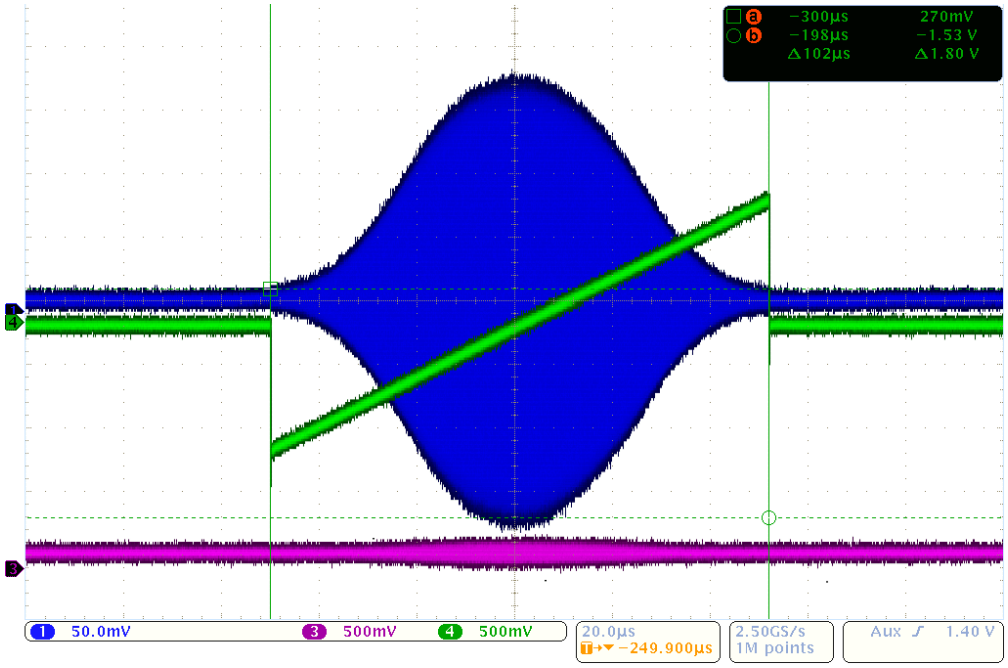


Figure 4.20: Scope trace of a Gaussian-shaped ARP pulse used for the efficient population transfer from the $|\mathrm{F}=1,\mathrm{m_F}=-1\rangle$ state to the $|\mathrm{F}=2,\mathrm{m_F}=-2\rangle$ state. We use a pickup antenna to observe the amplitude profile (blue trace) of a Gaussian pulse ($\sigma = 17\,\mu$s and duration of $6\,\sigma = 102\,\mu$s). We use a coupled port (green trace) of an arbitrary waveform generator, which sends the FM information to a frequency synthesizer, to look at the frequency sweep of the pulse, which starts at $391\,\mathrm{MHz} - 150\,\mathrm{kHz}$ and ends at $391\,\mathrm{MHz} + 150\,\mathrm{kHz}$. The frequency sweep starts and ends $2\,\mu$s before and after RF power is sent to the antenna.

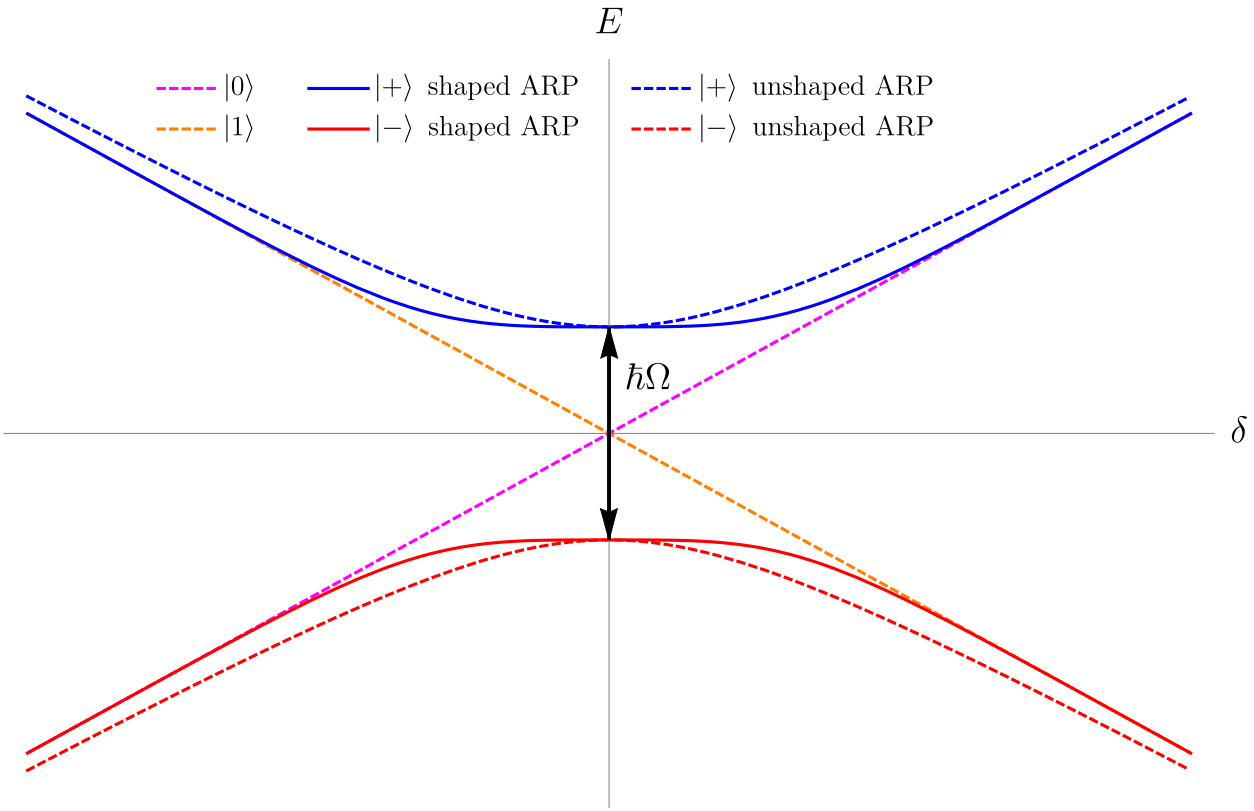


Figure 4.21: Dressed state picture of a shaped ARP. The goal is to transfer atoms from the undressed state $|0\rangle$ to the undressed state $|1\rangle$. In the presence of an RF coupling field with Rabi frequency $\Omega$ and detuning $\delta$ from the resonance, the two dressed states $|+\rangle$ and $|-\rangle$ are the eigenstates of the interaction Hamiltonian, which are split by $\hbar\Omega$ energy at $\delta = 0$. For large RF $\delta$, the dressed state energies are similar to those of the undressed states. One can transfer atoms from $|0\rangle$ to $|1\rangle$ by sweeping the RF frequency from negative to positive detuning during the pulse. For a standard/unshaped ARP, $\Omega$ is constant throughout the sweep and the dressed state energies approach the undressed state energy values slower (away from the resonance) than if one were to change $\Omega$ dynamically during the sweep. A shaped ARP enables efficient population transfer with smaller frequency sweeps than the standard ARP, while allowing the same/fast transfer times (set by the energy gap between the dressed states). Likewise, a shaped ARP enables faster sweeps than a standard ARP, if the detuning span is fixed to be the same for both. Here $\delta$ spans $3\Omega$ and the shaped ARP has a Gaussian-shaped profile that decays to $\pm 3\sigma$ amplitudes at the starting and ending $\delta$ values.

Figure 4.22: Behavior of the expelled $|\mathrm{F}=2,\mathrm{m_F}=-2\rangle$ atoms versus blast power and duration. The blast beam is directed along gravity, towards smaller $y$–values, and utilizes the $|\mathrm{F}=2,\mathrm{m_F}=-2\rangle \rightarrow |\mathrm{F}'=3,\mathrm{m_{F'}}=-3\rangle$ cycling transition. These images are taken 3 ms after blast pulses, which occur immediately before trap release. Note the OD scales vary from image to image.

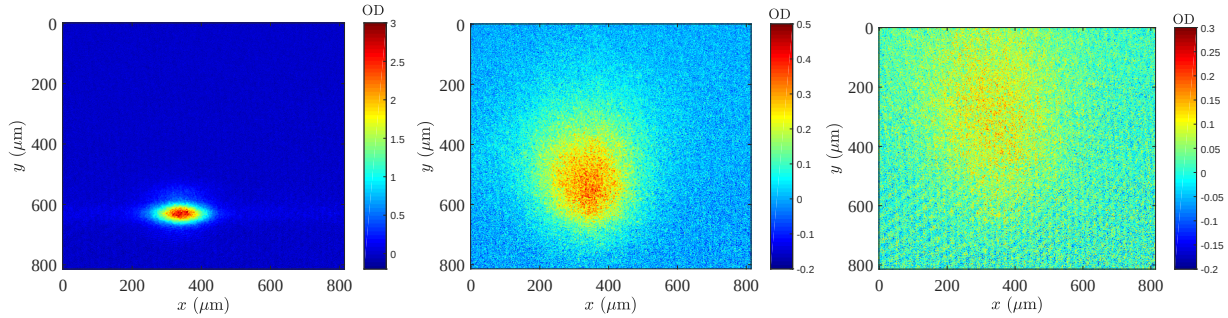


(a) Barely any atoms are expelled for a 40 $\mu$s and $\sim 2\,\mu\mathrm{W/cm^2}$ blast pulse.

(b) Atoms start to get expelled from the trap for a 40 $\mu$s and $\sim 20\,\mu\mathrm{W/cm^2}$ blast pulse.

(c) Most atoms are expelled from the trap for a 100 $\mu$s and $\sim 20\,\mu\mathrm{W/cm^2}$ blast pulse.

Figure 4.23: We see molecules and expelled unpaired atoms in the same image frames when the dwell time between the blast and imaging pulses is small. Here, immediately after the blast pulse, we dissociate $\sim$ 7000 molecules ($E_b = 508$ kHz) with a 480 $\mu$s RF pulse and image them after a short 1.2 ms TOF. Additionally, we see a significant distortion of the dimer cloud for large RF detunings: a Gaussian distribution in (b) evolves to a flat-top–shaped distribution in (c).

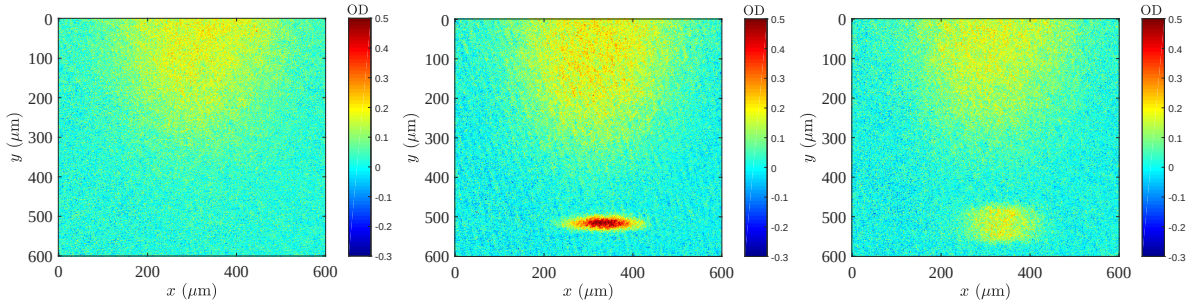


(a) Only the expelled unpaired atoms (diffuse cloud) are seen for RF detuning = 430 kHz $< E_b$.

(b) Dissociated dimers right above the threshold (here RF detuning = 516 kHz $\gtrsim E_b$) have minimal size.

(c) At RF detuning = $\frac{4}{3}E_b$, where the Franck-Condon factor is the largest and most molecules are dissociated.

to off-resonant light, we use an optical blast pulse with a relatively long duration of 100 $\mu$s (but short enough with respect to the molecular lifetime) and low intensity. We look simultaneously at the expelled atoms and the remaining molecules, as shown in Fig. 4.22 and Fig. 4.23, to optimize RF transfer and optical blast pulses.

While the forementioned procedures successfully eliminate $\sim 99\%$ of unpaired atoms, the remaining population (on the order of few thousand atoms) can still affect dimer lifetimes and distort molecular spectra of a few thousand molecules. Therefore, we use another series of cleaning RF ($6\,\mu$s rectangular $\pi$–pulse) and optical ($20\,\mu$s) pulses to completely deplete the $|\mathrm{F}=1,\mathrm{m_F}=-1\rangle$ unpaired atom population and leave us with a pure molecular sample. Aside from cleaner molecular dissociation lineshapes, we notice an increase in dimer lifetimes after getting rid of residual atoms, as depicted in Fig. 4.24. With the lack of atom-dimer inelastic collisions, a significant increase in dimer lifetime at high $a$ enables us to achieve high spectral resolution by using long-duration RF dissociation pulses.

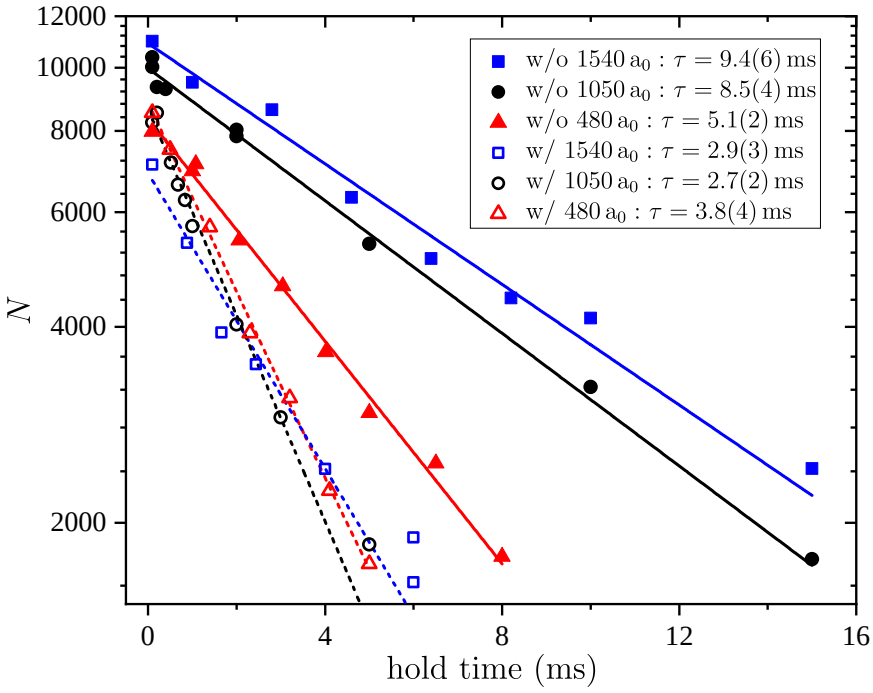


Figure 4.24: Molecular lifetimes with and without the presence of unpaired atoms. While dimer lifetime at low $a$ is primarily limited by spontaneous dissociation, lifetimes at high $a$ are limited by atom-dimer inelastic collisions. The measured dimer lifetimes agree with the prediction (see Fig. 4.18) in the absence of unpaired atoms.

## 4.5 Precision RF Spectroscopy of Dimer Binding Energies

### 4.5.1 More Experimental Considerations and the Spectroscopy Procedure

We've carefully considered our experimental procedure and conditions prior to taking precision $E_b$ spectroscopy data. We changed the $B$–field to the final value (where we perform dissociation spectroscopy) immediately after expelling the unpaired atom population. Since RF dissociation pulse durations range from 600 $\mu$s at high $E_b$ to 12 ms at low $E_b$, we need to verify the $B$–field stability over time. We find that when we use relatively slow $B$–field ramp to go from 35.76 G to the final $B$–field value of interest (33.74–36.73 G range), the field stabilizes to within 2 mG in several ms (see Fig. 4.25). Additionally, since we use long Gaussian-shape RF dissociation pulses for low $E_b$ spectra, the field is even more stable for those measurements. We use a 1.5 ms ramp and wait 1 ms before applying RF dissociation pulses.

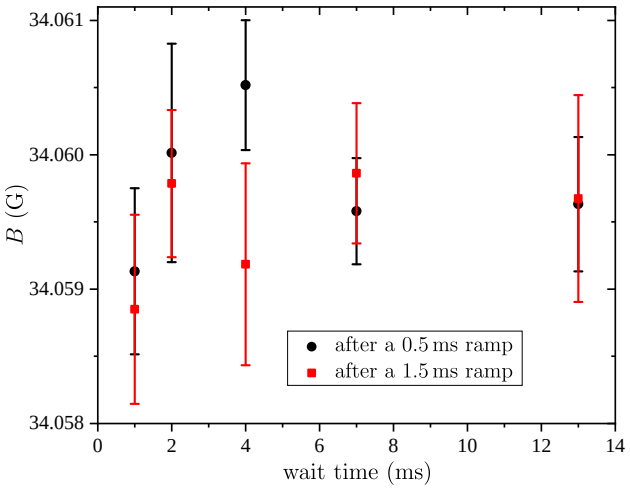


Figure 4.25: $B$–field stability over time after a ramp from 35.76 G to 34.060 G. Using a slower ramp of 1.5 ms allows the field to stabilize to within 2 mG in several ms. This measurement was done using the same sequence as used for measuring $E_b$ (see Fig. 4.19), but with different RF frequency sweep rates and powers during the atom cleaning procedure to keep some atoms for spectroscopy. Each $B$–field point was extracted from an atom lineshape taken at that wait time, using the $|\mathrm{F}=1,\mathrm{m_F}=-1\rangle \rightarrow |\mathrm{F}=2,\mathrm{m_F}=0\rangle$ RF transition. The Gaussian-shaped pulse ($\sigma = 67\,\mu$s and duration of $6\sigma$) started at the specified wait time. We randomized detunings and wait times (a 2D scan) during this measurement. The $B$–field uncertainty is mainly limited by the number of data points taken.

We chose the $|\mathrm{F}=1,\mathrm{m_F}=-1\rangle \rightarrow |\mathrm{F}=2,\mathrm{m_F}=0\rangle$ RF transition ($\sim 447\,\mathrm{MHz}$) that is the least magnetically sensitive transition in the vicinity of the Feshbach resonance: $\Delta\mu = -171\,\mathrm{Hz/mG}$ at $33.74\,\mathrm{G}$ (where $E_b \approx 2\,\mathrm{kHz}$) and $\Delta\mu = -122\,\mathrm{Hz/mG}$ at $36.73\,\mathrm{G}$ (where $E_b \approx 1170\,\mathrm{kHz}$). Field stability is more critical for low $E_b$ spectroscopy, the field drift limits the lowest $E_b$ values we can measure. The dissociation spectra at high $E_b$ values is less sharp near the threshold (as illustrated in Fig. 4.9), and therefore is less impacted by magnetic field drift.

We measure the magnetic field value for each $E_b$ spectrum by using atomic spectroscopy, converting the lineshape center to a $B$ value using the Breit-Rabi formula. We take atom lineshapes before and after performing dissociation spectroscopy at each $E_b$ value to take into account $B$–field drift during measurements. For this purpose, we use the same procedure as used for molecular spectroscopy, but modify RF parameters in the atom cleaning part to leave an atomic population. After magneto-association procedure, we wait an extra $10\,\mathrm{ms}$ after molecular-association ramp to decay away all dimers (only atoms remain; we also kill off most atoms, to be discussed shortly) and perform all $B$–field ramps in a similar manner. To mitigate systematic error arising from $B$–field dynamics (as in Fig. 4.25), the $\pi$–pulse used for atom spectroscopy is centered (time-wise) on what would be the molecular dissociation pulse if we had done molecular spectroscopy. Additionally, we limit systematic shifts arising from mean-field by using a small atomic population for spectroscopy. We found that by varying the ARP frequency sweep span during atom cleaning procedure, we are able to control the atom number and have repeatable conditions. We can estimate the interaction energy shift (per particle) of a thermal gas using [125]:

$$\Delta\mathcal{E} = \frac{4\pi\hbar^2}{m} na \left(1 + \frac{128}{15\sqrt{\pi}}\sqrt{na^3} + \mathcal{O}(na^3) + \cdots\right), \tag{4.14}$$

where $n = \langle n \rangle$ is the density-weighted density. Only the first term in the expression is regarded as the mean-field term, while the second as the LHY correction. Considering that the magnetic sensitivity $\Delta\mu$ of the $|\mathrm{F}=1,\mathrm{m_F}=-1\rangle \rightarrow |\mathrm{F}=2,\mathrm{m_F}=0\rangle$ transition is small, even moderate interaction shifts can significantly affect the $B$–field measurement. Therefore, we use relatively small atom densities spanning from $\langle n \rangle = 3\times10^{10}\,\mathrm{cm^{-3}}$ at high $a$ to $\langle n \rangle = 1\times10^{10}\,\mathrm{cm^{-3}}$ at low $a$, where

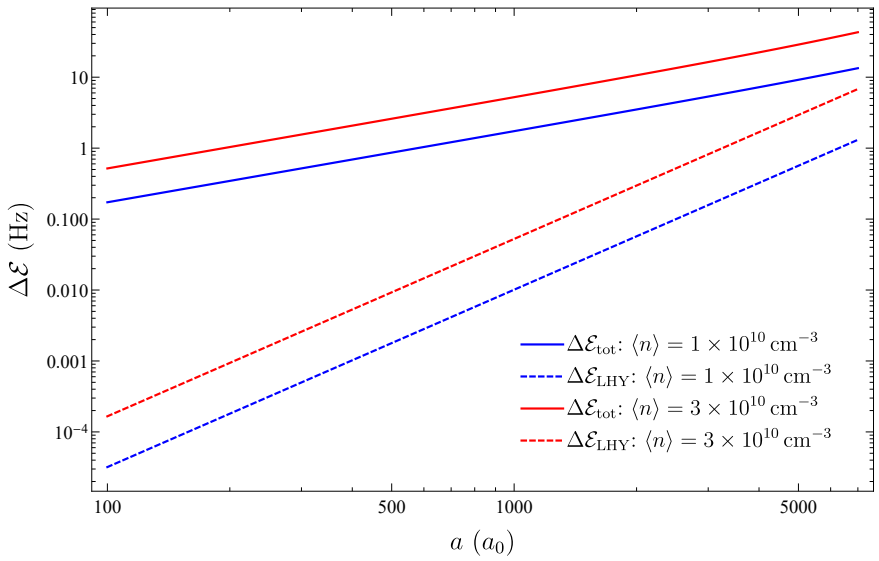


Figure 4.26: The total interaction energy shift $\Delta\mathcal{E}_{\rm tot}$ and its LHY correction term contribution $\Delta\mathcal{E}_{\rm LHY}$, as described by Eq. 4.14, versus $a$ at two different densities.

we reduce the atom number for high $a$ measurements. We expect a negligible interaction energy shift for these densities (see Figure 4.26), corresponding to a $\ll 1\,$mG systematic shift on the $B$–field measurement. Additionally, since our molecular density is also low, at $\langle n\rangle = 3\times10^{10}\,{\rm cm}^{-3}$, and the final state $|{\rm F}=2,{\rm m_F}=0\rangle$ is nearly non-interacting ($a\approx -19a_0$), we also expect a negligible interaction-related shifts affecting the dimer dissociation spectra.

The biggest systematic error affecting our molecular spectra arises from the confining potential. Since we require long interrogation times for high spectral resolution, dissociation must be performed in the optical trap and we need to understand the effect the confinement has on our measurements. Dimer dissociation in free space involves a continuum of final states and is adequately described by Eqs.4.6 and 4.7. However, dissociation under confinement involves a discrete spectrum of final states with energies (approximately):

$$E_b^{\rm trap} \approx E_b^{\rm free} + \hbar\left(\omega_r + \frac{1}{2}\omega_z\right) + \hbar\left(j\omega_r + k\omega_z\right), \tag{4.15}$$

where $E_b^{\rm free} = E_b$ is the dimer binding energy measured in free space (whose value we seek to determine), $j$ and $k$ are even integers. In our case the radial trap frequency $\omega_r/2\pi = 28.64(66)\,$Hz is in the $(x,y)$–plane and $\omega_z/2\pi = 117.3(1.0)\,$Hz. The first correction term to $E_b$ is the zero-point

energy $E_0^{\mathrm{ho}}$, in our case $E_0^{\mathrm{ho}} = 87.3(1.4)\,\mathrm{Hz}$. The second correction term describes the excited harmonic states that must be symmetric (integers $j$ and $k$ must be even) due to parity of the initial molecular state. However, we do not resolve these trap levels. First, our transition sensitivity $\Delta\mu \sim 170\,\mathrm{Hz/mG}$ and field stability of $\sim 1\,\mathrm{mG}$ wash away spectral features $< 100\,\mathrm{Hz}$. Second, we use Gaussian probe pulses with a maximal duration of $6\sigma_t \sim 12\,\mathrm{ms}$ (limited by dimer lifetime), corresponding to a minimal spectral width of $\Delta f_{\mathrm{FWHM}} = \sqrt{\ln(2)}/(\pi\sigma_t) \sim 133\,\mathrm{Hz}$, that further cloak these fine trap features.

While Eq. 4.15 is useful for comprehension, it is only an approximation and does not describe the true energy spectrum of an interacting two-body quantum system in a trap. The Hamiltonian of this system is

$$H = -\frac{\hbar^2}{2m}\nabla_1^2 - \frac{\hbar^2}{2m}\nabla_2^2 + V_{\mathrm{trap}}(\mathbf{r_1}) + V_{\mathrm{trap}}(\mathbf{r_2}) + V_{\mathrm{int}}(\mathbf{r_1} - \mathbf{r_2}), \tag{4.16}$$

$$V_{\mathrm{trap}}(\mathbf{r}) = \frac{1}{2}m\left(\omega_r^2\rho^2 + \omega_z^2 z^2\right), \tag{4.17}$$

$$V_{\mathrm{int}}(\mathbf{r_1} - \mathbf{r_2}) = \frac{4\pi\hbar^2 a}{m}\delta(\mathbf{r_1} - \mathbf{r_2})\frac{\partial}{\partial r}r, \tag{4.18}$$

where $\mathbf{r_1}$ and $\mathbf{r_2}$ are the locations of the two atoms, $\rho^2 = x^2 + y^2$ and $V_{\mathrm{int}}$ is the contact interaction potential with $s$–wave scattering length $a$. By decoupling center of mass and relative motions, one can determine the eigenstate energies as a function of scattering length using two expressions (Ref. 126):

$$\mathcal{F}(x) = 11.137\left[\frac{\eta}{2\pi}\sum_{n=0}^{\infty}\left(\frac{\Gamma(x+n\eta)}{\Gamma(x+n\eta+1/2)} - \frac{1}{\sqrt{\eta(n+1)}}\right) + \frac{\sqrt{\eta}}{2\pi}\zeta\left(\frac{1}{2}\right)\right], \tag{4.19}$$

$$\frac{1}{a} = -\frac{1}{\sqrt{\pi}}\mathcal{F}(-\mathcal{E}/2), \tag{4.20}$$

where $\Gamma$ is the Euler gamma function, $\zeta$ is the Riemann zeta function, $\eta = \omega_r/\omega_z$ is the trap aspect ratio, the summation index $n$ corresponds to the radial quantum number and $\mathcal{E} = E - E_0^{\mathrm{ho}}$ is the difference between the absolute energy and the zero-point energy. Here, all energies and lengths are expressed in units of $\hbar\omega_z$ and the harmonic oscillator length $l_z = \sqrt{\hbar/(\omega_z m/2)}$. We determined that a prefactor of 11.137 is needed in Ref. 126.

The ground state is the dimer/bound state and it exists for energies $\mathcal{E} < 0$, while the excited harmonic states exist for $\mathcal{E} > 0$. To determine the spectrum $E(a)$, we first numerically evaluate the summation at each energy and then we find the corresponding $a$ using Eq. 4.20. In practice, solving Eq. 4.19 is computationally expensive and we tend to use its integral form [126] that is only valid for the ground state (for energies $\mathcal{E} < 0$):

$$\mathcal{F}(x) = \int_0^\infty dt \left( \frac{\eta e^{-xt}}{\sqrt{1-e^{-t}}\,(1-e^{-\eta t})} - \frac{1}{t^{3/2}} \right), \tag{4.21}$$

where $x > 0$.

Figure 4.27 shows the energy spectrum for our trap configuration, with an aspect ratio of $\eta = 0.244$. We see that the ground state energy is approximately equal to the universal expression $E_b = -\hbar^2/\left(ma^2\right)$ (note a different sign convention), which is valid for dimers in an unconfined/free space, for small positive $a$ values, or equivalently large $|E_b|$ values. We determine that our confinement-related energy shift of the dimer binding energy (with respect to universal relation) is relatively small: 0.7 Hz for $a = 10^4\, a_0$ ($E_b \sim 0.9$ kHz) and even smaller for decreasing values of $a$ (increasing values of $E_b$). Such a small shift of the initial/molecular state energy is primarily because our confining trap is relatively weak and because the mass of $^{39}$K atoms is relatively large. We also determine the confinement shift of our final state in dimer dissociation. We only consider the ground state for the final state, as the excited states are unresolvable in our dissociation spectroscopy. Since the final scattering length $a \approx a_{\mathrm{bg}} = -19\, a_0$ (very small compared to the harmonic oscillator length) for $|\mathrm{F} = 2, \mathrm{m_F} = 0\rangle$, the confinement-related energy shift of our final state is equal to the zero-point energy $E_0^{\mathrm{ho}}/h = 87.3$ Hz. When performing dissociation spectroscopy, we are interested in the free-space dimer binding energy. Hence, during such a measurement, the total confinement shift is the difference between the final state shift and the initial state shift, and approximately (to within 1.4 Hz uncertainty on our trapping frequencies) is equal to the zero-point energy. We extract the free-space $E_b$ by subtracting the total confinement shift frequency from the measured dissociation threshold frequency.

Overall, our experimental procedure for measuring $E_b$ for different $B$–field values is as follows.

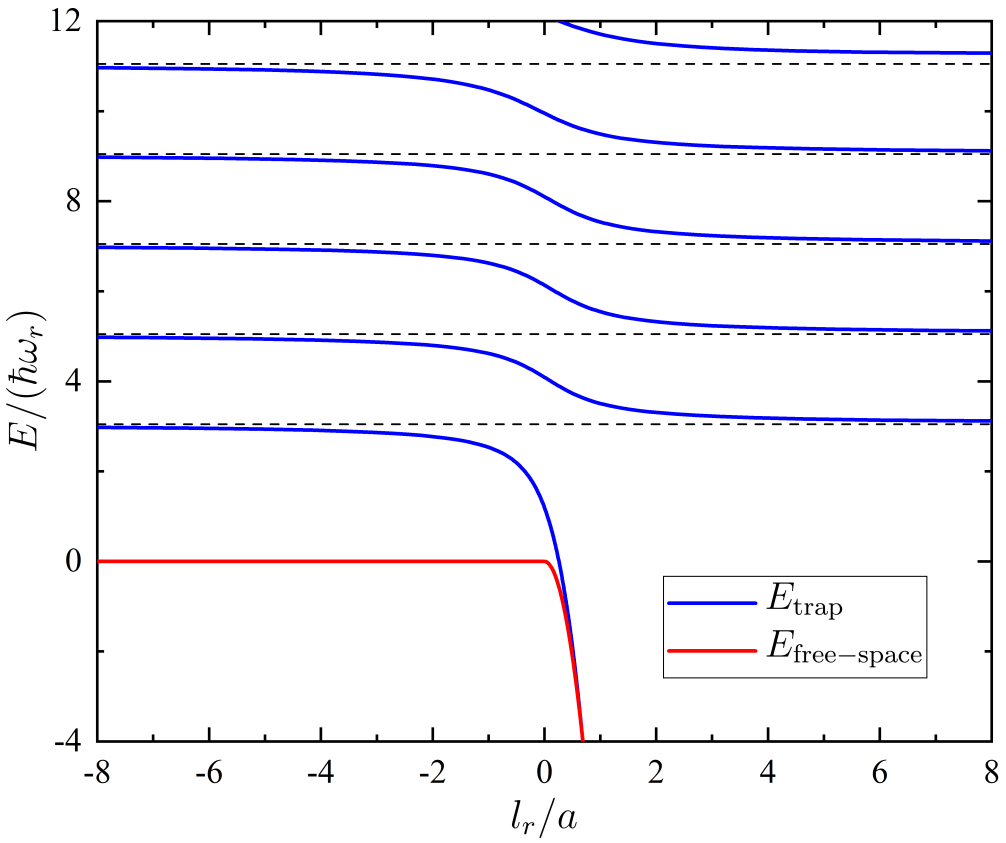


Figure 4.27: Energy spectrum of two atoms in a trap with an aspect ratio of $\eta = \omega_r/\omega_z = 0.244$. The energy $E$ is determined in a relative frame of reference. In our case the radial frequency $\omega_r/2\pi = 28.64(66)\,\text{Hz}$ and the harmonic oscillator length $l_r = \sqrt{\hbar/(\omega_r m/2)} = 8.05 \times 10^4\, a_0$. For small positive $a$ (away from the Feshbach resonance), the ground state energy approaches the universal expression (red) $E_b = -\hbar^2/\left(ma^2\right)$ (for $a < 0$ $E_b = 0$), which is valid for dimers in an unconfined/free space. For small negative $a$, the ground state energy approaches the zero-point energy $E_0^{\text{ho}} = \hbar\omega_r\left(1 + (2\eta)^{-1}\right)$, which in our case $E_0^{\text{ho}} = 3.04\,\hbar\omega_r$ or $E_0^{\text{ho}}/h = 87.3\,\text{Hz}$. The excited states approach the even harmonic oscillator states of the trap (dashed), whose energies are separated by factors of $2\,\hbar\omega_r$, for small values of $a$. Due to our unique value $\eta^{-1} \sim 4$, $\omega_z$ oscillator state energies coincide with $\omega_r$ and are unresolvable on this plot (see Fig. 4.28, where these states are resolvable).

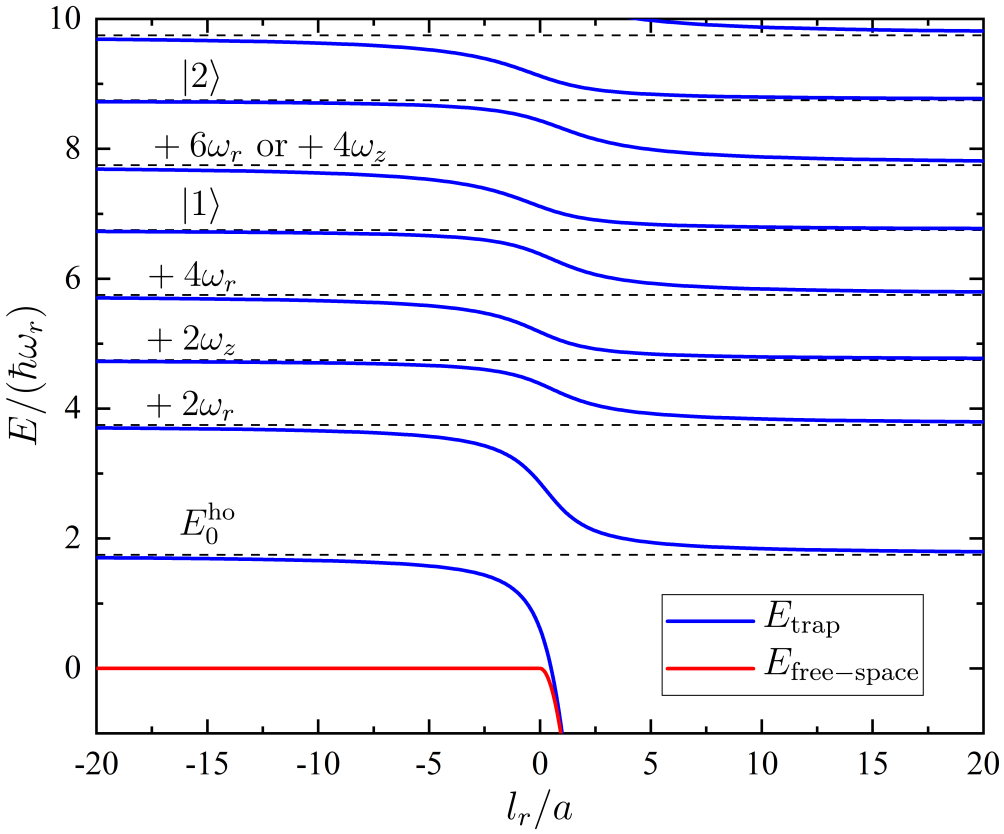


Figure 4.28: Energy spectrum of two atoms in a trap with an aspect ratio of $\eta = 2/3$. Energy spectra are generally complex, unlike in the special case with $\eta^{-1} \approx 4$ shown in Fig. 4.27. Here, $\eta$ is specifically chosen to show even $\omega_r$ and $\omega_z$ harmonic levels and their combinations (states $|1\rangle$ and $|2\rangle$). For example, energies of states $|1\rangle$ and $|2\rangle$ can be formed by combinations such as $E_0^{\rm ho} + 2\hbar\omega_r + 2\hbar\omega_z$ and $E_0^{\rm ho} + 4\hbar\omega_r + 2\hbar\omega_z$, respectively.

First, we determine the $B$–field value by taking an atomic lineshape with a small number of atoms. Second, we take a dissociation spectrum and extract the dissociation threshold frequency by fitting the measured spectrum to a function that is a convolution of Eq. 4.7 and the spectrum of a Gaussian probe pulse. Third, we determined the $B$–field value again. Last, we use these spectroscopic measurements and our understanding of confinement-related frequency shifts to determine the true free-space $E_b$ value with a corresponding $B$–field value. Overall, one $E_b$ value measurement takes 2–3 hrs. Aside from RF amplitude, power and duration, we vary the TOF for different $E_b$ measurements. We decrease the TOF for high-$E_b$ values to limit cloud's shape distortion at large RF detunings. While shorter TOF decreases our overall signal (the quantization field does not fully turn on), we get better image fits and overall signal-to-noise ratio. We verified that our experimental procedure is immune from the discussed systematic effects and that it consistently results in the same (within error) $E_b$ measurement.

### 4.5.2 Precise Binding Energy Data

Precision spectroscopy data are shown in Table 4.1. For each individual measurement, we take weighted mean $\bar{f}_{\mathrm{A}}$ of the two measured atomic lineshape centers $f_{\mathrm{A},1}$ and $f_{\mathrm{A},2}$ to extract a single $B$–field value using the Breit-Rabi formula. The weighted mean lineshape center and its uncertainty are defined as

$$\bar{f}_{\mathrm{A}} = \left( \sum_{i=0}^{N} \sigma_{\mathrm{A},i}^{-2} \right)^{-1} \sum_{i=0}^{N} f_{\mathrm{A,i}} \sigma_{\mathrm{A},i}^{-2} \tag{4.22}$$

$$\bar{\sigma}_{\mathrm{A}} = \left( \left( \sum_{i=0}^{N} \sigma_{\mathrm{A},i}^{-2} \right)^{-1} \frac{1}{N-1} \sum_{i=0}^{N} \frac{\left( f_{\mathrm{A,i}} - \bar{f}_{\mathrm{A}} \right)^2}{\sigma_{\mathrm{A},i}^2} \right)^{1/2}, \tag{4.23}$$

where $f_{\mathrm{A,i}}$ and $\sigma_{\mathrm{A},i}$ are lineshape centers and uncertainties of individual measurements and $N$ is the number of measurements (in our case $N = 2$). We subtract the mean atomic frequency $\bar{f}_{\mathrm{A}}$ from the frequency in the dimer dissociation spectrum. Then, we fit the molecular spectrum to a function function that is a convolution of Eq. 4.7 and the spectrum of a Gaussian probe pulse, fixing the pulse duration and floating an overall scaling amplitude, to extract the dimer dissociation threshold

frequency $f_{\mathrm{D}}$. The uncertainty on $f_{\mathrm{D}}$ is taken as the sum in quadrature of the fit error and the uncertainty on the atomic transition $\bar{\sigma}_{\mathrm{A}}$, which is the dominant uncertainty at small $f_{\mathrm{D}}$. The energy $hf_{\mathrm{D}}$ corresponds to the binding energy of a dimer in a trap. To determine the confinement-related frequency shift of initial and final states, we approximate the scattering length of initial state as $a = \sqrt{hf_{\mathrm{D}}m/\hbar^2}$ and $a = -19\,a_0$ for the final state. We also take $a$ values from theory (using $B$ as input) and determine similar shift values. The total confinement-related shift is similar for all our measurements and is approximately equal to the zero point energy $E_0^{\mathrm{ho}} = 87.3(1.4)\,\mathrm{Hz}$, where the uncertainty is from uncertainty on our trapping frequencies. We subtract the total confinement shift from the dissociation threshold frequency $f_{\mathrm{D}}$ to extract the dimer binding energy in free space $E_b$.

Table 4.1: Precise binding energy spectroscopy data. The $B$–field is determined from the weighted mean $\bar{f}_{\mathrm{A}}$ of two atomic lineshape centers $f_{\mathrm{A},1}$ and $f_{\mathrm{A},2}$, taken before and after the molecular spectrum. The molecular dissociation threshold frequency $f_{\mathrm{D}}$ corresponds to the dimer binding energy in a trap, while $E_b$ corresponds to the free-space dimer binding energy.

| atom lineshape center $f_{\mathrm{A},1}$ (MHz) | atom lineshape center $f_{\mathrm{A},2}$ (MHz) | atom lineshapes mean $\bar{f}_{\mathrm{A}}$ (MHz) | corresponding $B$–field (G) | mol. threshold $f_{\mathrm{D}} - \bar{f}_A$ (kHz) | free-space $E_b/h$ (kHz) |
|---|---|---|---|---|---|
| 446.870 873(67) | 446.870 945(63) | 446.870 911(52) | 33.7420(3) | 2.190(56) | 2.103(56) |
| 446.861 460(78) | 446.861 312(76) | 446.861 384(76) | 33.7978(4) | 3.989(78) | 3.901(78) |
| 446.852 714(79) | 446.852 546(82) | 446.852 634(82) | 33.8494(5) | 6.095(85) | 6.008(85) |
| 446.834 376(61) | 446.834 445(57) | 446.834 413(48) | 33.9575(3) | 12.274(57) | 12.187(57) |
| 446.826 070(69) | 446.825 957(59) | 446.826 004(60) | 34.0078(4) | 15.708(67) | 15.621(67) |
| 446.816 781(61) | 446.817 086(55) | 446.816 950(116) | 34.0622(7) | 20.139(122) | 20.052(122) |
| 446.800 019(79) | 446.800 145(76) | 446.800 085(71) | 34.1644(4) | 29.919(83) | 29.832(83) |
| 446.783 321(76) | 446.783 547(73) | 446.783 439(96) | 34.2663(6) | 41.847(103) | 41.760(103) |
| 446.748 851(78) | 446.748 911(73) | 446.748 883(57) | 34.4812(4) | 74.382(93) | 74.295(93) |
| 446.731 051(77) | 446.731 033(101) | 446.731 045(61) | 34.5940(4) | 95.395(137) | 95.307(137) |
| 446.667 723(82) | 446.667 598(77) | 446.667 657(71) | 35.0060(5) | 200.293(406) | 200.205(406) |
| 446.621 332(86) | 446.621 191(74) | 446.621 252(75) | 35.3198(5) | 308.716(436) | 308.628(436) |
| 446.559 027(89) | 446.558 891(79) | 446.558 951(76) | 35.7593(6) | 508.003(582) | 507.916(582) |
| 446.505 076(79) | 446.505 255(85) | 446.505 160(86) | 36.1582(7) | 742.262(1071) | 742.175(1071) |
| 446.432 524(82) | 446.432 562(79) | 446.432 544(58) | 36.7303(5) | 1167.324(1031) | 1167.237(1031) |

### 4.5.3 Using $E_b$ Data to Characterize our Feshbach Resonance

We use precision spectroscopy dimer binding energy data to accurately determine the Feshbach resonance location $B_0$. One can extract the Feshbach resonance properties by using the dimer energy equation $E_b = \hbar^2/\left(ma^2\right)$ together with the scattering length relation

$$a(B) = a_{\mathrm{bg}}\left(1 - \frac{\Delta B}{B - B_0}\right), \tag{4.24}$$

where the background scattering length $a_{\mathrm{bg}}$, the resonance location $B_0$ and the width $\Delta B$ are the parameters that characterize a Feshbach resonance [19]. However, based on previous studies of scattering properties in $^{39}$K [59, 38], the resonance near $B = 34\,\mathrm{G}$ is affected by a nearby resonance (see Fig. 4.29), making the isolated-resonance Eq.4.24 inapplicable. In such a scenario, a more appropriate equation includes information about the nearby resonance [127]

$$a(B) = a_{\mathrm{bg}}\left(1 - \frac{\Delta B}{B - B_0} - \frac{\Delta B_2}{B - B_{0,2}}\right), \tag{4.25}$$

where $B_{0,2}$ and $\Delta B_2$ are the location and the width of the second resonance. To be able to use this equation for characterizing our Feshbach resonance we would need to know the details about the second resonance. Since we didn't perform measurements near $B_{0,2}$, we would need to rely on previous studies [59, 38] for such details. We take a rather different approach, relying on a coupled-channel two-body model for $^{39}$K [128]. Such a model is able to predict many two-body physical observables (for all spin states and for any $B$–field), including $a$, $E_b$, inelastic collision rate and Feshbach resonances, with only two free parameters: the singlet and triplet scattering lengths $a_{\mathrm{s}}$ and $a_{\mathrm{t}}$ characterizing interaction potentials. The model we started with was already state-of-the-art and only required fine-tuning to match out precise $E_b$ data, similar to Refs. [20, 111]. Therefore, we were able to accurately predict most observables before the final fine-tuning procedure.

The first thing we do with the model is see what value of $B_0$ does it predict and if that value is consistent with our data. We can use Eq. 4.25 to fit the numerical map $a(B)$ given by the model and extract $a_{\mathrm{bg}} = -19.69\,a_0$, $B_0 = 33.5808\,\mathrm{G}$, $\Delta B = 54.50\,\mathrm{G}$, $B_{0,2} = 162.34\,\mathrm{G}$ and $\Delta B_2 = -36.13\,\mathrm{G}$, where all these are free parameters in the fit spanning 0–200 G. If we fix the

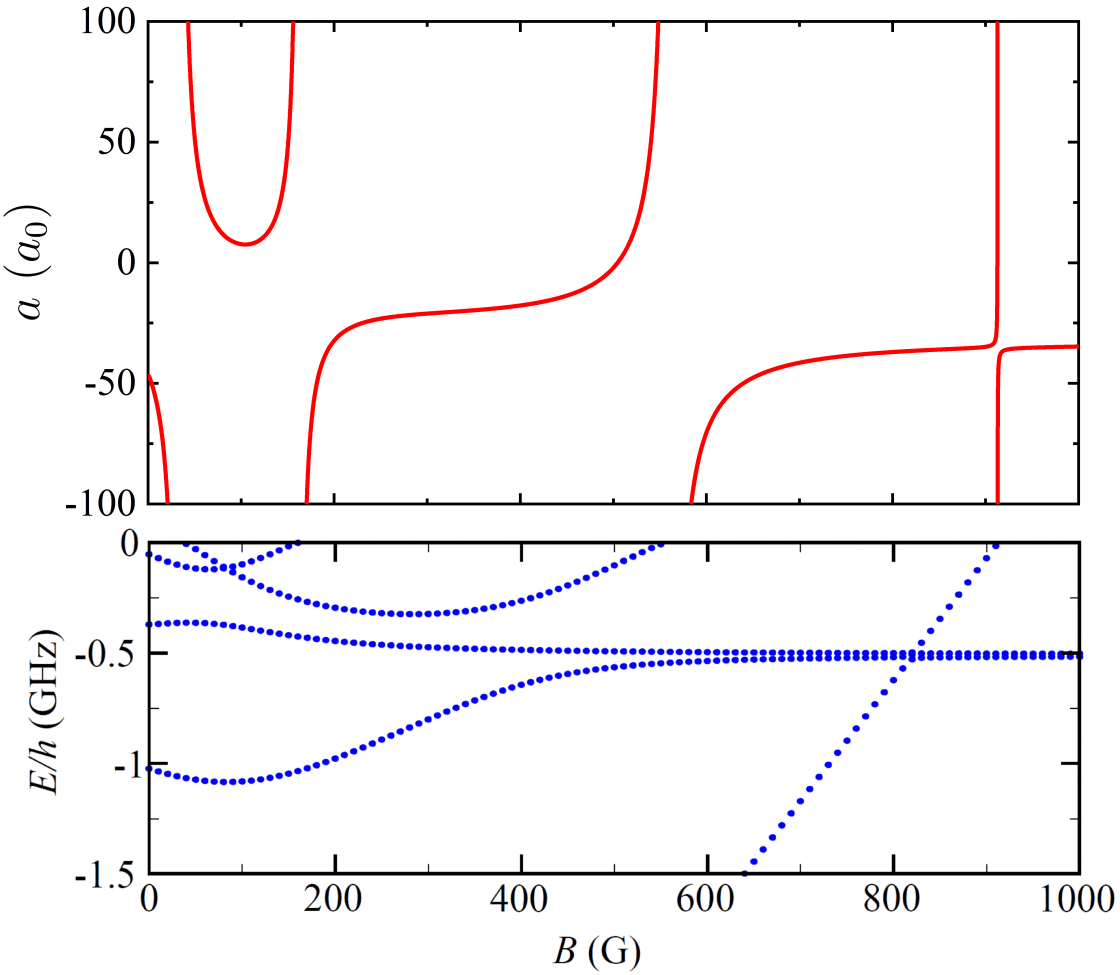


Figure 4.29: Feshbach resonances and the corresponding molecular states for $|\mathrm{F}=1,\mathrm{m_F}=-1\rangle$ hyperfine state. The scattering lengths (top) and energies of molecular states (bottom) were extracted from a coupled-channel model [128]. The Feshbach resonance located at $B \approx 34\,\mathrm{G}$ is being affected by the nearby resonance located at $B \approx 162.3\,\mathrm{G}$. This is evidenced by the lack of a scattering length zero-crossing in the region between the resonances and by the crossing of the two molecular states.

second resonance values to be constant in the fit to Eq. 4.25 or if we fit to Eq. 4.24 (on a smaller $B$–field scale), we extract the same values for $B_0$ and for the product $a_{\rm bg}\Delta B$ (the values $a_{\rm bg}$ and $\Delta B$ do change). This demonstrates the robustness of finding an analytic map of $a$ versus $B$. Now, we can use Eq. 4.25 along with the universal equation for $E_b$ to compare with our $E_b(B)$ data. The first thing we notice is that the universal relation for $E_b$ becomes inapplicable for most of our data and we resort to the well-known higher-order corrections to the binding energy:

$$E_b = \frac{\hbar^2}{ma^2}, \tag{4.26}$$

$$E_b = \frac{\hbar^2}{m\left(a-\bar{a}\right)^2}, \tag{4.27}$$

$$E_b = \frac{\hbar^2}{m\left(a-\bar{a}\right)^2}\left(1+g_1\frac{\bar{a}}{a-\bar{a}}+g_2\frac{\bar{a}^2}{\left(a-\bar{a}\right)^2}\right), \tag{4.28}$$

where $\bar{a} = 4\pi r_{\rm vdW}/\Gamma(1/4) = 0.955978\ldots r_{\rm vdW}$ is the mean scattering length of the background scattering potential [28], $g_1 = \Gamma(1/4)^4/(6\pi^2) - 2 = 0.9179\ldots$ and $g_2 = (5/4)g_1^2 - 2 = -0.9468\ldots$ [129]. In our case, the van der Waals length $r_{\rm vdW} = \frac{1}{2}\left(mC_6/\hbar^2\right)^{1/4} = 64.49\,a_0$, where the $C_6$ coefficient [49, 50] characterizes the strength of the van der Waals potential $V_{\rm vdW}(r) \propto -C_6/r^6$ at large inter-atomic distances $r$, determines the relevant length and energy scales $\bar{a} = 61.65\,a_0$ and $\bar{E} = \hbar^2/m\bar{a}^2 = 24.37\,\text{MHz}$ for $E_b$ corrections.

We look at the applicability of Eqs. 4.26–4.28 by plotting $E_b(a-\bar{a})^2m/\hbar^2$ (see Fig. 4.30), where $E_b(B)$ is our data and $a(B)$ is from Eq. 4.25 with parameters taken from the model. The data should converge to $E_b(a-\bar{a})^2m/\hbar^2 = 1$ if the model predicts a correct value for $B_0$. We vary $B_0$ in the analytic expression for $a(B)$ (Eq. 4.25) and (visually) find that the $B_0 = 33.5808\,\text{G}$ predicted by the model is (coincidentally) a good value to within a few-mG. First, we note that only Eq. 4.27 (with first-order $\bar{a}$ correction) matches our data. Additionally, we note that our data does not agree with any of the Eqs. 4.26–4.28 relations away from the resonance, where $E_b$ is large. Such tweaking of $B_0$ cannot make the theory match our data for all $E_b$ values, as small adjustments in $B_0$ mostly affect the $E_b(a-\bar{a})^2m/\hbar^2$ points near $B_0$ and have little affect on the points away from the resonance.

The applicability of simple relations for $E_b$ discussed above is only valid when the dimer

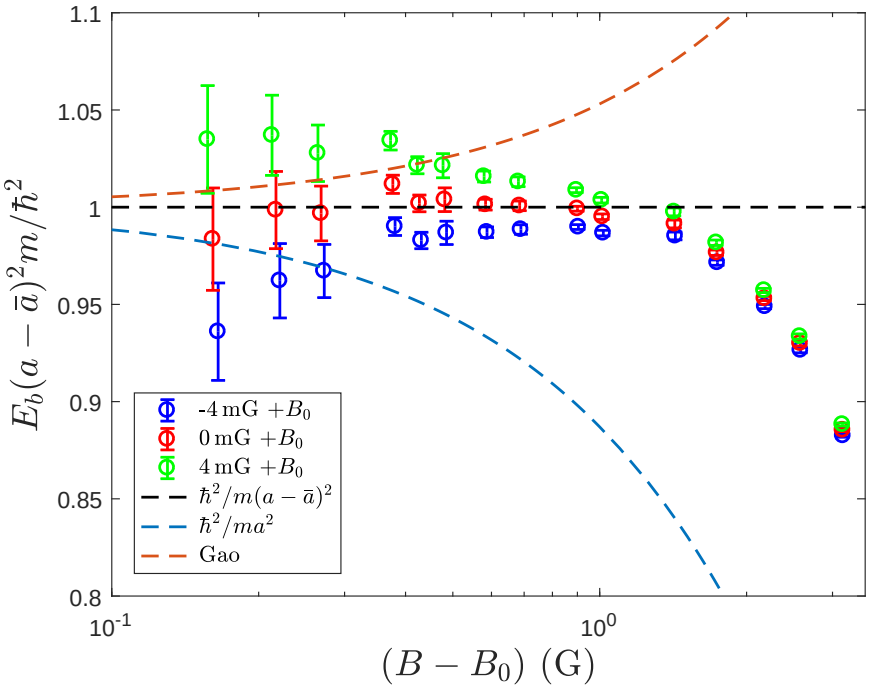


Figure 4.30: Comparing our $E_b$ data with the expressions Eqs. 4.26–4.28 and approximating the Feshbach resonance location $B_0$. Here, $E_b(B)$ is our data and $a(B)$ is from Eq. 4.25 with parameters taken from the model. The different relations for $E_b$ agree near the resonance, where $E_b$ corrections are small ($a \gg \bar{a}$, $E_b \ll \bar{E}$), and differ away from the resonance. We find that the universal expression (dashed blue) with a first-order correction $E_b = \hbar^2/m\,(a-\bar{a})^2$ (dashed black, horizontal) is sufficient in describing our data near the resonance. An expression with a higher-order correction (dashed orange, Eq. 4.28, Gao) does not match our data. Additionally, we vary $B_0 = 33.5808\,\mathrm{G}$ by $\pm 4\,\mathrm{mG}$ (in Eq. 4.25) to see if the model predicts a correct Feshbach resonance location.

bound state has a spin character of the entrance channel [19]. A dimensionless resonance strength parameter $s_{\mathrm{res}}$ classifies Feshbach resonances into broad (entrance channel dominated) resonances for $s_{\mathrm{res}} \gg 1$ and narrow (closed channel dominated) resonances for $s_{\mathrm{res}} \ll 1$:

$$s_{\mathrm{res}} = \frac{a_{\mathrm{bg}}}{\bar{a}} \frac{\Delta\mu_{\mathrm{b}} \Delta B}{\bar{E}}, \tag{4.29}$$

where $\Delta\mu_{\mathrm{b}}$ is the magnetic moment of the bound state near $B_0$ (in our case $\Delta\mu_{\mathrm{b}} = 2.6\,\mathrm{MHz/G}$, which is extracted from molecular spectra similar to that shown in Fig. 4.29). For narrow Feshbach resonances, the dimer binding energy follows the universal expression only in a very narrow region near $B_0$ and follows the energy of the closed-channel bound state $\Delta\mu_{\mathrm{b}}(B - B_0)$ away from the resonance. While our resonance is broad in terms of width $\Delta B$, it is of moderate width according

to the stated classification, with $s_{\mathrm{res}} = 1.9$.

A coupled-channel (cc) model is required to accurately describe observables near Feshbach resonances of narrow and intermediate strength. We use such a model to predict the dimer binding energies $E_b$ for same $B$–field values as in our data. While the initial predictions matched our data well, there was a clear trend in the relative residuals, defined as $(E_b^{\mathrm{data}} - E_b^{\mathrm{theory}})/E_b^{\mathrm{data}}$, that was much larger than our experimental uncertainty. Therefore, we fine-tune the model's singlet and triplet potentials to accurately match most of our measurements to within 1%, as shown in Fig. 4.31 inset.

We adjust the model's parameters by performing a global fit to our $E_b(B)$ data. Specifically, we adjust two parameters (we call $\delta_{\mathrm{S}}$ and $\delta_{\mathrm{T}}$) that fine-tune the singlet and triplet potentials, respectively, and which ultimately determine the singlet and triplet scattering lengths $a_{\mathrm{S}}$ and $a_{\mathrm{T}}$. The realistic two-body model is fully determined by $a_{\mathrm{S}}$ and $a_{\mathrm{T}}$, allowing extraction of two-body observables, including $a(B)$ and molecular spectra (as shown in Fig. 4.29).

To perform the fit, we generate a grid of predicted $E_b$ values vs. $\delta_{\mathrm{S}}$ and $\delta_{\mathrm{T}}$ for every experimental $B$–field value that we have $E_b$ data for, an example is shown in Fig. 4.32. We note that the predicted $E_b$ values at each magnetic field are predominately determined by a particular linear combination of $\delta_{\mathrm{S}}$ and $\delta_{\mathrm{T}}$, as evidenced by the linearity of $E_b$-contour lines in Fig. 4.32. Similarly, the Feshbach resonance location $B_0$ is predominately determined by the same linear combination. We are able to get a better fit, and thus place tighter constraints on $B_0$, by performing the fit in the rotated $\delta_{\mathrm{S}}$ and $\delta_{\mathrm{T}}$ basis. The rotation angle is chosen to give the smallest $B_0$ error; the angle value is particular for our Feshbach resonance, varies negligibly for different fields and does not affect the $B_0$ value (to within error, see Fig. 4.33). A "local" fit uses the observed $E_b$ value to constraint $\delta_{\mathrm{S}}$ and $\delta_{\mathrm{T}}$ for each $B$. We use a "global" fit that constraints $\delta_{\mathrm{S}}$ and $\delta_{\mathrm{T}}$ using all $E_b(B)$ data at once, weighing each $E_b$ data value by its uncertainty.

The fit allows us to constrain the corresponding linear combination of $a_{\mathrm{S}}$ and $a_{\mathrm{T}}$ to a high precision: $\sin(0.2496)\, a_{\mathrm{S}} + \cos(0.2496)\, a_{\mathrm{T}} = 1.926(2)\, a_0$. Additionally, we deduce $B_0 = 33.5820(14)\,\mathrm{G}$, where the uncertainty is the fit error added in quadrature with 0.5 mG, the average uncertainty on

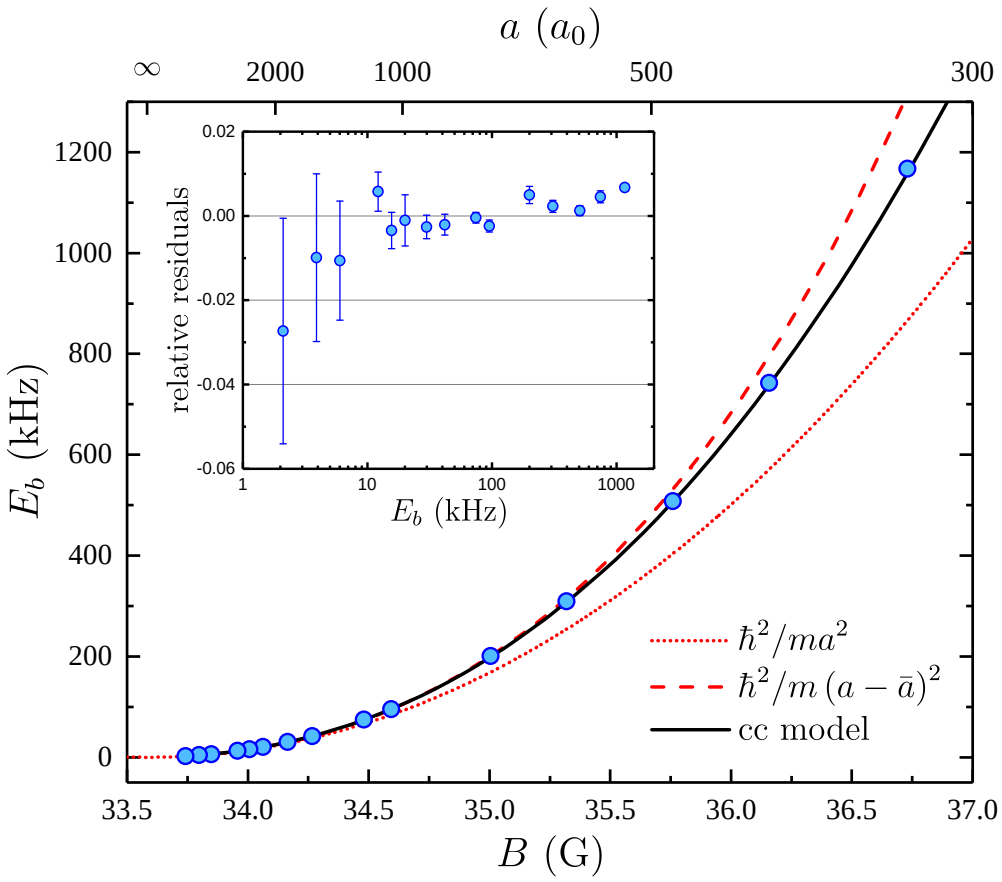


Figure 4.31: Precise measurement of Feshbach dimer binding energies $E_b$ as a function of magnetic field $B$. Small experimental uncertainties on $E_b$, spanning from 56 Hz at $E_b/h = 2.19$ kHz to 1.0 kHz at $E_b/h = 1167$ kHz, are not resolvable in the figure. A coupled-channel (cc) model is required to describe our data. The solid curve shows the resulting fit and the inset shows remarkably small fractional residuals. Contrary to applicability near broad Feshbach resonances, universal expressions Eqs. 4.26, 4.27 (dashed and dotted curves) are insufficient for describing $E_b$ near our intermediate strength resonance.

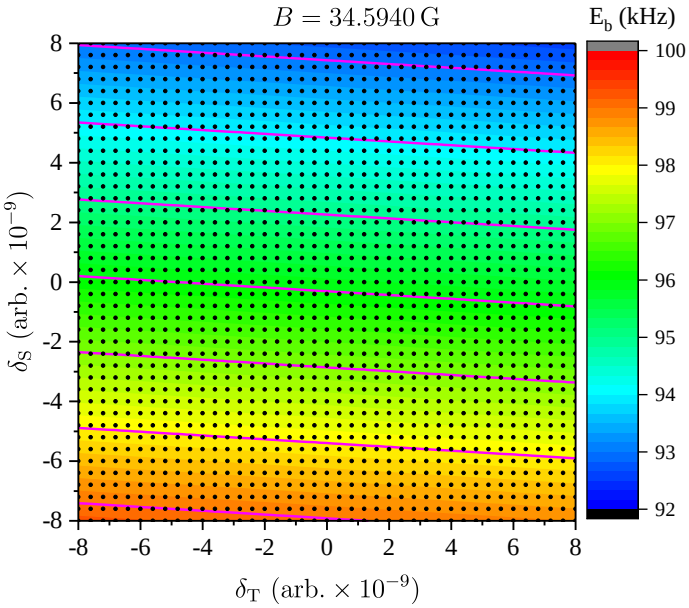


Figure 4.32: A contour map shows an example of CC-model tuning at 34.5940 G. The model predicts $E_b$ values for a fine $\delta_S$ and $\delta_T$ grid (points). The contour lines (magenta, spaced at 1 kHz) show that $E_b$ values depend on a particular linear combination of $\delta_S$ and $\delta_T$. The measured value $E_b(34.5940\,\mathrm{G}) = 95.395(137)\,\mathrm{kHz}$ can be used to constrain the model's $\delta_S$ and $\delta_T$ values.

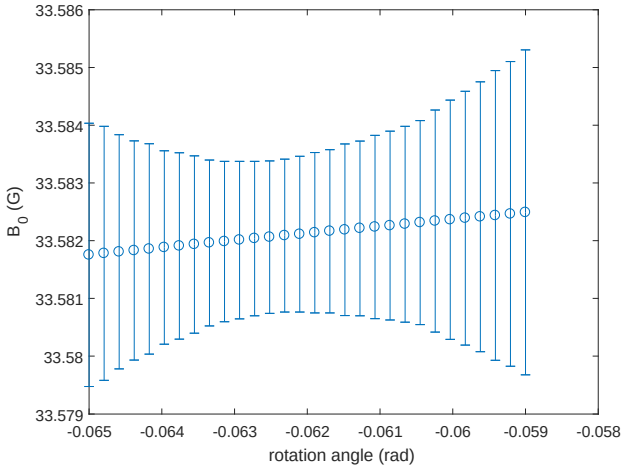


Figure 4.33: There is negligible dependence of the extracted $B_0$ value on the angle used to rotate $\delta_S$ and $\delta_T$ basis before the fit. Here, we perform a global fit on all points, excluding the $E_b$ point at 36.7303 G.

$B$ in our $E_b$ spectroscopy data. The $E_b(36.7303\,\mathrm{G}) = 1167\,\mathrm{kHz}$ data point leads to a significant increase in our reduced-$\chi^2$ and we exclude it in our final fit. However, note that masking any data (single or multiple points) in our global fit results in the same $B_0$ value, within the quoted error.

We can combine our result with the location constraint on the 560.72(20) G (measured elsewhere [38]) Feshbach resonance to extract $a_S = 138.85\,a_0$ and $a_T = -33.40\,a_0$ (see Fig. 4.34), where $a_S$ value is predominately determined by the resonance at 560.72(20) G. These values are similar to the previously-reported values extracted from many Feshbach resonances: $a_S = 138.49(12)\,a_0$ and $a_T = -33.48(18)\,a_0$ from [50] and $a_S = 138.90(15)\,a_0$ and $a_T = -33.3(3)\,a_0$ from [59].

The fine-tuned model, with determined $a_S$ and $a_T$, predicts many two-body observables, including $a(B)$ map, $E_b(B)$, and the two-body inelastic coefficient $L_2(B)$. Due to the presence of a nearby Feshbach resonance, we fit $a(B)$ to a two-resonance expression Eq. 4.25 to extract additional resonance parameters: $a_{bg} = -19.599\,a_0$, resonance widths $\Delta B = 54.772$ G and $\Delta B_2 = -36.321$ G, the second resonance location $B_{0,2} = 162.341$ G (consistent with the previously-measured result $B_{0,2} = 162.35(18)$ G [38]) and $s_{res} = 1.9$ (using Eq. 4.29 and $\Delta\mu_b = 2.6$ MHz/G).

While the final fit relative residual is greater than the fraction experimental uncertainty at large $E_b$, we do not expect the cc-model to fully capture all short-range physics and are content with its accuracy. Overall, our $B_0 = 33.5820(14)$ G measurement is two-orders of magnitude improvement over the previous measurement of this resonance: $B_0 = 33.64(15)$ G [38]. Additionally, considering the resonance width $54.772\,\text{G} \gg 1.4\,\text{mG}$ uncertainty, our scattering length values have unprecedented accuracy when compared to previous measurements in many atomic species [20].

## 4.6 Measurement of Molecular Lifetimes

We build further confidence in our coupled-channel model by comparing its predictions with a different two-body observable, the dimer lifetime. We made this choice based on our interest to understand the inelastic loss rate for our other studies. The model introduces two-body loss by allowing spin relaxation to lower-energy states via $d$–wave coupling. As a result of loss, $a$ is no longer (fully) divergent at $B_0$ and scattering properties near such a decaying resonance are best

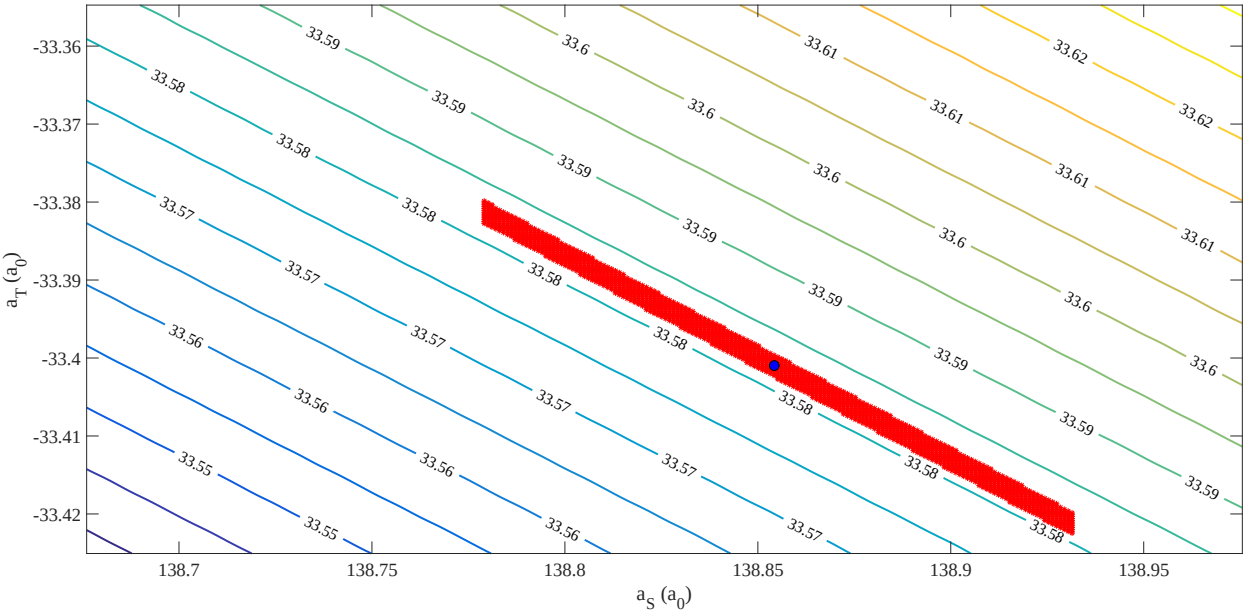


Figure 4.34: Constraints on the singlet $a_{\mathrm{S}}$ and triplet $a_{\mathrm{T}}$ scattering lengths using our $E_b$ data near the $B_0 = 33.5820(14)\,\mathrm{G}$ Feshbach resonance and the location of the $560.72(20)\,\mathrm{G}$ (measured elsewhere [38]) Feshbach resonance. While our data constrains a particular linear combination of $a_{\mathrm{S}}$ and $a_{\mathrm{T}}$ to a high precision: $\sin(0.2496)\,a_{\mathrm{S}} + \cos(0.2496)\,a_{\mathrm{T}} = 1.926(2)\,a_0$, the $a_{\mathrm{S}}$ value is predominately determined by the resonance at $560.72(20)\,\mathrm{G}$. The red region represents our uncertainty on the mean values $a_{\mathrm{S}} = 138.85\,a_0$ and $a_{\mathrm{T}} = -33.40\,a_0$ (blue point). The contour lines, spaced $5\,\mathrm{mG}$ apart, represent the predicted $B_0$ for given $a_{\mathrm{S}}$ and $a_{\mathrm{T}}$ values.

described by a complex scattering length $\tilde{a} = a - ib$ [19]:

$$a(B) = a_{\mathrm{bg}} - a_{\mathrm{res}} \frac{\gamma\,(B - B_0)}{(B - B_0)^2 + (\gamma/2)^2}, \tag{4.30}$$

$$b(B) = \frac{1}{2} a_{\mathrm{res}} \frac{\gamma^2}{(B - B_0)^2 + (\gamma/2)^2}, \tag{4.31}$$

where $b$ is the inelastic scattering length, $\gamma$ is the (Lorentzian) width of the Feshbach resonance near $B_0$ and $a_{\mathrm{res}}$ is the maximum amplitude of the scattering length. In presence of a nearby Feshbach resonance, the background scattering length is taken as $a_{\mathrm{bg}}(B) = a_{\mathrm{bg},2}\,(1 - \Delta B_2/(B - B_{0,2}))$. Using the values $a(B)$ (or $b(B)$) predicted by the model, we extract $\gamma = 0.101\,\mathrm{mG}$ and $a_{\mathrm{res}} = -1.06 \times 10^7\,a_0$ for our resonance; note that the resonance pole strength $\gamma a_{\mathrm{res}} = a_{\mathrm{bg}}\Delta B$ from Eq. 4.24 definition. The closed channel bare state lifetime $\tau_{\mathrm{res}} = (2\pi\gamma\mu_{\mathrm{b}})^{-1} = 610\,\mu\mathrm{s}$ sets the relevant timescale of two-body loss processes. For example, the inelastic two-body loss coefficient $L_2$, characterizing atom loss $dN/dt = -L_2\langle n\rangle N$, is determined from [130]

$$L_2(B) = \frac{16\pi\hbar}{m} b(B). \tag{4.32}$$

Additionally, the spontaneous one-body dimer decay time $\tau_{1\mathrm{b}}$, initially introduced in Sec. 4.4.1, relates to $L_2$ only by a volume term [104, 120]

$$\tau_{1\mathrm{b}}(B) = \frac{4\pi a^3}{L_2(B)}. \tag{4.33}$$

We perform dimer lifetime measurements of pure molecular samples, prepared in a similar fashion as described in Sec. 4.4.2. We hold molecular samples at specified $B$–field values for a varied duration. Instead of using RF dissociation for molecular detection (as shown in Fig. 4.19), we dissociate dimers by ramping the magnetic field back across the resonance to $a \approx -100\,a_0$, an "inverse" magneto-association method. There, we use a 5.3 ms rectangular ARP pulse to transfer all remaining atoms from the $|\mathrm{F} = 1, \mathrm{m_F} = -1\rangle$ state to the $|\mathrm{F} = 2, \mathrm{m_F} = -2\rangle$ before imaging. This method of counting molecules has several advantages over the method used for $E_b$ spectroscopy. We gain a factor of 2 in signal by detecting both atoms in the molecular pair and a factor of $\sim 1.7$ by using the $|\mathrm{F} = 2, \mathrm{m_F} = -2\rangle$ state for imaging rather than $|\mathrm{F} = 2, \mathrm{m_F} = 0\rangle$ state, which has no

optical cycling transitions. Additionally, the efficiency and stability of the ARP and the magneto-dissociation procedure improve our shot-to-shot number noise. These signal improvements were crucial and allow us to measure dimer lifetimes of small-density molecular samples, whose lifetimes were not affected by dimer-dimer inelastic loss (Eq. 4.11).

A compilation of our dimer lifetime data is presented in Fig. 4.35. We measure molecular lifetimes from $B = 33.743\,\mathrm{G}$ to $B = 55.947\,\mathrm{G}$, corresponding to ranges $E_b = 0.0021$–$45.6\,\mathrm{MHz}$ and $a = 6642$–$35\,a_0$. We observe an intriguing maximum near $E_b = 24\,\mathrm{MHz}$ ($a = 61\,a_0$, $B = 48.09\,\mathrm{G}$) with a lifetime of 43 ms. We can compare our data with the coupled-channel predictions in two different ways. First, we perform a local fit to $a(B)$ from theory using Eq. 4.30 to extract $b(B)$ and $L_2$ near the resonance, and therefore $\tau_{1\mathrm{b}}(B)$ via the universal relation in Eq. 4.33. While we find a good agreement between theory and our data at intermediate and high scattering lengths, the predicted $\tau_{1\mathrm{b}}(B)$ values are feature-less at small $a$. Second, we use $L_2(B)$ values (or $b(B)$) directly predicted by the model, which have a complicated structure, as depicted in Fig. 4.36. While theory does predict an $L_2$ maximum, and hence a lifetime maximum, at small $a$, its position ($B = 42\,\mathrm{G}$, $a = 114\,a_0$) is significantly different from the observed lifetime maximum location. Such deviations at small scattering lengths are not surprising, considering that the universal Eq. 4.33 does not encompass short-ranged physics nor the proper spin channel composition of the deeply-bound states. Future theoretical advancements, with models that are capable to directly predict molecular lifetime, are required to fully understand our data.

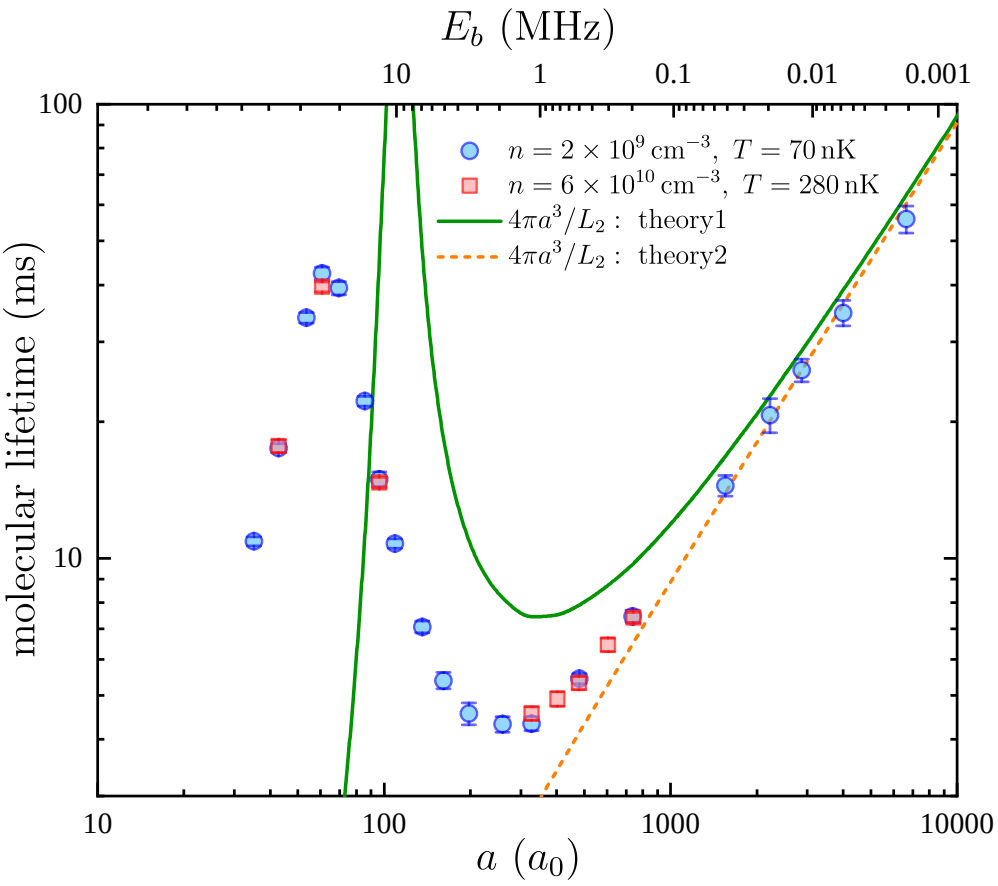


Figure 4.35: Molecular lifetimes at different scattering lengths. Observation of similar lifetimes with different densities and temperatures suggests the one-body nature of the decay. Dimer lifetime is related to the inelastic coefficient $L_2$ by a simple relation Eq. 4.33. While the coupled-channel predictions match our data at high $a$ values, a complicated structure at low $a$ is hard to predict. The solid curve (theory1) uses $L_2$ values directly from theory (see Fig. 4.36). The dashed curve (theory2) uses $L_2$ values extracted from parameters of a local fit to the resonance Eq. 4.30, using select $a(B)$ values from theory.

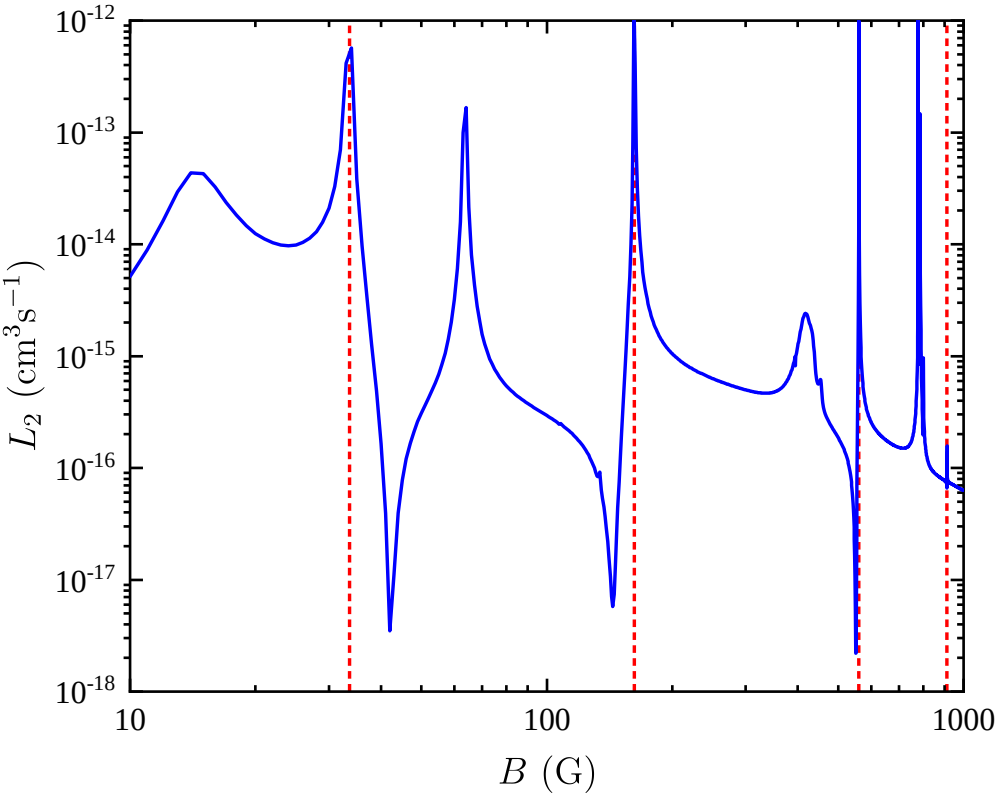


Figure 4.36: The coupled-channel model predicts a complicated behavior of the $L_2$ inelastic coefficient. The vertical dashed lines correspond to the known Feshbach resonances, shown in Fig. 4.29.

# Chapter 5

## Measurement of a Nonuniversal Efimov Ground State Location

Building on our understanding of two-body physics (discussed in Ch. 4), we seek to provide some insight on the exotic three-body Efimov physics. Specifically, we precisely measure the Efimov ground state location near our Feshbach resonance and find significant deviation from the value predicted by van der Waals universality. I begin with an overview of how our work fits into the bigger picture of previous Efimov studies. I detail the experimental procedure, along with the many systematic error sources we've considered, to build confidence in our measurement. I briefly mention our attempts to find signatures of the second Efimov state and four-body Efimov physics.

### 5.1 Previous Studies of Efimov Physics in Ultracold Gases

Although the Efimov effect was initially introduced for nuclear physics in 1970 [29], it only gained considerable interest in the last decade after experimental observations in ultracold atomic gases. The first evidence of an Efimov state was observed via atom-loss spectroscopy [30] in $^{133}$Cs. The degeneracy of the Efimov trimer state energy with the three-atom threshold continuum ($E = 0$, $a < 0$) at $a = a_-$ (see Fig 5.1) results in new decay pathways to deeply-bound molecular states (via recombination) and leads to an enhancement of the three-body inelastic rate coefficient $L_3$ near $a = a_-$, an Efimov resonance. Since detection methods based on populating the Efimov state via RF- [131, 132, 133] and magneto-association [134] are difficult and are limited by short trimer lifetimes $\mathcal{O}(100\,\mu\text{s})$, atom-loss spectroscopy proves to be the simplest and most widely-used method for studying Efimov physics. For example, this method enabled observation of the second

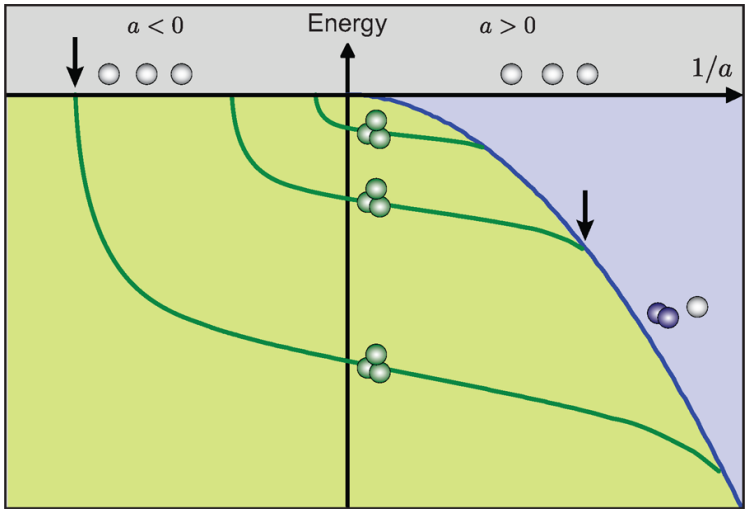


Figure 5.1: Energy spectrum of Efimov trimer states (green lines). For $a < 0$, Efimov states intersect the three-atom threshold continuum (gray region), with the ground state intersecting at $a = a_-$ (arrow). For $a > 0$, Efimov states intersect the atom-dimer continuum (blue region $-\hbar^2/ma^2 < E < 0$). Each consecutive Efimov state has a spatial extent $\mathcal{O}(|a|)$ that is $\approx 22.7\times$ larger than that of the previous state and an energy $\approx 22.7^2\times$ smaller. This figure is borrowed from Ref. 138. For illustration purposes, Efimov scaling was changed to 2 and not all excited Efimov states are shown.

Efimov state (and hence confirming Efimov series spacing $\approx 22.7$) [43], Efimov features at $a > 0$ [32, 135, 33], four- and five-body Efimov states (tied to the individual three-body Efimov states) [136, 33, 40, 137], and locations $a_-$ in multiple atomic species [52, 47, 97].

One of the biggest surprises in Efimov studies was an observed correlation between the three-body parameter $a_-$ and the van der Waals length $r_{\mathrm{vdW}} = \frac{1}{2}\left(mC_6/\hbar^2\right)^{1/4}$, which characterizes the physical range of the van der Waals potential $V_{\mathrm{vdW}}(r) \propto -C_6/r^6$ at large inter-atomic distances $r$. Measurements across many atomic species and different Feshbach resonances indicate $a_-$ value always within 20% of $-9\,r_{\mathrm{vdW}}$ [37, 46, 47, 48]. While the Efimov spacing was predicted to be universal, $a_-$ was originally thought to depend on the (complicated) short-range physics at inter-atomic distances $r \lesssim r_{\mathrm{vdW}}$, and therefore be non-universal. It is perplexing to find that $a_-$ depends only on the long-range part of the interaction potential. This additional universal aspect of Efimov physics was later (thought to be) theoretically understood, predicting a value $a_- = -9.73\,r_{\mathrm{vdW}}$ close to observations, and deemed it "van der Waals universality" [51, 52]. Physically, a strong

suppression of three-body wavefunction at short distances is responsible for van der Waals universality, preventing particles from accessing nonuniversal regions of interacting potentials. Value $a_- = -9.73\, r_{\mathrm{vdW}}$ is predicted by a model with a hard-wall potential that masks the nonuniversal short-range interaction region. Additionally, multiple theoretical models always predict $a_-$ values [51, 52, 46, 47] that are within $\pm 15\%$ of $-9.73\, r_{\mathrm{vdW}}$, where theoretical uncertainty includes the results of multiple universal models with different details in the short-ranged region.

In principle, as a consequence of van der Waals universality and the universal Efimov spectrum scaling, one can predict the full Efimov spectrum to arbitrary energy and length scales, given only the chosen atomic species mass and the strength of van der Waals potential tail $C_6$, a powerful result. Therefore, understanding the applicability and robustness of van der Waals universality is important.

Most studies of van der Waals universality focus on broad Feshbach resonances, where $s_{\mathrm{res}} \gg 1$ (defined in Eq. 4.29) and universal behavior is expected. For example, $s_{\mathrm{res}}$ can be thought of as the dimensionless parameter that characterizes the region of scattering lengths over which two-body physics follows the universal binding energy relation $E_b = \hbar^2/(ma^2)$: $|a| \gtrsim 4r_{\mathrm{vdW}}/s_{\mathrm{res}}$. Similarly, since two-body interactions mediate three-body attraction in the Efimov effect, there is a notion that three-body Efimov resonances would be more universal as they fall more deeply within the range of $a$ for which the two-body Feshbach resonant structure is universal.

Recent theoretical models incorporating narrow ($s_{\mathrm{res}} \ll 1$) and broad Feshbach resonances suggest that $a_-$ should also, in addition to the van der Waals length, depend on the background scattering length $a_{\mathrm{bg}}$, on $s_{\mathrm{res}}$, and on the details of short-range forces (e.g. three-body forces not directly arising from two-body physics, as is the case for the Efimov effect) [53, 54, 55, 56, 57]. Previous experiments on homonuclear Efimov states [32, 33, 34, 35, 36, 37, 38, 39, 40, 41, 42, 43, 44, 45] suggest some evidence that smaller $s_{\mathrm{res}}$ should correspond to less universal $a_-$ values, see the blue circles in Fig. 5.2. Similarly, a recent indirect measurement of the $a_-$ value in a heteronuclear system [97] suggests the same conclusion. However, such a conclusion is not concrete due to large experimental uncertainties in the measured $a_-$, large systematic uncertainties in the knowledge of

the underlying two-body Feshbach resonance [32, 38, 40, 33] and mysterious temperature-dependent behavior [45]. Precise measurements of $a_-$ are needed to provide clarity on the applicability of van der Waals universality near narrow and intermediate-width Feshbach resonances.

While the strongest observed departure (not including our measurement) from van der Waals universal theory ($3.7\,\sigma$ deviation) occurs in a $^6$Li–$^{133}$Cs system near a narrow Feshbach resonance with $s_{\text{res}} = 0.05$ [97], the nature of heteronuclear systems complicates interpretation of this result. First, heteronuclear systems have more parameters, including two van der Waals lengths, two uncorrelated scattering lengths and a mass ratio. Only specific mass ratios (large mass imbalance) and scattering lengths conditions give rise to interspecies Efimov physics (with a modified Efimov scaling that depends on the mass ratio) and approximate universality [139]. Second, the sign of the scattering length between the two heavy bosons influences the $a_-$ location [140]. Third, molecular two-body physics of heavy bosons can affect and suppress Efimov resonances [140]. In fact, in the aforementioned result of Ref. 97, the ground Efimov resonance is completely absent and the authors extract $a_-$ from an indirect measurement of the second Efimov resonance. Such complications in heteronuclear systems result in a weak evidence for the inapplicability of van der Waals universality near narrow Feshbach resonances.

Previously, the largest deviation ($1.5\,\sigma$) from van der Waals universal theory in a homonuclear system was observed in $^{39}$K near a narrow Feshbach resonance with $s_{\text{res}} = 0.11$ [38]. In addition to that particular Feshbach resonance, the authors of Ref. 38 perform measurements near other Feshbach resonances in $^{39}$K and claim evidence for extension of van der Waals universality to narrow and intermediate Feshbach resonances. This conclusion is incorrect, as their measurements are only consistent with universal theory as a result of large uncertainty on $a_-$ values. Furthermore, an inconsistent use of multiple empirical fit models for $a_-$ extraction and a lack of systematic checks (e.g. finite-temperature) leads to inconclusive results.

With many other instances of $a_-$ measurements having large statistical and systematic uncertainties, we attempt to do better and provide compelling evidence for departure from van der Waals universality. In our work, we accurately determine $a_-$ value near a Feshbach resonance

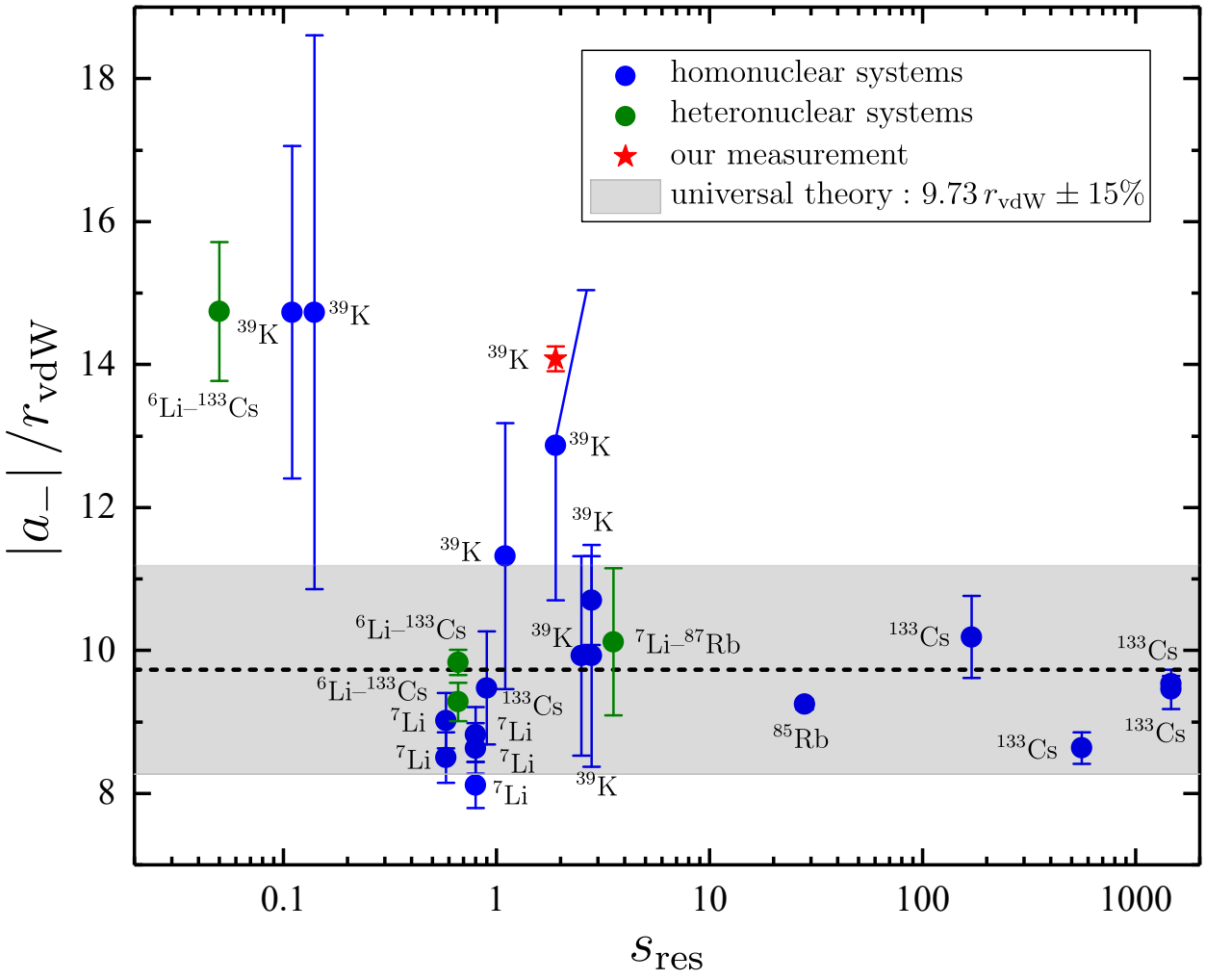


Figure 5.2: A survey of the three body-parameter $a_-$ vs. resonance strength parameter $s_{\mathrm{res}}$ for multiple atomic species and Feshbach resonances. The shown values are taken from previous measurements in homonuclear (blue) [32, 33, 34, 35, 36, 37, 38, 39, 40, 41, 42, 43, 44, 45, 100] and heteronuclear (green) systems [97, 41, 42, 44]. Most values are conveniently found in Ref. 97 suppl. material. For plotting purposes, heteronuclear measured values are rescaled such that universal predictions would occur at $-9.73\,r_{\mathrm{vdW}}$. Our measurement (red) is the strongest evidence of departure from the value predicted by van der Waals universality $a_- = -9.73 \pm 15\%\, r_{\mathrm{vdW}}$ (dashed line and gray region).

of intermediate strength ($s_{\rm res} = 1.9$) by having a precise control of experimental parameters and understanding of systematic error. As a result, we observe $a_- = -14.08(17)\, r_{\rm vdW}$, a significant deviation from the value $-9.73\, r_{\rm vdW}$ predicted by van der Waals universality. Our measurement is the strongest evidence of departure from the value predicted by van der Waals universality and is the first (statistically significant) evidence of departure near a Feshbach resonance of an intermediate strength, as depicted in Fig. 5.2. The deviation we observe is intriguing, considering that previous measurements of the $a_-$ near Feshbach resonances with similar $s_{\rm res}$ were consistent with van der Waals universality and that our background scattering length $a_{\rm bg} = -19.60\, a_0$ is small compared to $\bar{a} = 61.65\, a_0$. Therefore, such a deviation cannot be explained by models with simple corrections to universal theory [53, 54, 55, 56, 57]. We require data comparison with a state-of-the-art three-body multi-channel model [141], constructed using realistic hyperfine and Zeeman spin structure and with singlet and triplet potentials with details constrained by our two-body binding energy measurements. Such a realistic model shows a better agreement with our $a_-$ measurements and is able to, for the first time in the field, to accurately predict the Efimov resonance inelasticity parameter $\eta$.

## 5.2 Experimental Considerations

To accurately determine $a_-$ from atom-loss spectroscopy, we consider and check multiple experimental parameters that can lead to systematic error. I briefly discuss our experimental procedure and parameters that can affect our Efimov resonance measurements, including uncertainty on $a(B)$, trap parameters, uncertainty on atom number and temperature, high phase-space density (PSD) effects, thermalization rate, high-density effects, two- and four-body loss, finite-temperature systematic shifts and finite-range effects.

A typical experimental sequence for measuring three-body recombination is shown in Fig. 5.3. A desired temperature is reached by optimizing evaporation parameters (final trap depths and frequencies, duration,exponential time constant and $B$–field value). The density is varied by enabling three-body loss, holding the sample at a moderate $a \approx 200$–$500\, a_0$ for a duration $\mathcal{O}(10\,\mathrm{s})$ before

and after the two evaporation stages. We do not use a large $a$ for this loss process; doing so would result in unnecessary heating and lack of thermalization, as the three-body loss would be faster than thermalization/evaporation timescales. We verify the sample is thermalized by checking the cloud's temperature along orthogonal directions (should be equal) and if needed, hold the sample for an extra duration before proceeding. Next, since we want to accurately measure loss and heating associated with three-body recombination, we adiabatically increase the trap depth (ramp up horizontal and vertical beam powers) by a factor of 2–4 to prevent any further evaporation. As a result, the mean trapping frequency increases to $\bar{\omega}_f = (U_f/Ui)^{1/2}\,\bar{\omega}_i$, where $U_i$ and $U_f$ are the initial and final trap depths (assuming the same trap depth in all directions) and $\bar{\omega}_i$ is the initial trap frequency. Adiabatic compression also results in heating and density increase:

$$T_f = \frac{\bar{\omega}_f}{\bar{\omega}_i} T_i, \tag{5.1}$$

$$n_f = \left(\frac{\bar{\omega}_f}{\bar{\omega}_i}\right)^{3/2} n_i. \tag{5.2}$$

For example, due to such heating, the trap depth must be increased by a factor of 4 to have a final temperature 1/2 of evaporation threshold temperature ($T \sim U/8$). The adiabatic compression ramp rate depends on the initial density and $a$, being $\mathcal{O}(5s)$ for our lowest density $\langle n \rangle \sim 10^{10}\,\mathrm{cm}^{-3}$ at $100\,a_0$. It is always good to check the atom lifetime and the heating rate to verify that the trap depths are sufficiently-high.

Next, we get rid of $|\mathrm{F}=1, \mathrm{m_F}=0\rangle$ impurity in a similar manner as described in Sec. 4.4.2. We ramp the field across the Feshbach resonance to $B = 21.37\,\mathrm{G}$ ($a = -102\,a_0$) in 10 ms, perform another thermalization check and ramp the field to the value of interest (for loss measurement) in 5 ms. After a varied hold duration, we ramp the $B$–field back to $B = 21.37\,\mathrm{G}$ ($a = -102\,a_0$) in 5 ms, transfer atoms to the $|\mathrm{F}=2, \mathrm{m_F}=-2\rangle$ imaging state using an efficient ARP (duration 5.3 ms, center $f_0 = 418.360\,\mathrm{MHz}$, sweep $\pm 4\,\mathrm{MHz}$ and full 20 W power, note that here our antenna is far from its $\sim 390\,\mathrm{MHz}$ resonance/match frequency), and finally image atoms after a time of flight using the $|\mathrm{F}=2, \mathrm{m_F}=-2\rangle \rightarrow |\mathrm{F}'=3, \mathrm{m_{F'}}=-3\rangle$ cycling transition, recording sample's $T$ and $N$. In order to prevent a significant atom loss for our highest density samples or to prevent significant

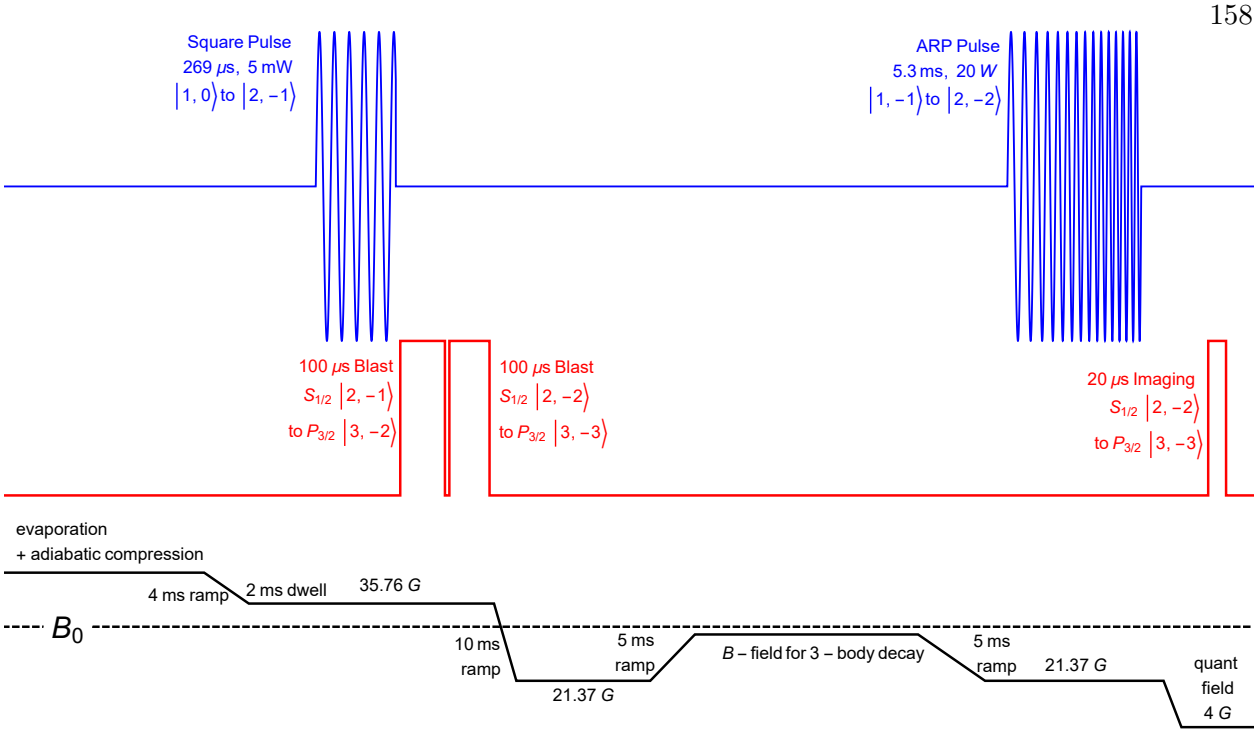


Figure 5.3: Experimental sequence for three-body loss measurements.

heating for our lowest temperature samples, we slightly modify this sequence: we perform the adiabatic trap compression step after going to $a < 0$ and shorten the respective $B$–field ramps from 10 ms to 1 ms and from 5 ms to 2 ms.

For each $B$–field of interest, we record atom number and temperature as a function of hold duration. We measure the corresponding $B$–field value by modifying the sequence shown in Fig. 5.3: instead of the ARP pulse, we use a 80 $\mu$s $|\mathrm{F} = 1, \mathrm{m_F} = -1\rangle \rightarrow |\mathrm{F} = 2, \mathrm{m_F} = 0\rangle$ pulse after the ramp to the field of interest to measure the atomic lineshape. Uncertainty on $B$–field ($< 2$ mG), along with uncertainty on Feshbach resonance location (1.4 mG), set the uncertainty on $a(B)$, allowing us to know $a$ to within $< 0.2\%$ near $a = -1000\, a_0$. Number loss due to three-body recombination is described by loss expression (briefly introduced in Ch. 4) [118]

$$\frac{1}{N}\frac{dN}{dt} = -L_3\langle n^2\rangle - \alpha, \tag{5.3}$$

where the constant $\alpha$ accounts for loss from background gas collisions (one-body and $a$–independent) and $\langle n^2\rangle = \frac{1}{N}\int n^3(\vec{x})d^3x = N^2\left(m\bar{\omega}^2/(\sqrt{12}\pi k_\mathrm{B}T)\right)^3$ is the density-weighted square density for

a harmonic trap with a mean frequency $\bar{\omega} = (\omega_x\omega_y\omega_z)^{1/3}$. Due to density inhomogeneity in a harmonic trap, such loss results in anti-evaporation described by [118]

$$\frac{1}{T}\frac{dT}{dt} = \frac{1}{3}L_3\langle n^2\rangle, \tag{5.4}$$

assuming thermalization rate is higher than loss rate and there are no other heating sources. The analytic solutions to the coupled Eqs. 5.3–5.4 describe the sample's temperature and atom number time evolution

$$N(t) = e^{-\alpha t}\left(1 + \frac{1}{\sqrt{12}\alpha}L_3\left(\frac{m\bar{\omega}^2}{2\pi k_\mathrm{B}}\right)^3\left(1 - e^{-2\alpha t}\right)\frac{N_0^2}{T_0^3}\right)^{-1/3}N_0, \tag{5.5}$$

$$T(t) = \left(1 + \frac{1}{\sqrt{12}\alpha}L_3\left(\frac{m\bar{\omega}^2}{2\pi k_\mathrm{B}}\right)^3\left(1 - e^{-2\alpha t}\right)\frac{N_0^2}{T_0^3}\right)^{1/9}T_0, \tag{5.6}$$

where $N_0$ and $T_0$ are the initial atom number and temperature. For small $a$ and $n$, three-body loss is negligible and number loss becomes purely exponential with a time constant $1/\alpha$. In the limit $\alpha \to 0$ (valid for high $a$ and $n$, specifically when $L_3\langle n^2\rangle \gg \alpha$), time evolution simplifies to

$$N(t) = \left(1 + \frac{1}{\sqrt{3}}L_3\left(\frac{m\bar{\omega}^2}{2\pi k_\mathrm{B}}\right)^3\frac{N_0^2}{T_0^3}t\right)^{-1/3}N_0, \tag{5.7}$$

$$T(t) = \left(1 + \frac{1}{\sqrt{3}}L_3\left(\frac{m\bar{\omega}^2}{2\pi k_\mathrm{B}}\right)^3\frac{N_0^2}{T_0^3}t\right)^{1/9}T_0. \tag{5.8}$$

A typical time evolution is shown in Fig. 5.4, where initial $N_i = 5900$ and $T_i = 46\,\mathrm{nK}$ (corresponding to $\langle n\rangle_i = 7\times10^{10}\,\mathrm{cm}^{-3}$). We extract $\alpha = (43\,\mathrm{s})^{-1}$ at $a = -101\,a_0$ (we use $a = -62\,a_0$ when we measure $L_3$ for our highest density samples), where the expected three-body loss on $\mathcal{O}(10^4\,\mathrm{s})$ is negligible. While the measured $1/\alpha$ varies slightly on trap configuration and cloud size, it is typically 42–46 s and is always $> 40\,\mathrm{s}$.

While we can use Eq. 5.5 to extract an (almost accurate) $L_3$ value from number loss, complex loss dynamics (e.g. residual evaporation and additional heating sources) can result in a temperature evolution that is not described by Eq. 5.6, as depicted in Fig. 5.4. Therefore, we do two things to extract a more accurate $L_3$ value. First, we only decay 20–30% of initial $N$. This ensures that the final temperature is not near the evaporation threshold, the absolute temperature rise

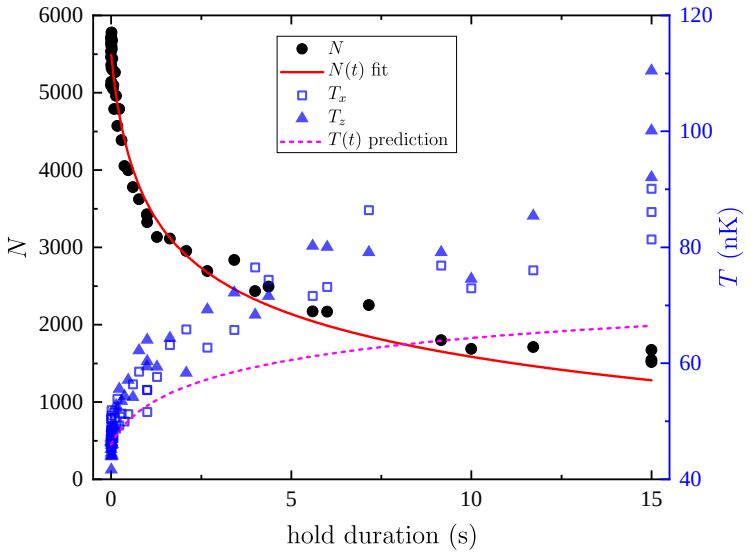


Figure 5.4: A typical atom number and temperature (along the two imaging directions) time evolution resulting from three-body decay. Here, $a = -640\,a_0$, $(\omega_x, \omega_y, \omega_z)\,/2\pi = (26.6, 26.6, 96.4)$ Hz and $1/\alpha = 43$ s (measured at low $|a|$). We fit (solid) $N(t)$ to Eq. 5.5 and extract $L_3 = 1.2\times10^{-22}$ cm$^6$s$^{-1}$. We can use this value of $L_3$ to predict the expected temperature evolution $T(t)$ (dashed) resulting from anti-evaporation. Sometimes, as in this case, the loss dynamics are too complex and the measured temperatures don't agree with the predicted heating.

is small (important as $L_3$ value is $T$–dependent, to be discussed shortly) and the density doesn't change significantly during the decay (such that loss is fully dominated by three-body loss and not other few-body processes). Second, we fit $T(t)$ to an empirical formula (exponential or polynomial) and use the fit result, along with $N(t)$ data, to numerically solve Eq. 5.3 for $L_3$. This procedure ensures that we accurately follow the actual density evolution, irrespective of complexities in the observed temperature behavior. We also extract the time-averaged temperature $\bar{T}$ and density $\bar{n}$ that correspond to each $L_3$ value.

Generally, three-body recombination coefficient scales as $a^4$ [118, 142, 143]:

$$L_3 = n_l C \frac{\hbar}{m} a^4, \tag{5.9}$$

where $n_l$ is the number of atoms lost during a recombination event (for $a < 0$ recombination is only to deep molecular states with energies $\gg$ trap depth, and hence $n_l = 3$) and $C$ is a numerical constant that depends on the sign of $a$ and recombination physics (can be $a$–dependent). For $a < 0$

the degeneracy of Efimov states with $E = 0$ threshold leads to enhanced loss (Efimov resonances) and the three-body inelastic coefficient is described by a zero-temperature zero-range (universal) expression [31]:

$$L_3^{T=0}(a) = \frac{3\hbar a^4}{m} \frac{4590 \sinh(2\eta)}{\sin^2(s_0 \ln(a/a_-)) + \sinh^2(\eta)}, \tag{5.10}$$

where the dimensionless inelasticity parameter $\eta$ characterizes the Efimov resonance width and the constant $s_0 \approx 1.00624$ fixes Efimov series spacing $e^{\pi/s_0} \approx 22.7$.

Figure 5.5 shows a compilation of our initial $L_3$ measurements at many scattering lengths for a specific $T \approx 100\,\mathrm{nK}$. Many systematic problems affected these initial measurements (labeled "data 1–3"), before a measurement (labeled "data 4") was accurately described by Eq. 5.10. Each data set is fit to Eq. 5.10 with free parameters $a_-$, $\eta$ and fit amplitude, whose departure from unity characterizes the uncertainty in the measured absolute density. The asymmetry in $L_3/a^4$ about the center (and the resulting shift in the fit center), as is the case for "data 1–2", is typically an indication of residual evaporation loss resulting from insufficient trap depth. "Data 3" suffers from imaging systematics, such as inaccurate probe frequency calibration, OD saturation and lineshape broadening (from high probe intensity $\mathrm{I/I_{sat}}$ and duration), resulting in incorrect absolute density estimation and hence inaccurate absolute $L_3$ values, as evidenced by a fit amplitude = 2.1. "Data 4" is same as "Data 3", but with imaging corrections and has a fit amplitude close to unity, at 0.89, indicating the absolute density is correctly measured to within 6% (see Eq. 5.3), (falsely) assuming finite-temperature corrections are minimal and Eq. 5.10 is fully applicable. Since, $L_3$ values at small $a$ values are minimally affected by finite-temperature effects (discussion to follow), the observed agreement of $L_3$ data at small $a$ with Eq. 5.10 (or Eq. 5.9) gives further confidence in understanding of systematic uncertainty on absolute density. Regarding statistical uncertainty, our typical shot-to-shot stabilities are 2–3% for $N$ and $< 4\%$ for $T$ (corresponding to $\sim 7\%$ for density) at a fixed hold duration, resulting in $L_3$ fit error $\sim 10\%$ (combining multiple $N$ and $T$ at different hold durations).

Some other systematic errors on the measured $L_3$ arise from high PSD, lack of thermalization

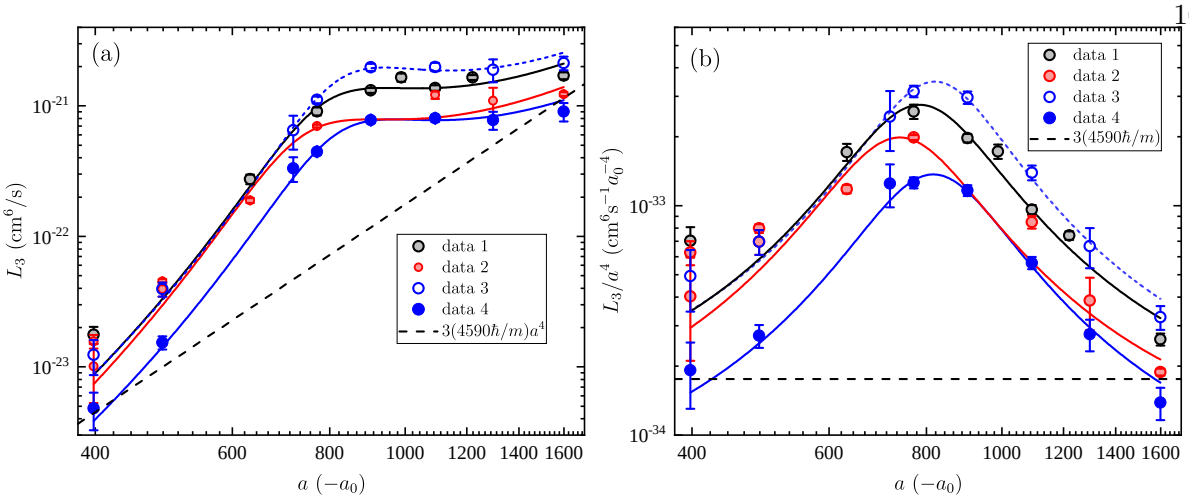


Figure 5.5: $L_3$ data, shown in (a), are affected by systematic shifts. The same data is plotted as $L_3/a^4$ in (b) for a better visualization of the Efimov resonance. The dashed lines represent $a^4$ scaling of $L_3$ loss in absence of Efimov physics.

and other (than three-body) inelastic loss processes. If the sample's PSD is high enough for degeneracy ($n\lambda^3 \gtrsim 2.612$, where $\lambda = h/\sqrt{2\pi m k_B T}$), then the number loss dynamics become complicated for $a < 0$ [117] and $L_3$ values cannot be accurately extracted. For example, authors of Ref. 45 saw unexpected behavior in the $L_3(a)$ spectrum with degenerate samples. Additionally, a lack of thermalization leads to an incorrect assumption about the measured density distribution, and hence results in $L_3$ uncertainty. To limit this effect, the inelastic collision rate $\sim L_3\langle n^2\rangle$ must be less than the two-body elastic thermalization collision rate $\langle n\rangle\sigma\langle v_{\rm rel}\rangle/\alpha_{\rm col}$, where $\langle n\rangle$ is the density-weighted density, $\sigma = 8\pi a^2$ is the s-wave collision cross-section, $\langle v_{\rm rel}\rangle = 4\sqrt{k_B T/(\pi m)}$ is the average relative velocity between two atoms in a harmonic trap and $\alpha_{\rm col} \approx 2.5$–$2.7$ (for equal-mass atoms with s-wave interactions in a harmonic trap) is a numerical constant describing the number of elastic two-body collisions needed for thermalization [81, 60, 82]. Therefore, for proper thermalization, we desire low densities and high temperatures. However, if the density is too low, then loss becomes dominated by the two-body inelastic rate (introduced in Sec. 4.6) $(1/N)dN/dt = -L_2\langle n\rangle$ and the extraction of $L_3$ values becomes difficult. The two-body coupled-channel model (see Sec. 4.6 and Fig. 4.36) predicts $L_2 \sim 2\times10^{-13}\,\mathrm{cm^3 s^{-1}}$ near $a = -1000\,a_0$, while Eq. 5.10 predicts $L_3 \sim 10^{-21}\,\mathrm{cm^6 s^{-1}}$ for $a = -1000\,a_0$, $a_- = -908\,a_0$ and $\eta = 0.25$. For three-body loss to completely dominate near

$a = -1000\,a_0$, we limit our initial sample densities to $\langle n \rangle > 10^{10}\,\mathrm{cm}^{-3}$.

We typically verify that total loss is dominated by three-body recombination and not some other-body term. There are several ways to do this. First, one can perform the same procedure as been mentioned (decay a small fraction of atomic population and extract $L_3$ value from Eq. 5.3) for different initial densities. If the total loss is dominated by three-body term, then fits to Eq. 5.3 will result in same $L_3$ values for different initial density conditions. The second method relies on recording the sample's decay for long durations to significantly vary the atom density during the decay [136, 33, 43]. While the latter method is cruder, relying on good imaging (need to detect a large dynamic range in $N$ and $T$) and assuming complete thermalization during the decay, it is easier to implement than the first method. One can fit the number decay to a modified Eq. 5.3, with other-body terms (e.g. $L_2$ and $L_4$) in addition to $L_3$, or to an equation with a single arbitrary $z$–body inelastic loss coefficient $L_z$:

$$\frac{1}{N}\frac{dN}{dt} = -L_z \langle n^{z-1} \rangle \tag{5.11}$$

$$= -L_z \frac{N^z}{\zeta \left(T^{3/2}\right)^{z-1}}, \tag{5.12}$$

where $\langle n^{z-1} \rangle = \frac{1}{N} \int n^z(\vec{x}) d^3x$ and the constant $\zeta$ are (for a harmonic trap):

$$\langle n^\gamma \rangle = \frac{N^\gamma (2\pi)^{-3\gamma/2} (m/(k_\mathrm{B}T))^{3\gamma/2} (\bar{\omega})^{3\gamma}}{(1+\gamma)^{3/2}} \tag{5.13}$$

$$\zeta = 128\sqrt{2}\pi^{9/2} \left(\frac{k_\mathrm{B}}{m\bar{\omega}^2}\right)^{9/2}. \tag{5.14}$$

Equation 5.11 is easier to fit to than to an equation with multiple free parameters (e.g. loss coefficients $L_2$, $L_3$, $L_4$) and departure from $z = 3$ is an indication that other-body loss is present. We find that for initial atom densities $10^{10}\,\mathrm{cm}^{-3} < n_\mathrm{pk} < 10^{12}\,\mathrm{cm}^{-3}$ the decay solely dominated by three-body loss, where the upper limit is consistent with preliminary predictions for $L_4$ values [141].

While higher temperatures are beneficial for good thermalization, finite temperature affects the $L_3(a)$ spectrum and gives rise to the largest known systematic error. The $L_3(a)$ spectra saturate when $|a|$ values becomes comparable to the thermal wavelength $\lambda = h/\sqrt{2\pi m k_\mathrm{B} T}$. Saturation at

unitarity ($a \to \pm\infty$) leads to a maximum three-body recombination rate coefficient $L_3$ value, that is only limited by the temperature and the Efimov resonance width $\eta$ [39]:

$$L_3^{\max}(T) = (1 - e^{-4\eta}) \frac{36\sqrt{3}\pi^2\hbar^5}{m^3 (k_B T)^2}. \tag{5.15}$$

We check this unitary limit by performing loss measurements at $a > 0$ and $a < 0$, recording $L_3$ values of saturated $L_3(a)$ spectra at different temperatures. A good agreement between our results and Eq. 5.15, as depicted in Fig. 5.6, indicates a good understanding of systematic error (arising from e.g. calibration of absolute density and temperature) and confirms our direct measurements of $\eta = 0.25$ from $L_3(a)$ spectra.

While Eq. 5.10 adequately describes $L_3(a)$ in the limit of $\lambda \gg a$, for increasing temperatures it becomes less valid and a finite-temperature zero-range model [39, 144] is required to describe the three-body loss spectrum, for $a < 0$:

$$\begin{aligned} L_3(a,T) = & \frac{72\sqrt{3}\pi^2\hbar\left(1 - e^{-4\eta}\right)}{m k_{\text{th}}^6 a^2} \\ & \times \int_0^\infty \frac{\left(1 - |s_{11}(x)|^2\right) e^{-x^2/(k_{\text{th}}a)^2} x}{\left|1 + s_{11}(x) \left(\frac{-xa_-}{1.017|a|}\right)^{-2is_0} e^{-2\eta}\right|^2} dx, \end{aligned} \tag{5.16}$$

where $k_{\text{th}} = \sqrt{m k_B T}/\hbar$, $x = k|a|$ and the complex function $s_{11}(x)$ is an S-matrix element from Refs. [39] and [145], plotted in Fig. 5.7. The universal single-variable function $s_{11}(x)$ is analogous to the reflection coefficient in two-port networks (e.g. optical and electrical) and has a complex structure for small $-ka$ values. For large $a$ or high temperatures, $s_{11}(x)$ function is approximately 0 and Eq. 5.16 reduces to Eq. 5.15. If desired, one can extract $L_3$ behavior for $a > 0$ using relation $s_{11}(-ka) = e^{-2\pi s_0}/s_{11}^*(ka)$ and replacing $1 - |s_{11}|^2$ with $1 - |s_{11}|^2 - |s_{12}|^2$ in Eq. 5.16 [146, 39], where $s_{12}$ characterizes recombination to shallow dimers via atom-dimer inelastic scattering (in addition to typical recombination into deeply bound molecular states).

Figure 5.8 shows the predicted $L_3(a)$ behavior for various temperatures. While $L_3$ saturation at higher temperatures severely affects the second (first-excited) Efimov resonance and limits the possibility of its observation, the first (ground) Efimov resonance is expected to have a good contrast

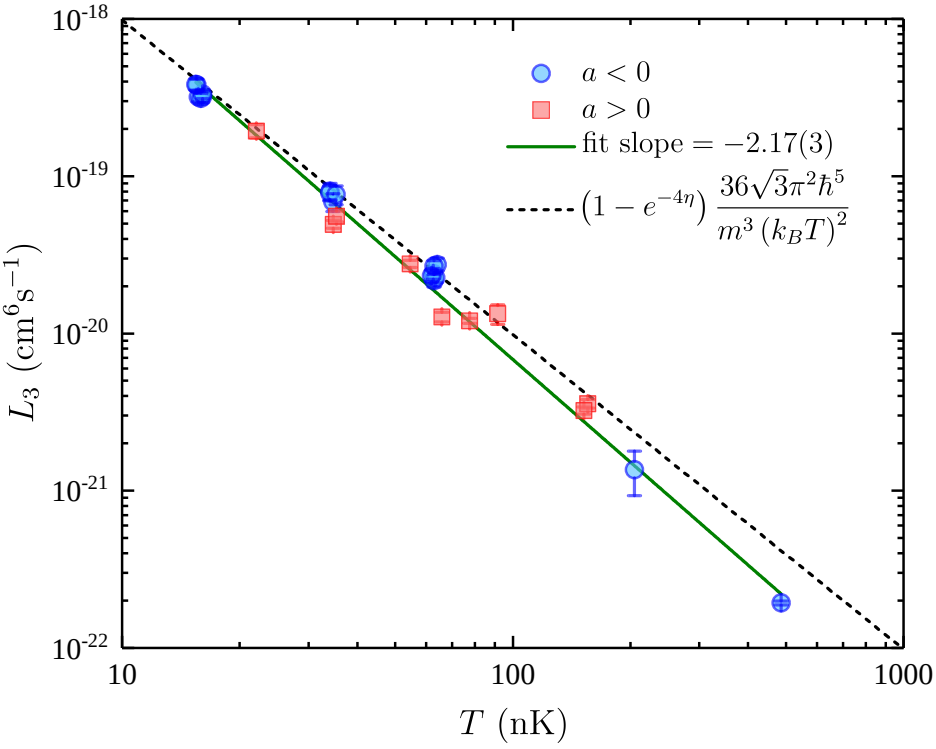


Figure 5.6: Temperature dependence of saturated $L_3(a)$ spectra values. For each temperature, we only select $L_3$ values from $L_3(a)$ spectra that appear saturated and show a strong deviation from the zero-temperature Eq. 5.10. The dashed line represents unitary limit ($a \to \pm\infty$) Eq. 5.15 with no free parameters (fix $\eta = 0.25$, found from direct measurements from $L_3(a)$ spectra). Our data agrees well with universal prediction, aside from deviations at high $T$. The solid line is a linear fit (on log-log scale) to all our data, resulting in a slope $= -2.17(3)$, confirming the predicted $T^{-2}$ scaling.

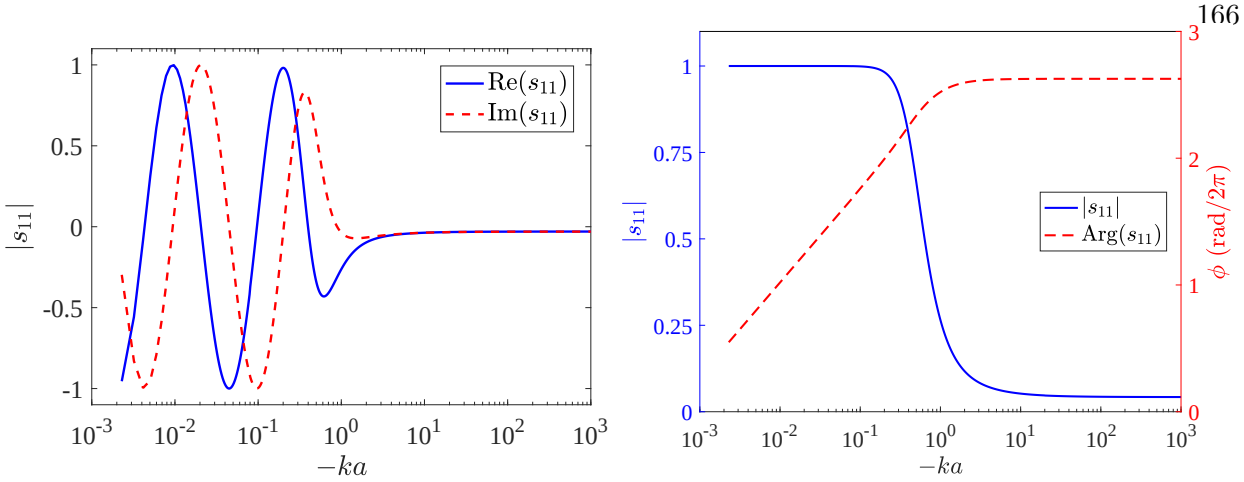


Figure 5.7: Universal function $s_{11}(ka)$ used in the finite-temperature zero-range model, where $k = \sqrt{mk_{\rm B}T}/\hbar$.

even for moderate temperatures. For a better visualization of finite-temperature effects on the ground Efimov resonance, the same predictions are plotted as $L_3(a)/a^4$ in Fig. 5.9. Now, one can clearly see the suppression and shift of the Efimov feature at higher temperatures. A finite-temperature model is required to accurately extract $a_-$ and $\eta$ values; one would get incorrect results if were to use Eq. 5.10 for fitting data. I note that empirical equations, such as $L_3(a,T) = \left(\left(L_3^{T=0}(a)\right)^{-1} + \left(L_3^{\rm max}(T)\right)^{-1}\right)^{-1}$ used in Refs. [38] and [45], are inadequate to correctly describe $L_3(a)$ data for intermediate (compared to the thermal wavelength) scattering length values.

There are two other interesting effects associated with a finite temperature. First, due to oscillations in $s_{11}(-ka)$ (see Fig. 5.7), $L_3$ can have modulations vs. $T$ at fixed $a$, as shown in Fig. 5.10. While these oscillations are intriguing, their contrast is small and would be hard to observe (limited by atom $N$ and $T$ noise). On the bright side, since the modulation amplitude is small near $a = -1000\,a_0$, we are able to accurately extract Efimov resonance parameters ($a_-$ and $\eta$) from Eq. 5.16 without the need to fully characterize these oscillations. The second interesting finite-temperature effect relates to the finite-range correction that is not taken into account in Eq. 5.16. Authors of Ref. [147] suggest that a finite-range correction, characterized by the van der Waals length $r_{\rm vdW}$, to Eq. 5.16 results in a shifted (observed) resonance location: $a_-^{\rm zr}/a_-^{\rm true} = 1 + \sqrt{2\pi}c(kr_{\rm vdW})$, where $a_-^{\rm zr}$ is the zero-range Efimov resonance location extracted from fit to

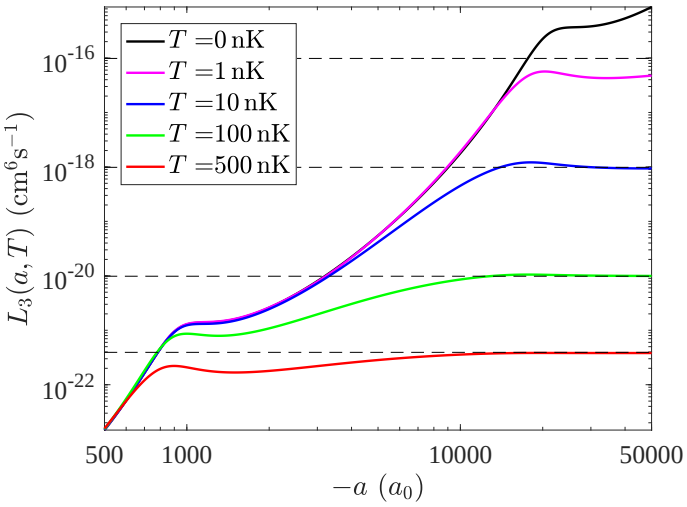


Figure 5.8: Finite-temperature model prediction for $L_3(a)$ behavior for various temperatures. The $T = 0$ curve represents the zero-temperature Eq. 5.10 and the dashed lines represent unitary limit for each temperature, given by Eq. 5.15. The range of $a$ is limited to show two Efimov resonances, with $a_- = -908\,a_0$, $\eta = 0.25$ and $\approx 22.7$ Efimov series spacing.

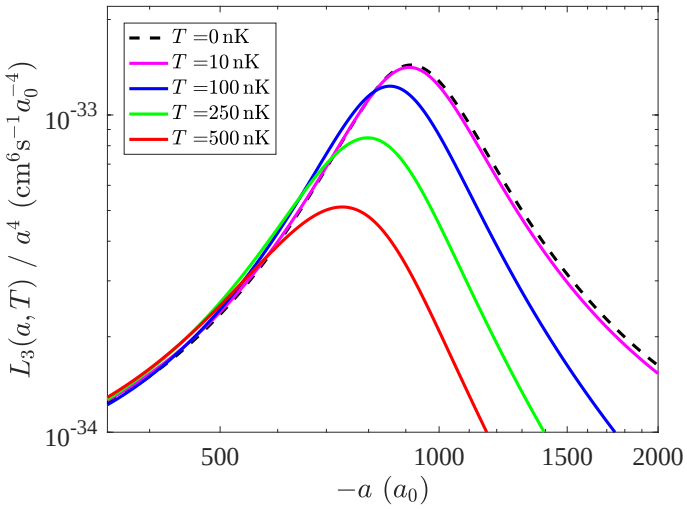


Figure 5.9: Finite-temperature model prediction for $L_3(a)/a^4$ behavior for various temperatures. The dashed $T = 0$ curve represents the zero-temperature Eq. 5.10.

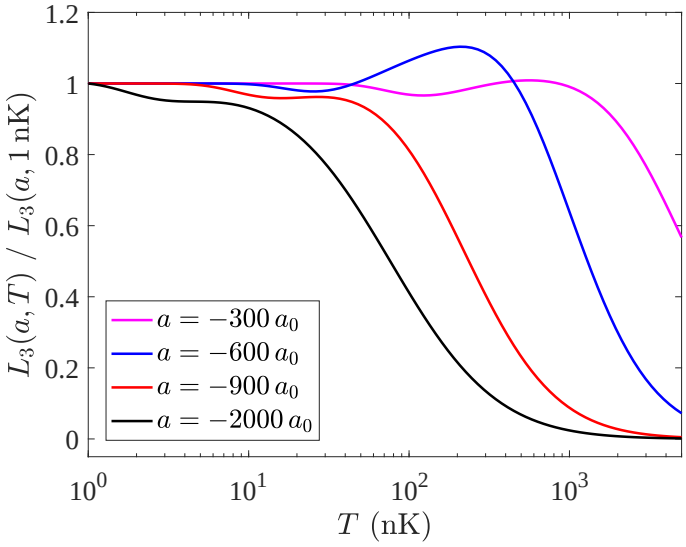


Figure 5.10: Modulation in $L_3$ vs. $T$ for different $a$ values. Each $L_3(a,T)$ curve is normalized to its value at 1 nK to compare the contrast of oscillations at different $a$ values. Since oscillations in the $s_{11}(-ka)$ function quickly damp out for $-ka > \mathcal{O}(1)$, the modulation amplitude is largest for small $a$ values and decreases for high $a$.

Eq. 5.16 and $c = 0.60(3)$ is (though to be) a universal constant determined by authors of Ref. [147] from fits to $^{133}$Cs Efimov data. However, even if such finite-range corrections are applicable to $^{39}$K, $a_-$ temperature shifts would be small, 5% at $T = 500\,\mathrm{nK}$ and 1% at $T = 30\,\mathrm{nK}$, and we do not include such corrections in our analysis.

## 5.3 Precise Measurement of the Efimov Ground State Location

Fits to Eq. 5.16 enable us to extract $a_-$ and $\eta$ directly from $L_3(a)$ data at any temperature. However, we still take multiple $L_3(a)$ measurements at different temperatures to verify finite-temperature corrections and other effects that can lead to systematic error on $a_-$ and $\eta$ values. A compilation of our $L_3(a)$ measurements is shown in Fig. 5.11. A compilation of Efimov resonance measurement conditions and fit results is presented in Table 5.1. Each temperature data set is described by a time-averaged temperature $\bar{T}$, initial temperature $T_\mathrm{i}$, initial mean density $< n >_\mathrm{i}$ and a mean trap frequency $\bar{\omega}$.

We analyze our data in two different ways. First, for each temperature, we fit our data

Table 5.1: Efimov resonance measurement conditions and fit results. We do not include fit results for $T \sim 200\,\mathrm{nK}$ high-density data, as they suffer from non-trivial effects (see Sec. 5.4.2).

| $\bar{T}$ nK | $T_\mathrm{i}$ nK | $< n >_\mathrm{i}$ $10^{11}\,\mathrm{cm}^{-3}$ | $\bar{\omega}/2\pi$ Hz | peak location $-a_0$ | peak width | peak height | $a_-$ $-a_0$ | $\eta$ | ampl. |
|---|---|---|---|---|---|---|---|---|---|
| 30 | 27 | 0.40 | 33.7 | 891(8) | 0.22(1) | 1.29(4) | 910(9) | 0.24(1) | 1.40(4) |
| 53 | 46 | 0.70 | 40.8 | 856(10) | 0.22(1) | 1.28(5) | 904(12) | 0.24(1) | 1.43(6) |
| 94 | 85 | 1.07 | 51.4 | 829(7) | 0.24(1) | 0.92(3) | 890(7) | 0.24(1) | 1.08(2) |
| 206 | 186 | 1.21 | 65.7 | 807(14) | 0.30(2) | 0.65(3) | 921(6) | 0.25(1) | 0.91(1) |
| 510 | 407 | 3.52 | 89.9 | 811(46) | 0.44(3) | 0.54(5) | 917(9) | 0.26(1) | 0.89(1) |
| 173 | 160 | 2.18 | 51.1 | | | | | | |
| 221 | 194 | 8.76 | 51.1 | | | | | | |

using a zero-temperature zero-range model (Eq. 5.10) to extract Efimov $L_3/a^4$ peak properties, limiting fits to $|a| < \lambda/10$ and redefining $a_- \rightarrow$ peak location, $\eta \rightarrow$ peak width and peak height as the fit prefactor. The $|a| < \lambda/10$ cutoff is chosen such that Eq. 5.10 is able to describe all unmasked data; perturbing the cutoff around $|a| < \lambda/10$ gives similar fit results. As depicted in Table 5.1, the Efimov feature is suppressed, broadened and shifted towards smaller $|a|$ values for higher temperatures. Second, we fit our data to the finite-temperature zero-range model Eq. 5.16 to directly extract the Efimov ground state location $a_-$ and $\eta$. Here, the fit amplitude prefactor deviation from 1.0 accounts for uncertainty in our absolute density calibration for each $L_3(a)$ measurement at same $T$. Fit amplitudes being $\mathcal{O}(1)$ for all temperatures gives confidence in our results and our understanding of systematic error. Due to (small) heating for increased $a$ values, each $L_3$ measurement point (at fixed $a$) has a slightly different temperature (within each data set), therefore we use "local" temperatures in Eq. 5.16 to fit each temperature data set.

Figure 5.12 shows peak locations and $a_-$ values extracted using the two methods. At low temperature the Efimov peak position and width values coincide, as expected, with $a_-$ and $\eta$ values, respectively. We take the weighted mean across all temperatures and extract $a_- = -908(11)\,a_0$ and $\eta = 0.25(1)$. While Eq. 5.16 adequately describes most of our data, the reduced $\chi^2$ is large for the two lowest temperatures data sets. This is evidenced by a small departure between the fit and observed $L_3$ values at high $a$, as depicted in Fig. 5.11(a). We believe that such departure can

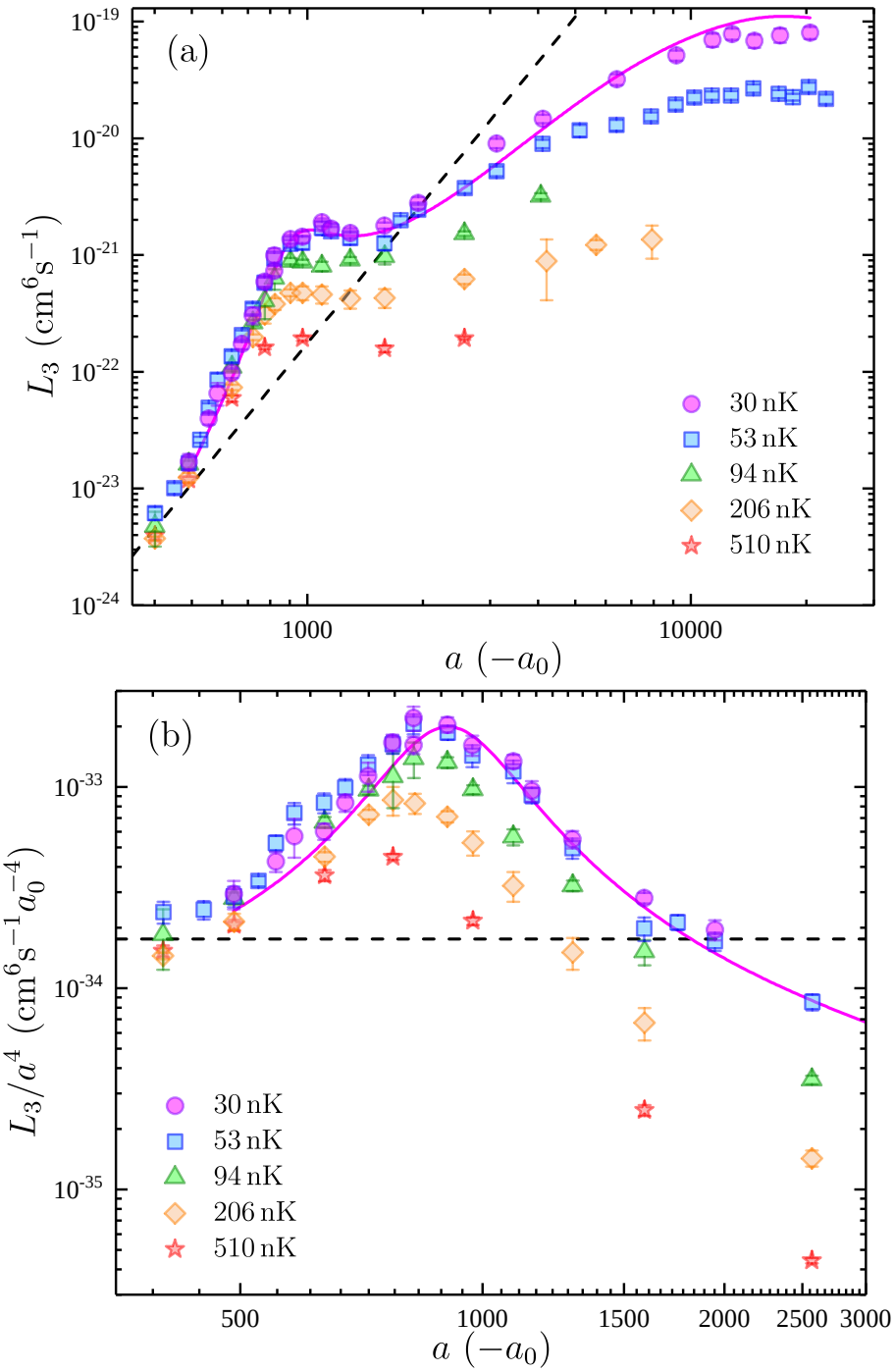


Figure 5.11: Precise $L_3(a)$ measurements at different temperatures. The same data is plotted as $L_3/a^4$ in (b) with limited $x$-axis range, for a better visualization of the Efimov resonance. The dashed line represents $a^4$ scaling of $L_3$ loss in absence of Efimov physics and temperature saturation. The solid curve shows a fit of $L_3(a)$ data at $\bar{T} = 30\,\text{nK}$ to zero-range finite-temperature Eq. 5.16.

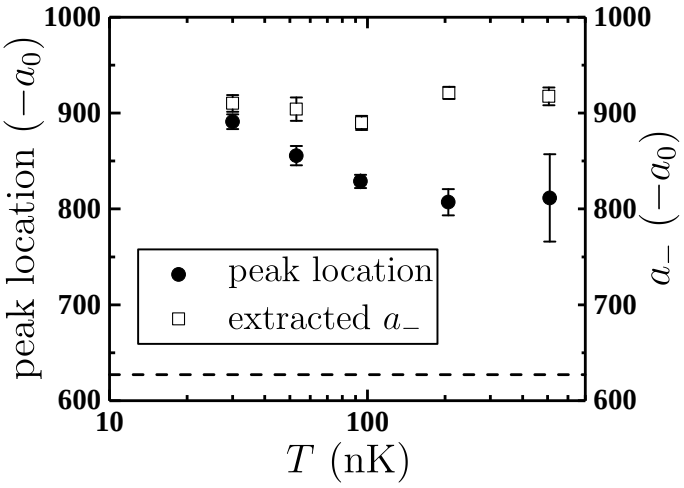


Figure 5.12: Extracted Efimov $L_3/a^4$ peak locations (using zero-temperature Eq. 5.10) and $a_-$ (using finite-temperature Eq. 5.16) from $L_3(a)$ data at different temperatures. The dashed line represents $a_- = -9.73\, r_{\mathrm{vdW}} = -627\, a_0$ value predicted by Van der Waals universality [51].

result from high $n\,|a|^3$ or from a non–22.7 Efimov series spacing, expected with a non-universal $a_-$ location. Therefore, we vary the fit range from all $a$ to only $|a| < \lambda/10$ and take the maximal spread of all fit errors as the uncertainty on weighted mean $a_-$ and $\eta$ values. For individual $a_-$ and $\eta$ values at each temperature (as shown in Table 5.1), we use all $a$ points for three-highest temperatures and only $|a| < \lambda/5$ points for the two-lowest temperature data sets, where reduced–$\chi^2$ stops varying below cutoffs $|a| = \lambda/4$. However, all extracted $a_-$ and $\eta$ values (the weighted mean or individual values for each temperature) are consistent with the quoted results (within the quoted uncertainties), regardless if we mask high-$a$ data or not.

The observed $a_- = -908(11)\, a_0$ value is a $17\,\sigma$ deviation from the $a_- = -9.73 \pm 15\%\, r_{\mathrm{vdW}} = -627 \pm 15\%\, a_0$ value predicted by multiple theories investigating van der Waals universality [51, 52, 46, 47]. Our result is intriguing, considering this Feshbach resonance has an intermediate $s_{\mathrm{res}} = 1.9$ and relatively-small $a_{\mathrm{bg}} = -19.6\, a_0$ (compared to $\bar{a} = 61.65\, a_0$). Other Efimov resonance $a_-$ measurements near Feshbach resonances with similar $s_{\mathrm{res}}$ and $a_{\mathrm{bg}}$ values were consistent with universal prediction (see Fig. 5.2), albeit with large experimental and systematic uncertainties. Previous theoretical studies dealing with corrections to van der Waals universality [53, 54, 55, 56, 57] cannot adequately explain our data. A preliminary three-body coupled-channel model [141] suggests

Table 5.2: State-of-the-art predictions for the Efimov resonance location $a_-$ and the inelasticity parameter $\eta$ [141]. The predicted values approach the experimental values (last line) as the number of singlet $N_s$ or triplet states $N_t = N_s - 1$ increases. The total number of bound states is $N_{total}$, where the model includes all partial waves and hyperfine interactions.

| $N_s$ | $N_{total}$ | $a_-/r_{vdW}$ | $\eta$ |
|---|---|---|---|
| 2 | 6 | −7.61 | 0.10 |
| 3 | 27 | −11.20 | 0.19 |
| 4 | 59 | −12.27 | 0.20 |
| 5 | 105 | −12.69 | 0.21 |
| Exp. | | −14.08(17) | 0.25(1) |

that the number of two-body bound states (set by the depth of the singlet and triplet interaction potentials) in the theory is important to match our measured non-universal Efimov ground state location $a_-$, see Fig. 5.2. Additionally, we find that this state-of-the-art three-body model is able to accurately predict $\eta$ value, previously thought to be an unattainable goal.

## 5.4 Our Other Efimov Studies

### 5.4.1 An Attempt to Measure the Second Efimov State

While the first (ground) Efimov state and its location $a_-$ has been extensively studied in many systems [46, 47], the second (first-excited) Efimov state has been observed only once in a homonuclear system [43]. The authors of Ref. [43] use ultracold $^{133}$Cs to measure the first and second Efimov resonance locations $a_- = -943(2)\,a_0$ and $a_-^{(2)} = -19930(1200)\,a_0$ [147], respectively, thereby providing the only experimental evidence for universal 22.7 Efimov series spacing, with $a_-^{(2)}/a_- = 21.1(1.3)$. These measurements were performed in very weak optical traps, having $(\omega_x, \omega_y, \omega_z)/2\pi = (3.97, 3.36, 1.34)$ Hz, with a magnetic field gradient (to compensate for gravity) and temperatures $\sim 9$ nK. While this sounds like a low temperature, it must be compared to the very large scattering length at the second resonance $a_-^{(2)}$. At 9 nK and at the reported experimental value in $^{39}$Cs, $a_-^{(2)} = -19930(1200)\,a_0$ and $ka = 1.7$. If we were to translate this to the ground-state Efimov resonance of $^{39}$K, $a_- = -908\,a_0$, the same value of $ka$ would be reached only at $T = 15\,\mu$K.

This is considerably higher than 500 nK, the highest temperature in Figure 5.11b, for which our resonance is already significantly washed out. This comparison caused us to question whether the resonance observed in Ref. [43] is perhaps some spurious effect. It should be noted, though, that the cesium experiment has a value of $\eta = 0.10$, measured for the ground state, while our $^{39}$K value is higher, $\eta = 0.25$. In any case, it seemed worth having a look. We went into the process with two possible hypotheses about the second Efimov resonance in $^{39}$K: that $a_-^{(2)}$ is at the universal value of $22.7 \times (-9.73\, r_{\rm vdW}) = -14200\, a_0$, or that it is universally scaled from our observed $a_-$ value, which would make it $a_-^{(2)} = 22.7 \times (-14.08\, r_{\rm vdW}) = -20600\, a_0$. In the former hypothesis, to achieve the same (or a smaller) value of $ka$ that characterized the $^{133}$Cs experiment, we would need to be at $T < 30$ nK. In the latter hypothesis, we would need $T < 60$ nK. These temperatures seemed achievable and, with the positive example from the $^{133}$Cs work, we decided to try.

Since we did not observe the second Efimov resonance at time-averaged $\bar{T} = 30$ nK (see Fig. 5.11(a)), we tried measuring $L_3$ values at high $a$ with the lowest temperatures attainable without significant (hardware) modifications. Since we cannot use degenerate samples for loss measurement at $a < 0$, the lower temperature limit is set by the density. We minimize the atom density by utilizing the weakest trapping potentials permitted by gravitational sag. We do not use magnetic field gradient for levitation, as this would introduce further complications. We were able to create 8 nK thermal samples with 1800 atoms in a $(\omega_x, \omega_y, \omega_z)/2\pi = (7, 7, 49)$ Hz optical trap. However, small OD, image frame imperfections, small cloud size ($\sigma = 6\,\mu$m approaching imaging resolution $\sigma = 1.4\,\mu$m), trap intensity instability (in this case, we do not adiabatically increase trap depths) and closeness to degeneracy (PSD $\sim 1$), result in a relatively-poor signal-to-noise, with $\sim 4\%$ $N$ instability and $\sim 10\%$ $T$ instability for a minimal hold duration and even worse after some decay. Of course, one can also compensate for gravity by performing the experiment in free-fall, as in the Cold Atom Laboratory in the International Space Station.

In the end, we compromised reaching the lowest temperature for better signal stability, creating samples with $T_{\rm i} = 14$ nK and 3600 atoms in a $(\omega_x, \omega_y, \omega_z)/2\pi = (8, 8, 61)$ Hz optical trap. Figure 5.13 shows that we expect (using Eq. 5.16) a significant suppression of the second Efimov

peak for $\bar{T} = 16\,\mathrm{nK}$, when compared to the zero-temperature limit (using Eq. 5.10). We take multiple $L_3$ measurements in the vicinity of the aforementioned possible $a_-^{(2)}$ values and do not see an Efimov feature, as depicted in Fig. 5.14. There are several possible reasons for the absence of an Efimov feature. First, $T = 16\,\mathrm{nK}$ is still a relatively-hot temperature and results in a feature with a small contrast, as shown in Fig. 5.13, consistent with data within experimental error. Second, a relatively-strong confinement along gravity corresponds to a relatively-small (compared to $a_-^{(2)}$) harmonic oscillator length $\sim 4 \times 10^4\, a_0$, can result in a suppression of Efimov-related loss at such high $a$ values [148]. Last, non-trivial density effects can play a role in the suppression of three-body physics, even with the sample's relatively-low density (at $\langle n \rangle_i = 1.7 \times 10^{10}\,\mathrm{cm}^{-3}$), considering $\left|na^3\right|$ is already 0.02 at $-20000\, a_0$. Some future prospects for observing the second Efimov resonance with our system include using a better imaging system, which would enable a better detection of small atom populations, and using repulsive optical potentials to compensate for gravity, which would enable smaller sample densities and temperatures with reasonable atom number.

### 5.4.2 An Attempt to Measure Four-Body Efimov Resonances and High-Density Peculiarities

The Efimov spectrum contains a more complex structure that goes beyond the infinite series of trimer states. For example, each individual trimer state has two corresponding four-body Efimov states [149]. Near $a_-$, the two ground tetramer states intersect the four-atom continuum at $0.43\, a_-$ and $0.90\, a_-$ locations [149]. There has been some experimental evidence for the existence of such states [136, 33, 40]. We attempted to find evidence of such states near our trimer Efimov resonance using atom-loss spectroscopy.

Four-body loss follows Eq. 5.11 (with $z = 4$) and leads to an enhanced overall loss near $0.43\, a_-$ and $0.90\, a_-$ locations. Such loss can be measured using the same procedure as we did for $L_3$ (with 20-30% number decay) and would appear as a density-dependent $L_3$ feature. In order to distinguish four-body loss from three-body loss, the density must be high enough. Given preliminary four-body loss rate coefficient $L_4$ values from José D'Incao [141], the average atom density must approach or

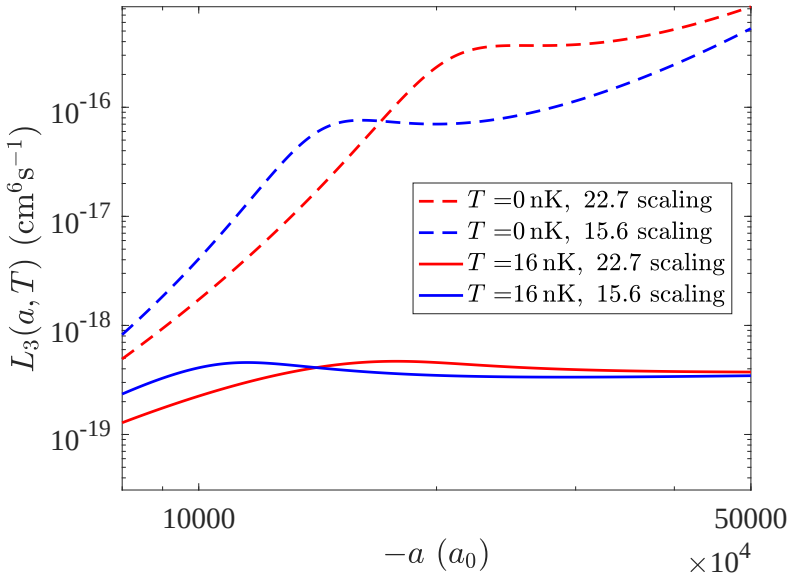


Figure 5.13: Predicted finite-temperature suppression of the second Efimov resonance. Since we do not know the location of the second Efimov resonance, we plot two possible values: $a_-^{(2)} = 22.7 \times a_- = -20600\,a_0$ (red) and $a_-^{(2)} = 22.7 \times (-9.73\,r_{\mathrm{vdW}}) = -14200\,a_0$ (blue), corresponding to Efimov series spacing 22.7 and 15.6, where we fix $a_- = -908\,a_0$ and $\eta = 0.25$. The solid lines represent finite-temperature model Eq. 5.16 and dashed lines represent zero-temperature model Eq. 5.10.

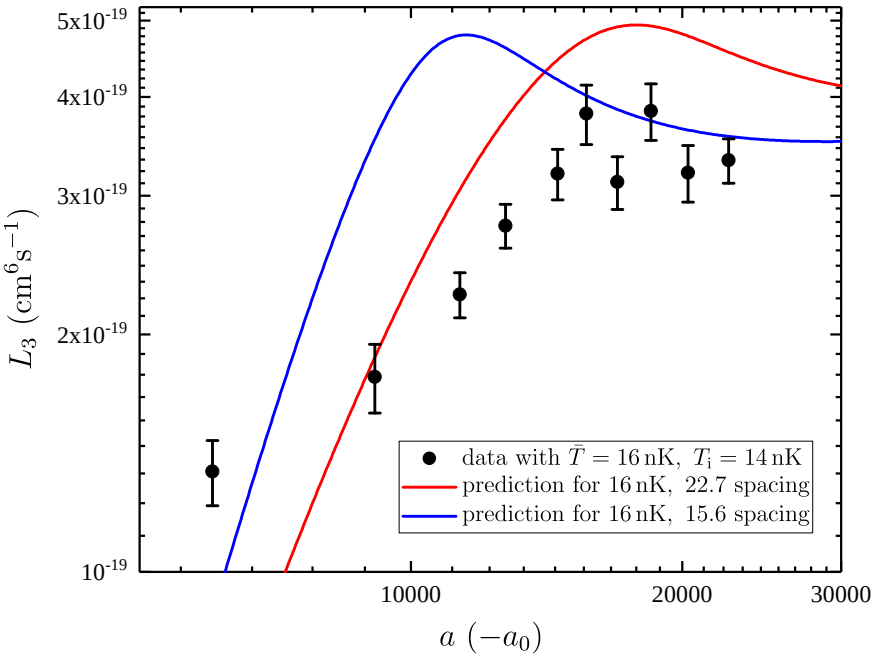


Figure 5.14: The absence of the second Efimov resonance in our data. The finite-temperature predictions are the same as in Fig. 5.13. Since we do not directly measure the trapping frequencies for this particular measurement (we extrapolate them from previous measurements), there can be a global systematic shift of all $L_3$ points resulting from an imprecise knowledge absolute density.

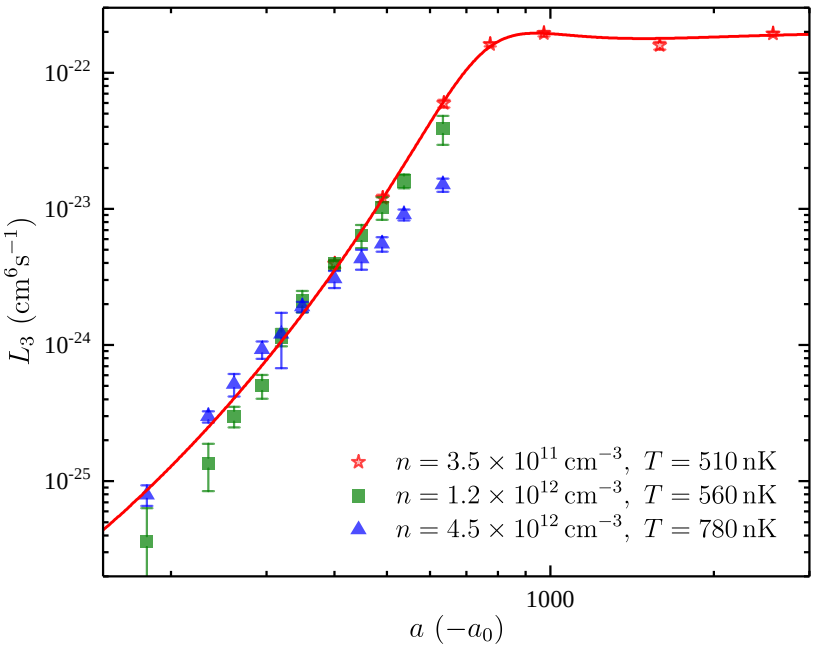


Figure 5.15: An attempt to find a four-body Efimov resonance in a high-density gas. The first tetramer state should appear near $0.43\,a_-$ location. We do not notice a statistically significant change in $L_3$ values as the density is increased, a null result for a four-body resonance. Due to thermal saturation, the four-body resonance predicted at $0.90\,a_-$ location was not expected to be visible, hence the lack of data in that region. The lowest-density data (red stars) are the same as in Fig. 5.11, along with the corresponding fit (solid red).

exceed $10^{12}\,\mathrm{cm}^{-3}$ to resolve the $0.90\,a_-$ four-body feature. Due to the overall $a^7$ of $L_4$ coefficient, observation of the $0.43\,a_-$ feature requires even higher atomic densities.

Since we cannot use degenerate samples, the maximal atomic density is limited by temperature. While using hotter clouds will allow higher densities, Efimov features will be suppressed by thermal effects. Therefore, we use two different types of conditions in an attempt to find $0.43\,a_-$ and $0.90\,a_-$ four-body peaks. For the lower peak, we probe dense yet hot clouds. For the higher peak, since thermal effects can significantly suppress the Efimov resonances at those $a$ values, we probe clouds with temperatures $\sim 200\,\mathrm{nK}$ and vary the density.

We find a null result for the four-body Efimov resonance predicted at $0.43\,a_-$, see Fig. 5.15. We suspect our density is not high enough to observe the lower-$a$ feature. The conditions used in Fig. 5.15 are too hot to observe the higher-$a$ feature.

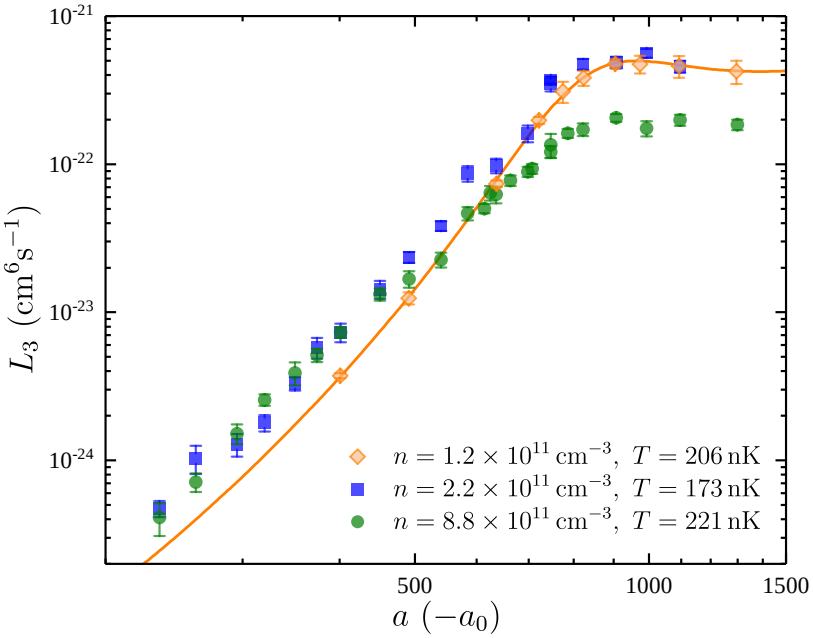


Figure 5.16: Suppression of the Efimov resonance in a high-density gas. Measurements of high- and intermediate-density samples are performed with the same experimental conditions, contrasting only in the initial atom number. As a result, differential comparison of $L_3$ values between those two measurements is of greatest interest. Small $L_3$ deviations at low $a$ between the lowest-density data, same as in Fig. 5.11 and with a corresponding fit (solid), and the other data are attributed to differing trap conditions that result in evaporation. However, a strong suppression of $L_3$ amplitude near $a = a_-$ in the highest-density data is unexpected.

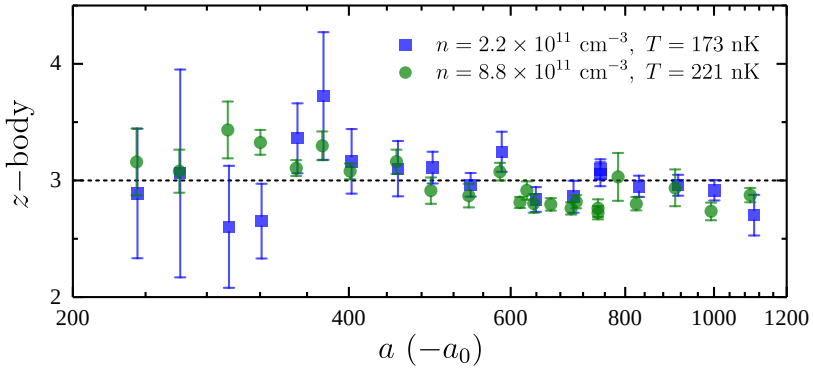


Figure 5.17: Type of loss present in a high-density gas. We fit the two-highest density decay data to $z$-body decay Eq. 5.11, with $z$ as a free-parameter and find decay is predominately of three-body origin. Note that this type of analysis is to be taken with a grain of salt.

Likewise, we find a null result for the four-body Efimov resonance predicted at $0.90\,a_-$, see Fig. 5.16. In fact, we observe a suppression of $L_3$ amplitude near $a_-$ and a shift of $L_3$ loss peak for

our highest-density gas, a counter-intuitive result. These trends are similar to those seen in a recent study [45], whose unexpected results are difficult to interpret due to additional complications arising from the use of degenerate samples. For our data, we suspect high $|na^3|$ effects are responsible for these nontrivial observations. We attempt to extract the type of loss present in the two-highest density samples by fitting the data to Eq. 5.11, now including data points with up to 80% number loss. We leave $z$ as a free-parameter and find that loss in high density samples is still of three-body origin, as depicted in Fig. 5.17. Note this analysis is to be taken with a grain of salt and I am not confident in stating that no many-body effects are present. Further theoretical and experimental studies are required to fully understand the origin of the unexpected result.

# Chapter 6

# Conclusion and Outlook

Over the past several decades, the development of cooling, trapping and manipulation of quantum gases enabled the exploration of various quantum phenomena and quantum simulation of condensed matter systems. Additionally, the recent use of sensitive spectroscopic techniques enabled precise probing of few-body physics, important for understanding the fine details in interacting systems. For example, in probing two-body interactions, state-of-the-art RF Rabi and Ramsey spectroscopy enabled precise determination of Feshbach dimer binding energies [103, 20], Feshbach resonance parameters [111] and two-body contact (short-ranged pair correlations) [150, 100]. Similarly, in probing three-body interactions, spectroscopic tools (RF and atom-loss) enabled probing Efimov trimer state locations [30], trimer binding energies [131, 132, 133, 151] and three-body contact [152, 21]. Such studies inspired the work discussed in this thesis, and my hope is that similar precision few-body measurements will follow in the near future.

In this thesis, I presented a new apparatus used for the production and probing of ultracold $^{39}$K gas samples. The immense stability of the machine, along with precise control of experimental conditions, enabled precision measurements of few-body physics in an interacting quantum gas. Having small experimental uncertainties and a good understanding of systematic error in our two- and three-body physics measurements allowed us to probe physics beyond predicted by universal theories.

For example, our precise measurements of dimer binding energies cannot be encapsulated by the universal $E_b = \hbar^2/(ma^2)$ equation or its version with small-order corrections. Therefore,

we required data comparison to predictions from a state-of-the-art coupled-channel model with real interaction potentials. Even then, to accurately match most of our measurements to within 1%, we performed a global fit to our binding energy data by fine-tuning the singlet and triplet potentials of the realistic model. Such fine-tuning is unprecedented [20, 111], considering that our data constrains the Feshbach resonance location to within 1.4 mG, a very small value compared to the Feshbach resonance width of 55 G. While such a match is impressive, due to our small experimental uncertainty, we still notice deviations between the observed and predicted values at large binding energies. Such discrepancies likely arise from incompleteness of the state-of-the-art coupled-channel model at short interatomic distances. Further theoretical advancements are needed to fully describe our precise binding energy measurements. Also, additional improvements to the current two-body models must be made in order to accurately describe all features in our dimer lifetime data.

Likewise, our precise Efimov trimer state location measurement cannot be predicted by van der Waals universality. A state-of-the-art coupled-channel three-body model, whose singlet and triplet potentials were set to equal that of the two-body model, was required to better understand our data [141]. Such a model is realistic enough that, for the first time in the field, it predicted an accurate value for the Efimov resonance width (inelasticity parameter) $\eta$. However, while now there is a better agreement for the measured and the newly predicted Efimov ground state location $a_-$, the agreement is not ideal due to our small experimental uncertainty, suggesting further theoretical advancements must be made. Lastly, the Efimov resonance peak suppression at high atom density, as observed by us and Ref. [45], needs a better understanding.

There are many possible future directions for exploring few-body and universal physics with ultracold Bose gases. For example, while there is some evidence of a second Efimov resonance feature (the first excited Efimov state) [43], it is the only observation in a homonuclear system and is affected by large systematic effects (e.g. finite-temperature and finite-range [147]). Further experimental evidence is needed to fully understand the robustness of the homonuclear universal Efimov spectrum spacing factor 22.7. Such experiments are difficult due to necessary nK-level

temperatures and small confinement-related effects [148]. NASA's Cold Atom Laboratory has plans [153] to cool down $^{39}$K atoms to temperatures $< 1\,\mathrm{nK}$ and measure the second Efimov resonance (the first excited state) in microgravity. Complimentary experiments can be performed on Earth: using magnetic field gradients or optical potentials (e.g. a repulsive potential formed by blue-detuned beams) to support atoms against gravity. In principle, one should be able to achieve few-nK temperatures and weak confinement with a $^{39}$K system like ours.

The Efimov trimer state phase diagram (see Fig. 6.1) is complex and has features that go beyond the loss maxima at the $a_-$ locations of the Efimov states at $a < 0$ [31, 46, 47, 48]. While the $a > 0$ region should be universally related to $a < 0$ features, the presence of a shallow dimer state and overall smaller length scales lead to additional complexity and potential of nonuniversal behavior. For example, the trimer states intersect (or get close to, as is the case for the Efimov ground state) the atom-dimer continuum at $a_*$ locations, leading to an enhanced inelastic atom-dimer scattering rate near $a_*$. These additional recombination pathways undergo quantum interference and lead to interference minima in the three-body recombination rate at $a_+$ locations, even in the absence of a dimer population. Our ongoing measurements of $a_*$ and $a_+$ near the 34 G Feshbach resonance are attempts to find nonuniversal physics related to our observed $a_-$ nonuniversal location.

Similarly, the concept of the Efimov effect has been extended to other few-body states (tied to individual three-body Efimov states) [154, 149, 155]. While some observations of four- and five-body states have been made [136, 33, 40, 137], precise measurements of such states will be of great interest. While our previous measurements were not able to resolve tetramer-related recombination peaks near $a_-$ (see the Efimov tetramer state phase diagram in Fig. 6.2), our ongoing measurements show preliminary evidence of four-body Efimov physics in the dimer-dimer inelastic scattering rate. Further improvements in the ability to prepare dense and cold dimer, atomic or mixture samples will aid such explorations.

Most Efimov features are probed via loss spectroscopy, measuring the inelastic component of scattering near Efimov resonances. It is enticing to be able to measure the enhanced elastic

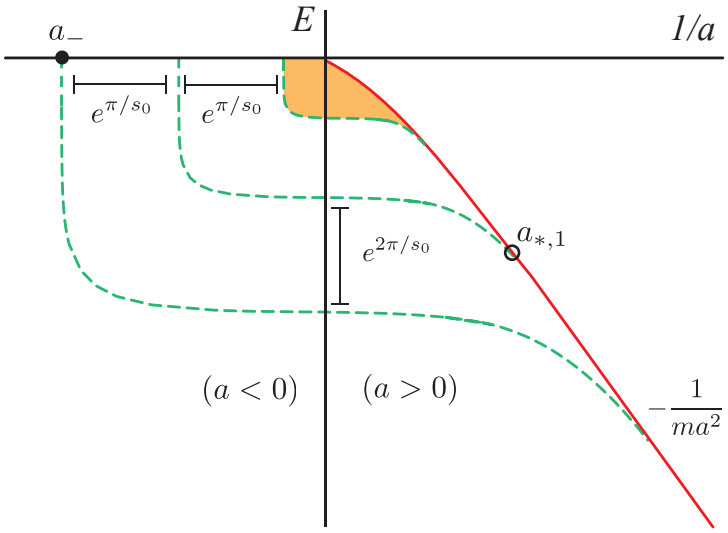


Figure 6.1: Predicted three-body Efimov spectrum. The Efimov ground state (bottom dashed green) intersects the three-atom continuum at $a_-$, while the succeeding excited state locations are determined by the Efimov spacing $e^{\pi/s_0} \approx 22.7$. For $a > 0$ region, the trimer states intersect the atom-dimer threshold (red) at $a_{*,j}$. However, note that the intersection for the Efimov ground state $a_{*,0}$ does not exist. Note that the states beyond the third excited state are not shown (orange region). This figure is a modified version of the illustration borrowed from [48].

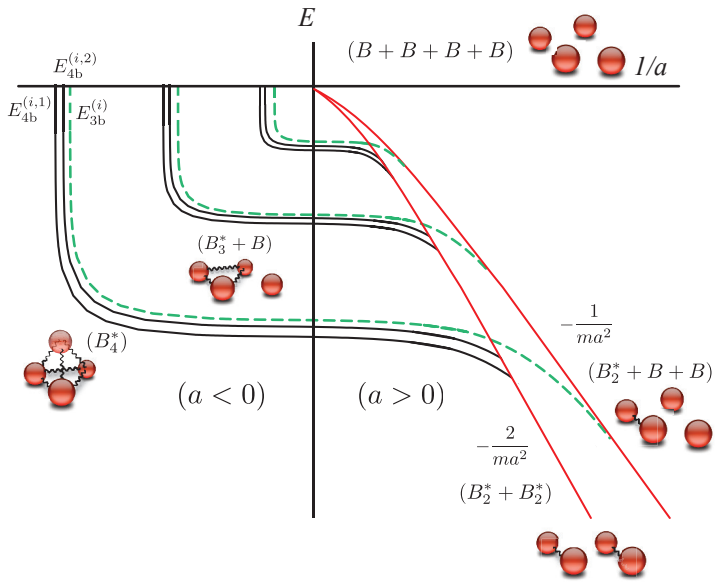


Figure 6.2: Predicted Efimov spectrum containing three- and four-body states. Universal theory predicts two tetramer states (solid black) tied to each trimer state (dashed green); the two ground tetramer states intersect the four-atom continuum at $0.43\,a_-$ and $0.90\,a_-$ locations [149]. Efimov tetramer states intersect the dimer-dimer threshold $2E_b = 2\hbar^2/(ma^2)$ in the $a > 0$ region. This figure is a modified version of illustration borrowed from [48].

component near an Efimov resonance. For example, such measurements can be performed near atom-dimer and dimer-dimer Efimov resonances, where Efimov states intersect their respective thresholds at $a > 0$. RF spectroscopy (Rabi or Ramsey) can be employed to measure energy shifts near such resonances, while cross-thermalization technique can be employed to probe the enhanced atom-dimer and dimer-dimer elastic collisional cross-sections. Again, any method measuring the elastic component near an Efimov resonance would be limited by the ability to prepare dense cold samples, and any method's signal contrast would be ultimately limited by the Efimov resonance width $\eta$ [48], whose value is related to the trimer lifetime. Due to the expected small signal contrast, one can enhance sensitivity by utilizing the two-photon dimer dissociation transition, discussed in Sec. 4.3.2, or by performing spectroscopy on the Feshbach dimer to deep molecular bound state transition; we are currently exploring the feasibility of such methods.

Another interesting direction would be to further develop spectroscopic tools to directly probe Efimov states. For example, authors of Ref. [134] have shown that a macroscopic population of Efimov trimers can be produced via magneto-association technique (a quench to unitarity). Given a sufficient trimer lifetime, the trimer binding energy can be extracted by RF spectroscopic means.

The topics of universal and few-body physics in interacting quantum systems have recently gained considerable amount of interest. Ongoing efforts in ultracold (including homonuclear bosonic, heteronuclear bosonic and distinguishable fermion), molecular and nuclear systems are exploring the question of how well universal aspects translate across all branches of physics [46, 47]. Recent tremendous progress has been aided by the development of experimental tools that enable more accurate and precise measurements of universal and few-body physics in ultracold systems. Our precise two- and three-body measurements reveal nonuniversal aspects that we hope the field will soon understand. I am confident that the universal and few-body physics fields will continue to progress and provide invaluable information on how the more complex many-body quantum systems behave.

## Bibliography


[1] Wolfgang Ketterle, N. J. Van Druten, Benjamin Bederson, and Herbert Walther. Evaporative cooling of trapped atoms. In Advances In Atomic, Molecular, and Optical Physics, volume 37, pages 181–236. Academic Press, January 1996.

[2] Harold J. Metcalf and Peter van der Straten. Laser Cooling and Trapping of Neutral Atoms. American Cancer Society, 2007.

[3] M. H. Anderson, J. R. Ensher, M. R. Matthews, C. E. Wieman, and E. A. Cornell. Observation of bose-einstein condensation in a dilute atomic vapor. Science, 269(5221):198, July 1995.

[4] B. DeMarco and D. S. Jin. Onset of fermi degeneracy in a trapped atomic gas. Science, 285(5434):1703, September 1999.

[5] Luigi De Marco, Giacomo Valtolina, Kyle Matsuda, William G. Tobias, Jacob P. Covey, and Jun Ye. A degenerate fermi gas of polar molecules. Science, 363(6429):853, February 2019.

[6] Seth Lloyd. Universal quantum simulators. Science, 273(5278):1073, August 1996.

[7] Immanuel Bloch, Jean Dalibard, and Sylvain Nascimbène. Quantum simulations with ultracold quantum gases. Nature Physics, 8:267, April 2012.

[8] I. M. Georgescu, S. Ashhab, and Franco Nori. Quantum simulation. Rev. Mod. Phys., 86:153–185, Mar 2014.

[9] Christian Gross and Immanuel Bloch. Quantum simulations with ultracold atoms in optical lattices. Science, 357(6355):995, September 2017.

[10] Torma Paivi and Sengstock Klaus. Quantum Gas Experiments: Exploring Many-Body States, volume 3. World Scientific, 2014.

[11] John L. Bohn, Ana Maria Rey, and Jun Ye. Cold molecules: Progress in quantum engineering of chemistry and quantum matter. Science, 357(6355):1002, September 2017.

[12] J. T. Stewart, J. P. Gaebler, and D. S. Jin. Using photoemission spectroscopy to probe a strongly interacting fermi gas. Nature, 454:744, August 2008.

[13] J. P. Gaebler, J. T. Stewart, T. E. Drake, D. S. Jin, A. Perali, P. Pieri, and G. C. Strinati. Observation of pseudogap behaviour in a strongly interacting fermi gas. Nature Physics, 6:569, July 2010.

[14] Yoav Sagi, Tara E. Drake, Rabin Paudel, Roman Chapurin, and Deborah S. Jin. Breakdown of the fermi liquid description for strongly interacting fermions. Phys. Rev. Lett., 114:075301, Feb 2015.

[15] Immanuel Bloch, Jean Dalibard, and Wilhelm Zwerger. Many-body physics with ultracold gases. Rev. Mod. Phys., 80:885–964, Jul 2008.

[16] Rahul Nandkishore and David A Huse. Many-body localization and thermalization in quantum statistical mechanics. Annu. Rev. Condens. Matter Phys., 6(1):15–38, 2015.

[17] Jean Dalibard, Fabrice Gerbier, Gediminas Juzeliūnas, and Patrik Öhberg. Colloquium: Artificial gauge potentials for neutral atoms. Rev. Mod. Phys., 83:1523–1543, Nov 2011.

[18] Victor Galitski, Gediminas Juzeliūnas, and Ian B Spielman. Artificial gauge fields with ultracold atoms. arXiv preprint arXiv:1901.03705, 2019.

[19] Cheng Chin, Rudolf Grimm, Paul Julienne, and Eite Tiesinga. Feshbach resonances in ultracold gases. Rev. Mod. Phys., 82(2):1225, 2010.

[20] G. Zürn, T. Lompe, A. N. Wenz, S. Jochim, P. S. Julienne, and J. M. Hutson. Precise characterization of $^6$Li feshbach resonances using trap-sideband-resolved rf spectroscopy of weakly bound molecules. Phys. Rev. Lett., 110:135301, Mar 2013.

[21] Richard J Fletcher, Raphael Lopes, Jay Man, Nir Navon, Robert P Smith, Martin W Zwierlein, and Zoran Hadzibabic. Two-and three-body contacts in the unitary bose gas. Science, 355(6323):377–380, 2017.

[22] Sylvain Nascimbène, Nir Navon, Frédéric Chevy, and Christophe Salomon. The equation of state of ultracold bose and fermi gases: a few examples. New Journal of Physics, 12(10):103026, October 2010.

[23] Eric Braaten, Daekyoung Kang, and Lucas Platter. Universal relations for identical bosons from three-body physics. Phys. Rev. Lett., 106:153005, Apr 2011.

[24] Eric Braaten. Universal relations for fermions with large scattering length. In The BCS-BEC Crossover and the Unitary Fermi Gas, pages 193–231. Springer, 2012.

[25] P. Makotyn, C. E. Klauss, D. L. Goldberger, E. A. Cornell, and D. S. Jin. Universal dynamics of a degenerate unitary bose gas. Nature Physics, 10:116, January 2014.

[26] Christoph Eigen, Jake A. P. Glidden, Raphael Lopes, Eric A. Cornell, Robert P. Smith, and Zoran Hadzibabic. Universal prethermal dynamics of bose gases quenched to unitarity. Nature, 563(7730):221–224, November 2018.

[27] Kerson Huang and C. N. Yang. Quantum-mechanical many-body problem with hard-sphere interaction. Phys. Rev., 105:767–775, Feb 1957.

[28] G. F. Gribakin and V. V. Flambaum. Calculation of the scattering length in atomic collisions using the semiclassical approximation. Phys. Rev. A, 48:546–553, Jul 1993.

[29] V. Efimov. Energy levels arising from resonant two-body forces in a three-body system. Phys. Lett. B, 33(8):563–564, December 1970.

[30] T. Kraemer, M. Mark, P. Waldburger, J. G. Danzl, C. Chin, B. Engeser, A. D. Lange, K. Pilch, A. Jaakkola, H.-C. Nägerl, and R. Grimm. Evidence for efimov quantum states in an ultracold gas of caesium atoms. Nature, 440:315, March 2006.

[31] Eric Braaten and H.-W. Hammer. Universality in few-body systems with large scattering length. Phys. Rep., 428(5):259–390, June 2006.

[32] M. Zaccanti, B. Deissler, C. D'Errico, M. Fattori, M. Jona-Lasinio, S. Müller, G. Roati, M. Inguscio, and G. Modugno. Observation of an efimov spectrum in an atomic system. Nat. Phys., 5:586, July 2009.

[33] Scott E. Pollack, Daniel Dries, and Randall G. Hulet. Universality in three- and four-body bound states of ultracold atoms. Science, 326(5960):1683, December 2009.

[34] Noam Gross, Zav Shotan, Servaas Kokkelmans, and Lev Khaykovich. Observation of universality in ultracold $^7$Li three-body recombination. Phys. Rev. Lett., 103:163202, Oct 2009.

[35] Noam Gross, Zav Shotan, Servaas Kokkelmans, and Lev Khaykovich. Nuclear-spin-independent short-range three-body physics in ultracold atoms. Phys. Rev. Lett., 105:103203, Sep 2010.

[36] Noam Gross, Zav Shotan, Olga Machtey, Servaas Kokkelmans, and Lev Khaykovich. Study of efimov physics in two nuclear-spin sublevels of 7li. Comptes Rendus Physique, 12(1):4–12, January 2011.

[37] M. Berninger, A. Zenesini, B. Huang, W. Harm, H.-C. Nägerl, F. Ferlaino, R. Grimm, P. S. Julienne, and J. M. Hutson. Universality of the three-body parameter for efimov states in ultracold cesium. Phys. Rev. Lett., 107:120401, Sep 2011.

[38] Sanjukta Roy, Manuele Landini, Andreas Trenkwalder, Giulia Semeghini, Giacomo Spagnolli, Andrea Simoni, Marco Fattori, Massimo Inguscio, and Giovanni Modugno. Test of the universality of the three-body efimov parameter at narrow feshbach resonances. Phys. Rev. Lett., 111(5):053202, 2013.

[39] B. S. Rem, A. T. Grier, I. Ferrier-Barbut, U. Eismann, T. Langen, N. Navon, L. Khaykovich, F. Werner, D. S. Petrov, F. Chevy, and C. Salomon. Lifetime of the bose gas with resonant interactions. Phys. Rev. Lett., 110:163202, Apr 2013.

[40] P. Dyke, S. E. Pollack, and R. G. Hulet. Finite-range corrections near a feshbach resonance and their role in the efimov effect. Phys. Rev. A, 88:023625, Aug 2013.

[41] R. Pires, J. Ulmanis, S. Häfner, M. Repp, A. Arias, E. D. Kuhnle, and M. Weidemüller. Observation of efimov resonances in a mixture with extreme mass imbalance. Phys. Rev. Lett., 112:250404, Jun 2014.

[42] Shih-Kuang Tung, Karina Jiménez-García, Jacob Johansen, Colin V. Parker, and Cheng Chin. Geometric scaling of efimov states in a $^6$Li$-^{133}$Cs mixture. Phys. Rev. Lett., 113:240402, Dec 2014.

[43] Bo Huang, Leonid A. Sidorenkov, Rudolf Grimm, and Jeremy M. Hutson. Observation of the second triatomic resonance in efimov's scenario. Phys. Rev. Lett., 112:190401, May 2014.

[44] R. A. W. Maier, M. Eisele, E. Tiemann, and C. Zimmermann. Efimov resonance and three-body parameter in a lithium-rubidium mixture. Phys. Rev. Lett., 115:043201, Jul 2015.

[45] L. J. Wacker, N. B. Jørgensen, K. T. Skalmstang, M. G. Skou, A. G. Volosniev, and J. J. Arlt. Temperature dependence of an efimov resonance in $^{39}$K. Phys. Rev. A, 98:052706, Nov 2018.

[46] Pascal Naidon and Shimpei Endo. Efimov physics: a review. Rep. Prog. Phys., 80(5):056001, 2017.

[47] Chris H. Greene, P. Giannakeas, and J. Pérez-Ríos. Universal few-body physics and cluster formation. Rev. Mod. Phys., 89:035006, Aug 2017.

[48] José P. D'Incao. Few-body physics in resonantly interacting ultracold quantum gases. Journal of Physics B: Atomic, Molecular and Optical Physics, 51(4):043001, January 2018.

[49] A. Derevianko, W. R. Johnson, M. S. Safronova, and J. F. Babb. High-precision calculations of dispersion coefficients, static dipole polarizabilities, and atom-wall interaction constants for alkali-metal atoms. Phys. Rev. Lett., 82:3589–3592, May 1999.

[50] Stephan Falke, Horst Knöckel, Jan Friebe, Matthias Riedmann, Eberhard Tiemann, and Christian Lisdat. Potassium ground-state scattering parameters and born-oppenheimer potentials from molecular spectroscopy. Phys. Rev. A, 78:012503, Jul 2008.

[51] Jia Wang, J. P. D'Incao, B. D. Esry, and Chris H. Greene. Origin of the three-body parameter universality in efimov physics. Phys. Rev. Lett., 108:263001, Jun 2012.

[52] Pascal Naidon, Shimpei Endo, and Masahito Ueda. Physical origin of the universal three-body parameter in atomic efimov physics. Phys. Rev. A, 90:022106, Aug 2014.

[53] D. S. Petrov. Three-boson problem near a narrow feshbach resonance. Phys. Rev. Lett., 93:143201, Sep 2004.

[54] Alexander O. Gogolin, Christophe Mora, and Reinhold Egger. Analytical solution of the bosonic three-body problem. Phys. Rev. Lett., 100:140404, Apr 2008.

[55] R. Schmidt, S. P. Rath, and W. Zwerger. Efimov physics beyond universality. Eur. Phys. J. B, 85(11):386, November 2012.

[56] Yujun Wang and Paul S. Julienne. Universal van der waals physics for three cold atoms near feshbach resonances. Nat. Phys., 10:768, August 2014.

[57] Christian Langmack, Richard Schmidt, and Wilhelm Zwerger. Efimov states near a feshbach resonance and the limits of van der waals universality at finite background scattering length. Phys. Rev. A, 97:033623, Mar 2018.

[58] Rabin Paudel. Probing Local Quantities in a Strongly Interacting Fermi Gas and the Construction of an Ultracold Fermi Gas Apparatus. PhD thesis, 2017.

[59] Chiara D'Errico, Matteo Zaccanti, Marco Fattori, Giacomo Roati, Massimo Inguscio, Giovanni Modugno, and Andrea Simoni. Feshbach resonances in ultracold 39 k. New Journal of Physics, 9(7):223, 2007.

[60] Huang Wu and Christopher J. Foot. Direct simulation of evaporative cooling. Journal of Physics B: Atomic, Molecular and Optical Physics, 29(8):L321–L328, April 1996.

[61] N. F. Mott and H. S. W. Massey. The theory of atomic collisions. 1949.

[62] John L. Bohn, James P. Burke, Chris H. Greene, H. Wang, P. L. Gould, and W. C. Stwalley. Collisional properties of ultracold potassium: Consequences for degenerate bose and fermi gases. Phys. Rev. A, 59:3660–3664, May 1999.

[63] Private communication John L. Bohn.

[64] J.P. Covey. Enhanced Optical and Electric Manipulation of a Quantum Gas of KRb Molecules. PhD thesis, 2018.

[65] C. Klempt, T. van Zoest, T. Henninger, O. Topic, E. Rasel, W. Ertmer, and J. Arlt. Ultraviolet light-induced atom desorption for large rubidium and potassium magneto-optical traps. Phys. Rev. A, 73:013410, Jan 2006.

[66] TG Tiecke. Properties of potassium. University of Amsterdam, The Netherlands, Thesis, pages 12–14, 2010.

[67] C. J. Cooper, G. Hillenbrand, J. Rink, C. G. Townsend, K. Zetie, and C. J. Foot. The temperature of atoms in a magneto-optical trap. Europhysics Letters (EPL), 28(6):397–402, November 1994.

[68] Private communication John L. Hall.

[69] L. Richter, H. Mandelberg, M. Kruger, and P. McGrath. Linewidth determination from self-heterodyne measurements with subcoherence delay times. IEEE Journal of Quantum Electronics, 22(11):2070–2074, 1986.

[70] Hanne Ludvigsen, Mika Tossavainen, and Matti Kaivola. Laser linewidth measurements using self-homodyne detection with short delay. Optics Communications, 155(1):180–186, October 1998.

[71] J. Catani, P. Maioli, L. De Sarlo, F. Minardi, and M. Inguscio. Intense slow beams of bosonic potassium isotopes. Phys. Rev. A, 73:033415, Mar 2006.

[72] Wolfgang Petrich, Michael H. Anderson, Jason R. Ensher, and Eric A. Cornell. Behavior of atoms in a compressed magneto-optical trap. J. Opt. Soc. Am. B, 11(8):1332–1335, August 1994.

[73] J. Dalibard and C. Cohen-Tannoudji. Laser cooling below the doppler limit by polarization gradients: simple theoretical models. J. Opt. Soc. Am. B, 6(11):2023–2045, November 1989.

[74] D. C. McKay, D. Jervis, D. J. Fine, J. W. Simpson-Porco, G. J. A. Edge, and J. H. Thywissen. Low-temperature high-density magneto-optical trapping of potassium using the open $4s \rightarrow 5p$ transition at 405 nm. Phys. Rev. A, 84:063420, Dec 2011.

[75] D. Rio Fernandes, F. Sievers, N. Kretzschmar, S. Wu, C. Salomon, and F. Chevy. Sub-doppler laser cooling of fermionic40k atoms in three-dimensional gray optical molasses. EPL (Europhysics Letters), 100(6):63001, December 2012.

[76] Dipankar Nath, R Kollengode Easwaran, G. Rajalakshmi, and C. S. Unnikrishnan. Quantum-interference-enhanced deep sub-doppler cooling of $^{39}$k atoms in gray molasses. Phys. Rev. A, 88:053407, Nov 2013.

[77] G. Grynberg and J.-Y. Courtois. Proposal for a magneto-optical lattice for trapping atoms in nearly-dark states. Europhysics Letters (EPL), 27(1):41–46, July 1994.

[78] G. Salomon, L. Fouché, P. Wang, A. Aspect, P. Bouyer, and T. Bourdel. Gray-molasses cooling of39k to a high phase-space density. EPL (Europhysics Letters), 104(6):63002, December 2013.

[79] Manuele Landini. A tunable Bose-Einstein condensate for quantum interferometry. PhD thesis, University of Trento, 2012.

[80] Wolfgang Petrich, Michael H. Anderson, Jason R. Ensher, and Eric A. Cornell. Stable, tightly confining magnetic trap for evaporative cooling of neutral atoms. Phys. Rev. Lett., 74:3352–3355, Apr 1995.

[81] C. R. Monroe, E. A. Cornell, C. A. Sackett, C. J. Myatt, and C. E. Wieman. Measurement of cs-cs elastic scattering at t=30 $\mu$k. Phys. Rev. Lett., 70:414–417, Jan 1993.

[82] B. DeMarco, J. L. Bohn, J. P. Burke, M. Holland, and D. S. Jin. Measurement of $p$-wave threshold law using evaporatively cooled fermionic atoms. Phys. Rev. Lett., 82:4208–4211, May 1999.

[83] M. Landini, S. Roy, G. Roati, A. Simoni, M. Inguscio, G. Modugno, and M. Fattori. Direct evaporative cooling of $^{39}$k atoms to bose-einstein condensation. Phys. Rev. A, 86:033421, Sep 2012.

[84] S. J. M. Kuppens, K. L. Corwin, K. W. Miller, T. E. Chupp, and C. E. Wieman. Loading an optical dipole trap. Phys. Rev. A, 62:013406, Jun 2000.

[85] D. Comparat, A. Fioretti, G. Stern, E. Dimova, B. Laburthe Tolra, and P. Pillet. Optimized production of large bose-einstein condensates. Phys. Rev. A, 73:043410, Apr 2006.

[86] Li-Wei Wei. High-power laser system for Advanced Virgo gravitational wave detector : coherently combined master oscillator fiber power amplifiers. Theses, Université Nice Sophia Antipolis, December 2015.

[87] S Blatt, A Mazurenko, MF Parsons, CS Chiu, F Huber, and M Greiner. Low-noise optical lattices for ultracold li 6. Physical Review A, 92(2):021402, 2015.

[88] TA Savard, KM O'hara, and JE Thomas. Laser-noise-induced heating in far-off resonance optical traps. Physical Review A, 56(2):R1095, 1997.

[89] C.J. Foot and D.P.C.J. Foot. Atomic Physics. Oxford Master Series in Physics. OUP Oxford, 2005.

[90] B.H. Bransden, C.J. Joachain, and T.J. Plivier. Physics of Atoms and Molecules. Pearson Education. Prentice Hall, 2003.

[91] L. Allen and J.H. Eberly. Optical Resonance and Two-level Atoms. Dover books on physics and chemistry. Dover, 1987.

[92] James R Janesick, Kenneth P Klaasen, and Tom Elliott. Charge-coupled-device charge-collection efficiency and the photon-transfer technique. Optical engineering, 26(10):261072, 1987.

[93] Sebastian Alexander Blatt. Ultracold Collisions and Fundamental Physics with Strontium. PhD thesis, 2011.

[94] Heather J Lewandowski, DM Harber, Dwight L Whitaker, and Eric A Cornell. Simplified system for creating a bose–einstein condensate. Journal of low temperature physics, 132(5-6):309–367, 2003.

[95] G. Reinaudi, T. Lahaye, Z. Wang, and D. Guéry-Odelin. Strong saturation absorption imaging of dense clouds of ultracold atoms. Opt. Lett., 32(21):3143–3145, November 2007.

[96] D. Genkina, L. M. Aycock, B. K. Stuhl, H.-I. Lu, R. A. Williams, and I. B. Spielman. Feshbach enhanceds-wave scattering of fermions: direct observation with optimized absorption imaging. New Journal of Physics, 18(1):013001, December 2015.

[97] Jacob Johansen, BJ DeSalvo, Krutik Patel, and Cheng Chin. Testing universality of efimov physics across broad and narrow feshbach resonances. Nat. Phys., 13(8):731, 2017.

[98] C. A. Regal and D. S. Jin. Measurement of positive and negative scattering lengths in a fermi gas of atoms.

[99] J. Ulmanis, S. Häfner, R. Pires, E. D. Kuhnle, M. Weidemüller, and E. Tiemann. Universality of weakly bound dimers and efimov trimers close to li-cs feshbach resonances. New Journal of Physics, 17(5):055009, 2015.

[100] RJ Wild, P Makotyn, JM Pino, EA Cornell, and DS Jin. Measurements of tan's contact in an atomic bose-einstein condensate. Phys. Rev. Lett., 108(14):145305, 2012.

[101] Cindy A. Regal, Christopher Ticknor, John L. Bohn, and Deborah S. Jin. Creation of ultracold molecules from a fermi gas of atoms. Nature, 424:47, July 2003.

[102] Elizabeth A. Donley, Neil R. Claussen, Sarah T. Thompson, and Carl E. Wieman. Atom-molecule coherence in a bose-einstein condensate. Nature, 417:529, May 2002.

[103] N. R. Claussen, S. J. J. M. F. Kokkelmans, S. T. Thompson, E. A. Donley, E. Hodby, and C. E. Wieman. Very-high-precision bound-state spectroscopy near a $^{85}$Rb feshbach resonance. Phys. Rev. A, 67:060701, Jun 2003.

[104] S. T. Thompson, E. Hodby, and C. E. Wieman. Ultracold molecule production via a resonant oscillating magnetic field. Phys. Rev. Lett., 95:190404, Nov 2005.

[105] S. B. Papp and C. E. Wieman. Observation of heteronuclear feshbach molecules from a $^{85}\mathrm{Rb} - -^{87}\mathrm{Rb}$ gas. Phys. Rev. Lett., 97:180404, Oct 2006.

[106] C. Klempt, T. Henninger, O. Topic, M. Scherer, L. Kattner, E. Tiemann, W. Ertmer, and J. J. Arlt. Radio-frequency association of heteronuclear feshbach molecules. Phys. Rev. A, 78:061602, Dec 2008.

[107] C. Weber, G. Barontini, J. Catani, G. Thalhammer, M. Inguscio, and F. Minardi. Association of ultracold double-species bosonic molecules. Phys. Rev. A, 78:061601, Dec 2008.

[108] A. D. Lange, K. Pilch, A. Prantner, F. Ferlaino, B. Engeser, H.-C. Nägerl, R. Grimm, and C. Chin. Determination of atomic scattering lengths from measurements of molecular binding energies near feshbach resonances. Phys. Rev. A, 79:013622, Jan 2009.

[109] Cheng Chin and Paul S. Julienne. Radio-frequency transitions on weakly bound ultracold molecules. Phys. Rev. A, 71:012713, Jan 2005.

[110] M. Bartenstein, A. Altmeyer, S. Riedl, R. Geursen, S. Jochim, C. Chin, J. Hecker Denschlag, R. Grimm, A. Simoni, E. Tiesinga, C. J. Williams, and P. S. Julienne. Precise determination of $^6$Li cold collision parameters by radio-frequency spectroscopy on weakly bound molecules. Phys. Rev. Lett., 94:103201, Mar 2005.

[111] Paul S. Julienne and Jeremy M. Hutson. Contrasting the wide feshbach resonances in $^6$Li and $^7$Li. Phys. Rev. A, 89:052715, May 2014.

[112] Constantine Shkedrov, Yanay Florshaim, Gal Ness, Andrey Gandman, and Yoav Sagi. High-sensitivity rf spectroscopy of a strongly interacting fermi gas. Phys. Rev. Lett., 121:093402, Aug 2018.

[113] Jens Herbig, Tobias Kraemer, Michael Mark, Tino Weber, Cheng Chin, Hanns-Christoph Nägerl, and Rudolf Grimm. Preparation of a pure molecular quantum gas. Science, 301(5639):1510, September 2003.

[114] E. Hodby, S. T. Thompson, C. A. Regal, M. Greiner, A. C. Wilson, D. S. Jin, E. A. Cornell, and C. E. Wieman. Production efficiency of ultracold feshbach molecules in bosonic and fermionic systems. Phys. Rev. Lett., 94:120402, Mar 2005.

[115] Steven A. Moses, Jacob P. Covey, Matthew T. Miecnikowski, Bo Yan, Bryce Gadway, Jun Ye, and Deborah S. Jin. Creation of a low-entropy quantum gas of polar molecules in an optical lattice. Science, 350(6261):659, November 2015.

[116] Thorsten Köhler, Krzysztof Góral, and Paul S. Julienne. Production of cold molecules via magnetically tunable feshbach resonances. Rev. Mod. Phys., 78:1311–1361, Dec 2006.

[117] Elizabeth A. Donley, Neil R. Claussen, Simon L. Cornish, Jacob L. Roberts, Eric A. Cornell, and Carl E. Wieman. Dynamics of collapsing and exploding bose-einstein condensates. Nature, 412:295, July 2001.

[118] Tino Weber, Jens Herbig, Michael Mark, Hanns-Christoph Nägerl, and Rudolf Grimm. Three-body recombination at large scattering lengths in an ultracold atomic gas. Phys. Rev. Lett., 91:123201, Sep 2003.

[119] S. T. Thompson, E. Hodby, and C. E. Wieman. Spontaneous dissociation of $^{85}$Rb feshbach molecules. Phys. Rev. Lett., 94:020401, Jan 2005.

[120] Thorsten Köhler, Eite Tiesinga, and Paul S. Julienne. Spontaneous dissociation of long-range feshbach molecules. Phys. Rev. Lett., 94:020402, Jan 2005.

[121] Eric Braaten and H.-W. Hammer. Enhanced dimer relaxation in an atomic and molecular bose-einstein condensate. Phys. Rev. A, 70:042706, Oct 2004.

[122] J. P. D'Incao and B. D. Esry. Scattering length scaling laws for ultracold three-body collisions. Phys. Rev. Lett., 94:213201, Jun 2005.

[123] F. Ferlaino, S. Knoop, M. Mark, M. Berninger, H. Schöbel, H.-C. Nägerl, and R. Grimm. Collisions between tunable halo dimers: Exploring an elementary four-body process with identical bosons. Phys. Rev. Lett., 101:023201, Jul 2008.

[124] J. P. D'Incao, J. von Stecher, and Chris H. Greene. Universal four-boson states in ultracold molecular gases: Resonant effects in dimer-dimer collisions. Phys. Rev. Lett., 103:033004, Jul 2009.

[125] T. D. Lee and C. N. Yang. Many-body problem in quantum mechanics and quantum statistical mechanics. Phys. Rev., 105:1119–1120, Feb 1957.

[126] Zbigniew Idziaszek and Tommaso Calarco. Analytical solutions for the dynamics of two trapped interacting ultracold atoms. Phys. Rev. A, 74:022712, Aug 2006.

[127] Krzysztof Jachymski and Paul S. Julienne. Analytical model of overlapping feshbach resonances. Phys. Rev. A, 88:052701, Nov 2013.

[128] Private communication Paul S. Julienne, José P. D'Incao and Jeremy M. Hutson.

[129] Bo Gao. Binding energy and scattering length for diatomic systems. Journal of Physics B: Atomic, Molecular and Optical Physics, 37(21):4273, 2004.

[130] John L. Bohn and P. S. Julienne. Prospects for influencing scattering lengths with far-off-resonant light. Phys. Rev. A, 56:1486–1491, Aug 1997.

[131] Thomas Lompe, Timo B. Ottenstein, Friedhelm Serwane, Andre N. Wenz, Gerhard Zürn, and Selim Jochim. Radio-frequency association of efimov trimers. Science, 330(6006):940, November 2010.

[132] Shuta Nakajima, Munekazu Horikoshi, Takashi Mukaiyama, Pascal Naidon, and Masahito Ueda. Measurement of an efimov trimer binding energy in a three-component mixture of $^6$Li. Phys. Rev. Lett., 106:143201, Apr 2011.

[133] Olga Machtey, Zav Shotan, Noam Gross, and Lev Khaykovich. Association of efimov trimers from a three-atom continuum. Phys. Rev. Lett., 108:210406, May 2012.

[134] Catherine E. Klauss, Xin Xie, Carlos Lopez-Abadia, José P. D'Incao, Zoran Hadzibabic, Deborah S. Jin, and Eric A. Cornell. Observation of efimov molecules created from a resonantly interacting bose gas. Phys. Rev. Lett., 119:143401, Oct 2017.

[135] S. Knoop, F. Ferlaino, M. Mark, M. Berninger, H. Schöbel, H.-C. Nägerl, and R. Grimm. Observation of an efimov-like trimer resonance in ultracold atom-dimer scattering. Nature Physics, 5:227, February 2009.

[136] F. Ferlaino, S. Knoop, M. Berninger, W. Harm, J. P. D'Incao, H.-C. Nägerl, and R. Grimm. Evidence for universal four-body states tied to an efimov trimer. Phys. Rev. Lett., 102:140401, Apr 2009.

[137] Alessandro Zenesini, Bo Huang, Martin Berninger, Stefan Besler, Hanns-Christoph Nägerl, Francesca Ferlaino, Rudolf Grimm, Chris H. Greene, and Javier von Stecher. Resonant five-body recombination in an ultracold gas of bosonic atoms. New Journal of Physics, 15(4):043040, 2013.

[138] Francesca Ferlaino and Rudolf Grimm. Forty years of efimov physics: How a bizarre prediction turned into a hot topic. Physics, 3, January 2010.

[139] Yujun Wang, Jia Wang, J. P. D'Incao, and Chris H. Greene. Universal three-body parameter in heteronuclear atomic systems. Phys. Rev. Lett., 109:243201, Dec 2012.

[140] Juris Ulmanis, Stephan Häfner, Rico Pires, Eva D. Kuhnle, Yujun Wang, Chris H. Greene, and Matthias Weidemüller. Heteronuclear efimov scenario with positive intraspecies scattering length. Phys. Rev. Lett., 117:153201, Oct 2016.

[141] Private communication José P. D'Incao.

[142] P. O. Fedichev, M. W. Reynolds, and G. V. Shlyapnikov. Three-body recombination of ultracold atoms to a weakly bound $s$ level. Phys. Rev. Lett., 77:2921–2924, Sep 1996.

[143] B. D. Esry, Chris H. Greene, and James P. Burke. Recombination of three atoms in the ultracold limit. Phys. Rev. Lett., 83:1751–1754, Aug 1999.

[144] D. S. Petrov and F. Werner. Three-body recombination in heteronuclear mixtures at finite temperature. Phys. Rev. A, 92:022704, Aug 2015.

[145] Private communication D. S. Petrov.

[146] Eric Braaten, H.-W. Hammer, Daekyoung Kang, and Lucas Platter. Three-body recombination of identical bosons with a large positive scattering length at nonzero temperature. Phys. Rev. A, 78:043605, Oct 2008.

[147] Bo Huang, Leonid A Sidorenkov, Rudolf Grimm, et al. Finite-temperature effects on a triatomic efimov resonance in ultracold cesium. Phys. Rev. A, 91(6):063622, 2015.

[148] Jesper Levinsen, Pietro Massignan, and Meera M. Parish. Efimov trimers under strong confinement. Phys. Rev. X, 4:031020, Jul 2014.

[149] J. von Stecher, J. P. D'Incao, and Chris H. Greene. Signatures of universal four-body phenomena and their relation to the efimov effect. Nature Physics, 5:417, April 2009.

[150] J. T. Stewart, J. P. Gaebler, T. E. Drake, and D. S. Jin. Verification of universal relations in a strongly interacting fermi gas. Phys. Rev. Lett., 104:235301, Jun 2010.

[151] Yaakov Yudkin, Roy Elbaz, P Giannakeas, Chris H Greene, and Lev Khaykovich. A coherent superposition of feshbach dimers and efimov trimers. arXiv preprint arXiv:1901.02268, 2019.

[152] D. Hudson Smith, Eric Braaten, Daekyoung Kang, and Lucas Platter. Two-body and three-body contacts for identical bosons near unitarity. Phys. Rev. Lett., 112:110402, Mar 2014.

[153] Ethan R. Elliott, Markus C. Krutzik, Jason R. Williams, Robert J. Thompson, and David C. Aveline. Nasa's cold atom lab (cal): system development and ground test status. npj Microgravity, 4(1):16, August 2018.

[154] H-W Hammer and L Platter. Universal properties of the four-body system with large scattering length. The European Physical Journal A, 32(1):113–120, 2007.

[155] Javier von Stecher. Five- and six-body resonances tied to an efimov trimer. Phys. Rev. Lett., 107:200402, Nov 2011.